The Hydrodynamic Performance of an Oscillating Water Column Wave Energy Converter

Iain George Morrison

Doctor of Philosophy

The University of Edinburgh

1995

Abstract

A full description of the application of image shifting to the technique of particle image velocimetry (PIV) is given along with a discussion of the design and construction of a versatile rotating mirror image shifting system. The use of such a shifting system leads to systematic errors in the measured fluid velocities and it is shown that these errors can be accounted for and that a correction may be applied to eliminate them. A description of PIV itself and, in particular, the application of PIV to a study of the internal kinematics of an OWC in a wave flume is also provided. A simple semi-empirical model of the response of an OWC to a given wave climate is developed and its predictions are compared with air pressure and water level measurements obtained during flume tests of a model OWC. Finally detailed PIV time-series measurements, incorporating image shifting, are made of the flow within the OWC chamber and it is shown that as much as 7% of the wave energy may be lost due to viscous dissipation within the strong vortices which are formed around the submerged lip of the front wall of the model.

Declaration

This Thesis has been composed by me and, except where stated, the work contained is my own.

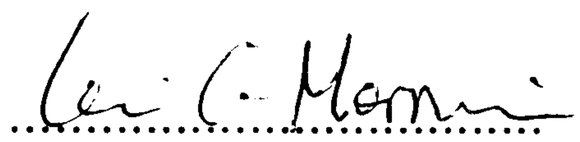

Iain Morrison

September, 1995

Acknowledgments

I would like to thank the following people for their assistance and advice during the course of this project: my supervisor, Clive Greated, for his guidance throughout; Paul Stansell for patiently reading and correcting large chunks of this thesis; Trevor Whittaker and Gerald Muller at Queens University for their help in the initial stages; Frank Morris for his invaluable technical help, and the rest of the technicians.

On a more personal note I would like to thank Cathe, my office mates, Heather and Anne and finally Julian, without whose positive attitude to beer this thesis would undoubtedly have been finished much sooner.

This research project was funded by the SERC and their support is gratefully acknowledged.

For my parents

Contents

Chapter 1

Introduction

1.1 Subject background

Although serious public interest in wave power dates only from the energy crises of the 1970s the concept of energy from the sea has been with us for over 200 years, resulting in over 350 patents in the United Kingdom alone [1]. Many of the proposed designs have proved to be impractical or, as in the case of the Salter duck [45], ingenious but overly complex. However a deep water device such as the duck, with its very high conversion efficiencies, probably represents the future of wave power once the engineering expertise has been developed and simpler devices have proved that this is a viable resource. Of the very few wave energy devices which appear to be commercially viable [46] the oscillating water column wave energy converter (OWC) [15] has received the greatest international attention.

Natural energy sources provide a challenge to designers and engineers in such cases where little or no control can be exerted over the rate of energy supply, and problems which arise may be difficult to overcome. In a reasonably controllable system such as a nuclear power station the steam pressure being fed to the turbines

is carefully governed to ensure that they are generating at peak efficiency. However in the case of the OWC one must make optimum use of the energy available by designing a device whose peak performance is realised within the portion of the wave frequency spectrum which contains the greatest energy. This means that it is impossible to extract all the available energy and so it becomes more important to realise a high efficiency of conversion from wave energy to electrical energy.

Many of the commercial advantages of the OWC stem from an extremely simple mechanism for energy extraction: the action of the waves on a chamber of air with an opening to the sea below mean water level causes pressure fluctuations within this volume of air; a second opening above mean water level leads to a turbine where electricity is generated by the movement of air to and from the chamber. A diagram of an OWC device is shown in figure 1.1.

OWC designs have been proposed both for deep and shallow water locations. The deep water devices have been floating structures such as those proposed by the Queen's University team [33], however these designs have since been abandoned due to problems with the mooring systems. Shallow water designs have included both sea bed mounted devices such as the National Engineering Laboratory breakwater system [33, 2] and shoreline devices such as those built by Queen's University on Islay [57, 58] and Kværner Brug on the Norwegian coast [8]. Unfortunately, however, this OWC capsised and sank in heavy seas.

In August 1995, amidst a great deal of press coverage, a floating OWC called the OSPREY was launched off the coast of Scotland. It was intended to supply electricity to the national grid from its twin turbines but, unfortunately, sank after only a few days at sea.

Takahashi et al [53] have successfully incorporated a 60 kilowatt device into a breakwater and this appears to be an intelligent situation for an OWC since it

provides the secondary function of reducing the destructive wave loads on the breakwater itself. Shore mounted devices have the advantages of cheaper construction and easy access, offset against a large wave power loss due to breaking and bottom friction as the waves approach the shore.

While several OWC devices worldwide are now operational and supplying energy to their respective local grids, in general they have failed to realise their predicted power conversion efficiencies. The axisymmetric Wells turbine [42] has now been widely adopted in OWC applications and it has demonstrated conversion efficiencies of over 80% but rather less is known about hydrodynamic losses within an OWC chamber. Studies have suggested the existence of energy dissipating vortices from the lower edge of semi-submerged vertical barriers on which surface waves are incident [51, 55]. It is important to study the effect of these sources of hydrodynamic energy loss on the overall conversion efficiency of an OWC.

1.2 Study of an OWC

1.2.1 Limitations

Physical experiments are performed with a view to increasing ones understanding of the subject of interest. In order to obtain the maximum amount of relevant information one would ideally like to perform experiments at full scale. However in modelling the behaviour of a super tanker at sea or studying a turbulent wake in the lee of a factory chimney, for example, such an approach is clearly impractical. Even at more modest scales, financial or technical restrictions may dictate the dimensions at which experiments must be performed.

In a wave flume experiments are typically carried out at a scale of about one or two

orders of magnitude less than the phenomena under study. The major parameters applying to waves in the flume can be modelled by Froude scaling but independent factors such as bed roughness are difficult to scale reliably and often have to be ignored for simplicity.

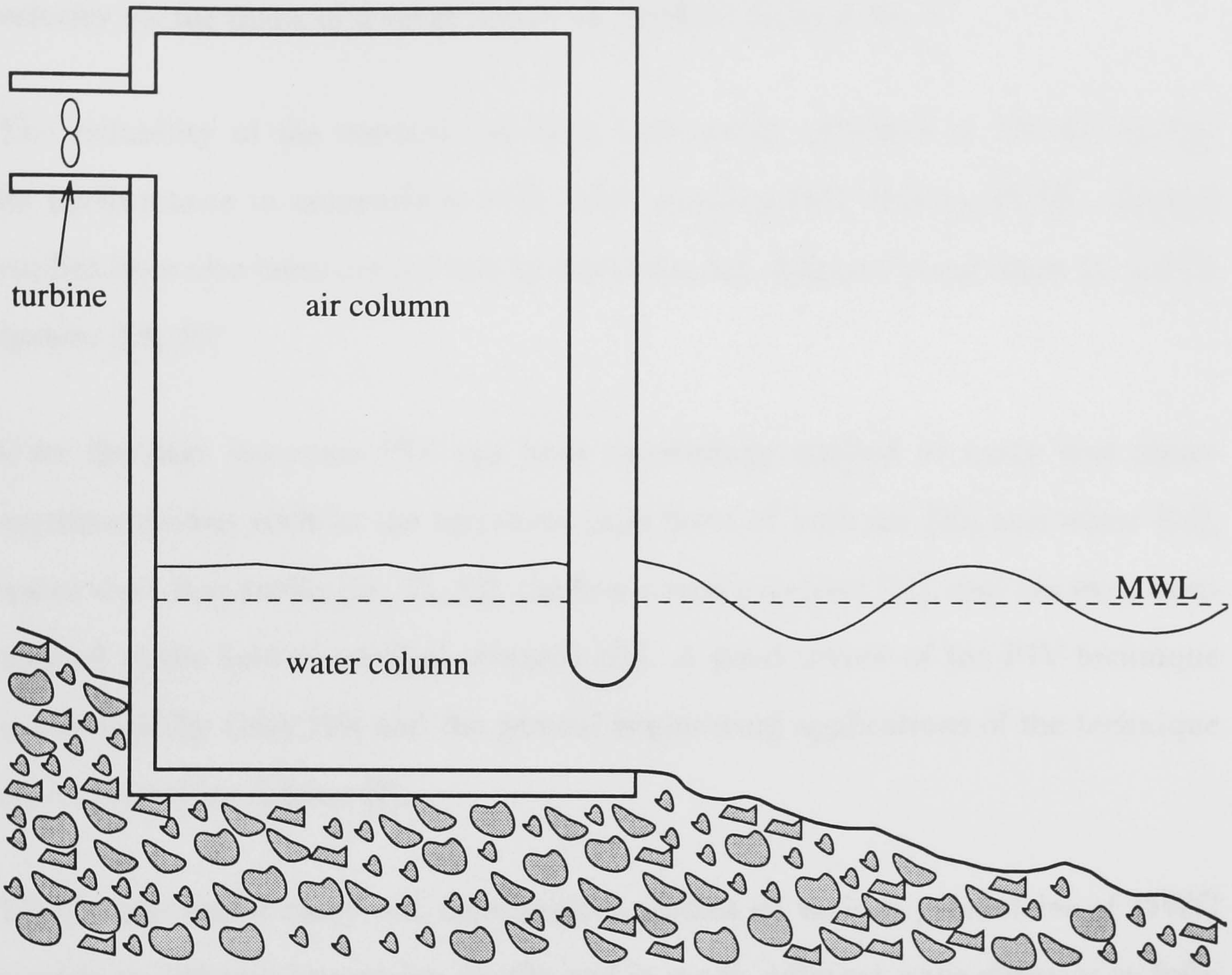

FIGURE 1.1: Diagram of an oscillating water column wave energy converter

There are many variations of OWC design in existence and each has its own individual characteristics. This study concentrates on a simplified 1/36 scale model of the prototype built by Queen's University on Islay. The working prototype has a front wall which is placed at an angle of 57 degrees to the vertical but this is purely intended to reduce the wave forces upon it. The scale model has this wall set vertically - a condition imposed by limitations of the flow measurement system as discussed in section 2.5.3.

1.2.2 Experimental techniques

Experimental velocity measurements in this study have been made with particle image velocimetry (PIV) [5, 6, 21, 18] which yields simultaneous, high resolution velocity vector maps of a large region of the flow under study.

The reliability of the method has been extensively reviewed [3, 38, 41] as has its performance in comparison with other measurement techniques [3]. Several studies have also been carried out to determine the optimum parameters for a PIV system [28, 26].

Over the past ten years PIV has been successfully applied to many flow measurement studies such as the turbulent pipe flows of both air [35] and water [14], water wave kinematics [18, 49, 52], the flow round pipelines [11], and has even been applied in the field of medical research [25]. A good review of the PIV technique is provided by Gray [19] and the general engineering applications of the technique are reviewed by Adrian [7].

Ideally one would carry out comparative studies of various geometries of OWC models at different immersion depths and in many different wave climates to fully understand the flow kinematics of these devices. However the pressures of time made that impossible within this study since the two hours taken to analyse a PIV negative and produce the velocity field plot is extremely large in comparison with the time taken to initially capture the image on film. This represents something of a bottleneck for the PIV process. However this problem has been addressed by Gray [20] in the development of a totally mathematical analysis system which utilises a digitised image of the PIV negative and calculates the velocity field plot without requiring the slow moving parts of the present analysis system. This reduces the time taken to analyse each frame by a factor of about thirty and when

coupled with a high quality CCD camera in place of a conventional one the time taken to develop films is eliminated, bringing us a step closer to real time full field velocity measurements. However the future of non-intrusive flow measurements probably lies with video based systems when the increasing power of personal computers makes particle tracking systems a viable option.

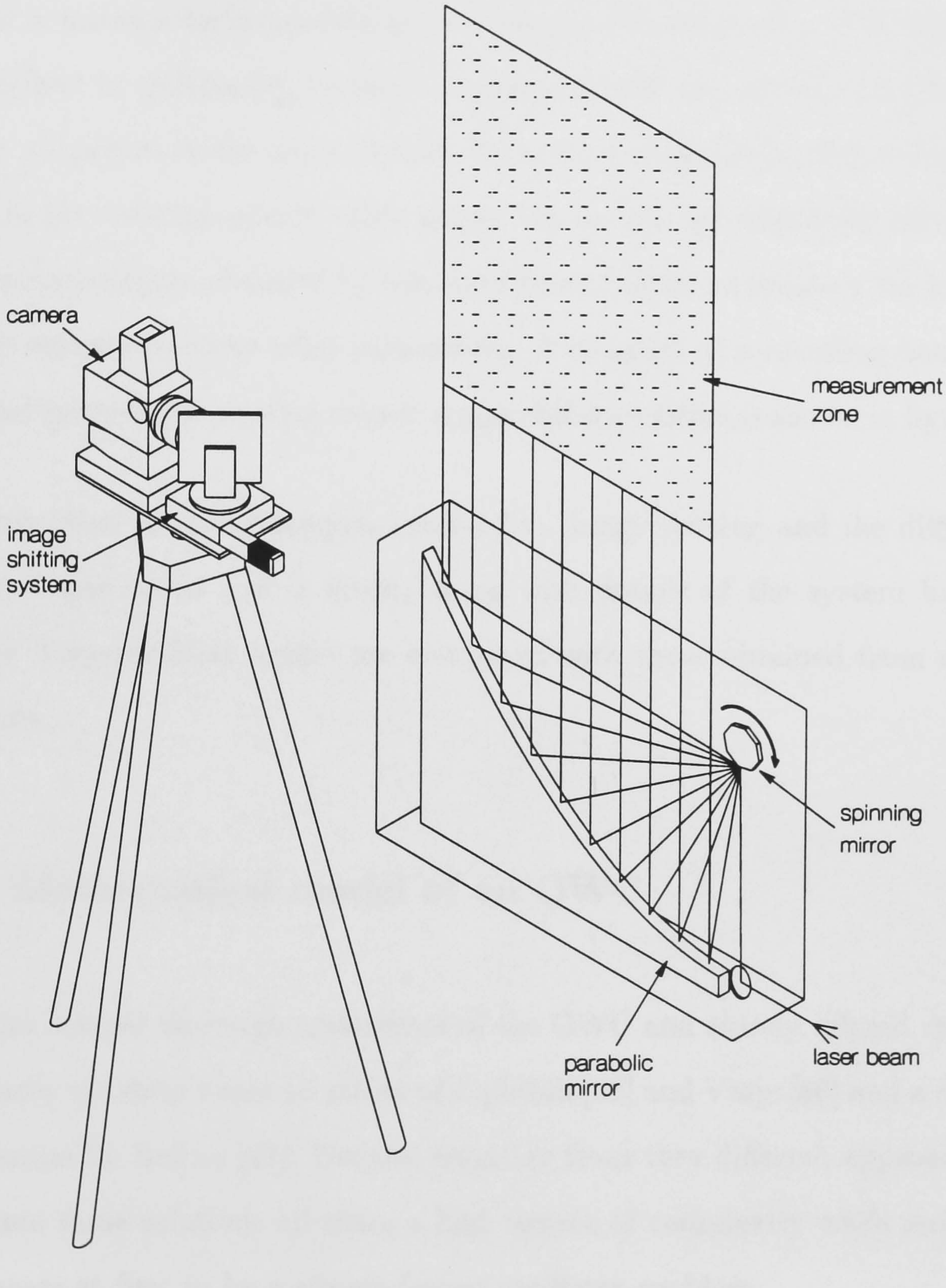

FIGURE 1.2: Diagram of a scanning beam PIV system incorporating a rotating mirror image shifting system

1.3 Thesis context

1.3.1 Image shifting applied to PIV

Measurements obtained using PIV have been enhanced in this study by the inclusion of a purpose built rotating mirror image shifting system. This approach, first described by Adrian [4], involves imposing an effective constant artificial velocity on all points in the measurement zone by photographing the reflection of the flow in the rotating mirror. This allows the directional ambiguity inherent in all PIV measurements obtained by autocorrelation [13] to be resolved while simultaneously optimising some other parameters. A diagram of a scanning beam PIV system incorporating a rotating mirror image shifting system is shown in figure 1.2.

A full discussion of the techniques involved in image shifting and the difficulties which arise due to its use is given, along with details of the system built for the study. Experimental results are compared with those obtained from derived expressions.

1.3.2 Mathematical model of an OWC

There exist several thorough treatments of the OWC and closely related systems, most notably the deep water solutions of Lighthill [32] and Vinje [56] and a shallow water solution by Reitan [43]. Despite resulting from very different approaches to the problem these solutions all share a high degree of complexity while modelling what appears at first to be a simple forced oscillator problem.

Here we consider a simple mechanical model of the OWC and attempt to solve it numerically. Some difficulties with such an approach soon become apparent and

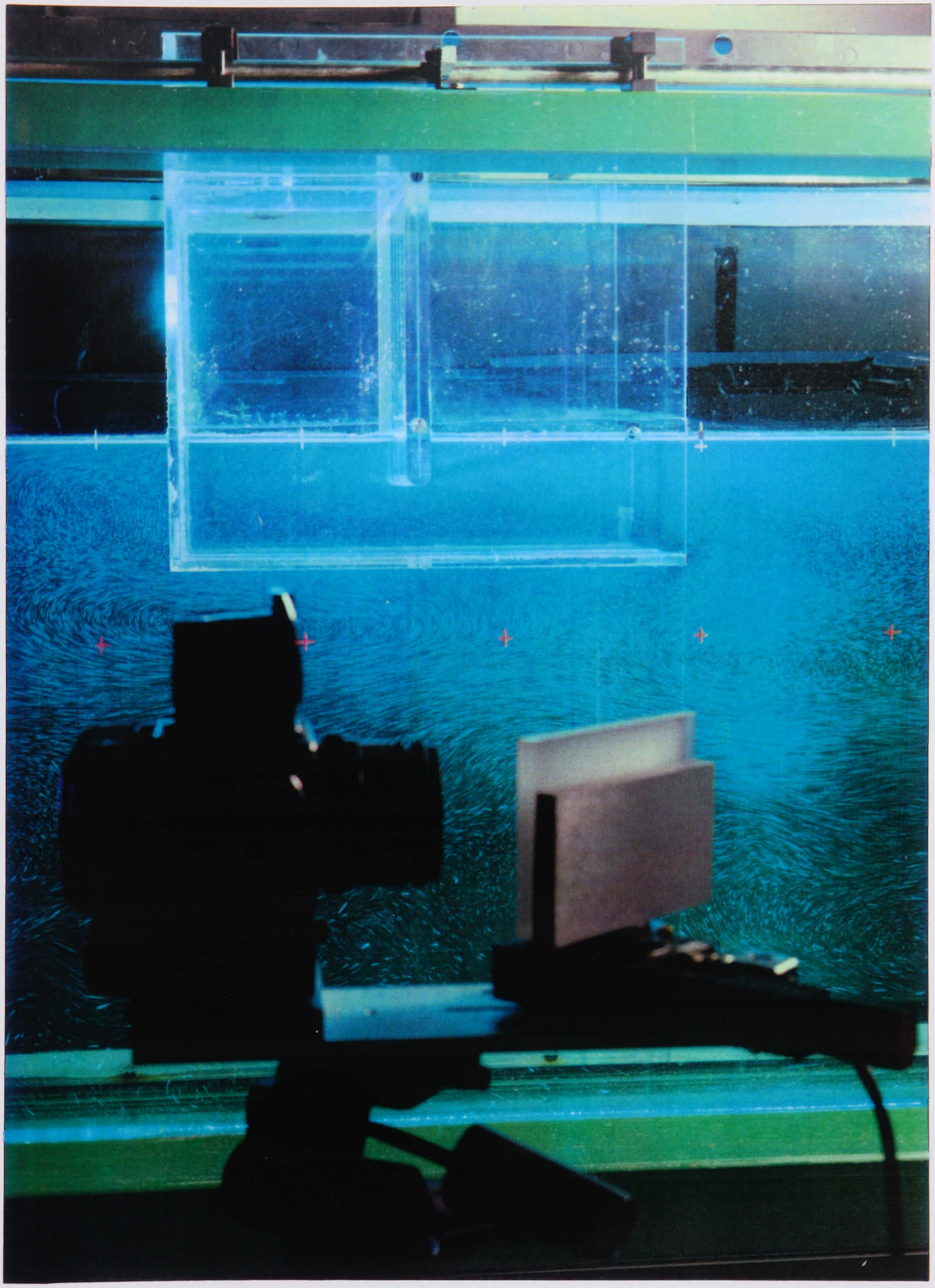

FIGURE 1.3: The OWC model in the flume illuminated by a one metre wide light sheet

as a result a semi-empirical model is proposed.

The numerical model is intended as a means of predicting some of the behaviour of the physical model to provide a basis for a predictive theory which could be applied at other scales.

1.3.3 Flume experiments on an OWC

OWC models have been tested in narrow wave flumes in the past but this study applies the PIV measurement technique for the first time, enabling more direct measurements of the energy dissipation rates to be made. The inclusion of image shifting allows detailed velocity field plots to be produced. This method of data presentation therefore provides a more easily accessible summary of the qualitative features of the flow than is possible with simpler flow visualisation techniques.

A series of flume experiments are carried out, measuring chamber air pressures and water levels in an attempt to provide empirical data for the mathematical model and to investigate its predictions. Data gathered from PIV experiments and backed by measurements of wave reflection from the device are used to infer the rates of energy dissipation due to hydrodynamic losses.

Chapter 2

Particle image velocimetry (PIV)

2.1 Introduction

PIV is a highly accurate two stage method of producing detailed two-dimensional vector representations of flows in both liquids and gases. Its use is increasing in laboratories worldwide but laser doppler anemometry (LDA) is still more widely used since it is not restricted by the need for a purpose built facility.

A number of researchers at the University of Edinburgh have participated in the development of the PIV system, notably Gray [18] and Skyner [49]. The main contribution of the author to this work has been the development and analysis of the image shifting technique (see chapter 3).

The first stage in the PIV method is to record the light scattered by neutrally buoyant seeding particles in the flow which are stroboscopically illuminated by laser light. This is done by photographing the flow with a stills camera to produce a negative. The developed negative shows the seeding particles as dark dots against a pale background. The stroboscopic laser illumination ensures that sev-

eral exposures of each seeding particle are recorded on each frame of film and this clearly shows the movement of each particle while the camera shutter is open (see figure 2.1)

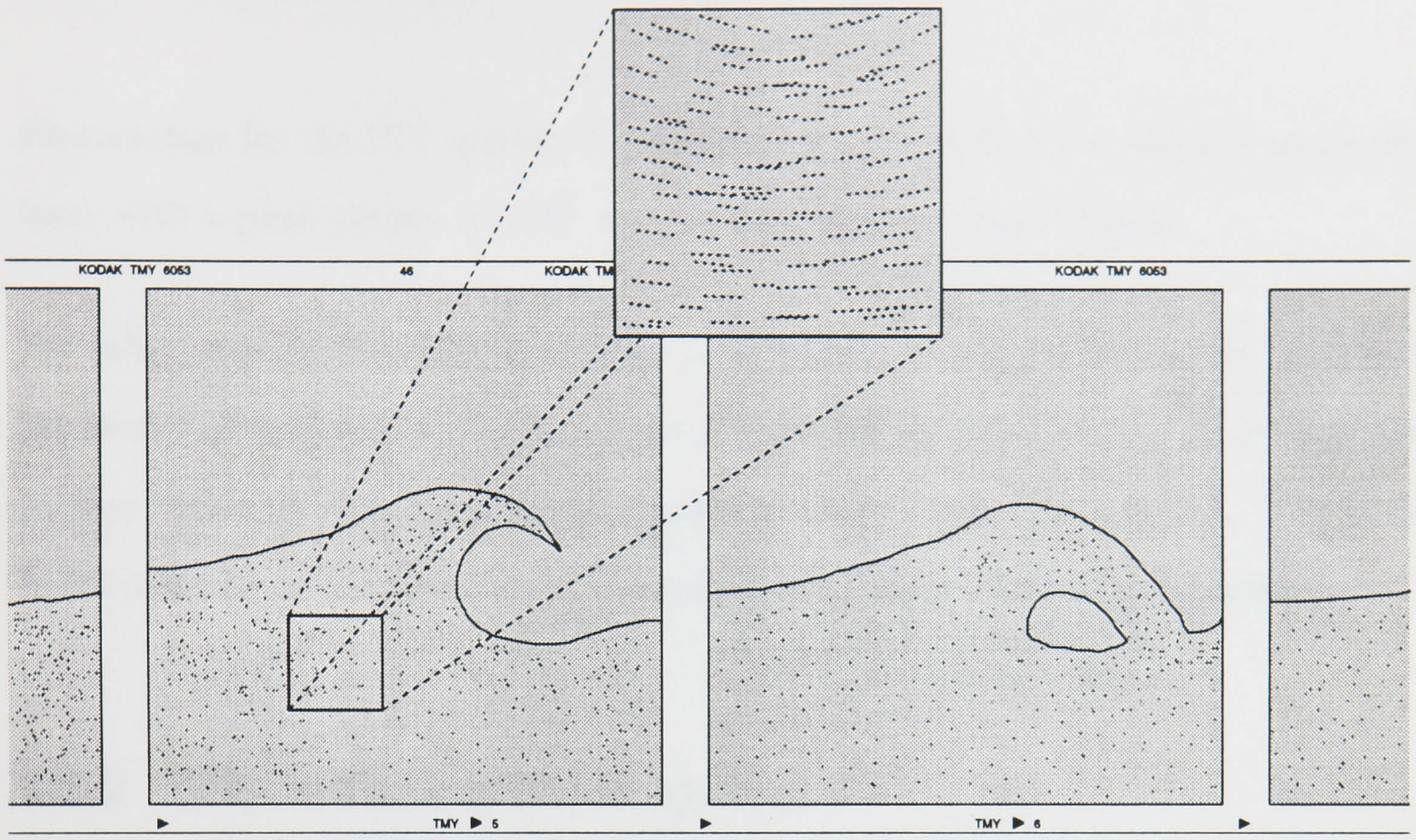

FIGURE 2.1: Developed PIV film showing multiple particle images

The second stage of the method is the automated analysis of the negative to yield the flow velocity information. This is achieved by shining a narrow laser beam of low intensity through the negative. The diffraction of light round the particle images gives rise to Young's fringes which are captured by a CCD camera. The spacing between the fringes is inversely proportional to the average spacing between the seeding particles in the small region of the negative 'interrogated' by the laser beam and the direction of the fringes is perpendicular to the direction of flow. This process is repeated automatically over many points on the negative to yield a vector representing the flow velocity at each interrogation point.

2.2 Experimental equipment

2.2.1 Illumination

Illumination for the PIV system is provided by a continuous wavelength argon ion laser with a peak output of 15W and a wavelength of about 490nm.

For safety reasons the laser is situated away from the flume in a room by itself and the laser beam travels to the flume along a totally enclosed path at floor level, its precise direction controlled by four independently adjustable mirrors. The laser beam can also be diverted to other experimental areas within the laboratory.

2.2.2 The scanning beam system

Although the author was not involved in the design of the scanning beam system a brief explanation of it is considered appropriate. There are two means of providing the stroboscopic laser illumination required by PIV. The simpler method is to expand the laser beam into a sheet by shining it through a cylindrical lens and then recollimating it with another lens so that the edges of the sheet are parallel. The pulsing of the light can then be controlled by shining the laser beam through a beam chopper, for example, a spinning disc with a gap cut in it. However the method employed at Edinburgh is the more complicated scanning beam system [23].

For this method the laser beam is directed, via focusing and collimating lenses, on to a spinning octagonal mirror under the flume which reflects the light onto a parabolic mirror. The spinning mirror is situated at the focus of the parabola ensuring that the beam is always reflected vertically upward from the parabolic mirror. As the octagonal mirror spins the laser beam is scanned up the parabola

and the effect in the flume is to produce a vertical laser beam which scans through the water from right to left eight times during each rotation of the mirror (see figure 2.2). The rotation rate of the spinning mirror can be varied from about 15rps to 250rps enabling PIV measurements to be carried out on flows of up to $10ms^{-1}$. At higher rotation rates the scanning laser beam appears as a solid, 1 metre wide, sheet of light within the flume. The box containing the scanning beam system sits on rails under the flume so it can be easily moved along, allowing PIV to be used in a large part of the flume.

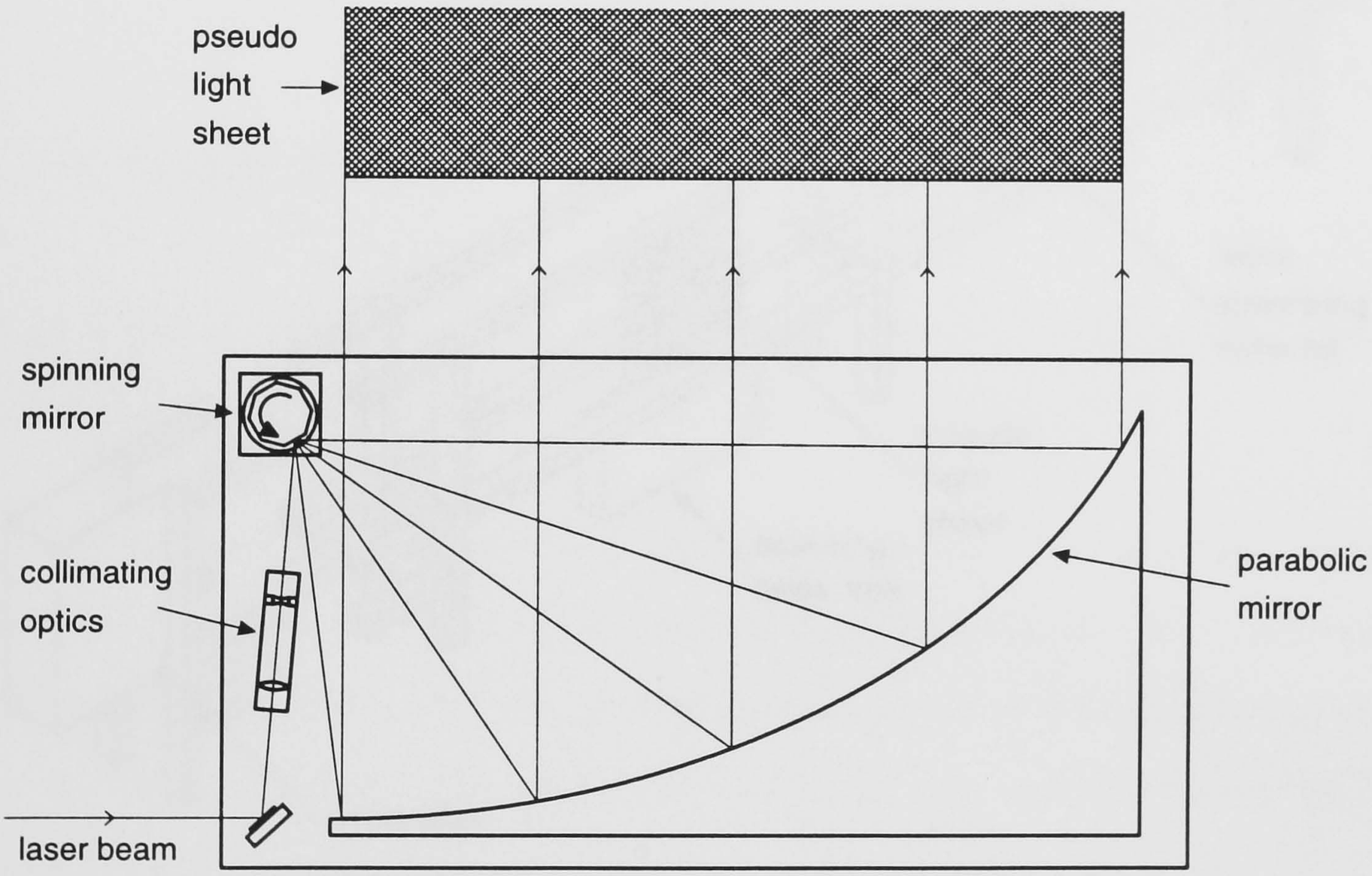

FIGURE 2.2: The scanning beam system

The main advantage of the scanning beam system is that it provides much higher levels of illumination than the cylindrical lens system since each seeding particle in the water is illuminated by the full intensity of the laser beam during each scan rather than by a lower intensity expanded beam. However it is limited by the maximum power of the cw laser to the study of lower speed flows.

2.3 Taking pictures

The process of taking PIV pictures is a very painstaking one since the preparation and setup of the experiment and the camera must be to the same order of accuracy as the analysis process in order to take full advantage of the PIV method. The PIV setup of the flume and the camera is shown in figure 2.3

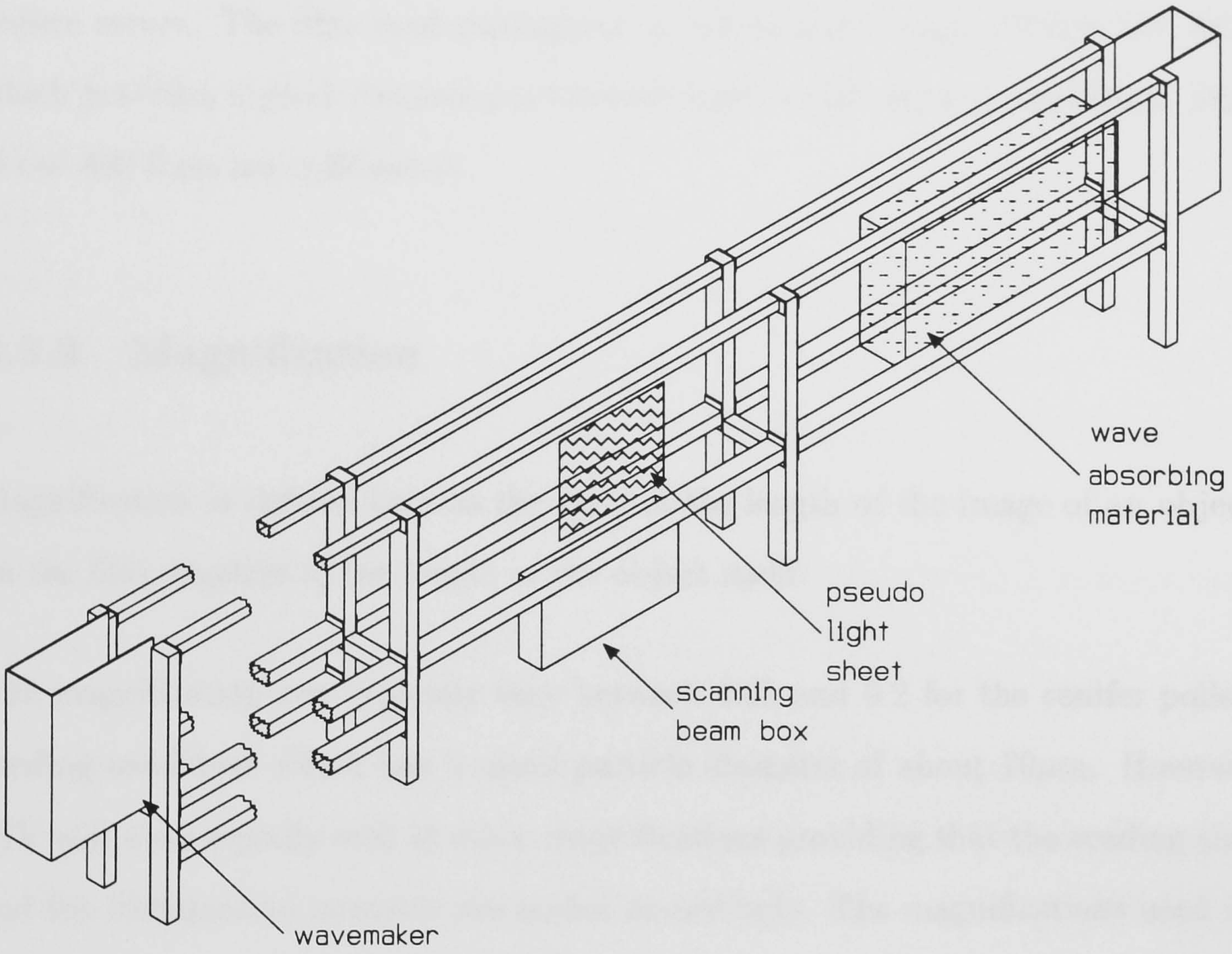

FIGURE 2.3: The wave flume showing the PIV setup

The pictures are taken with the aim of optimising the images with respect to the subsequent analysis. The variables which affect the quality of the fringes are: the quality of the photographic equipment; the magnification of the images; the camera shutter speed; aperture size and the focus of the image; the scan rate of the laser beam; the laser power; the seeding density and the water quality. The optimisation of these will be considered one at a time.

2.3.1 Photographic equipment

All the optical components in the PIV system are of very high quality. The camera used in this study is a medium format Hasselblad 500El/M fitted with an 80mm planar-T lens. This minimises aberration of the images due to lens edge effects which would increase the errors in velocity vectors. The camera mirror is locked up and the shutter cocked before each frame to minimise vibration and subsequently reduce errors. The film used throughout is 120 format Kodak TMAX 400 ASA which provides a good compromise between light sensitivity and resolution, with about 400 lines per millimetre.

2.3.2 Magnification

Magnification is defined here as the ratio of the length of the image of an object on the film negative to the length of the object itself.

The magnification can typically vary between 0.05 and 0.2 for the conifer pollen seeding used here which has a mean particle diameter of about 70μm. However PIV will work equally well at other magnifications providing that the seeding size and the illumination intensity are scaled accordingly. The magnifications used in this study lie in the range 0.08 to 0.1.

If the camera is moved between experiments then the new magnification must be determined before any more PIV pictures can be taken. This is done by placing a steel rule in the flume in the same plane as the sheet of laser light. This is then photographed and the magnification determined by studying the ruler graduation marks on the developed negative with a travelling microscope.

2.3.3 Camera settings

The camera shutter speed is totally governed by the rotation rate of the spinning octagonal mirror and is set to ensure that at least two, and preferably five or six images of each seeding particle are recorded on the film. For example a mirror rotation rate of 70rps would require a camera shutter speed of 1/100 second to produce five or six images on the film.

The optimum camera aperture is more difficult to determine. A small aperture minimises the effects of lens aberration and increases the depth of field. However it also reduces the amount of light reaching the film to an unacceptably low level and the effect of diffraction at the aperture increases the apparent size of the seeding particles on the film. The widest aperture allows maximum film exposure but makes focusing more difficult due to the decreased depth of field. It has been shown in a study by Gray [22] that the best compromise is achieved by setting the aperture to one f-stop below its widest opening since aberration is never a very serious problem with the very high quality lens used here.

Focusing the camera exactly on the sheet of laser light is time consuming since the optimum focus setting is not easy to obtain first time. A series of frames is taken for which the focusing ring on the lens is set at a number of marked positions surrounding the apparent point of optimum focus. This film is developed and a study of the quality of the Young's fringes identifies the best focus setting.

2.3.4 Spinning mirror rotation rate

Determination of the required spinning mirror rotation rate is done by working from the desired particle spacing on the film. The analysis system is capable of

analysing negatives with particle spacings ranging from 30μm to about 300μm and a mean figure of about 150μm is generally sought. The required rotation rate of the spinning mirror is given by

$$\text{Scan rate (rps)} = \frac{\bar{v}M}{8\delta r}$$

where $\bar{v}$ is the mean flow rate, M is the magnification on the film and δr is the desired particle image spacing on the film. For example with a flow rate of 1ms^{-1} and a magnification of 0.1 then a mirror rotation rate of 80rps will give a particle image spacing of just over 150μm.

2.3.5 Attenuation of laser light

The light leaving the argon ion laser is attenuated by mirrors and lenses at several points before reaching the flume but the greatest absorption of the light is by the water itself. Water left in the tank grows more opaque until eventually there are visible signs of life within it. This all contributes to the attenuation of the laser light so where possible the flume should be filled with fresh water the same day as experiments are to be carried out.

2.3.6 Seeding density

The quality of Young's fringes obtained from a PIV negative is greatest when there are of the order of 10 different seeding particles in each 1mm^2 interrogation region. With a typical magnification of about 0.1 this corresponds to a seeding density of about 15ml of conifer pollen for every 1m^3 of water. Generally a little more than

this is used since not all the seeding remains suspended in the water due to its tendency to float and to adhere to structures within the flume.

2.3.7 Camera alignment

It is important that the camera is accurately aligned before any PIV pictures can be taken since the edges of the negative provide the horizontal and vertical references for the analysis. To achieve this the camera is fixed to a tripod which has been placed the correct distance from the flume and levelled with the help of a spirit level. The camera is then adjusted so that its film plane is parallel to the side of the flume. This is done by panning and tilting the camera until the reflection of the centre of the lens in the glass wall of the tank appears in the centre of the viewfinder. The camera is then moved to the desired height - typically about 100mm below the mean water level (MWL) - so that it always has a clear view of the illuminated measurement zone without being obstructed by the water surface.

2.3.8 Camera triggering

The microcomputer controlling the wave paddle also has the ability to trigger the camera at any desired phase of a wave but in most of these experiments the trigger was provided by the image shifting system when it was at the correct position for a frame to be taken.

2.3.9 Developing film

All the PIV films were developed in a darkroom next to the laboratory. The film is wound on to a reel and placed in the development tank with Kodak T-Max developer typically for about 8 minutes but dependent upon the temperature of the developer. During the development period the tank is agitated every 30 seconds to replenish the surface of the negatives with fresh developer. After development the film is fixed in a bath of Amfix fixer for about 5 minutes, again agitating every 30 seconds. The final stage of development is to wash the film in running water for about 15 minutes to remove all trace of chemicals before hanging the film up to dry.

Push processing of films is sometimes necessary if seeding particle illumination is poor. This is usually due to the laser whose output drops below 15W when the mirrors at either end of the tube require cleaning. Under these circumstances the development time may be increased to 9 or 10 minutes.

2.4 Analysis of PIV negatives

All PIV negatives from this project were analysed on the present analysis system designed and built by Skyner and Bruce [49]. The negative to be analysed is held rigidly in a mount on a computer controlled two-axis micro-translation stage which is capable of moving both horizontally and vertically. The beam from the 1mW helium-neon (HeNe) laser is passed through a spatial filter which eliminates high frequency noise and then through collimating lenses which reduce its diameter to about 1mm before it passes through the negative to be analysed. The images of the seeding particles on the film cause interference of the laser beam and the resulting

Young's fringes are captured by a CCD camera situated at the back focal plane of a further convex lens. A frame grabber transfers the image to a PC where a two-dimensional fast fourier transform (FFT) with a resolution of 64×64 is performed. The resulting autocorrelation plane shows peaks corresponding to the correlations between particles in the interrogation region (see figure 2.4). The tall central peak is the result of the correlation of each particle with itself and this is removed since it yields no useful information. It is not necessary to remove the whole peak but only enough to ensure that the highest remaining points on the autocorrelation plane are the tips of the signal peaks e.g. in figure 2.4 the central peak must be removed at least up to the broken lines.

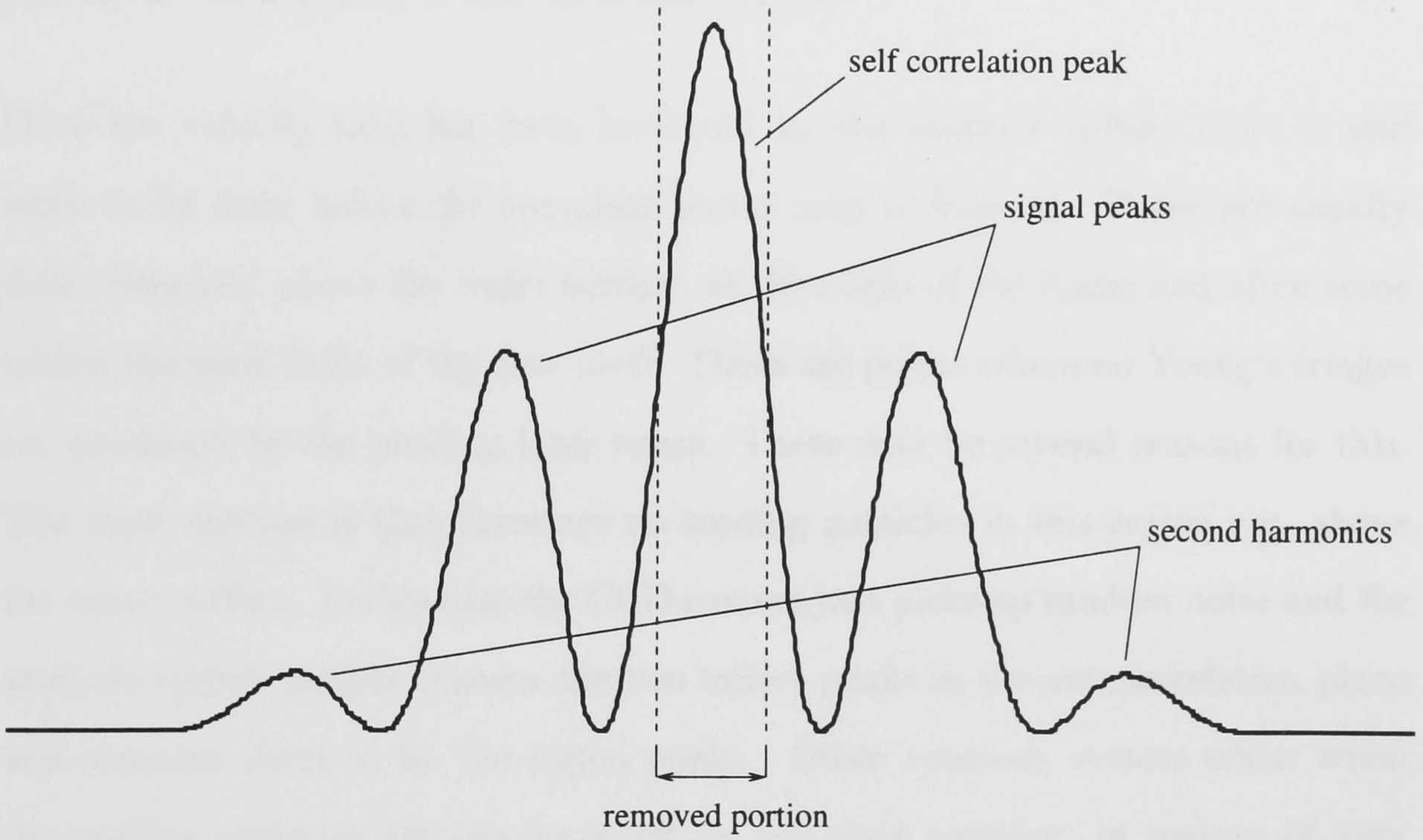

FIGURE 2.4: A section through the autocorrelation plane

The next tallest pair of peaks correspond to the correlation of each seeding particle with itself at the next time step and these are the peaks which are of interest. The PC detects the location of the centroids of these peaks and then calculates their spacing and relative orientation. The actual speed of the flow is then deduced from the uncalibrated value by combining it with the known scan time of the laser beam and the magnification from the flow to the film. The direction of flow is orthogonal

to the orientation of the Young's fringes which clearly leaves an ambiguity of 180° to be resolved. If the general direction of flow is known then this can be used to infer the direction of each vector, for example in the case of channel flow, but this may not be possible if the flow is more complex (see chapter 3 on image shifting).

The PC, which also controls the micro-translation stage, then moves the negative relative to the interrogating laser beam and the analysis process is typically repeated at many evenly spaced points on the negative to build up a detailed flow map from the whole frame. The analysis process takes about 2 seconds per point but may be sped up by reducing the resolution of the FFT to 32×32 with a slight penalty to the accuracy of the calculated vectors.

Once the velocity map has been produced by the analysis system there is still work to be done before the complete vector map is finished. There are usually data 'dropouts' above the water surface, at the edges of the frame and often some within the main body of the flow itself. These are points where no Young's fringes are produced by the probing laser beam. There may be several reasons for this. The most obvious is that there are no seeding particles in this region e.g. above the water surface. In this case the CCD camera just picks up random noise and the analysis system simply chooses the two tallest peaks in the autocorrelation plane and assumes them to be the signal peaks. Other spurious vectors occur when the seeding particles are too far apart or too close together, in regions of very high velocity or at stagnation points. In the former case this gives rise to signal peaks which are too close together and almost coincide with the central peak in the autocorrelation plane. These are usually then removed with the central peak and the resulting signal peaks detected are actually the first harmonic peaks giving rise to a velocity vector approximately twice as large as the actual flow velocity at that point.

The analysis system assigns a 'quality' value to each vector. This is a measure of the height of the signal peaks relative to the rest of the autocorrelation plane and in effect gives an indication of the signal-to-noise ratio. This value is used to filter out the spurious vectors by setting a threshold value of acceptability. Some manual editing of the vector map may still be necessary after this to remove spurious vectors which have evaded the above filtering process. They are detected by their lack of continuity with their neighbours, which can often be seen at a glance.

2.5 Errors in PIV

Despite the high accuracy of the PIV method the errors involved in it must still be considered. The overall uncertainty in any flow vector has contributions from many sources but most of these individual errors are very small due to the use of precision equipment or by exercising great care when carrying out the experiments.

2.5.1 Random errors

Random errors are potentially the most serious source of inaccuracy since they cannot be corrected for. The main sources of random errors inherent in the PIV method are listed below:

- measurement of illumination plane to film magnification
- focusing the camera
- measurement of the laser beam scan rate
- thickness of the illumination plane

- camera misalignment

- poorly defined Young's fringes due to regions of high acceleration

- the effect of random correlation noise on the detection of the centroid of the signal peaks

The measurement of magnification is made with a travelling microscope equipped with a vernier scale from a scaling photograph of a ruler placed in the plane of the measurement zone. This is subject to two errors: the first being in the accurate placing of the ruler and the second in the microscope measurement. Typically about 5 measurements are taken from the photograph to reduce the error in the calculated magnification.

Errors in camera focusing give rise to indistinct Young's fringes which result in poor 'quality' vectors with larger associated errors.

The rotation rate of the spinning mirror which in turn governs the scan rate of the laser beam has a tendency to vary over time. The effect of this variation is reduced by measuring the rotation rate just prior to taking each frame. The measurement is made by placing a photodiode at the edge of the laser sheet and connecting the output to a recording oscilloscope and averaging over about ten pulses on the screen.

The thickness of the light sheet increases as the laser beam travels upward through the water since it is impossible for the optics in the scanning beam box to precisely recollimate the incoming beam. The light sheet is ideally about 2mm thick at the water surface but dirt on the surface of the mirror or a misaligned laser beam both increase this, giving rise to a larger magnification error. A thicker light sheet reduces the illumination received by each seeding particle while increasing

the number of particles recorded by the camera in the measurement zone. This leads to increased background noise in the images and a subsequent decrease in the signal-to-noise ratio at the time of analysis due to increased cross correlations between the large number of particle images in each interrogation region.

The action of the shutter on the Hasselblad camera is controlled mechanically and is subject to large errors [49]. However the shutter speed affects only the number of particle images on each frame and the exposure so its associated error does not affect the overall error in the measured velocities.

Misalignment of the camera will result in a film plane which is not parallel to the plane of the measurement zone and may cause focusing problems and errors in the calculated vector velocities. If the camera is tilted such that the edge of the negative is no longer horizontal then this error is passed on directly to the velocity vectors since the analysis system uses this edge as a reference. The process of aligning the camera is described in section 2.3.7 and the associated error is very small subject to the walls of the flume being vertical and parallel.

Regions of high acceleration within the flow, in vortices for example, result in multiple particle images on the film which are neither regularly spaced nor collinear. This clearly results in large errors since the success of the autocorrelation technique depends upon the assumption that the flow is constant for the brief period of film exposure.

Irrespective of the quality of a PIV negative there will always be random correlation noise arising due to a contribution to the autocorrelation function from unrelated particle pairs. This noise adds an uncertainty to the detection of the centroid of the signal peaks.

2.5.2 Systematic errors

The systematic errors arising in the PIV method are as follows:

- refraction by the glass walls of the flume and the water
- edge effects due to lens aberration
- analysis rig calibration
- illumination plane distortion
- scanning beam return time
- discrepancy between water flow and seeding movements

It has been shown by Gray [22] that the effects of refraction in the water and glass of the flume, and edge effects due to lens aberration almost exactly offset one another since refraction acts to compress the frame at its edges while the lens aberration expands it.

The parabola which supports the mirror in the scanning beam box is machined in three parts which are then fastened together. The curve of the parabola has small discontinuities due to machining errors in each section and this, when coupled with the mirror's tendency to disassociate itself from its support over time, gives rise to a light sheet which has some kinks in it. Thus the measurement zone is not precisely a flat vertical section through the centre of the flume but possibly has some regions slightly outside the focal plane of the camera.

Due to the nature of the scanning beam system the precise scan time is different for each seeding particle in the flow since they typically have a component of velocity

in the direction of movement of the scanning beam.

Source of error	Systematic Error	Random Error
Photographic magnification		0.2%
Photographic distortion	0.0%-0.3%	
Illumination plane flatness	0.0%-0.3%	
Illumination plane thickness		0.1%
Illumination scan time	0.0%-0.2%	
Illumination interval		0.2%
Analysis rig calibration		0.1%
Positive seeding buoyancy	0.2%	
Totals	0.2%-0.8%	0.3%

TABLE 2.1: Summary of the errors inherent in the PIV method

The conifer pollen seeding particles follow the water flow quite faithfully but have a slight positive buoyancy and, if left in still water, rise with a speed of about 0.25mms^{-1}.

The major sources of error inherent in the PIV method and their associated errors are summarised in table 2.1. Where these values have a strong dependence upon the measured velocities then values of the order of 1ms^{-1} are assumed.

2.5.3 PIV applied to the oscillating water column

This section details the errors which arise from the application of PIV to the measurement of flow in and around an OWC. While most of these sources of error are inherent in many applications of PIV a full explanation is included to highlight

the limitations of the technique in this instance. The major sources of error are as follows:

- Absorption of laser light below model
- Refraction and reflection of laser beam by perspex
- Reduction of image quality due to perspex
- Effects of water aeration
- Regions of high acceleration
- Variable seeding density within OWC chamber
- Interruption of flow by leading edge of model

These are explained in more detail below.

Absorption of laser light below model

The OWC model stands at the head of a sloping false bed or 'beach' in the flume. The sections of this 'beach', designed by Quinn, are slightly narrower than the flume so that they can be put in place before filling when the walls bow out slightly due to water pressure. The edges of the beach in contact with the glass are coated with a spongy neoprene tape to ensure a tight fit at all times. This helps to isolate the volumes of water above and below the 'beach' to preserve the 'no perpendicular velocity' boundary condition at the interface. While this property is not essential for OWC studies the greatest benefit is that it reduces the amount of seeding which migrates below the OWC model to absorb the illuminating laser beam. However

with a particle diameter of only 70μm some seeding does permeate through gaps to increase the absorption of laser light by the water below, ultimately decreasing the contrast in the PIV negatives and hence the signal to noise ratio.

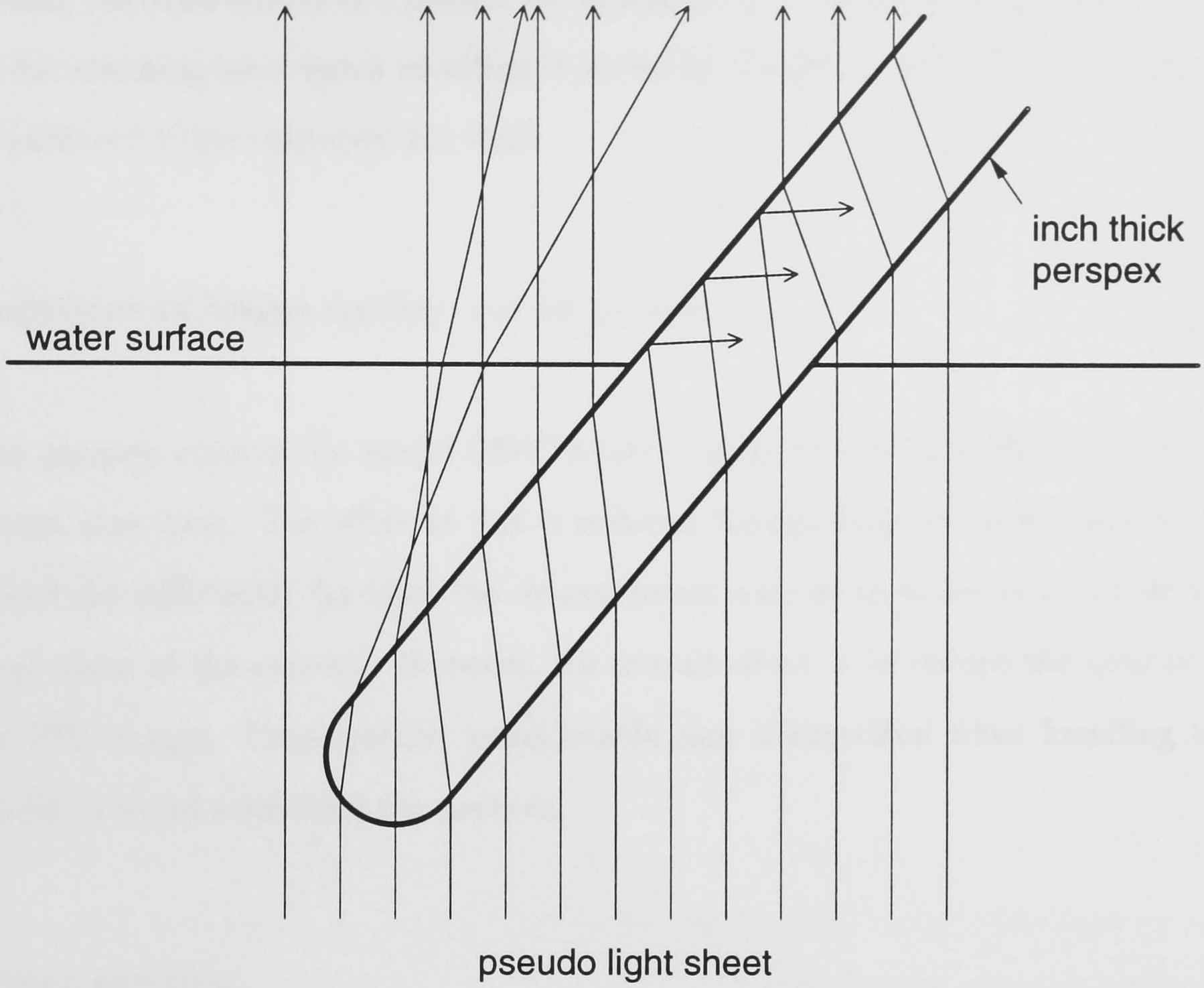

FIGURE 2.5: Refraction of light sheet through the perspex front wall of the OWC

Refraction and reflection of laser beam by perspex

Perspex has a refractive index of 1.50 - similar to that of the walls of the flume. The 10mm thick perspex base of the OWC model reflects about 10% of the laser light incident upon it and absorbs about 5% leaving a transmitted component of 85%. Internal reflections within the chamber e.g. from the roof are minimised by coating these surfaces with black plastic tape. An illumination problem would occur if measurements were carried out with the front wall of the model fixed at an angle

to the vertical. In this case refraction of the light sheet through the semi-circular lower edge of the front wall forms a caustic curve of high intensity illumination while there remains a region which is not illuminated at all (see fig. 2.5). The seeding particles within this caustic are illuminated for an extended period of time by the scanning laser beam resulting in streaked images on the film which cannot be analysed if the velocities are large.

Reduction of image quality due to perspex

The perspex walls of the model OWC scratch easily becoming slightly less transparent over time. The effect of this is reduced though since the side walls of the model are sufficiently far from the measurement zone so as to be well outside the focal plane of the camera. However, the overall effect is to reduce the quality of the PIV images. Consequently considerable care is exercised when handling the model to avoid scratching the perspex.

Water aeration

When the incident waves are of large amplitude the flow within the OWC chamber becomes highly aerated, especially in the region of the front wall. The air bubbles are trapped within vortices and reduce the quality of velocity vectors obtained from these areas since the bubbles are not neutrally buoyant and contain no seeding.

Regions of high acceleration

The flow around the front wall of the OWC typically contains areas of high vorticity with values of more than $100s^{-1}$. This corresponds to particle image spacing

variations of as much as 200μm within a single interrogation region on the film. This is clearly much greater than the acceptable variation of about 10μm and indeed is almost as much as the dynamic range of PIV itself. These regions yield no useful velocities as a result of large accelerations due to the rapid formation of strong vortices or of large values of $d\mathbf{v}/dx$ and $d\mathbf{v}/dy$. The latter problem may be reduced by increasing the area of film covered by the vortices, either by using a longer camera lens or by moving the camera closer to the flume.

The use of image shifting may yield velocities from such regions but this comes about only through a reduction of resolution.

Variable seeding density within OWC chamber

The conifer pollen seeding material initially has a slight positive buoyancy before it becomes saturated. This is not generally a problem since the rise velocity is only about 0.25mms^{-1}. However, near the back corner of the OWC chamber where the flow is oscillatory and has almost no vertical component, much of the seeding migrates upwards resulting in an uneven seeding distribution and a correspondingly poor vector quality in some regions.

A particular problem with large amplitude waves is that the OWC chamber is flushed with large quantities of unseeded water during each wave cycle. Over time this gradually lowers the seeding density within the measurement zone, the difference often being very noticeable when the first and last frames from a film are viewed side by side. The only satisfactory solution is to seed a large volume of the flume near the OWC with the unfortunate side effect of also increasing the seeding density below the model.

Interruption of flow by leading edge of model

The false bed in the flume is carefully aligned with the leading edge of the model to reduce unwanted vortex shedding which may interfere with the study of the flow into the chamber. A smooth flexible covering over the joint helps to cover any remaining gaps.

Chapter 3

Image shifting

3.1 Introduction

One of the drawbacks of the PIV method, with analysis by autocorrelation is that although it allows the speed of flows to be determined with great accuracy the sense of direction of the flow vectors is not known i.e. there is a 180° ambiguity in the direction of each vector. This is not a problem in situations where the overall flow direction is uniform e.g. in many pipe or channel flows since the direction of flow can easily be inferred by observation but in more complex situations where there are high levels of turbulence or vorticity then it is impossible to assign a direction to each vector with any confidence.

In some more complex flows it may still be possible to infer the directions of a few vectors by continuity providing the directions of a sufficiently large number are known already. For example in the case of a wave breaking in a flume it is known that water at the tip of the wave crest must move in the direction of travel of the wave and consequently the directions of all vectors can be inferred point by point from there.

Another problem arising in the PIV method is its finite dynamic range. The analysis system has the ability to cope with particle spacings which lie in a given range and in the case of a measurement zone with a large variety of speeds, this range may be exceeded and some regions within the flow will be unresolvable.

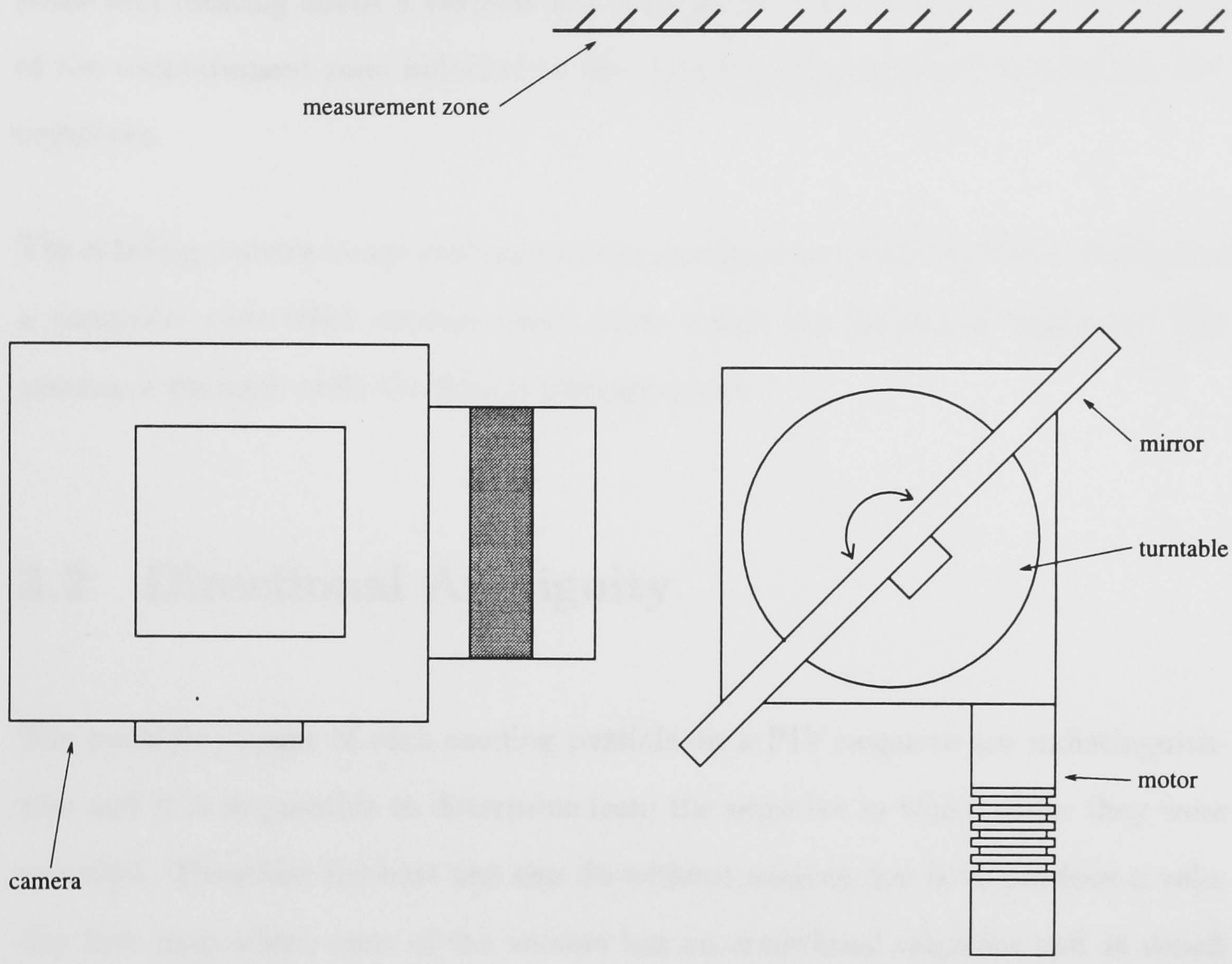

FIGURE 3.1: Plan view of a rotating mirror image shifting system

Two different designs of image shifting system, a rotating mirror device and a rotating camera system, are used in the Fluids Group at Edinburgh University.

These shifting systems overcome the aforementioned PIV problems by imposing a known shift on the flow vectors, forcing the sense of direction to be the same for each one. This also results in a compression of the dynamic range and by choosing an appropriate shift the particle spacings can all be forced to lie within the limits of the analysis system. Furthermore, in forcing a uniform sense of direction, the stationary seeding particles are now displaced in subsequent exposures allowing

these regions of the negative to be analysed. After analysis the known shift vector is subtracted from the vector plot to yield the true flow map.

The rotating mirror image shifting system consists of a mirror placed in a vertical plane and rotating about a vertical axis through its centre (figure 3.1). The image of the measurement zone reflected in the mirror is photographed to give the PIV negatives.

The rotating camera image shifting system, designed and built by Bruce, comprises a computer controlled rotation stage upon which the camera is mounted. The camera is panned while the flow is photographed.

3.2 Directional Ambiguity

The multiple images of each seeding particle on a PIV negative are indistinguishable and it is impossible to determine from the negative in which order they were recorded. Therefore the best one can do without assumption is to produce a velocity flow map where none of the vectors has an arrowhead since the end at which to place the arrow is not known. In practice the analysis system determines the speed of the flow and its direction subject to the 180° ambiguity at each interrogation point and automatically assigns a direction to the velocity vector such that the x component is positive (see figure 3.2). The vector map must then be edited manually and the correct direction assigned to each vector, initially using some a-priori knowledge and then by continuity for each subsequent vector (see figure 3.3). It should be noted, however, that continuity arguments can be applied without uncertainty only if the negative has been analysed with a step size smaller than the scale of the finest structure within the flow. If large regions of the measurement zone have a common flow direction e.g. flow round an object in a

wind tunnel then this direction can be input to the analysis system in the form of a polar angle. During analysis the vectors are chosen to align with this common direction as closely as possible. This reduces the amount of work necessary during post-analysis editing.

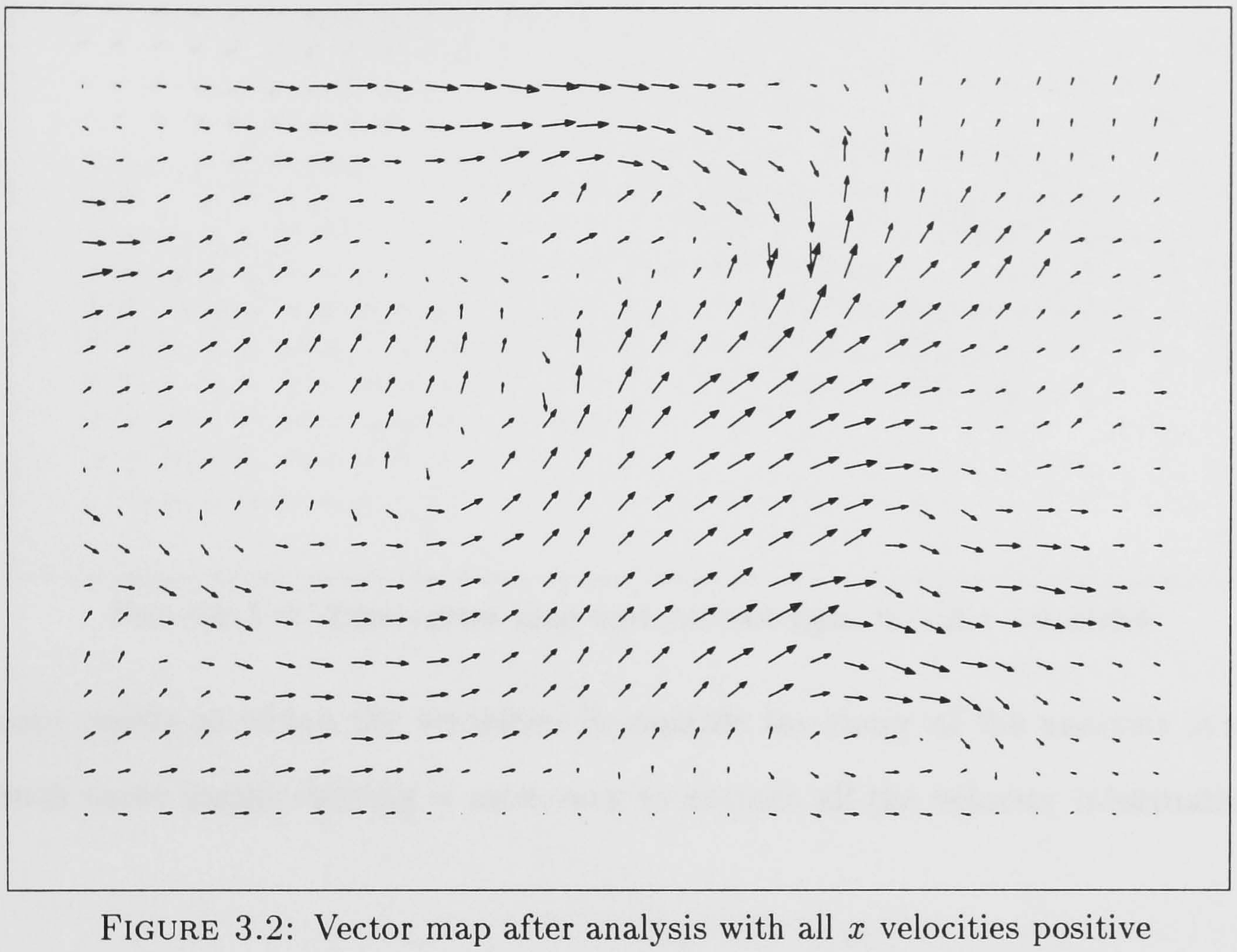

FIGURE 3.2: Vector map after analysis with all x velocities positive

3.3 Dynamic range of PIV

The PIV analysis system is capable of analysing negatives where the particle spacing lies between 30μm and 300μm. This governs the dynamic range of the technique for a particular magnification and laser scan rate and is fixed by the size and resolution of the CCD array (see chapter 2 on PIV). The scan rate should be chosen so as to maximise the number of points at which the velocity vector is resolvable and in flow situations where the dynamic range is small it is often possible to achieve this at all analysis points. However in most complex flows there

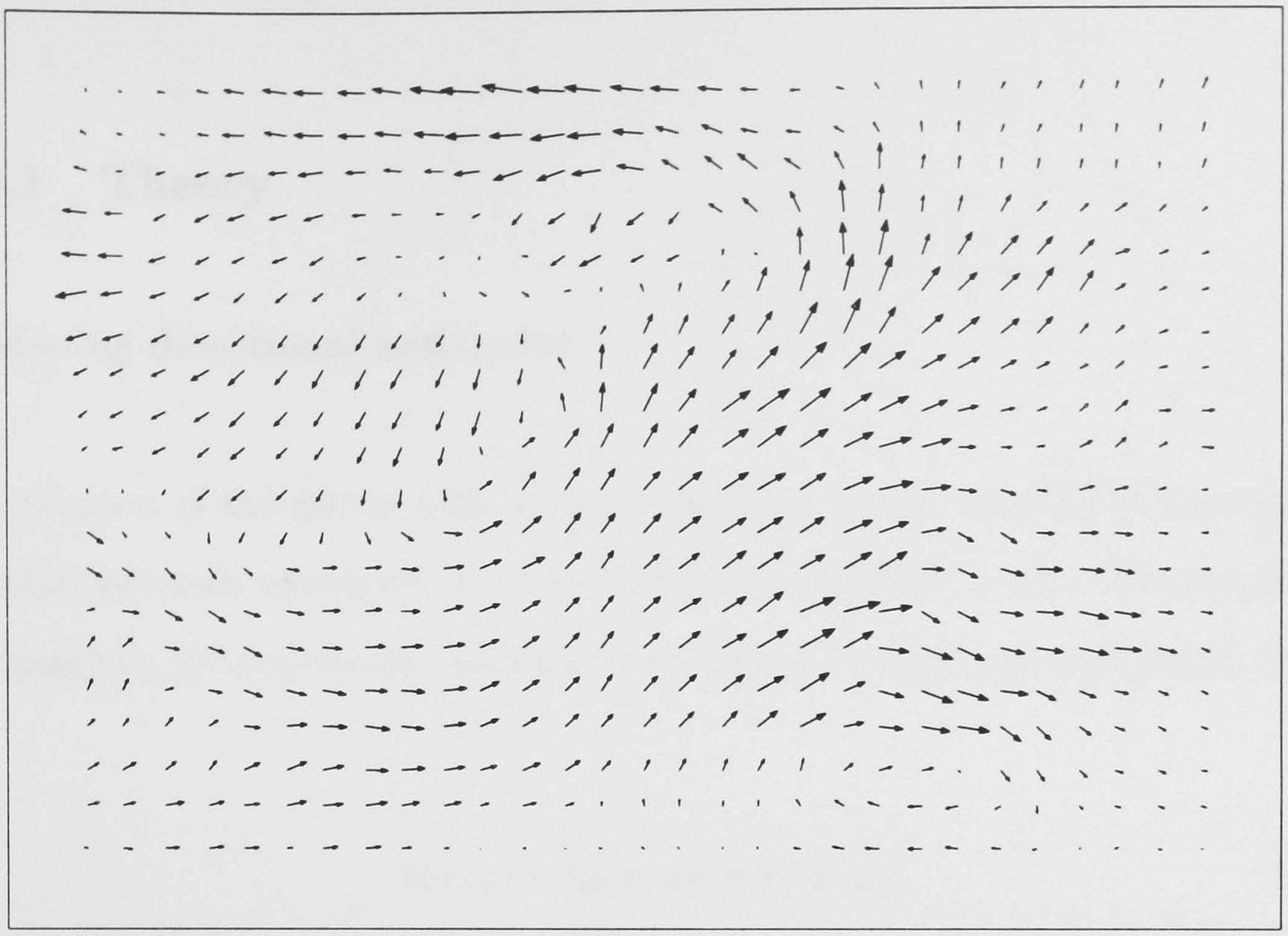

FIGURE 3.3: True vector map with correct signs for all x velocities

remain points at which the velocities lie outside the range of the analysis system. In such cases image shifting is necessary to extract all the velocity information.

3.4 The image shifting solution

The technique of image shifting provides a simple solution to the above problems. The rotating mirror image shifting system, first described by Adrian [4] and used successfully in many situations [17, 31, 16] is just one of many such devices which have been developed. Other systems include electro-optical devices utilising crystals with switchable refractive indices [30], cumbersome mechanisms which rotate or translate the camera [24], holographic methods [12, 13] and two-camera systems with many associated alignment difficulties. The problem of directional ambiguity has also been resolved with pulse tagging systems often incorporating different col-

ours of illuminating light to distinguish between particle pairs on the negative [50].

3.4.1 Theory

Resolving directional ambiguity

The rotation of the mirror adds an artificial displacement to each of the seeding particles between successive scans of the illuminating laser beam. The velocity at any point (x, y) in a two-dimensional flow is given in cartesian coordinates by

$$\mathbf{v}(x, y) = v_x(x, y)\mathbf{i} + v_y(x, y)\mathbf{j} \tag{3.1}$$

The application of a shift of magnitude v_s at an angle θ to the positive x direction transforms the vector field to

$$\mathbf{v}'(x, y) = \{v_x(x, y) + v_s \cos\theta\}\mathbf{i} + \{v_y(x, y) + v_s \sin\theta\}\mathbf{j} \tag{3.2}$$

The magnitude v_s is chosen to be large enough to ensure that the component of velocity in the direction of shifting has the same sign for each flow vector after analysis (see figure 3.4). The vectors are then aligned on this basis if the analysis system has not already done so. Finally the known shift velocity is subtracted from each vector to yield the true vector map with the 180° ambiguity removed.

The shift vector $\mathbf{v_s}$ is determined accurately by seeding the water in the flume and allowing it to settle before photographing it using the image shifting system. The subsequent analysis yields the shifting velocity.

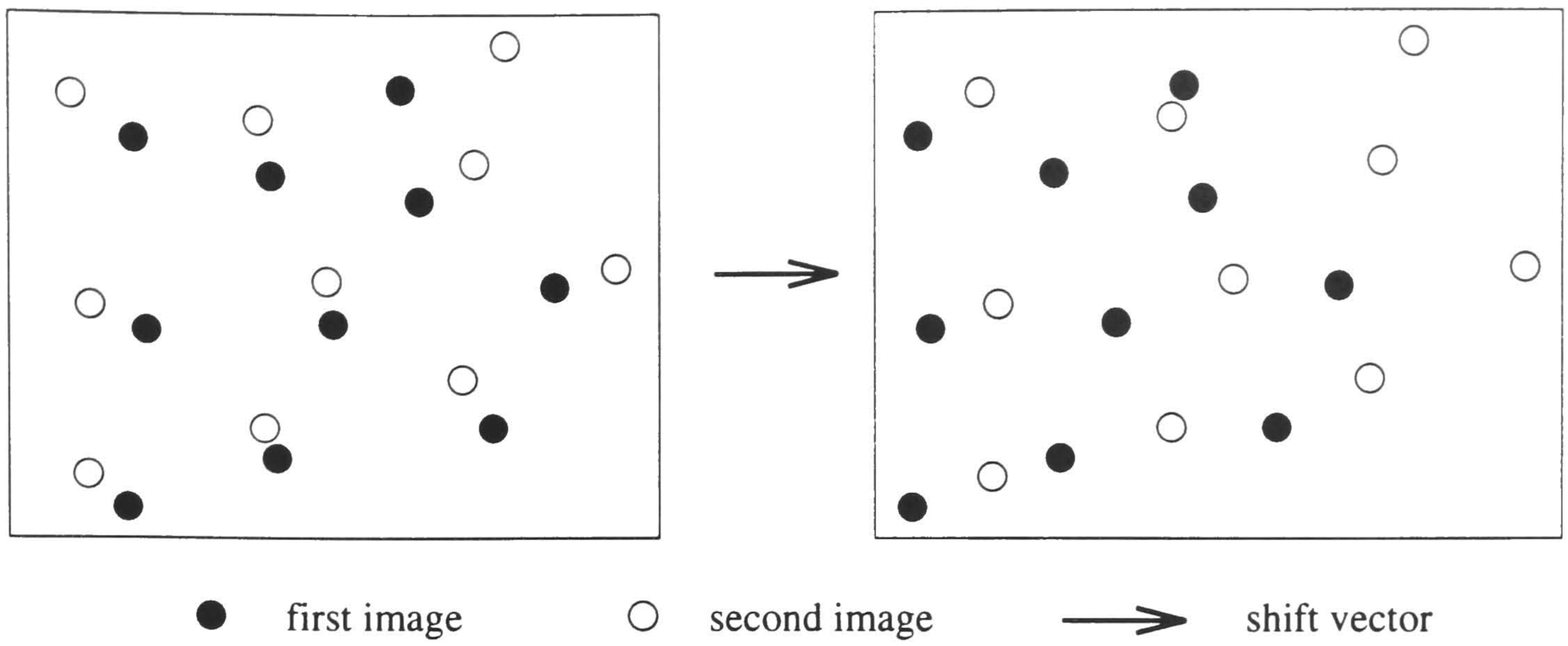

FIGURE 3.4: Seeding particle image pairs before and after shifting

Expanding the dynamic range

If the dynamic range of the flow in question is greater than that of the analysis system then image shifting may be used to allow the range of particle image spacings to be compressed. If the correct shifting velocity and laser scan rate are chosen then the flow velocities can be obtained at every analysis point.

Consider a case where the spacing of particle pairs varies between 0 and s_{max} on a PIV negative. If these limits lie outside the range of the analysis system, bounded by displacements d_{min} and d_{max}, then the resulting flow velocity map will be incomplete with regions of missing vectors. Figure 3.5 shows such a case where the shaded region denoting the analysable range falls within the circle enclosing the range of particle displacements. In this case the displacements denoted by vectors **a** and **b** are, respectively, too small and too large to be analysable whereas vector **c** falls within the suitable dynamic range.

If the same flow is now photographed but with the laser scan time T decreased to

$$T' < T\left(\frac{d_{max} - d_{min}}{2s_{max}}\right) \tag{3.3}$$

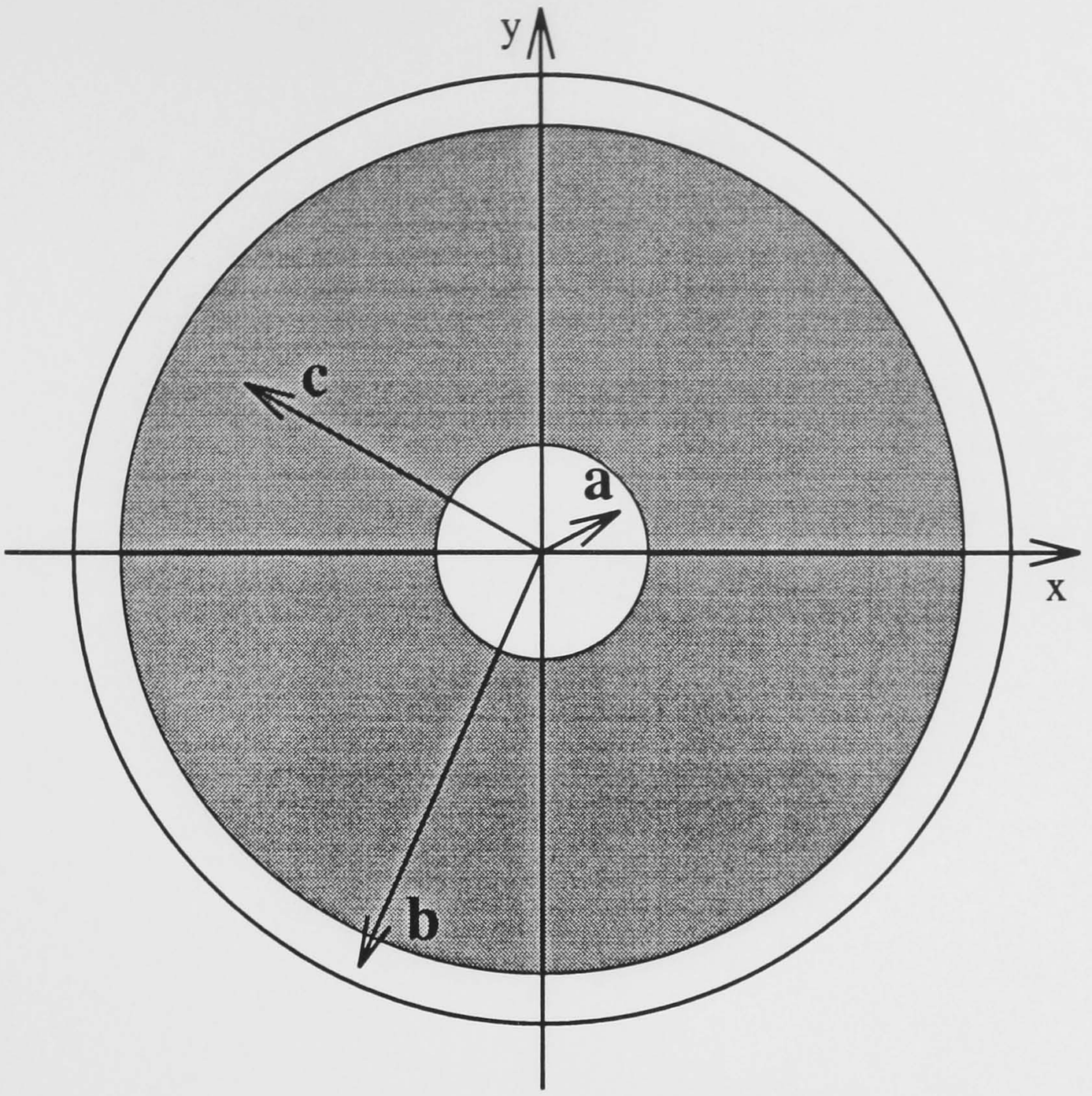

FIGURE 3.5: Unshifted image - some unresolvable velocities

and a shift applied which produces an additional x displacement, s_x, to the particle images on the negative where

$$s_x = \frac{d_{min} + d_{max}}{2} \tag{3.4}$$

then all the velocities will be analysable (see figure 3.6). This is analogous to the frequency shifting employed in the method of laser doppler anemometry (LDA).

Unfortunately , as one might expect there is a price to be paid for this expanded dynamic range since the spread of velocities now spans a reduced area of the autocorrelation plane with a comparable reduction in resolution. As a result one should always seek to maximise the area of the correlation plane spanned by the particle spacings on the film.

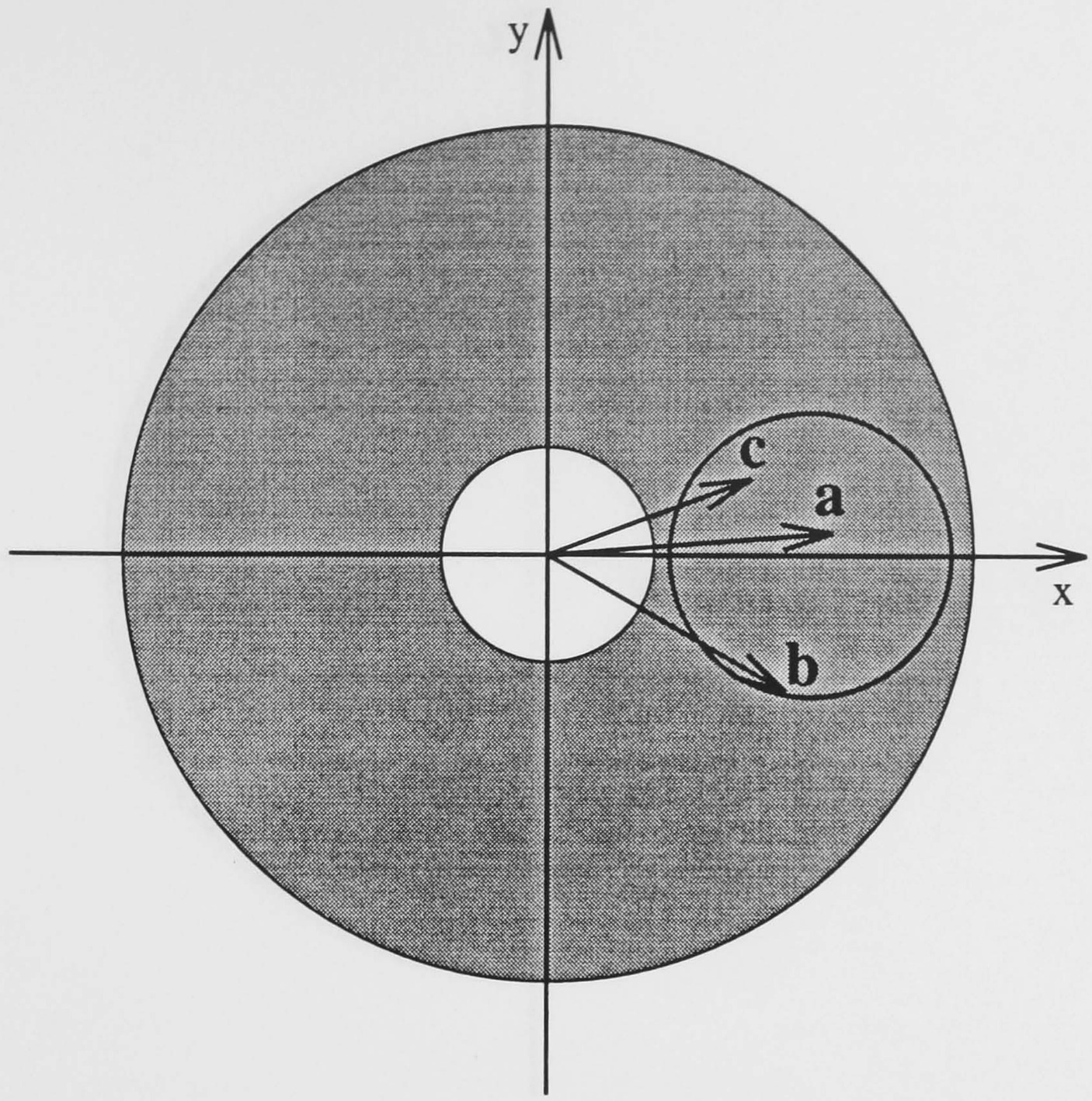

FIGURE 3.6: Shifted image - all velocities resolvable

Compressing the dynamic range

Although at first glance it may seem an unlikely application, image shifting may be usefully employed in reducing the dynamic range of the PIV technique. This is most useful if the flow under study has a range of velocities which differ only slightly from the mean e.g. in the study of turbulent flow in a wind tunnel where the fluctuations are very small compared with the average velocity (see figure 3.7). In such a case the variation of image particle spacings is small and indeed details of the fine structure will be lost if the variations are smaller than those which the analysis system can resolve.

The image shifting system may be used to shift in a direction opposing that of the mean flow and the illumination pulse interval increased so that the range of particle image spacings spans the maximum possible area of the autocorrelation

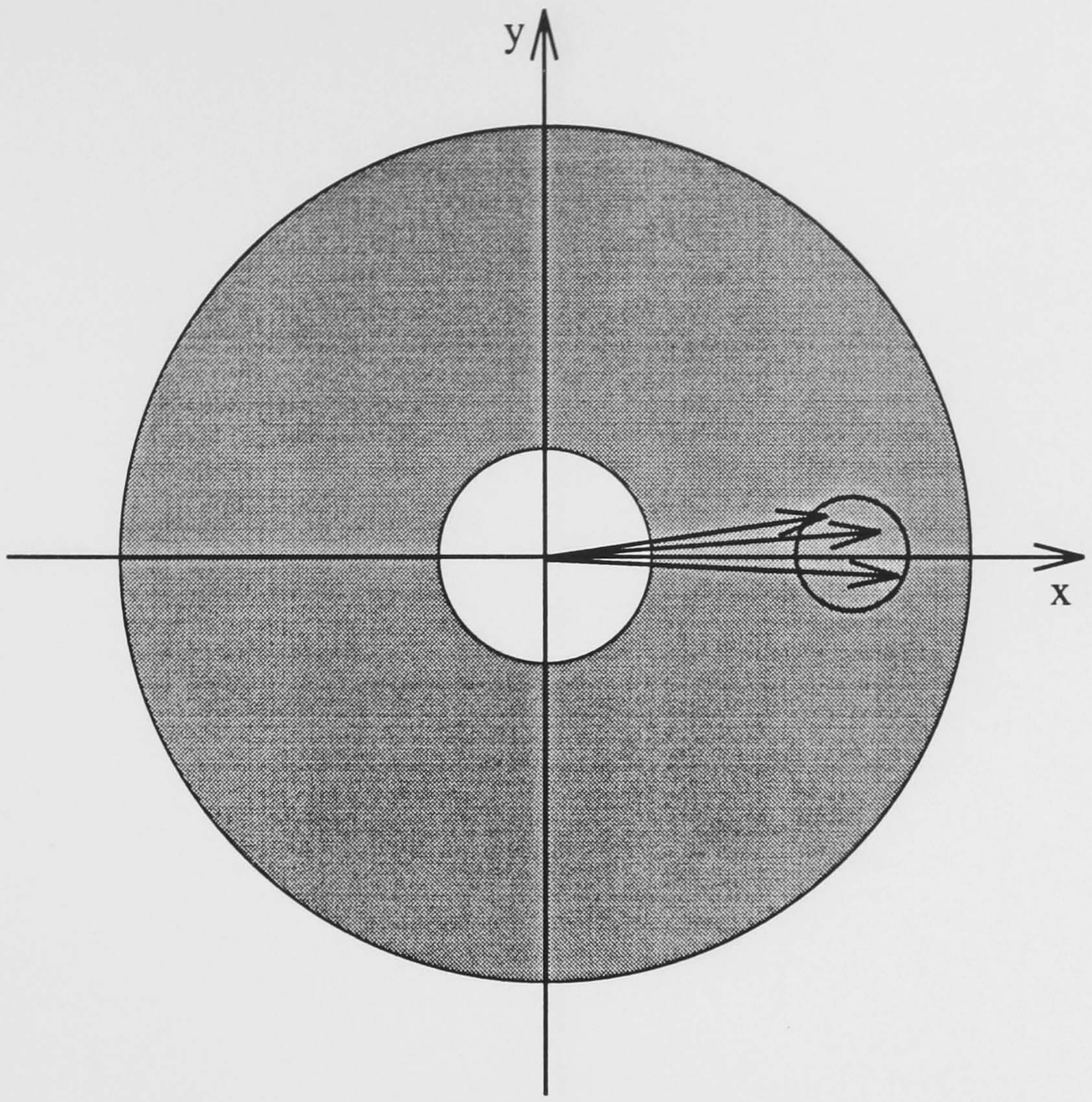

FIGURE 3.7: A small spread of image spacings reduces flow information

plane. This increases the range of velocity variations which the analysis system can resolve and, if the optimum shift speed and pulse interval are chosen, will maximise the information which can be extracted with PIV (see figure 3.8).

Measuring in regions of high acceleration

The analysis system is generally unable to obtain flow vectors from regions of the negative where the speed variation across the interrogation regions varies by more than 5%. Using image shifting to expand the dynamic range may allow these regions to be analysable by reducing the relative variation of speeds across each small interrogation area. However one is obtaining no additional useful information, this apparent improvement in the quality of analysis merely being due to an associated reduction in the resolution of the calculated vectors.

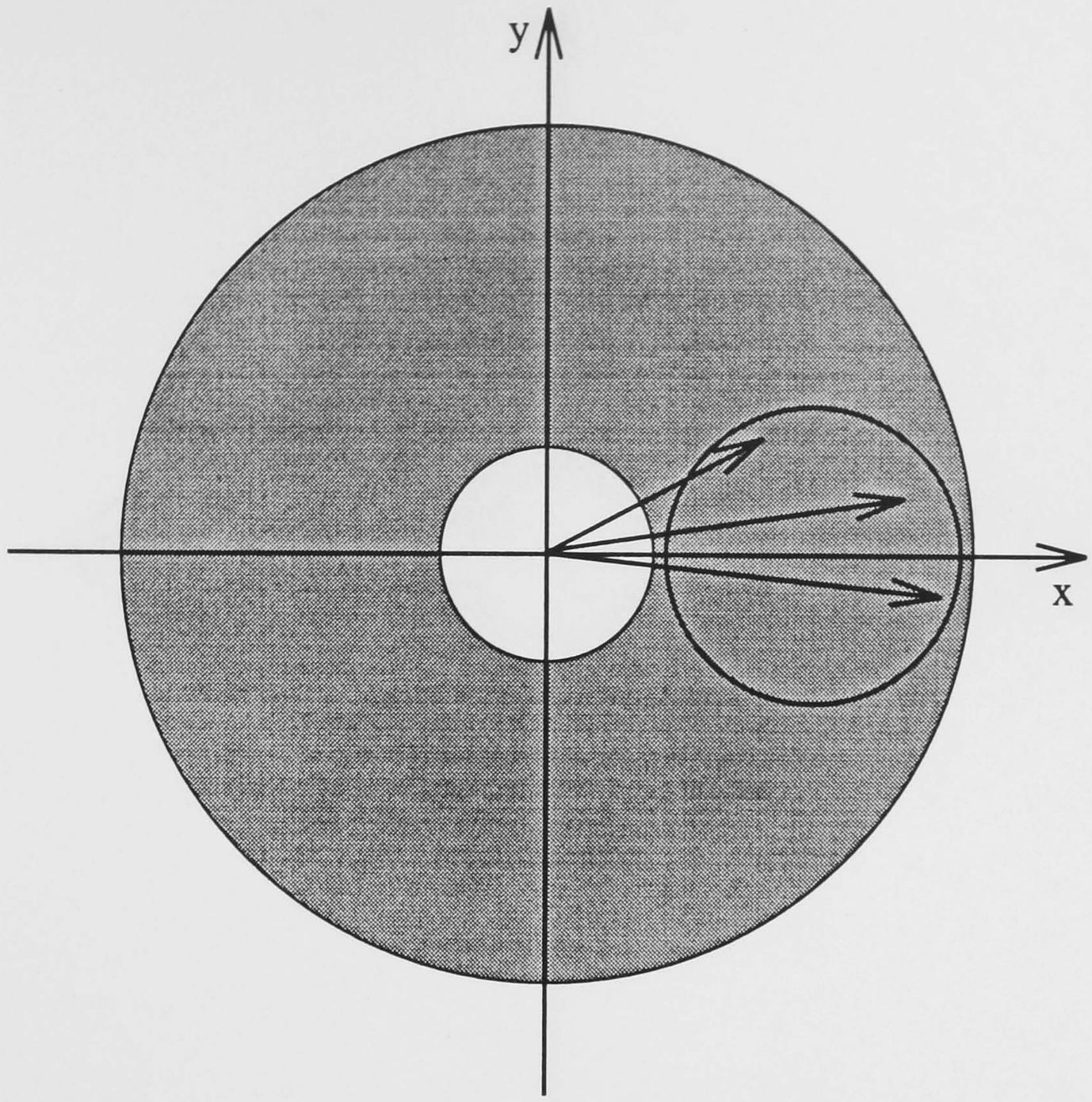

FIGURE 3.8: Image shifting increases the spread of image spacings and maximises the resolution

Choosing the shift direction

If the velocities in a measurement zone are generally aligned along a particular axis then it may be possible to choose the direction of shift in order to optimise the particle image spacings on the negative with respect to the analysis system. Often, however, the plane of image shifting will be dictated by the design of the image shifting system available. For example a turntable system suspended on a thrust bearing can only rotate about a near vertical axis unless the bearing is preloaded.

In general it is desirable for the direction of shift to be orthogonal to the principal flow direction. This allows the shifted particle images to span the greatest possible dynamic range thus retaining the maximum velocity resolution in the resulting flow map. Figure 3.9 illustrates the case where the velocities are predominantly aligned

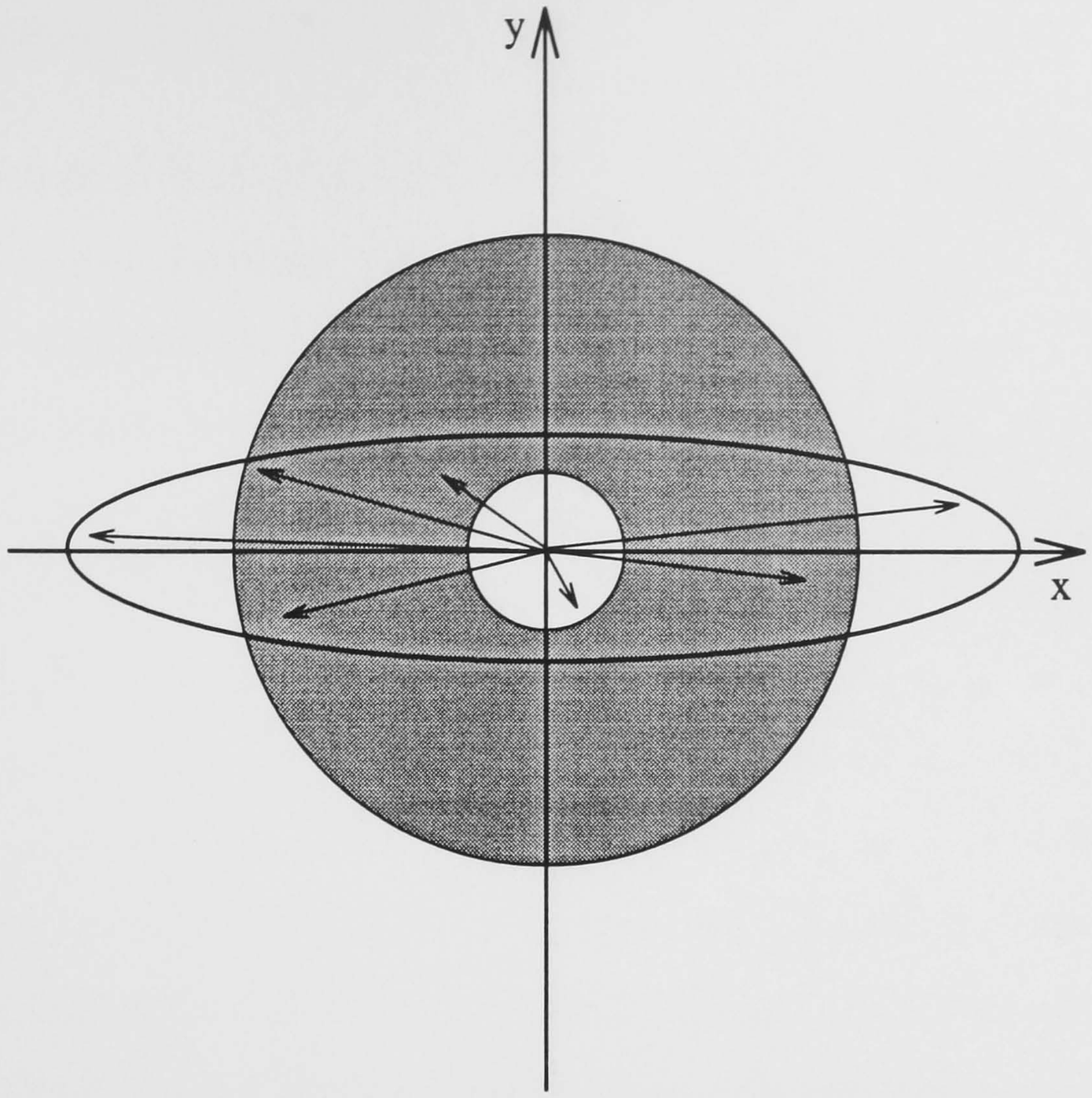

FIGURE 3.9: Envelope of velocities aligned along the x axis

along the x direction. In this case a shift in the x direction would compress all the velocities into a small region effectively reducing the resolution of the analysis system. A shift in the y direction, on the other hand, compresses the dynamic range by a lesser amount retaining as much detail as possible (see figure 3.10).

3.5 Design of first system

A rotating mirror image shifting system built solely for wave flume studies would ideally shift in a vertical direction since the horizontal component of velocity in the flume is generally larger than the vertical component (see section 3.4.1). However a system shifting in the horizontal plane was chosen since this allowed the use of a simple thrust bearing which enabled a low cost simple design to be used.

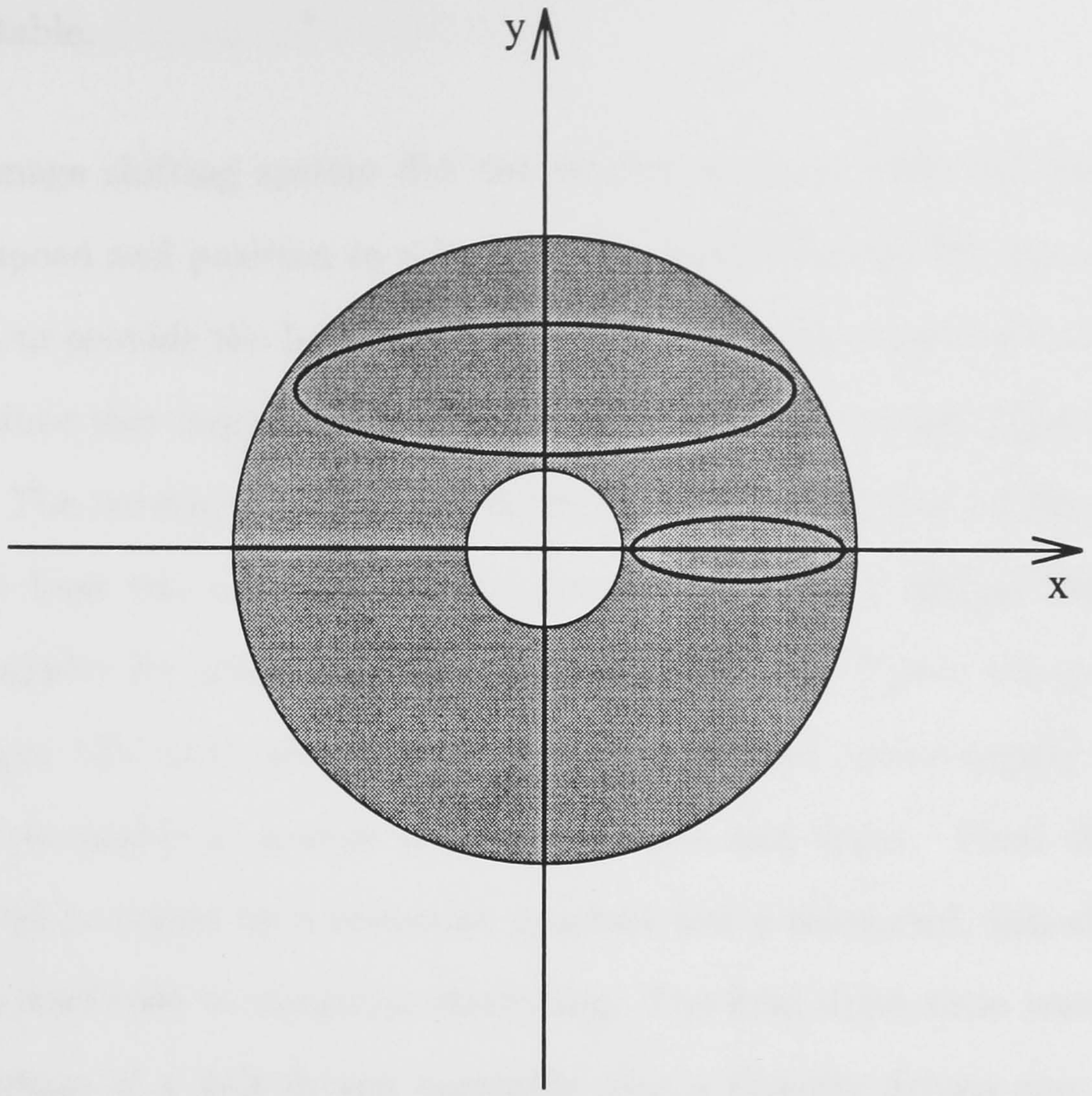

FIGURE 3.10: Optimal shift in y direction retains maximum detail

A 'vertical shift' system, while quite feasible, would require a more complex two bearing system to counteract gravitational force for complete stability.

At first approach it appears easy to build a system which will rotate a vertical mirror in a horizontal plane but the problems are considerable. The PIV method typically has overall errors of less than 5% when used in wave studies so an image shifting system must ideally contribute an error much smaller than this since it is just one part of a complete PIV system. The design target was a system which would contribute not more than a 2% error to a velocity vector map. Satisfying this condition calls for a much smaller relative error in the shifting velocity since its magnitude is often at least twice that of the largest flow vector. Some design aspects were suggested by the design of record turntables which are required to revolve with a constant angular velocity, however an image shifting system has the added complication that its axis of rotation must be at precisely 90° to the plane

of the turntable.

The first image shifting system did not employ a closed loop control system to govern its speed and position so a high inertia turntable with low bearing friction was chosen to provide the best speed stability. A 150mm diameter thrust bearing was used since this large size would give good stability to the 200mm diameter turntable. The turntable was milled from $1\frac{1}{2}''$ thick mild steel giving a mass of 9.4kg. The base was made of $\frac{1}{2}''$ aluminium plate with a tapped hole near the centre of balance for mounting on a heavy duty tripod. Power was provided by a high torque 12V D.C. servo motor with a smoothed power supply capable of driving the turntable at speeds of between 1rpm and 6rpm. Final drive to the turntable was provided by a reduction gearbox and a tensioned, non-slip toothed belt with a steel core to minimise stretching. The final drive ratio was 40:1. The main advantage of a belt driven turntable over a directly driven one is that the former is able to accommodate some wobble of the turntable shaft without affecting the speed whereas the latter is extremely sensitive to small machining errors in the placing of the shaft which can lead to large speed fluctuations due to variable loading on the motor.

3.6 Improved image shifting system

The original image shifting system operated satisfactorily but had several important drawbacks such as its lack of controllability and a considerable mass which resulted in an extremely unwieldy system. Furthermore the thrust bearing used in this way constrained rotation of the mirror to near horizontal planes.

These problems and others were addressed with the assistance of Jean-Baptiste Richon and Tim Campbell in the development of a more complex and versatile

shifting system, pictured in figure 3.11.

This improved system is based around a commercially available precision rotation stage designed to be used in automated machining applications. The combination of a compact turntable and a high speed motor coupled to an ultra low backlash worm drive is ideal for a shifting system.

A custom built control system with an interface to a PC allows easy preselection of the angular velocity during each exposure and fast resetting of the mirror position to reduce the necessary wait time between frames. The control system triggers the camera at the correct time and may also be linked to the computer driving the wavemaker allowing shifted pictures to be taken at predetermined phases of a passing wave for example.

The turntable incorporates a tachometer and an encoder which relay speed and positional information back to the control system allowing its rotation to be closely monitored and governed.

The optical quality of this improved system was greatly enhanced by the inclusion of a 150×100mm high precision front silvered mirror with a flatness equivalent to four wavelengths of red light across its surface (for reference this is equivalent to a mirror the size of Scotland having a worst distortion of less than 5m). This contributes greatly to the performance of the shifting system which is very sensitive to aberrations in the mirror surface.

The above mirror size was the closest to requirements which could be provided 'off the shelf' by the manufacturer although a smaller mirror would have been desirable for compactness.

The necessary mirror size is determined by the field width of the camera which is

about two thirds of the camera to object distance for the Hasselblad camera and 80mm lens at typical distances of 1m or more. However, where the rotating mirror is placed, close to the lens and far from the focal plane the relationship is less linear. Figure 3.12 shows experimental measurements of the minimum necessary mirror half-width based on the field width of view of the lens, at lens to mirror centre distances of less than 0.1m. The broken line shows the maximum half-width to avoid the mirror hitting the lens, so only points which lie below this line give possible mirror sizes. Based on these results the smallest possible mirror would have a width of about 120mm so the one used in the shifting system was not excessively large.

3.7 Using the shifting system

As with any part of the PIV setup the image shifting system requires accurate alignment to minimise the additional errors it contributes. The shifting system incorporating the camera platform is supported by a heavy duty tripod.

3.7.1 Alignment

The turntable is levelled carefully with the aid of a spirit level and the mirror rotated until it is angled at 45° to the direction of view of the camera. Then the whole apparatus is rotated upon its tripod until the reflection of the camera in the glass wall of the flume is centred in the crosshairs of the viewfinder. At this point further fine adjustments may be required to re-level the system after the rotation. Incorporating the camera as part of the shifting system makes this task as simple as possible minimising the degrees of freedom of movement.

FIGURE 3.11: The improved image shifting system

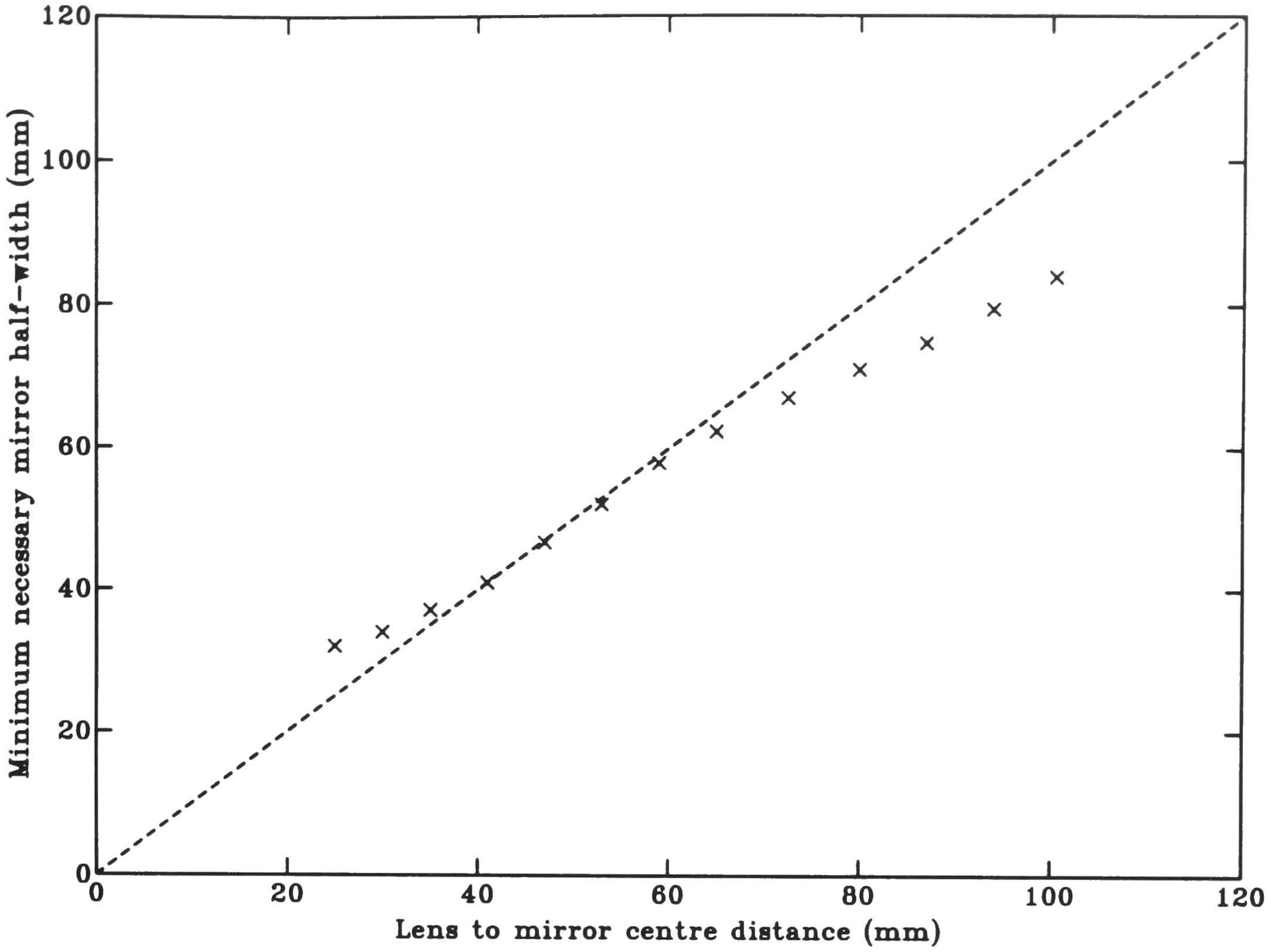

FIGURE 3.12: Experimental values of minimum necessary mirror half-width for various lens to mirror centre distances

3.7.2 Triggering the camera

The chosen rotation rate of the turntable and the shutter opening time of the camera are used to determine the point of rotation at which the camera should be triggered. This ensures that the average mirror angle is 45° during each exposure. Typically the mirror rotation is of the order of 0.5° in this time. It takes about 30ms for the shutter on the Hasselblad camera to be fully open after the trigger pulse is sent and this time is fairly repeatable within about 2ms. This relevant information is entered on the PC controlling the mirror and the system automatically calculates the necessary accelerations and the time at which to trigger the camera.

3.7.3 Determining the shift speed

If the rotation rate of the turntable is not known accurately then the shifting speed may be determined by seeding the measurement zone and waiting for it to settle before photographing it with the image shifting system. The shift speed is then found by analysing the resulting negative. The obvious drawbacks with this method are that the rotation rate must remain constant over a long period of time and the water in the flume will always be moving, however slightly, increasing the standard deviation of the calculated shift. Furthermore it is found that by the time the water motion has settled sufficiently the slight positive buoyancy of the seeding has resulted in a marked concentration gradient making analysis very difficult towards the bottom of the measurement zone.

If the rotation rate is known accurately then the shifting speed at the centre of the frame is given by $2\omega L$ where ω is the rotation rate and L is the optical distance from the mirror centre to the measurement zone.

The process of accurately determining the shift speed at all points in the frame however is considerably more complex than this and is discussed fully in section 3.9.2.

3.7.4 Optimising the system

To gain the best performance from the inclusion of image shifting in a PIV system, all the parameters should be carefully optimised. This helps to avoid common pitfalls such as the introduction of unnecessary errors into the measurements (see section 3.9).

Optimisation requires good prior knowledge of the velocity range in the flow under

study and this leads to an apparently intractable problem since one would have no need for PIV or image shifting if such information was readily to hand.

A good first guess as to the range of velocities can often be made by considering the known properties of the flow e.g. bulk flow rate if the flow is in a pipe, or the phase speed of a wave in a flume. However the necessary information is best gathered by first taking PIV measurements, without image shifting, over a range of illumination rates. This typically results in several fields of velocity data, each spanning a different range of magnitudes. These data may then be used, with some confidence, to select the plane of shifting, the magnitude of shift and the associated illumination rate and camera shutter speed.

The steps involved in optimising the system may be summarised as follows:

1. Use a-priori knowledge of the flow to approximate the range of velocity magnitudes.

2. Take a series of PIV pictures (without image shifting) with a range of illumination rates and shutter speeds which, altogether, should allow the full range of velocity magnitudes to be measured.

3. Analyse the frames to find the actual range of velocities present, repeating step 2 if there are still regions of the flow which cannot be successfully analysed.

4. Use this knowledge to choose the shift direction and the shift speed (see section 3.4.1) for the best possible results with image shifting.

3.8 Intrinsic effect of shifting on PIV errors

The technique of image shifting applied to PIV adheres to the common belief that 'you don't get anything for nothing' and there is a trade-off between the range of measurable velocities and the resolution.

The second fourier transform performed by the analysis system has a typical resolution of 64×64 and the system can generally locate the position of the signal peaks to about one tenth of a grid spacing resolving vectors with an accuracy of up to 0.1%.

Where image shifting is used to increase the dynamic range of PIV the reduction in resolution is of the same order as the increase in dynamic range since all measurable velocities are calculated from the effective 640×640 grid size. For most applications the expanded dynamic range is deemed to be worth the decreased resolution.

Conversely if image shifting is used to compress the dynamic range there is an associated decrease in the absolute errors since a smaller range of velocities is spanning the grid space.

3.9 Errors in image shifting

In the case of the rotating mirror system the inclusion of what is, in effect, an extra optical component in the PIV system inevitably leads to errors. For the most part the errors are due to the fact that this is a mechanical system external to the original PIV setup but there are other intrinsic difficulties which are explained below.

3.9.1 Random errors

By the nature of the system many of the random errors occurring in the motion of the mirror affect all the particle displacements on the film almost equally. As a result, on observation of a shifting speed calibration vector plot, a large error may appear systematic in nature although its source is random. The major sources of random error are as follows :

- Variations in angular velocity of the turntable
- Determination of shift speed
- Camera vibration

Variations in angular velocity of the turntable

In theory the rotation rate of the turntable need only be constant during the short exposure time of the film for the shifting system to be useful. However in practice either the rotation rate must be very stable as a function of both angle and time or else a control system must predetermine it during the steady part of its motion. This is because ultimately the shifting system is only as good as the accuracy with which the shift speed can be determined.

Determination of shift speed

As mentioned in section 3.7.3 the shift speed at the centre of the frame is given simply by $2\omega L$. While ω may be determined accurately with accurate timing and the turntable encoder, measurement of L presents more of a problem. It cannot

be directly measured with a ruler since it is dependent upon the refractive indices of the glass and water through which the measurement zone is photographed. If the refractive indices and optical path lengths are known then it can be calculated subject to the errors of each measurement. Alternatively it can be inferred from the value of photographic magnification but this also requires measurement of the angle of view of the camera lens (see section 3.9.2).

Camera vibration

Camera vibration due to the motor driving the turntable was evident with the first shifting system and leads to streaked particle images but the high quality motor and bearing assembly used latterly have virtually eradicated the problem.

3.9.2 Systematic errors

Systematic errors should not provide too many problems in general since by definition we can correct for them to a large extent. However, adequately describing the effect of the source of error on the resulting measurement can prove to be a complicated exercise. The major sources of systematic error are as follows :

- Variation of shift velocity across frame

- Mirror flatness

- Angle of mirror during exposure

- Translation of measurement zone

- Reduction of spatial resolution

Variation of shift velocity across frame

When using an image shifting system one generally assumes that the shift velocity is uniform across the measurement zone which of course is true in the case of a translating camera system. However in the case of systems based on a rotating camera or rotating mirror this assumption is false since it is based on the approximation that a curved surface (points equidistant from the axis of rotation of the mirror) is locally flat. Clearly this approximation improves as the camera to measurement zone distance is increased but at a typical distance of about 1m the variation of shift speed becomes much more significant.

The theoretical horizontal and vertical shifting speeds due to the rotating mirror image shifting system may be determined by considering the mapping of a point (x, y) relative to the centre of the film on to the measurement zone taking account of refraction due to the flume glass and the water. In the case of the 55×55mm medium format film used for this study the corresponding approximate horizontal and vertical coordinates are given respectively by

$$x_m = r\cos 2\phi - \frac{(L_1 + r\sin 2\phi)\left[r(\cos 2\phi - 1) + \dfrac{dr\tan\phi}{d\tan\phi + x}\right]}{r\sin 2\phi - \dfrac{xr\tan\phi}{d\tan\phi + x}} + \frac{L_2\sin\theta_x}{\sqrt{n_2^2 - \sin^2\theta_x}} + \frac{L_3\sin\theta_x}{\sqrt{n_3^2 - \sin^2\theta_x}} \tag{3.5}$$

and

$$y_m = \frac{(L_1 + r\sin 2\phi)yr\tan\phi}{\left(r\sin 2\phi - \dfrac{xr\tan\phi}{d\tan\phi + x}\right)(d\tan\phi + x)} + \frac{L_2\sin\theta_y}{\sqrt{n_2^2 - \sin^2\theta_y}}$$

$$+\frac{L_3 \sin\theta_y}{\sqrt{n_3^2 - \sin^2\theta_y}} \tag{3.6}$$

where

$$d = \frac{0.055}{2\tan\alpha} \tag{3.7}$$

$$L_1 = \frac{d}{M} - \frac{L_2}{n_2} - \frac{L_3}{n_3} - r \tag{3.8}$$

$$\theta_x = 2\phi + \tan^{-1}\left(\frac{x}{d}\right) - \frac{\pi}{2} \tag{3.9}$$

$$\theta_y = \tan^{-1}\left(\frac{y}{d}\right) \tag{3.10}$$

and r is the distance from the mirror centre to the 'virtual' aperture (see figure 3.13), α is the half-angle of view of the camera lens, M is the measurement zone to film magnification, L_2 and L_3 are the flume glass thickness and the glass to measurement zone distance respectively and n_2 and n_3 are the associated refractive indices of the glass and the water.

The horizontal and vertical components of the shift vector at each point are then given respectively by

$$V_x = \omega \frac{dx_m}{d\phi} \tag{3.11}$$

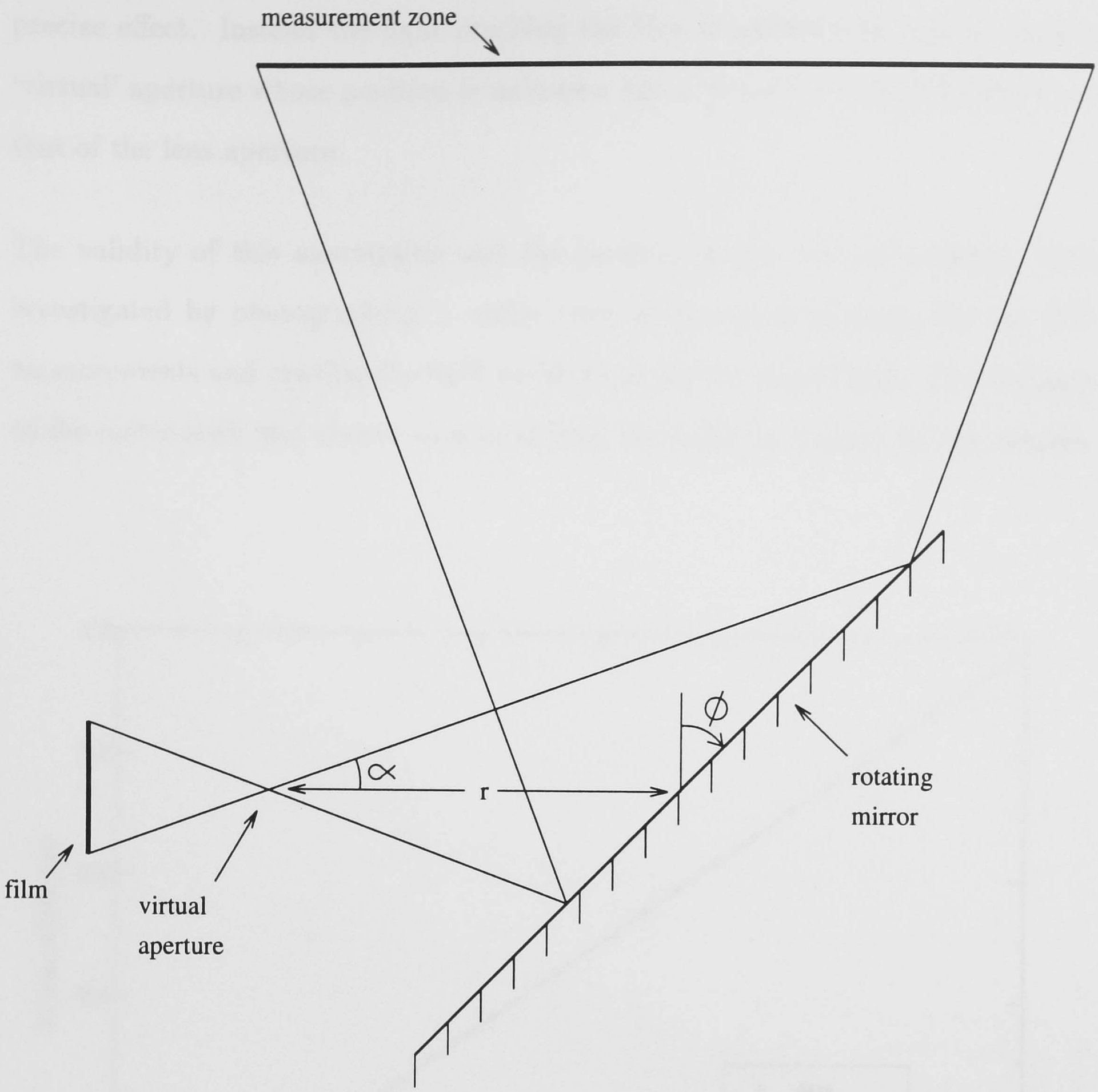

FIGURE 3.13: Schematic diagram of rotating mirror image shifting system

and

$$V_y = \omega \frac{dy_m}{d\phi} \tag{3.12}$$

The explicit forms of equations 3.11 and 3.12 are given in appendix 7.2.

The Hasselblad camera lens inverts the image onto the film and because the path of light through its many elements is unknown no attempt is made to model its

precise effect. Instead the light reaching the film is assumed to pass through a 'virtual' aperture whose position is unknown but is expected to be different from that of the lens aperture.

The validity of this assumption and the position of the 'virtual' aperture were investigated by photographing a metre stick at distances common for the PIV measurements and reading the field width from the developed film. The distance to the metre stick was always measured from the same fixed point on the camera.

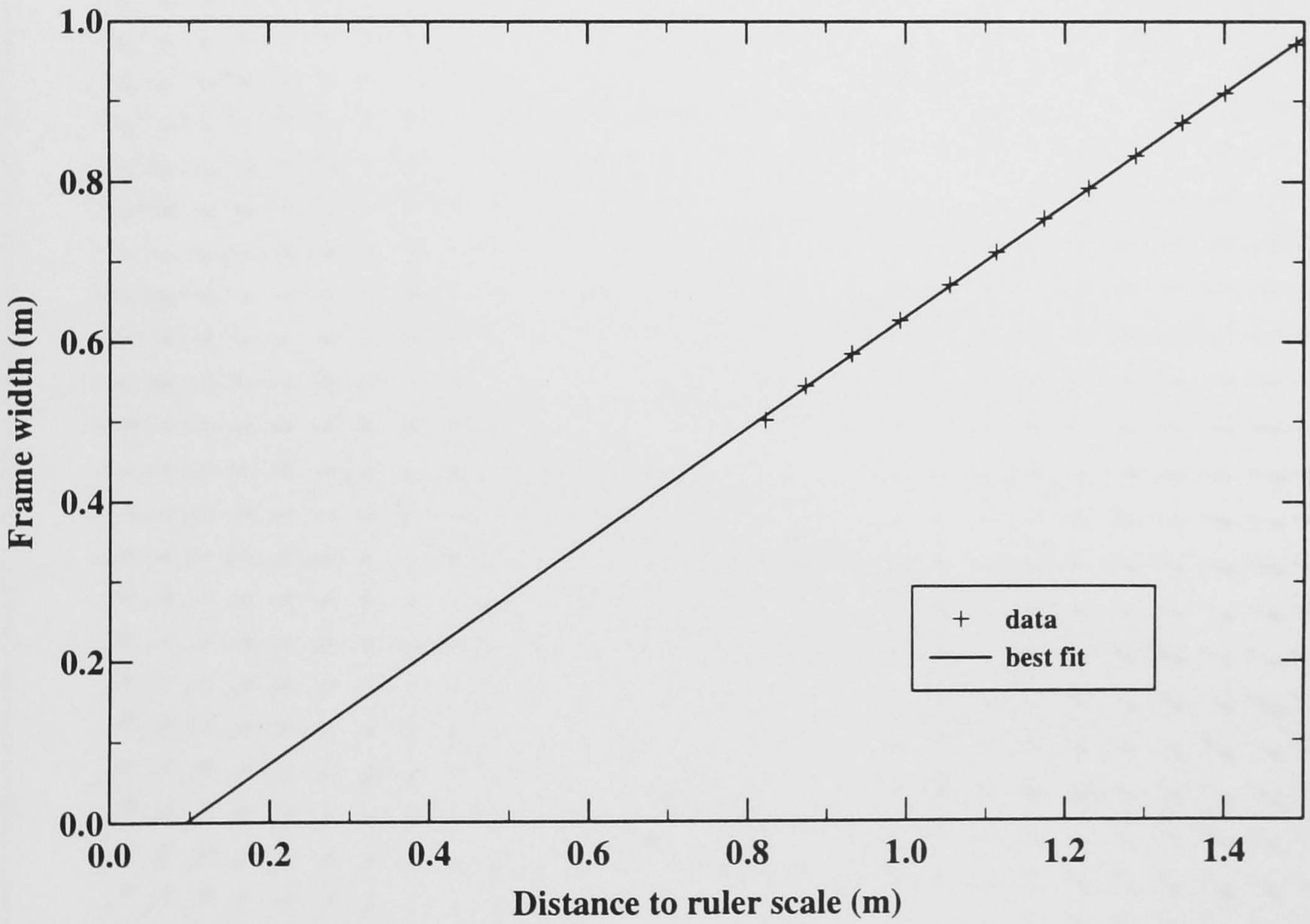

FIGURE 3.14: Relationship between 80mm lens field of view and distance from measurement zone

The results in figure 3.14 show a very good linear relationship within the required range which validates the simple model of the lens. The position of the 'virtual' aperture is given relative to the fixed point on the camera by extending the best fit straight line to the horizontal axis. Surprisingly this is found to be about 10cm

in front of the actual lens aperture. The graph shown in figure 3.14 yields a value for the angle of view of the lens of 2α=34.9° .

Figure 3.15 shows a typical theoretical variation of the shift velocities within a frame, the centre shift having been subtracted for clarity.

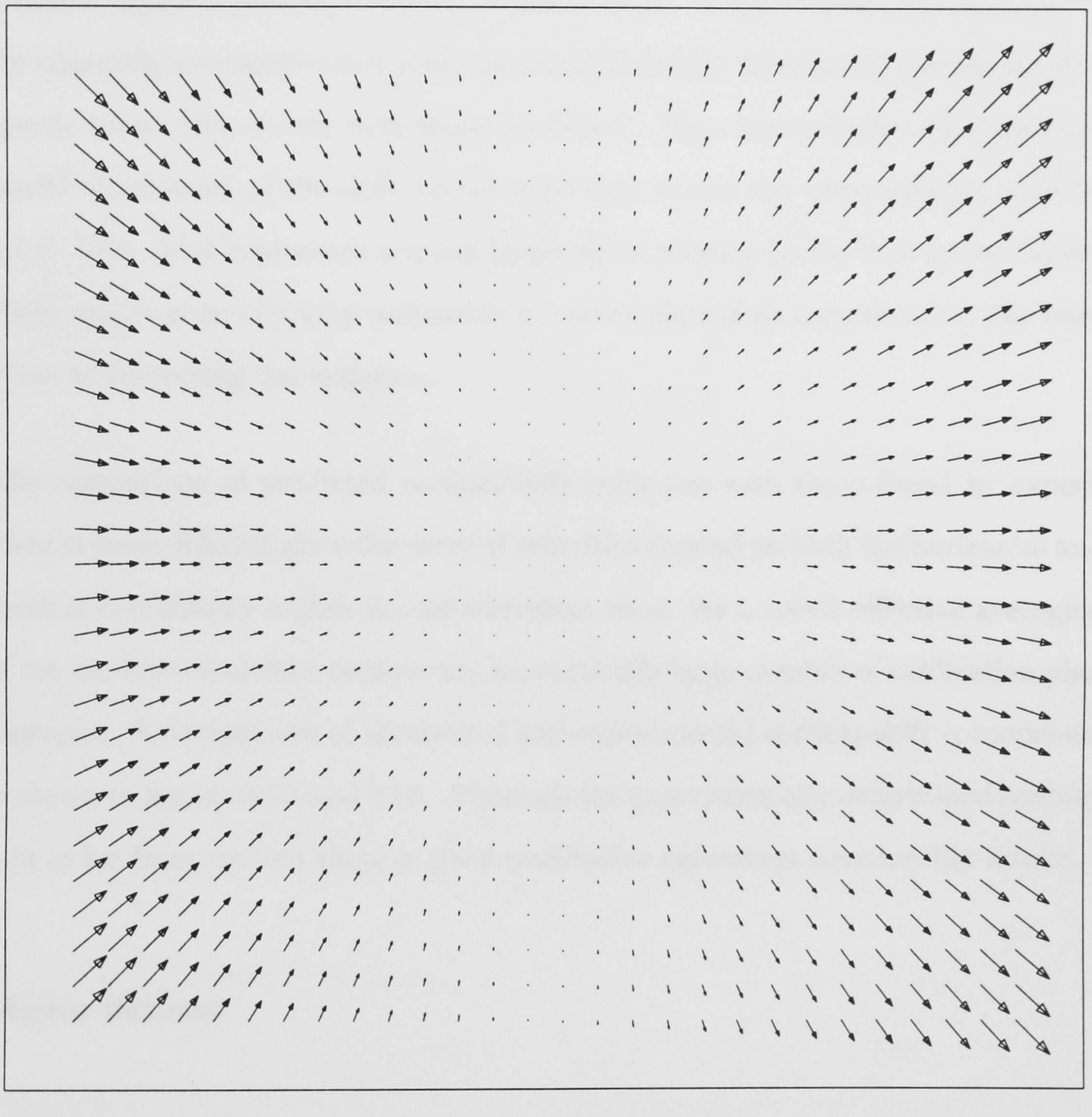

FIGURE 3.15: Theoretical shift variation due to rotating mirror system (centre shift subtracted)

These theoretical results may be easily checked with calibration pictures of still,

seeded water taken using the shifting system. In practice the water is never completely still leading to random fluctuations in the measured velocities. For comparison the effect of these variations may be reduced by first ensemble averaging several vector plots and then averaging all the horizontal components of the shift velocity with the same x coordinate since they are, by definition, independent of y. Figures 3.16 and 3.17 show comparisons from two separate experiments with different magnifications and mirror rotation rates. Despite some obvious noise in the ensemble averaged vector plots the experimentally determined horizontal shift speeds agree very closely with those predicted. This demonstrates that the horizontal component of the shift vector may vary across the measurement zone by up to 10%. This represents a much larger error relative to the flow speeds under study and is generally very noticeable in vector plots if no consideration has been given to correcting the variation.

The comparison of predicted vertical shift velocities with those found by experiment is more difficult since the vertical velocities depend on both the horizontal and vertical coordinates within the measurement zone. As a result effective averaging of the experimental data requires an impractically large number of calibration photographs. A comparison of theoretical and experimental vertical shift components is shown in figures 3.18 and 3.19. Although the experimentally determined contour plot is far from smooth there is good qualitative agreement between the results.

Mirror flatness

Any distortion of the reflecting surface of the mirror has an amplified effect on the photographed image of the measurement zone which may be very difficult to correct later. The mirror used has a flatness of 4-λ across its 150mm wide surface. This gives rise to a typical distortion of about 0.03% at the edges of the

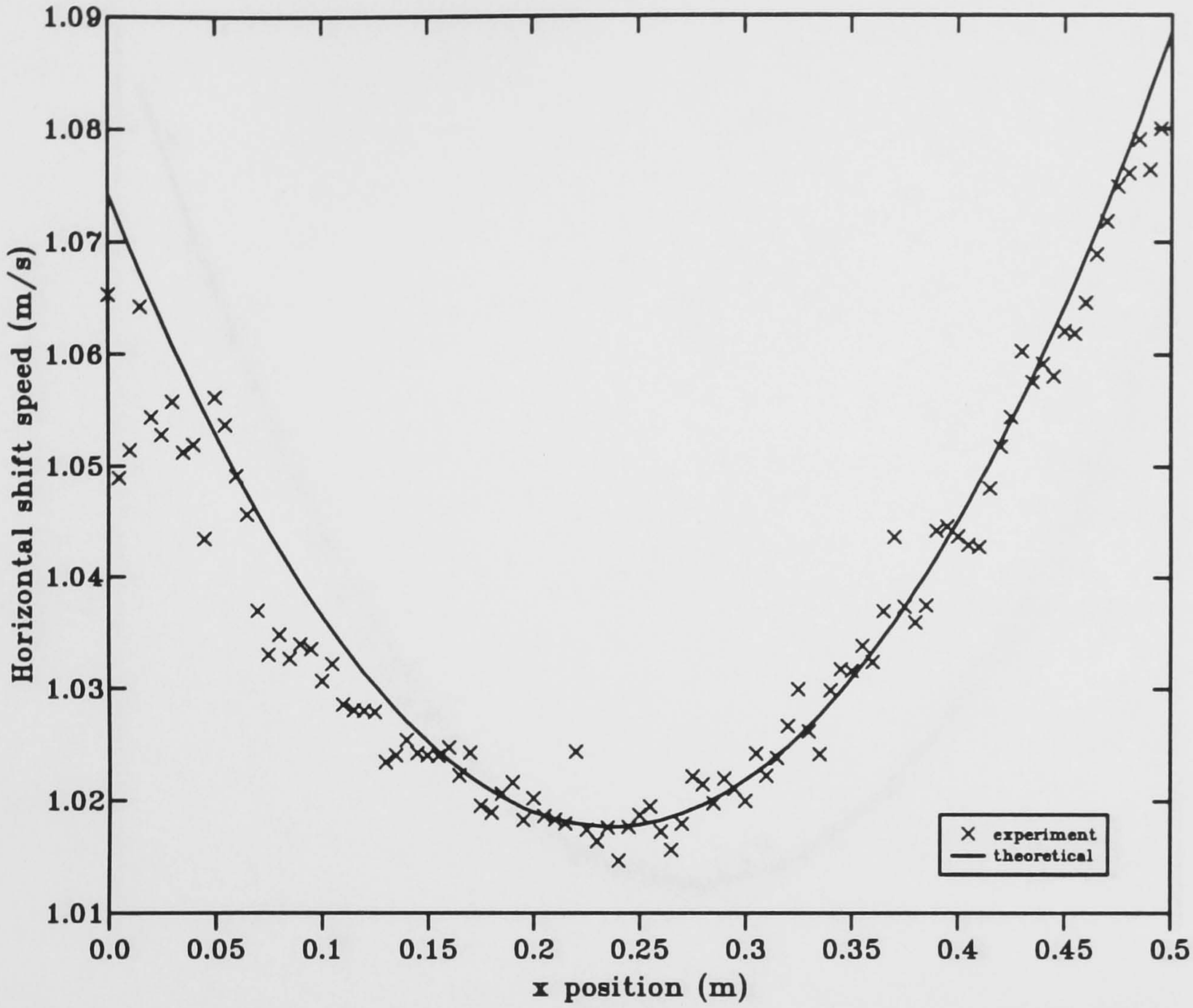

FIGURE 3.16: Comparison of experimental and theoretical x shift velocities (magnification = 0.0911, ω=35°s^{-1})

measurement zone and may be conveniently ignored.

Angle of mirror during exposure

If the mirror angle at which a frame is taken deviates significantly from 45° then the actual measurement zone not only becomes translated from the intended one but becomes distorted too. As a result of this the shifting speed is also altered since effectively the camera is no longer perpendicular to the plane of the measurement zone. The shifting speed is increased at one side of the frame and decreased at the

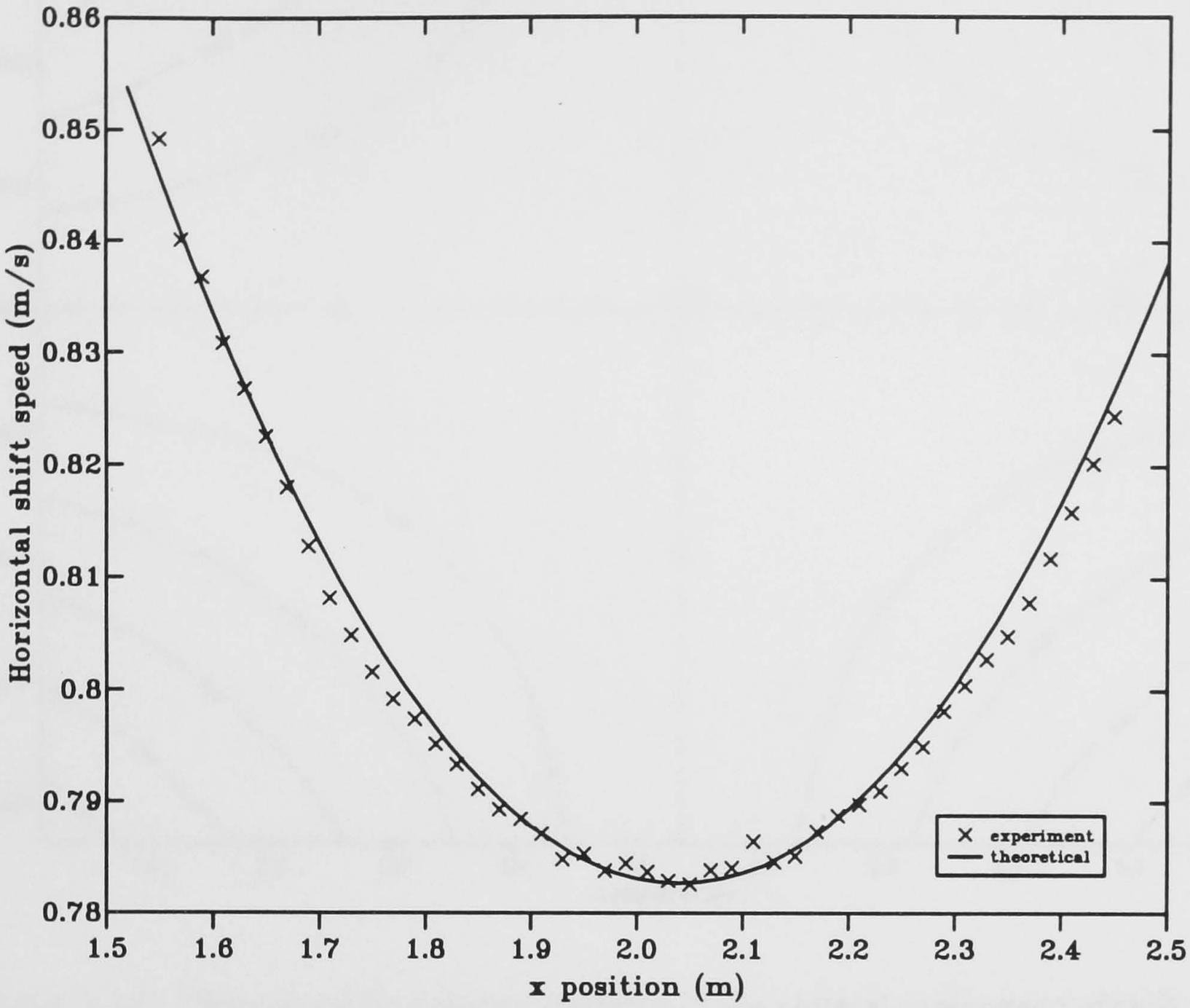

FIGURE 3.17: Comparison of experimental and theoretical x shift velocities (magnification = 0.0519, ω=13.6°s^{-1})

other typically by about 2.5% per degree for small angles of deviation.

Translation of measurement zone during exposure

During an exposure each point in the measurement zone is translated a distance approximately equal to $2\omega_m Rt$ where R is the distance from the camera to the measurement zone and t is the exposure time. This typically equates to a shift of the order of 1cm and may cause problems if the negative is to be aligned accurately on the analysis rig with respect to a reference point in the measurement zone. This

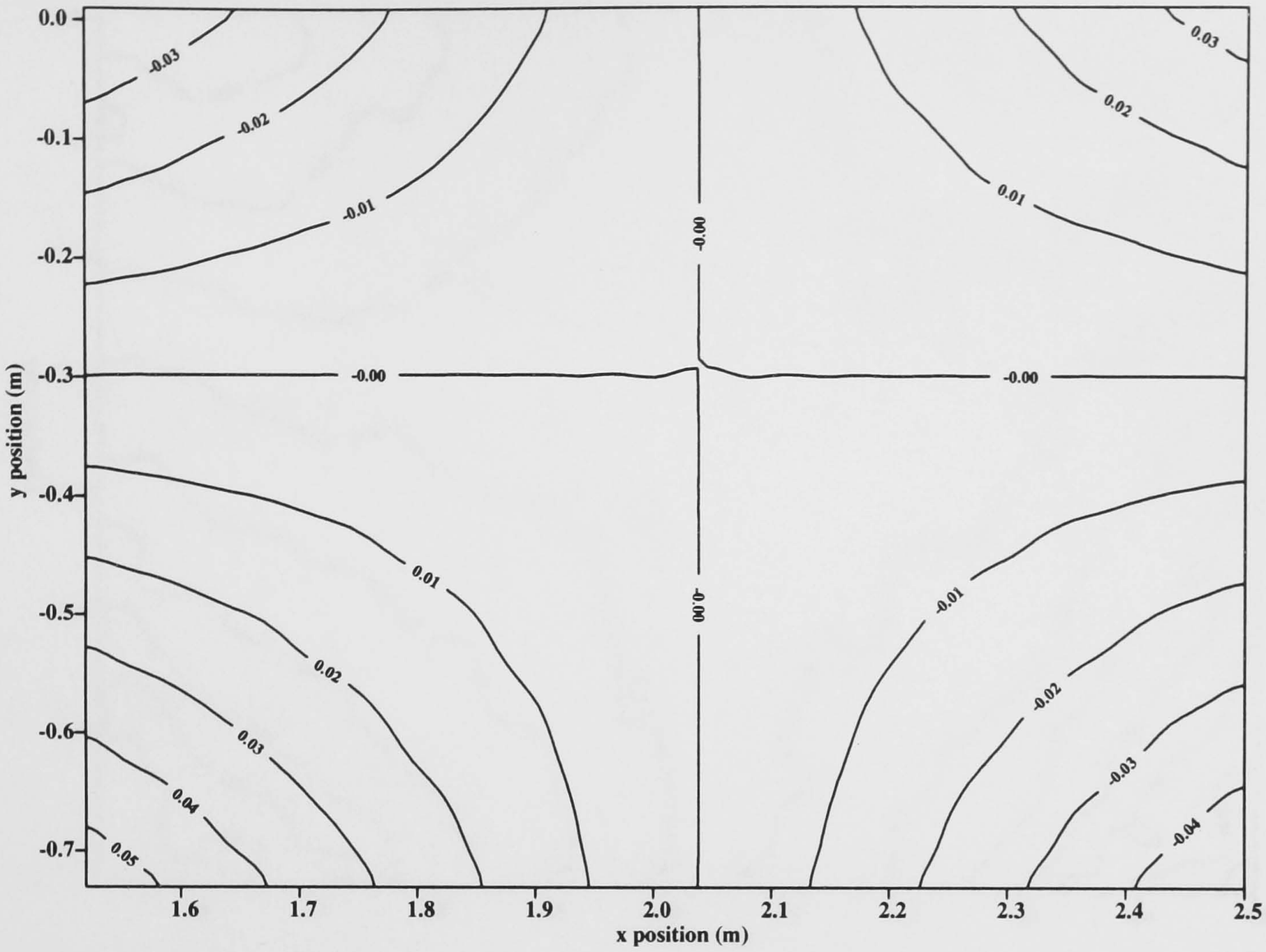

FIGURE 3.18: Theoretical iso-velocity contours of the vertical component of shift velocity. Values given in metres per second (magnification = 0.0519, ω=13.6°s^{-1})

problem is unavoidable and as with other errors involved in the use of image shifting it may only be reduced by choosing the minimum possible mirror rotation rate.

Reduction of spatial resolution

Another consequence of the translation of the measurement zone is a reduction in the spatial resolution of the PIV technique due to image shifting, with the length scale of the finest analysable structure in the plane of the shift being equal to the shifted distance during the exposure.

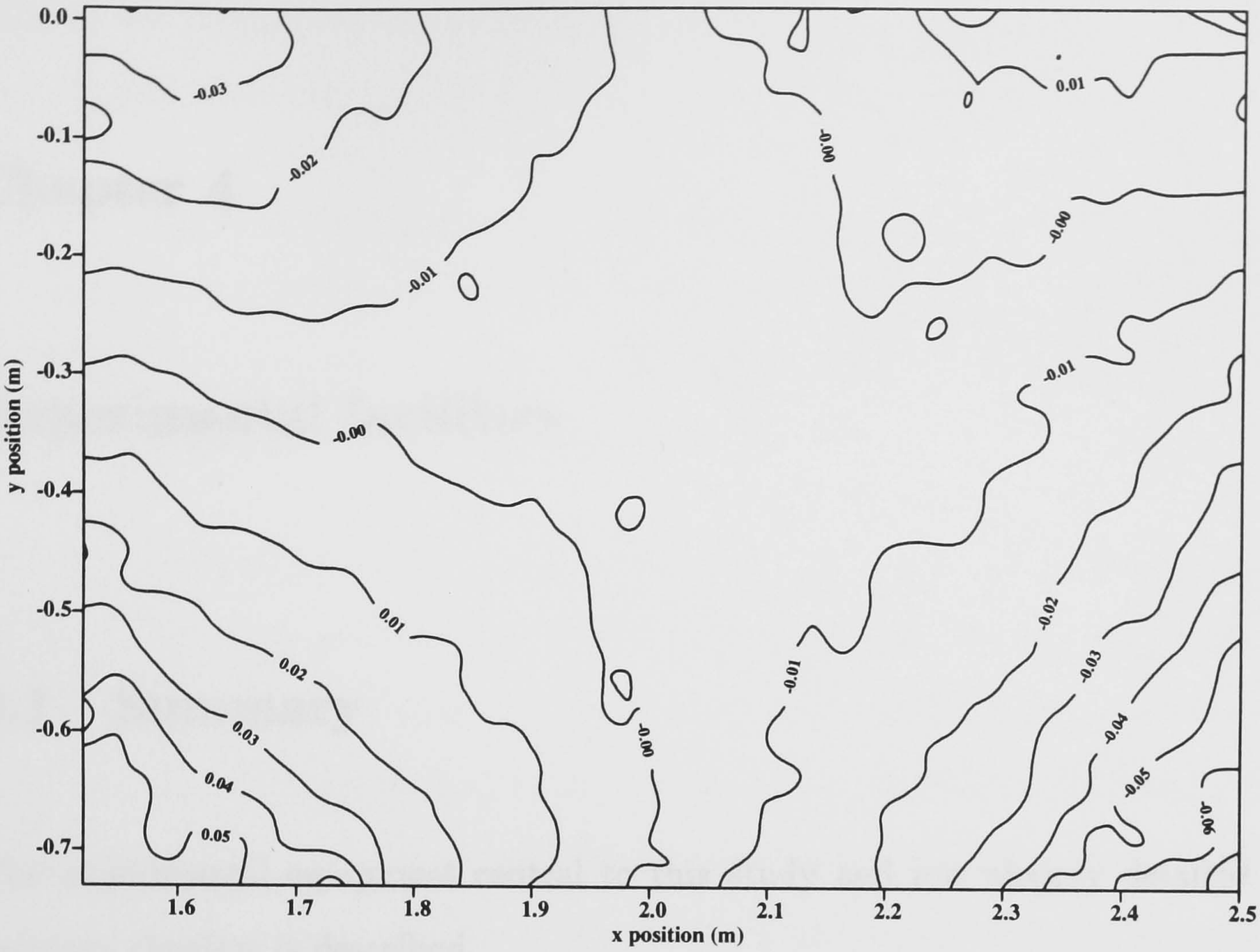

FIGURE 3.19: Experimental iso-velocity contours of the vertical component of shift velocity. Values given in metres per second (magnification = 0.0519, ω=13.6°s^{-1})

3.10 Conclusions

The technique of image shifting has been shown to be a very valuable addition to the PIV method allowing full field analysis of very complex flow types. However there is a price to be paid in the form of reduced spatial resolution and increased errors in the analysed velocities. Indeed if no attempt is made to correct for the systematic shift vector variations then velocity magnitudes near the edges of the measurement zone may be in error by more than 20%. It has been shown that these variations can be successfully accounted for and corrected theoretically.

Chapter 4

Experimental facilities

4.1 Summary

The experimental equipment central to this study and not already detailed in previous chapters is described.

4.2 Wave flume

The wave flume used throughout this study was designed by David Skyner [49]. It is 9.8m in length and 0.4m wide, with a mean water depth of 0.75m and consists of three bays. Waves are produced by a cam driven paddle which is hinged at its base. It incorporates a force transducer which allows the paddle to create the outgoing wave train and simultaneously absorb incoming reflections. This helps to prevent the formation of seiches within the flume and ensures that the water surface settles quickly after each experiment, greatly reducing the necessary waiting time before the next can begin.

The wavemaker is capable of producing waves with frequencies in the range 0.1Hz to about 2Hz, the maximum amplitudes governed by the range of paddle movement at low frequencies and by wave instability at high frequencies. The natural frequency of cross-waves in the flume, at a water depth of 0.75m, is 1.40Hz.

The combination of the wavemaker and the Archimedes microcomputer driving it is capable of producing complex wave profiles by superposition of the individual components. For example this allows deep water breaking waves and random wave spectra such as JONSWAP or Pierson-Moskowitz [39].

The final 2 metres of the flume are terminated by wedge shaped passive wave absorbers which prevent reflections from the end of the flume affecting experiments. Figure 4.1 shows a graph of the variation of the coefficient of reflectance from the foam across a large part of the frequency range of the wavemaker, calculated from wavegauge records. As one might expect the absorbance is greatest at higher frequencies where the two metre lengths of foam correspond to a greater number of wavelengths than at lower frequencies. The method of analysing wave records to calculate reflection coefficients is described in detail in section 6.4.2.

The walls and base of the flume are glass throughout to allow unimpeded optical access for the PIV system which may be employed at any point along a 6m section (see chapter 2).

A pair of 1″ diameter parallel rails which run the full length of the top of the flume provide stable fixing points for experimental equipment - a very important consideration since even the modest wave amplitudes generated in such a facility can result in surprisingly large forces at points of impact. Fixing points are provided within the flume itself in the form of vertical, square section aluminium channels between the sheets of glass.

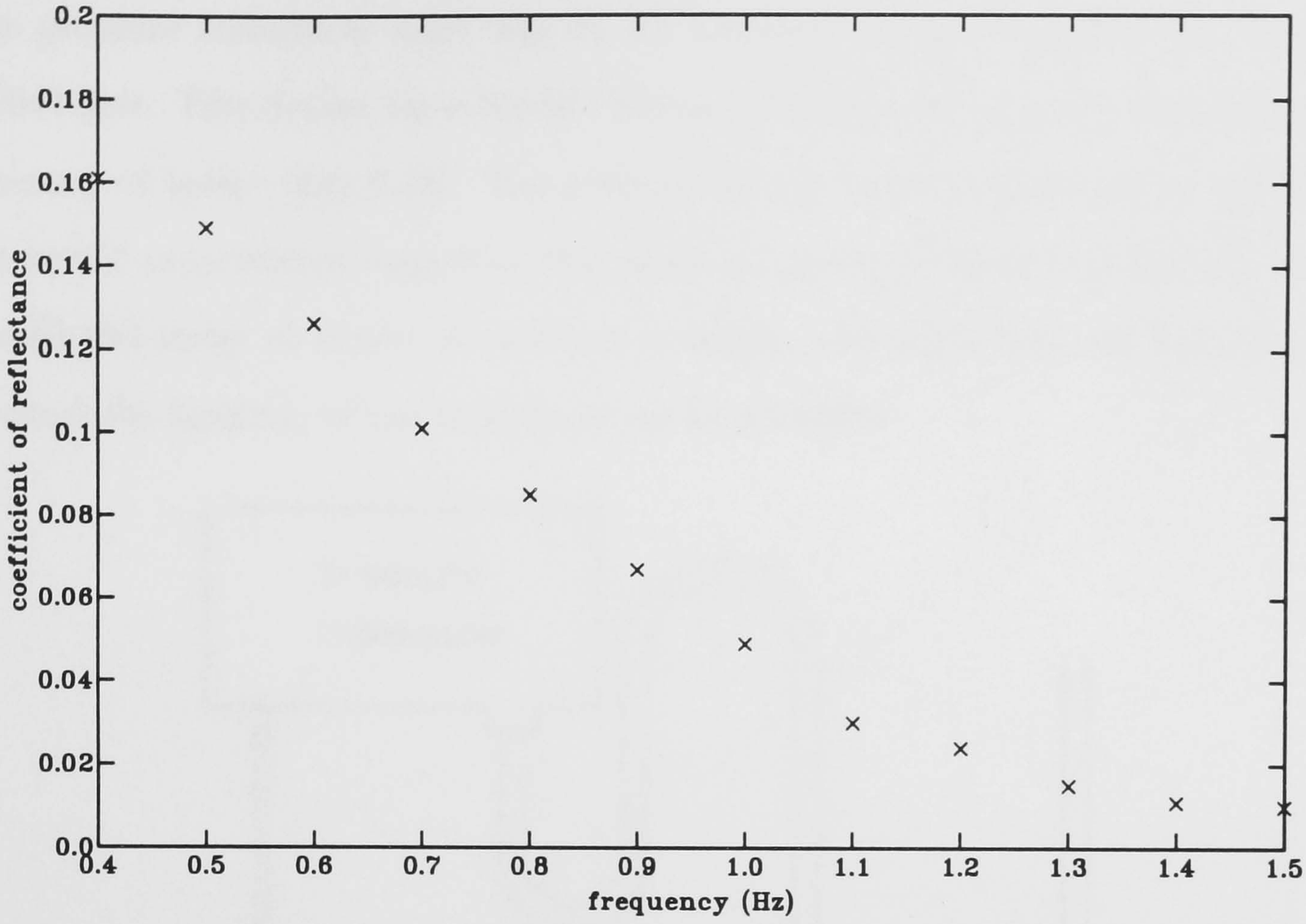

FIGURE 4.1: Measured reflectance coefficients of sinewaves incident upon absorbing foam, wave amplitude = 10mm

4.3 Pressure transducer

All air pressure measurements were made with a high precision differential pressure transducer. The main requirements of this device, aside from the measurement accuracy, were that it should be reasonably water resistant and that it should be capable of sampling rates about two orders of magnitude greater than the typical wave test frequencies.

The requirement of water resistance is an obvious precaution when using such a sensitive instrument so close to the flume and as an additional measure, a completely waterproof case was made for it.

The sampling rate condition was to ensure that there were a sufficiently large number of samples per wave cycle to allow reasonable comparison with other results.

The pressure transducer used was an RF shielded Furness Controls Ltd model FC044 unit. This device has a size of 120mm×100mm×40mm and a measurement accuracy of better than 0.1%. The instrument was factory calibrated to ±500Pa but initial experiments suggested that peak pressures in the OWC chamber may exceed this range at times. As a result a simple calibration test was carried out to check the linearity of the transducer up to ±1000Pa.

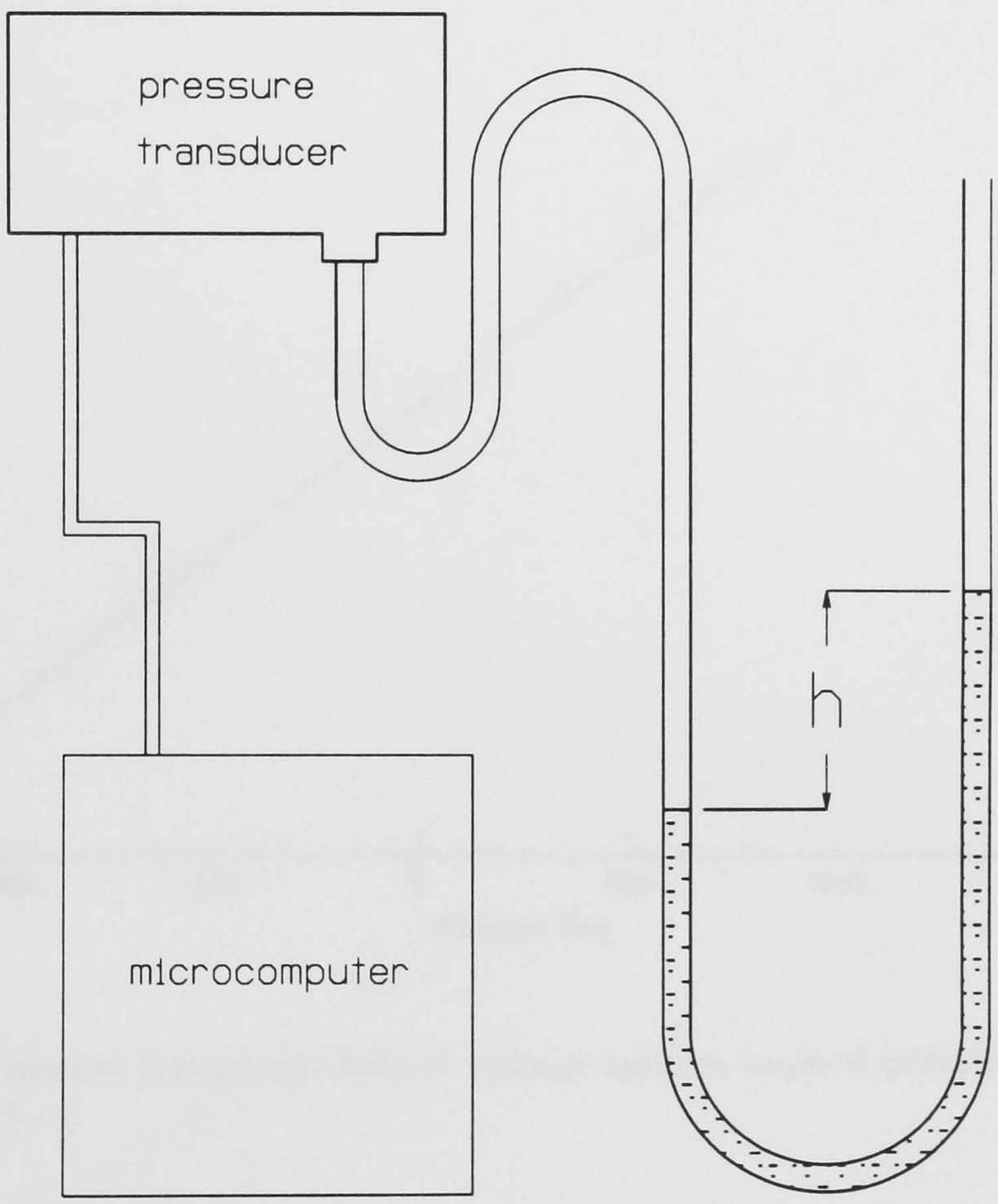

FIGURE 4.2: Calibration test setup for pressure transducer

A glass U-tube containing coloured water was fixed in an upright position with one end open to the air while the other was connected to the pressure transducer with a short, airtight flexible tube (see figure 4.2). The water column height difference, h,

in the two sides of the U-tube was varied and measured to find the static pressure difference ρgh. A microcomputer logged the output voltage from the transducer and values were taken for values of h in the range -10cm to +10cm.

The calibration graph in figure 4.3 shows the transducer response to be very linear outside its design range up to the required limits of $\pm$1000Pa.

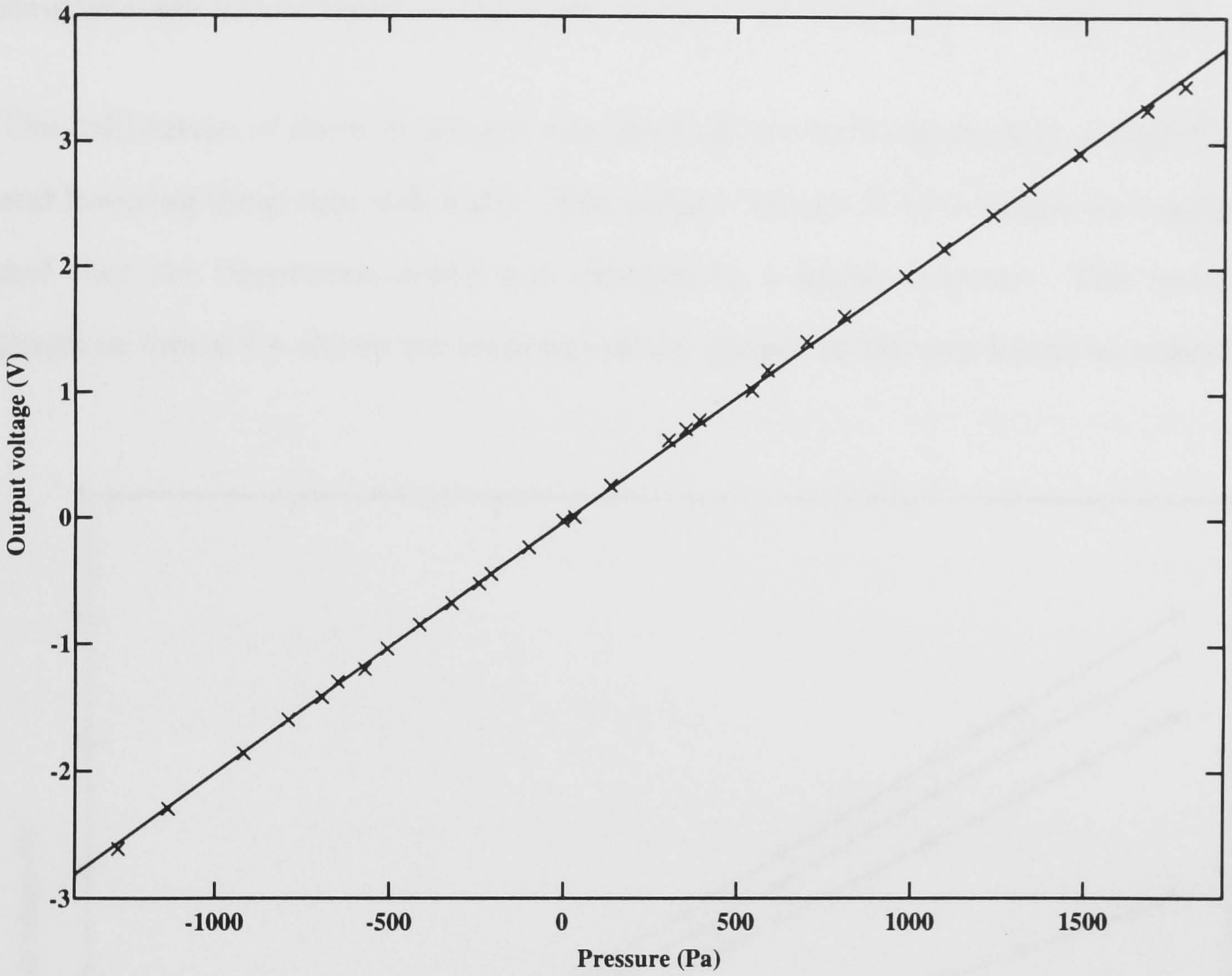

FIGURE 4.3: Pressure transducer output voltage against applied pressure ($\times$) and best fit straight line (—)

4.4 Wave gauges

In this study water elevations were measured with conductive wave gauges. They comprise two parallel, vertical metal rods about 2cm apart which are lowered into the water. The conductivity between the rods is measured and is proportional to the depth of immersion. A separate section at the bottom of one of the rods measures the conductivity of the water itself so allowance can be made for it.

The calibration of the four gauges was checked by attaching them to a rigid frame and lowering them into still water. The output voltage of each gauge was sampled and then the immersion depth was changed by a known amount. The resulting graph in figure 4.4 shows the response of the gauges to be very linear as expected.

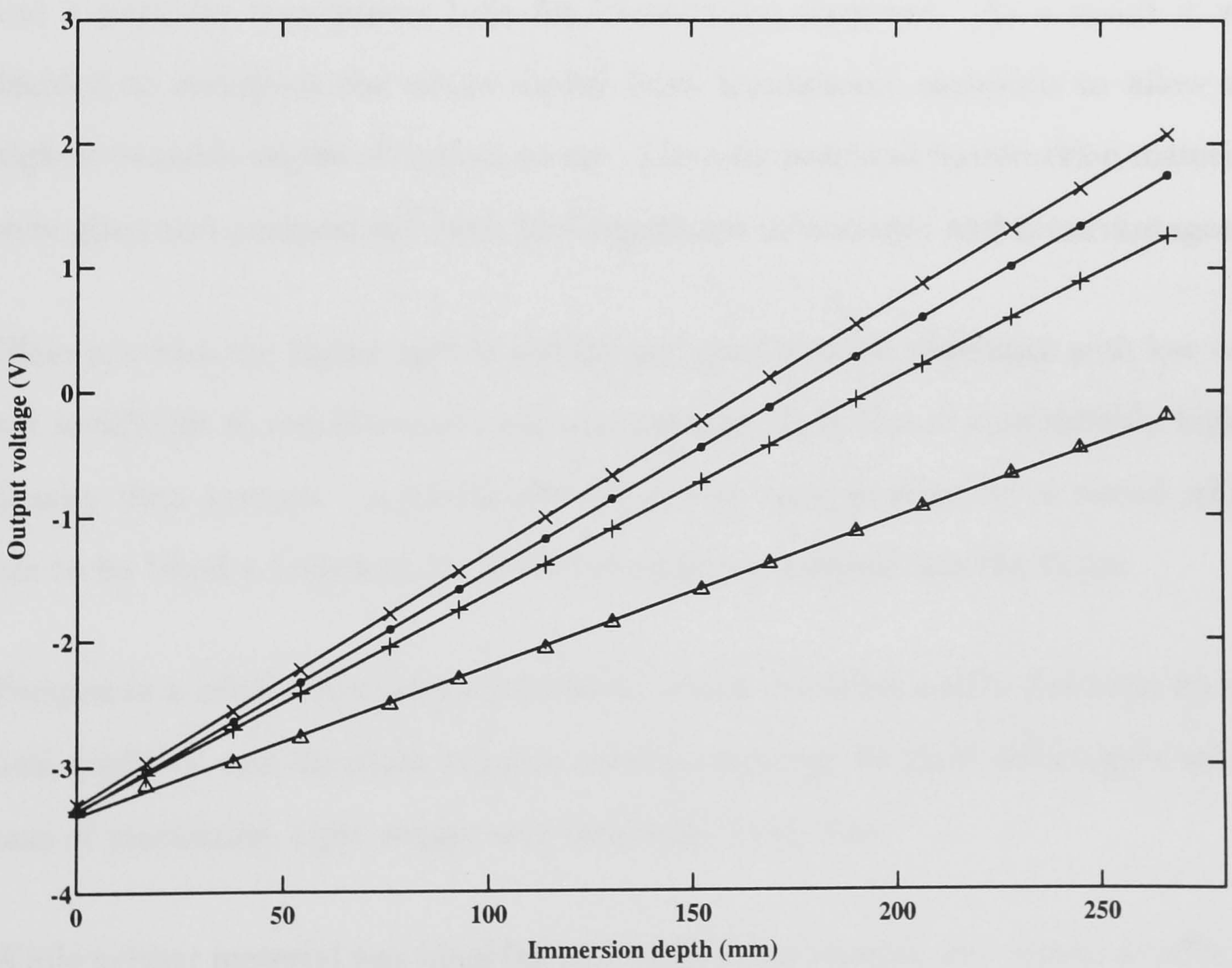

FIGURE 4.4: Output voltage against immersed depth for the four wave gauges

4.5 OWC model

The model OWC used throughout this study was built to the same proportions as one used in flume testing at Queens University, the precise dimensions being dictated by the width of the flume. Air moves in and out of the chamber through a square orifice of variable size. Two orthogonal views of the 0.5m×0.5m×0.4m OWC model are shown in figure 4.5.

4.5.1 Materials

The main requirement of the OWC model was that it should allow optical access for the PIV system so this demands at least one transparent side wall for photography and a partially transparent base for illumination purposes. As a result it was decided to construct the whole model from transparent materials to allow the highest possible degree of optical access. The only practical construction materials were glass and perspex and both had significant advantages and disadvantages.

Glass provides the higher optical quality and good scratch resistance with low cost but is difficult to machine and to fasten together. It is also of considerably higher density than perspex - a potentially important consideration for a model which has to be lifted a height of 2 metres before being lowered into the flume.

Perspex is a relatively expensive material which scratches easily, reducing its optical qualities, and therefore requires careful handling. Its main advantages are its ease of machining, light weight and resistance to shocks.

While neither material was ideal for this application perspex was chosen as offering the best compromises although the choice was not an easy one.

4.5.2 Construction

The 10mm thick side walls, base and roof of the model were bonded together with glue but the 1" thick front wall was fastened with screws for easy removal and refitting at different angles if necessary. All joints were further sealed with silastic sealant to allow the chamber to be made airtight.

The flexibility of the 10mm thick perspex was overcome by cross bracing the top of the model with two aluminium rods. Integral aluminium clamps allowed the model to be bolted firmly to the 1" diameter rails above the flume.

4.6 Beach sections

The transition between the deep water at the wave paddle and the shallow water at the OWC was achieved with a sloping false bed or 'beach' in the flume (see figure 4.6). This was designed by Quinn [41] and each 3 metre long section comprises two coplast [1] sections separated by a 15mm gap coincident with the central long axis of the flume. Each of these sections is supported by a strong polythene I-beam fixed at each end to horizontal aluminium bars which, in turn, are held by friction within the channels between the vertical sheets of glass. The gap between the coplast sheets is covered with thin transparent plastic through which the scanning laser beam can pass, hence allowing PIV measurements to be made along the length of the beach. This beach design works well, the only problem being that the I-beams have a tendency to flex under the pressure of large amplitude long waves. For this reason a more rigid beach would be desirable for studies requiring larger wave amplitudes.

[1] a light 10mm thick plastic - easily cut but brittle

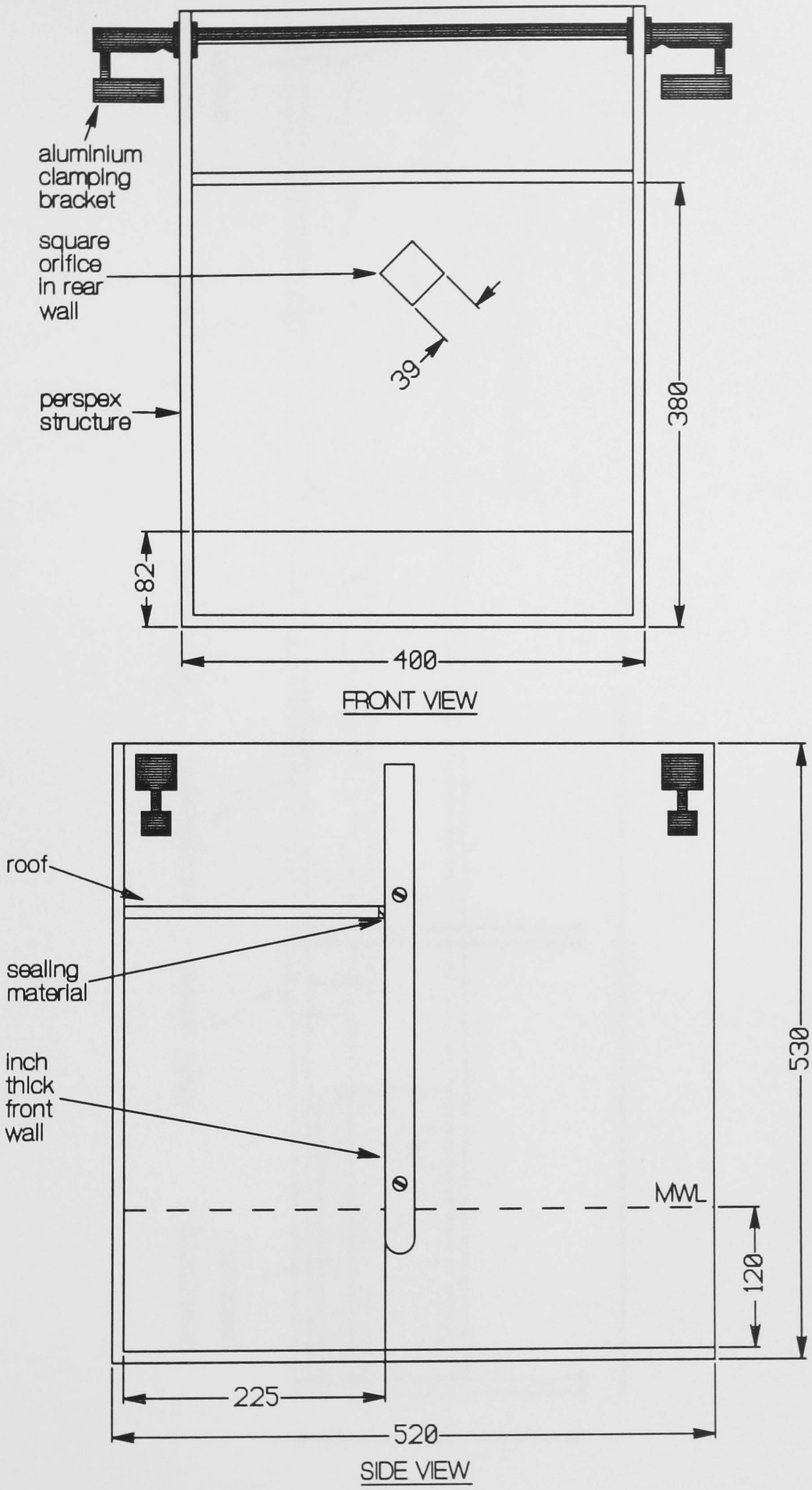

FIGURE 4.5: The model OWC built for the study (dimensions in millimetres)

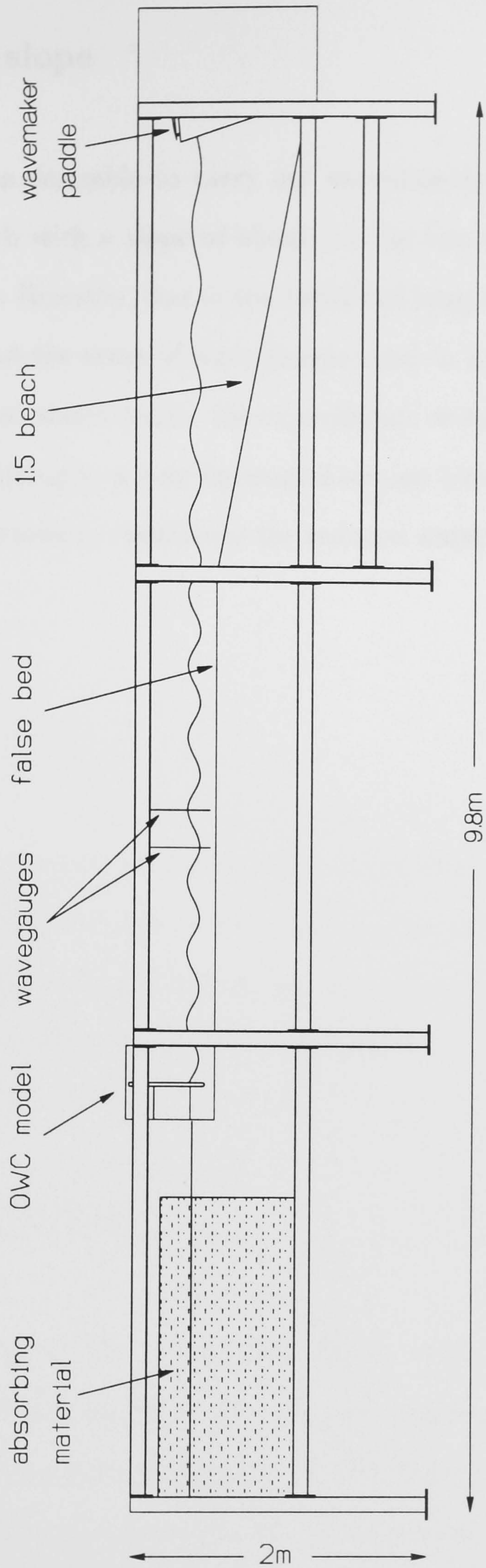

FIGURE 4.6: Diagram of the wave flume showing the beach sections and the model in position

4.6.1 Beach slope

It would have been desirable to carry out experiments with the OWC model at the head of a beach with a slope of about 1:12 in line with studies performed at Queens University. However, due to the restricted length of the flume (<10m) and the requirement that the array of wave gauges used to measure reflections must be placed in a constant water depth, the experiments were carried out with a beach of mean slope 1:5 rising to a long horizontal section before the OWC model. This allowed incoming waves to stabilise at the reduced water depth before reaching the wave gauges.

Chapter 5

Mathematical model of the OWC

5.1 Summary

A simple theoretical model of the response of the OWC to a known wave climate is described. The derived differential equations are solved numerically to obtain values for the variations in water level and air pressure within the OWC chamber. From these the available power may be predicted.

5.2 Introduction

The simplicity of operation of an OWC device would suggest that an equally simple theoretical model should be possible and, indeed, the analysis is very much simpler than for a complex device such as the Salter duck [45]. However some difficulties arise during the derivation of suitable equations and some parameters can be determined only by experiment.

An extensive analysis of a totally immersed deep water OWC model has been

carried out by Lighthill [32] and some aspects were verified in flume experiments by Knott and Flower [29] and later by Robinson and Murray [44] and Long and Whittaker [33]. A non-linear solution of the deep water OWC problem has also been proposed by Vinje [56] who considers the two-dimensional solution of the sinusoidal wave induced oscillation of the water level between a semi-infinite vertical wall and a finite depth, thin vertical plate. However he only considers the case where the distance from the front of the chamber to the back is very small compared with the water depth and he neglects the damping effects of a power take-off system. Malmo and Reitan [34] and Reitan [43] have proposed in-depth velocity potential linear solutions of several different configurations of single OWC devices and an infinitely wide wall containing several devices.

The emphasis in this thesis is on an alternative approach to modelling an OWC on a beach, with no wave transmission, which allows values for the water level and air pressure within the chamber to be obtained directly and compared with measurements made in the laboratory.

5.3 Problems encountered

Subject to some conditions which will be considered later, an OWC may be thought of, in its simplest form, as a mass on a spring with a natural frequency given by

$$f = \frac{1}{2\pi}\sqrt{\frac{k}{m}} \tag{5.13}$$

where k is the spring constant and m is the oscillating mass. However the first problems with this approach are encountered here.

The mass of fluid within the OWC chamber is variable and furthermore the mass taking an active part in the oscillation is not known since there is no reason to suppose that it is the same.

The spring constant cannot easily be determined since in an adiabatic system the pressure within a closed chamber varies as

$$p = CV^{-\gamma} \tag{5.14}$$

where V is the volume of gas, γ is the coefficient of isothermal compressibility and C is a constant. Clearly in the case of the OWC chamber this results in a nonlinear relationship between the elevation of the water surface and the restoring force.

The above considerations are for a closed OWC chamber and inclusion of a turbine orifice adds a damping force to the problem and shifts the resonant frequency away from the natural frequency of the closed chamber system.

Calculating the driving force due to the incident wave field is complicated by the need to consider the reflected component from the device since this clearly results in a modification of the hydrostatic pressures acting upon the water column.

5.4 Simple approach

In this simple approach to modelling the OWC all air flow is considered to be incompressible since the speeds involved are very much smaller than the speed of sound in air.

5.4.1 Closed chamber

If one considers only small oscillations of the water surface compared with the natural air column length, L, in an OWC chamber of fixed cross sectional area, A, and Taylor expands equation 5.14 to first order then it can easily be shown that

$$p = p_0 \left(1 + \frac{\gamma y}{L}\right) + O\left(\frac{y}{L}\right)^2 \tag{5.15}$$

where y is the displacement of the water surface relative to mean water level and p_0 is atmospheric pressure, resulting in a restoring force of the form

$$F_r = -ky \tag{5.16}$$

where

$$k = \frac{p_0 A \gamma}{L} \tag{5.17}$$

and, therefore, a natural frequency

$$f = \frac{1}{2\pi}\sqrt{\frac{p_0 A \gamma}{mL}} \tag{5.18}$$

where the mass, m, remains undetermined.

In the above equations the gravitational restoring force has been neglected since at model scale it is about two orders of magnitude smaller than that due to the excess pressure when the orifice is closed.

5.4.2 Open orifice modifications

The speed of steady flow through an open orifice is given by Bernoulli's equation as

$$u = \sqrt{\frac{2(p - p_0)}{\rho}} \tag{5.19}$$

but, as discussed in section 6.3, the Wells turbine acts as a linear damper and the bulk speed of flow through the tubes used to model its effect is given, from laminar pipe flow theory [54], as

$$u = \frac{a^2(p - p_0)}{8\mu l} \tag{5.20}$$

where a is the tube radius and l is the length of each tube such that $l >> a$. It should be expected, however, that the mean flow rate through the orifice will differ from this since the tubes are close packed allowing some flow between them.

The axial velocity of fluid in a tube of radius a subject to a sinusoidally varying pressure gradient with angular frequency ω is given by

$$u(r,t) = \mathrm{Re}\left\{\frac{Pe^{i\omega t}}{i\omega\rho}\left[1 - \frac{J_0\left(r\sqrt{\frac{-i\omega}{\nu}}\right)}{J_0\left(a\sqrt{\frac{-i\omega}{\nu}}\right)}\right]\right\} \tag{5.21}$$

where P is the maximum pressure gradient in the tube. However in the case of the OWC model the distance travelled by the gas in each half cycle of the pressure fluctuations, given by

$$\int_{-\frac{\pi}{2\omega}}^{\frac{\pi}{2\omega}} u(r,t)dt \tag{5.22}$$

is very large compared with the radius, a, and equation 5.21 is closely approximated by the steady state solution with the bulk flow velocity given by equation 5.20.

In view of the low differential pressures measured in the OWC chamber, which are of the order of 1% of atmospheric pressure, the problem of modelling the pressure fluctuations lends itself well to a quasi-static solution. If we consider compression and expansion of the air in the chamber due to the rise and fall of the water level and the movement of air through the orifice then equations 5.15 and 5.20 may be used to approximate the rate of change of pressure in the chamber as

$$\frac{\mathrm{d}p}{\mathrm{d}t} = \frac{\gamma p}{L}\left[\frac{\mathrm{d}y}{\mathrm{d}t} - \frac{a^2(p-p_0)}{8\mu l A}\left(\frac{p_0}{p}\right)^{\frac{1}{\gamma}}\right] \tag{5.23}$$

and the acceleration of the water surface in the chamber may be given by

$$\frac{\mathrm{d}^2y}{\mathrm{d}t^2} = \frac{1}{m}\left[F(t) - A(p-p_0) - A\rho_w g y\right] \tag{5.24}$$

where dissipative losses have been neglected. Here a gravitational term has been included since it may be significant in the open orifice case.

The values of pressure and water elevation obtained by the simultaneous solution of these equations can be used to calculate the instantaneous available power within the OWC chamber as expressed in equation 6.46.

5.5 Driving force

The driving force, $F(t)$, which appears in equation 5.24 depends entirely upon the incoming waves generated by the wavemaker. As these waves shoal their wavenumber and amplitude change and the new values at the OWC can be approximated by linear wave theory from the equations

$$\omega = \sqrt{gk \tanh kh} \tag{5.25}$$

$$c = \frac{\omega}{k} \tag{5.26}$$

$$c_g = \frac{1}{2}c\left(1 + \frac{2kh}{\sinh 2kh}\right) \tag{5.27}$$

$$a^2 c_g = \text{constant} \tag{5.28}$$

where k is the wavenumber, c and c_g are, respectively, the wave phase and group velocities and h is the local water depth.

Since waves cannot be transmitted past the OWC model a standing wave is set up in the flume which settles down over time to a system where the wavemaker is merely inputting energy sufficient to counteract the dissipative losses. Given a coefficient of reflectance $R(\omega)$ (< 1) from the OWC model the water elevation close to the OWC, for a fixed wave frequency ω, is given by

$$y(x,t) = a\left[\cos(\omega t - kx) + R\cos(\omega t + kx)\right] \tag{5.29}$$

and this has its maximum amplitude at the OWC resulting in a modified driving wave of amplitude $a(1+R)$ where a is given by the linear equations above.

Clearly considering only the amplitude of oscillation of the driving waves allows just the force due to the hydrostatic pressure to be taken into account. However using linear wave theory to calculate the fluid speed under a travelling wave gives

$$u(x_1, x_2, t) = \left(\frac{gak}{\omega \cosh^2 kh}\right) \sqrt{\cosh^2 k(x_2+h) - \sin^2(kx_1 - \omega t)} \tag{5.30}$$

and this leads to dynamic pressures which are typically two orders of magnitude smaller than the hydrostatic pressures. So for simplicity the dynamic pressure is ignored since it would be difficult to calculate in the vicinity of the open mouth of the OWC chamber.

Hence the uplift force acting on the mass of water taking part in the OWC oscillations is given approximately by

$$F(t) = \rho g A a(1+R) \sin \omega t \tag{5.31}$$

where the reflection coefficient has still to be determined.

5.6 Implementation

The amplitude of oscillation of the wavemaker ramps up to its maximum after about three strokes so in view of this equation 5.31 is modified to

$$F(t) = \rho g A a (1 + R) \left(1 - e^{-\alpha t}\right) \sin \omega t \tag{5.32}$$

with $\alpha = \frac{3}{2}$, chosen arbitrarily to ensure that the wave amplitude is at least 95% of its maximum value after three periods.

Equations 5.23 and 5.24 can be rewritten as three first order differential equations and are numerically solved using a fourth order Runge-Kutta scheme [40].

5.6.1 Determination of the oscillating mass

The equations proposed above for the simple solution of the OWC problem provide no information about the mass, m, of water involved in the oscillation.

Here no attempt is made to derive an expression for the mass involved, even if that is possible. In fact it is likely that an attempt to infer the mass empirically may also inadvertently help to overcome other deficiencies in the model. However, due to this simple modelling approach, it should be expected that it may not be possible to find a mass which produces results agreeing with experiment at all frequencies or orifice sizes.

Instead the mass has been chosen by normalising the numerical solution so that the calculated amplitude of response of the water column agrees with experimental measurement at about the mean point of the parameter ranges i.e. at a frequency of 1.016Hz and an orifice of 20×20mm. This is satisfied approximately by a mass $m = 1.25 m_0$ where $m_0 = \rho_w A d$ is the mass of water in the OWC chamber at the mean water depth d.

Chapter 6

Wave flume experiments

6.1 Summary

An experimental study of the performance of a model OWC device is described. Measurements of the power available from the device are compared with theoretical values and PIV measurements of flow within the device are used to estimate the hydrodynamic losses. Results are presented for a variety of wave frequencies and chamber orifice sizes.

6.2 Introduction

Flow visualisation pictures of flow into and out of an OWC chamber show the formation of a strong vortex just within the edge of the front wall of the model as a wave crest is incident and its subsequent dissipation as the water level within the chamber drops. While the strength of this vortex may be reduced by simply increasing the thickness of the front wall it is of interest to estimate the energy dissipation before further steps are taken to reduce it.

A time series of PIV pictures of the incident and receding wave may be used to show the 'life cycle' of a vortex and a program called ENERGY estimates the translational and rotational kinetic energies contained within the vortex at each time step. These results are compared with wave energy calculations made from wave gauge records of the waves incident upon and reflected from the OWC model. Further measurements of the air pressure within the chamber allow the instantaneous power available from the device to be calculated and compared with values given by the theoretical model proposed in chapter 5 and with calculations of energy dissipation.

6.3 Modelling the effect of a Wells turbine

The response of the OWC to an incident wave is largely characterised by the stiffness of the air column which in turn is greatly dependent upon the Wells turbine driving the generator.

This ingenious self-rectifying axisymmetric turbine [42] linearly damps the air column i.e. the speed of flow through the turbine is linearly proportional to the excess air pressure within the chamber.

This presents a problem for a scale model since the simplest case of an open orifice leads to quadratic damping i.e. speed of airflow proportional to the square root of the excess pressure. Building a scaled-down Wells turbine would not only be impractical but would also be unlikely to replicate the linear damping effect of a real turbine on the oscillation of the water column largely due to the relative increase in bearing friction at small scale.

As a result a number of alternative options were explored such as filling the orifice

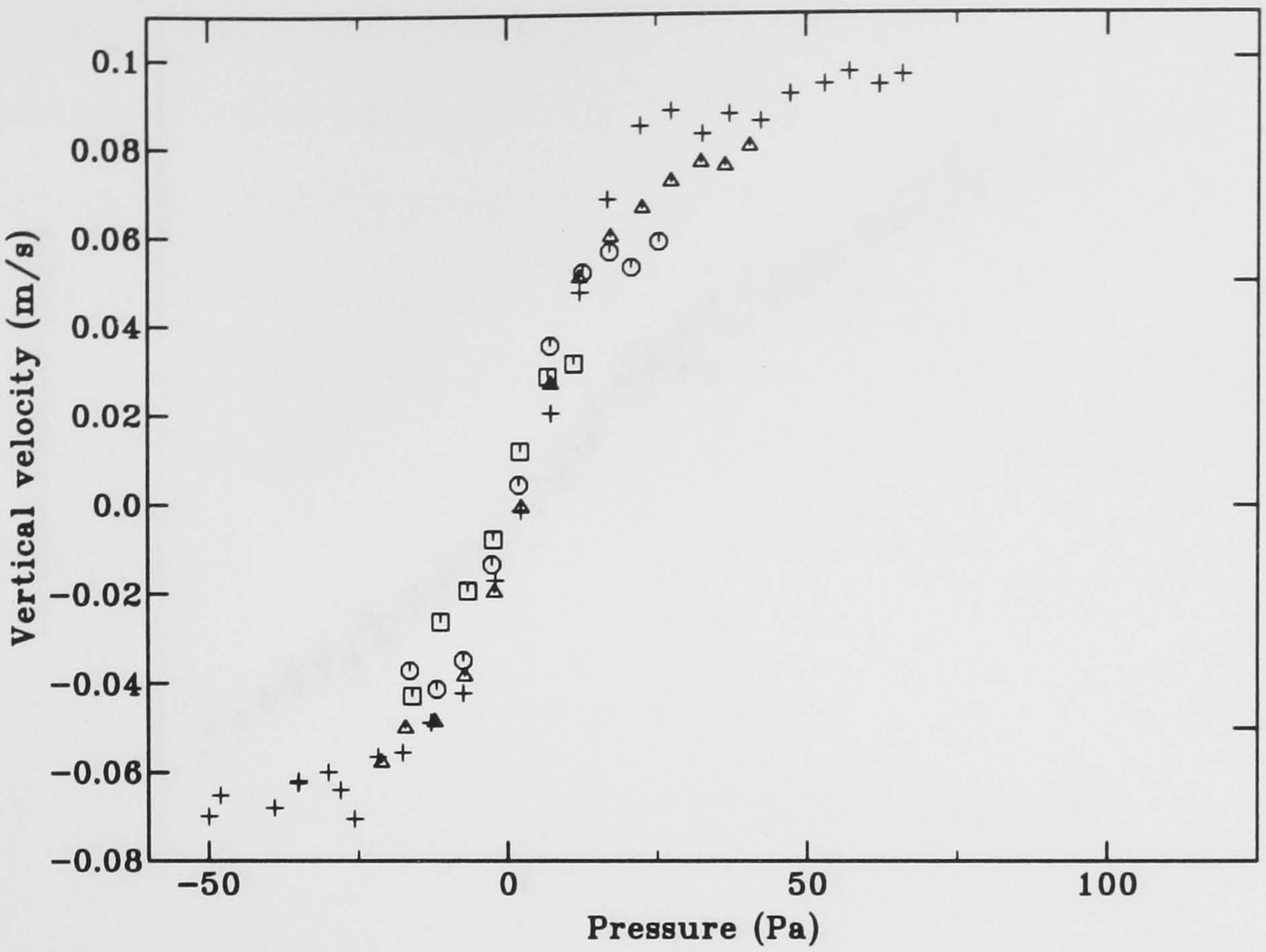

FIGURE 6.1: Vertical water velocity against excess air pressure in chamber, open orifice, frequency = 0.5Hz, amplitudes 5mm (□), 7.5mm (○), 10mm (△) and 12.5mm (+).

of the model with a porous sponge material or covering the orifice with a flexible membrane into which slits had been cut. However neither of these approaches was a success in this case although Sarmento [47] achieved some success with a filter system which he calibrated in a wind tunnel.

The most effective solution here was found to be that of packing the orifice with a bundle of hollow tubes of diameter 3mm and length 250mm in an attempt to reduce the Reynolds number of the air flow resulting in a laminar flow with speed proportional to the excess pressure. This method is similar to that employed by Robinson and Murray [44] which was deemed to be unsuccessful.

The effectiveness of this approach was tested in the flume with low amplitude sinusoidal waves incident on the model. Simultaneous measurements of water elevation and air pressure within the chamber were made at a rate of 80Hz. The

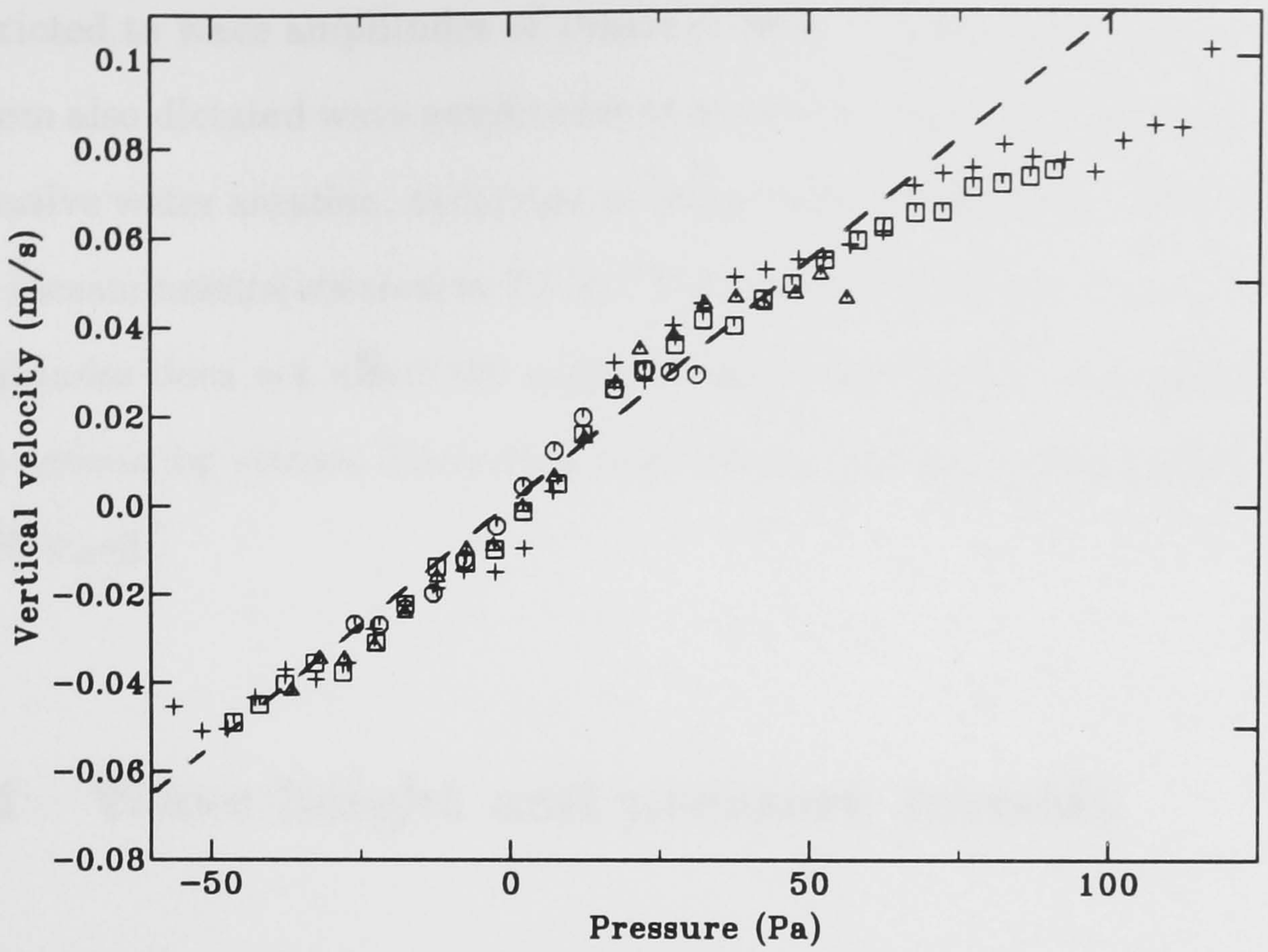

FIGURE 6.2: Vertical water velocity against excess air pressure in chamber, tubes in orifice, frequency = 0.5Hz, amplitudes 5mm (○), 7.5mm (△), 10mm (□) and 12.5mm (+). The broken line (- - -) shows the velocity predicted by equation 5.20

time derivative of the elevation records was used to infer the speed of the air flow through the orifice by applying continuity and assuming incompressibility and these values were compared with the pressure measurements.

Figure 6.1 shows the results for a simple open orifice with four different wave amplitudes ranging from 5mm to 12.5mm showing approximately the expected quadratic profile.

The effect of filling the orifice with the densely packed tubes is demonstrated in figure 6.2 with a more linear relationship between vertical velocity and excess pressure. As expected this holds best at low pressures and is less applicable at higher pressures as the Reynolds number increases.

The limitations of this attempt to model turbine effects led to all experiments being restricted to wave amplitudes of 10mm or less. The use of the PIV measurement system also dictated wave amplitudes of not more than about 10mm to ensure that excessive water aeration, occurring at larger wave amplitudes, did not affect velocity measurements(see section 2.5.3). The restriction of experiments to small wave amplitudes does not affect the scope of the project which is primarily concerned with measuring viscous dissipation rates rather than the overall performance of the OWC itself.

6.4 Wave height and pressure records

6.4.1 Choice of test conditions

Chamber geometry

In line with the simple OWC chamber shape modelled in chapter 5 all air pressure and water elevation measurements were made with the thick front wall of the model set in the vertical position. However this still allowed a large number of experimental configurations by virtue of the frequency range of the wavemaker and a variety of chamber orifice sizes.

Sampling rates

The choice of sampling rate for the water elevation and wave pressure measurements was a compromise between achieving a sufficiently high resolution while allowing the instruments adequate response time between samples. A further up-

per limit was placed on the sampling rate by attempting to keep the data files to a manageable size.

The sampling rate was arbitrarily chosen to be at least two orders of magnitude greater than the maximum wave frequency and the chosen rate of 160Hz equated to an acceptable 250 kilobytes of data from each half-minute long experimental run. These data files were transferred from the Archimedes micro computer to a mainframe machine using the Kermit file transfer protocol which operates at a rate of about 10 kilobytes per minute so with several hundred files to transfer during the course of experiments it was most important to limit the size of each. Even so an estimated seventy hours was spent just transferring data.

Wave frequencies

Wave frequencies used in this study were chosen to span most of the range of the wavemaker. The lower frequency limit was dictated by the maximum stroke of the wave paddle [49] and the upper frequency was chosen to fall short of the natural frequency of cross-tank oscillations to avoid exciting this normal mode.

To simplify analysis of the wave records using fast fourier transforms (FFTs) the wave frequencies were chosen so that there would be an integral number of wave cycles during each sampling period (see section 6.4.2). This condition is satisfied by choosing frequencies

$$f_i = \frac{R}{N} i \quad \text{for} \quad 1 \leq i \leq \frac{N}{2} \tag{6.33}$$

where R is the sampling rate, N is the number of samples and i are integers.

At the sampling rate of R=160Hz and with N=4096, the frequencies f_j ($j = 1, \cdots, 14$) were chosen satisfying equation 6.33 with i=2(j+5). This corresponds to frequencies in the range 0.469Hz to 1.484Hz.

6.4.2 Data analysis

Analysis of wave records

The energy dissipated within the OWC chamber may be estimated by calculating the coefficient of reflectance of the device. This may be determined by analysing the outputs of two wave gauges sampling simultaneously and placed at different distances from the OWC, similar to the technique of Knott and Flower [29]. If gauge 1 is taken to be nearest the wavemaker and gauge 2 nearest the OWC then the water elevations measured by the gauges are given respectively by

$$y_1(t) = \mathrm{Re}\left\{a_i e^{i(\omega t+\phi_i)} + a_r e^{i(\omega t+\phi_r)}\right\} \tag{6.34}$$

$$y_2(t) = \mathrm{Re}\left\{a_i e^{i(\omega t-kd+\phi_i)} + a_r e^{i(\omega t+kd+\phi_r)}\right\} \tag{6.35}$$

where a_i and a_r are the amplitudes of the incident and reflected waves, ϕ_i and ϕ_r are their phases, k is the wavenumber, ω is the angular frequency and d is the distance between the gauges.

The above equations may be simplified to

$$y_1(t) = \mathrm{Re}\left\{A_i e^{i\omega t} + A_r e^{i\omega t}\right\} \tag{6.36}$$

$$y_2(t) \;=\; \mathrm{Re}\left\{A_i e^{i(\omega t - kd)} + A_r e^{i(\omega t + kd)}\right\} \tag{6.37}$$

with $A_i = a_i e^{i\phi_i}$ and $A_r = a_r e^{i\phi_r}$.

Superposition of the incident and reflected waves allows us to write

$$y_1(t) \;=\; \mathrm{Re}\left\{c_1 e^{i\omega t}\right\} \tag{6.38}$$

$$y_2(t) \;=\; \mathrm{Re}\left\{c_2 e^{i\omega t}\right\} \tag{6.39}$$

where c_1 and c_2 are complex amplitudes found by taking the fourier transform of the time series $y_1(t)$ and $y_2(t)$. With the large size and number of wave records analysed in this study a FFT was used to improve computation time [10, 40].

Now combining equations 6.36, 6.37, 6.38 and 6.39 gives

$$c_1 \;=\; A_i + A_r \tag{6.40}$$

$$c_2 \;=\; A_i e^{-ikd} + A_r e^{ikd} \tag{6.41}$$

Simultaneous solution of these equations then gives

$$A_i \;=\; \frac{c_1 e^{ikd} - c_2}{2i \sin kd} \tag{6.42}$$

$$A_r = \frac{c_2 - c_1 e^{-ikd}}{2i \sin kd} \tag{6.43}$$

Clearly equations 6.42 and 6.43 are undefined if the gauges are placed exactly an integral number of half wavelengths apart and indeed care must be taken to ensure that the separation of the gauges differs considerably from this to avoid ill-conditioned simultaneous equations and possible spurious results.

Finally the real amplitudes a_i and a_r are found by taking the moduli of the complex amplitudes A_i and A_r, subject to a factor $\frac{1}{2}\sqrt{N}$ arising from the FFT, and the proportion of wave energy reflected from the OWC is given by

$$E_R = \left(\frac{a_r}{a_i}\right)^2 \tag{6.44}$$

The conditions imposed by the use of a FFT are easily satisfied. Firstly the number of samples must be given by

$$N = 2^n \tag{6.45}$$

for some integer n and secondly there must be an integral number of wave periods within the sampling time to allow the above simple analysis method to be used. This second condition ensures that a sharp peak occurs in the graph of the FFT rather than a spread out one resulting from a non-integral number of periods (see figures 6.3 and 6.4).

As an alternative to choosing the wave frequencies using equation 6.33 the data could have been 'windowed' before calculating the FFT i.e. a representative portion corresponding to an integral number of wave cycles would be isolated from a

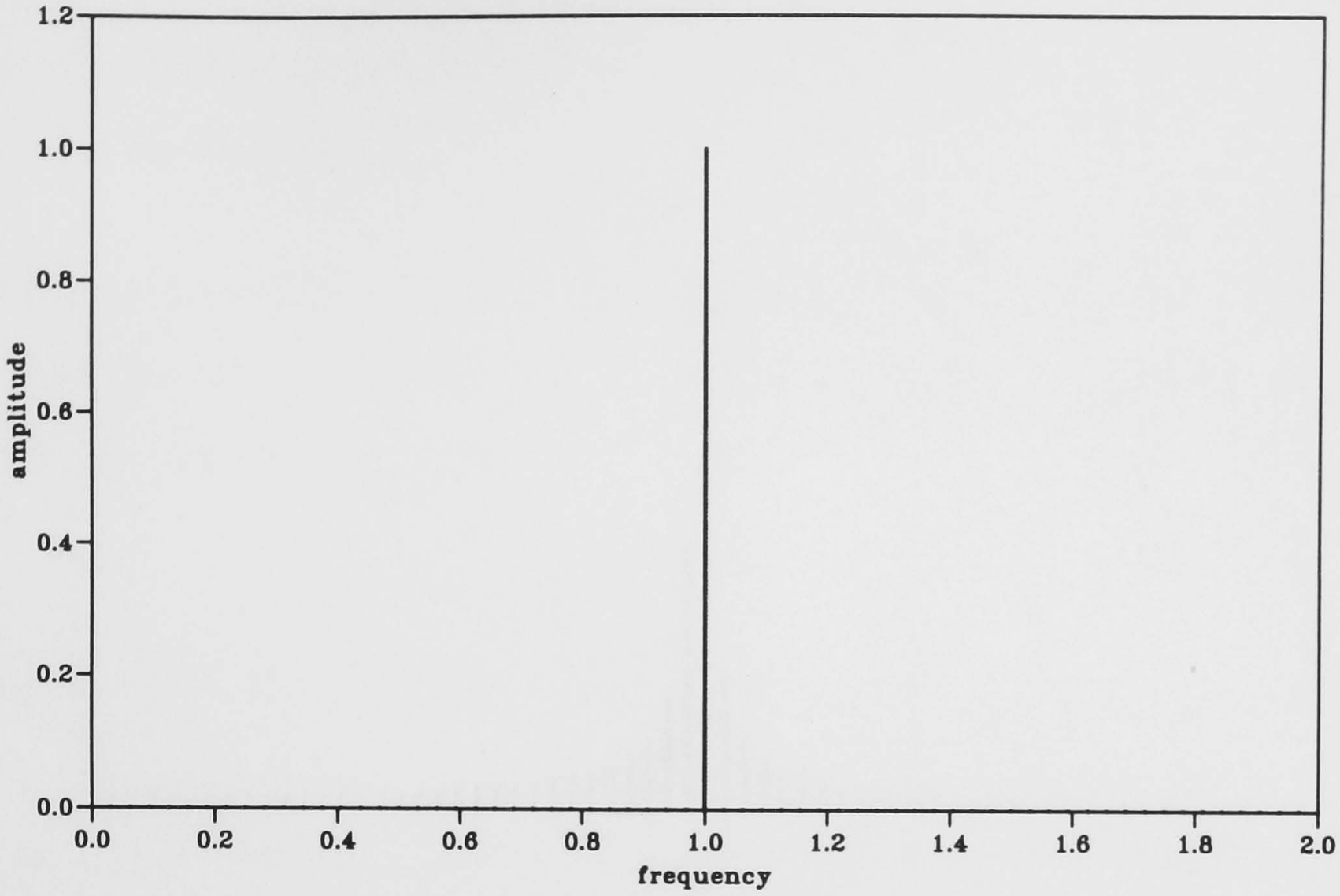

FIGURE 6.3: FFT of a sinewave with integral periods within the sampling time

larger dataset. However, since the precise choice of frequencies in this study was somewhat arbitrary, the above method provided a neater route to the same result.

Calculating available power within the OWC chamber

In calculating the power available within the OWC for conversion in a turbine it is assumed that the water surface within the chamber remains flat and that the differential air pressure measurements made at the roof agree with the average chamber pressure at any given time. The first assumption is expected to hold reasonably well at the low wave amplitudes used in this study while the second is expected to hold as a result of the low pressures and velocities within the chamber.

It may be shown [48] that the instantaneous available power within an OWC cham-

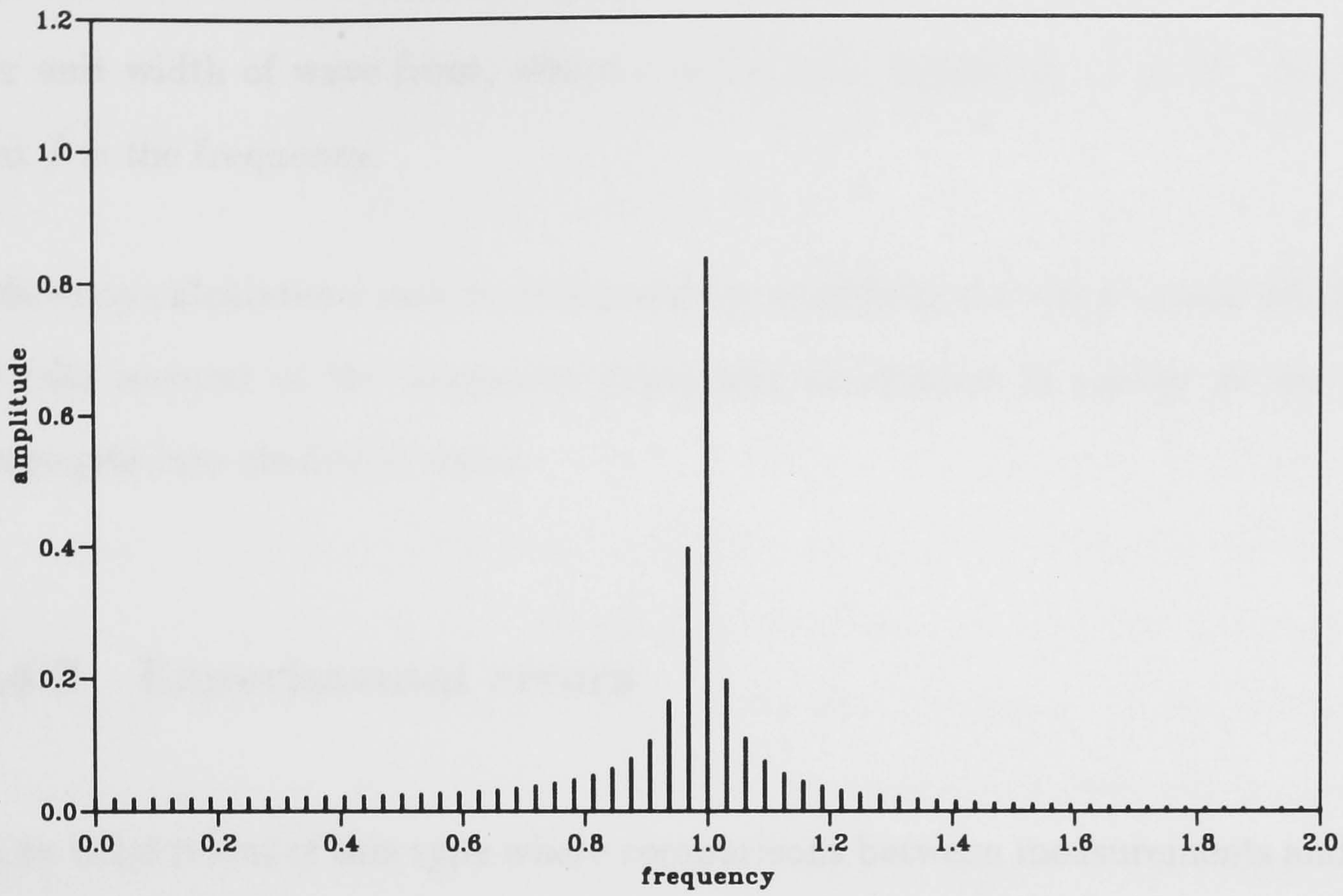

FIGURE 6.4: FFT of a sinewave with non-integral periods within the sampling time

ber with a constant cross-sectional area is given approximately by

$$P_c = \rho_w A_c \frac{\mathrm{d}y_c}{\mathrm{d}t}\left[\frac{p_c}{\rho_w} - g y_c + y_c \frac{\mathrm{d}^2 y_c}{\mathrm{d}t^2}\right] \tag{6.46}$$

where ρ_w is the density of water, A_c is the cross-sectional area of the chamber, y_c is the chamber water elevation relative to the still water level, p_c is the differential chamber air pressure and g is acceleration due to gravity.

Chamber efficiency calculations are made by comparing the instantaneous power calculated from water elevation and wave pressure records with the wave power calculated at the wave paddle in 'deep' water using linear wave theory and given by

$$P = \frac{1}{2}\rho_w g a^2 \lambda f \tag{6.47}$$

per unit width of wave front, where a is the wave amplitude, λ is the wavelength and f is the frequency.

Efficiency calculations may be improved by modifying the 'deep' water calculation to take account of the frequency dependent dissipation of energy as the waves propagate into shallower water.

6.4.3 Experimental errors

In an experiment of this type where comparisons between measurements and a developed numerical model are sought, errors fall into two main categories. These are errors which affect the ability to make precise measurements of physical quantities during experimentation and, less obviously, unexpected phenomena arising during experiments which reduce the applicability of the numerical model to the physical problem. These latter errors may be better described as limitations of experimental technique and manifest themselves in several ways within this study.

Ideally for comparison with numerical results one would sample the air pressure at several points within the chamber and employ some averaging process to the results. However only one pressure gauge was available for experiments and its sampling point within the roof of the chamber was chosen to be far away from the regions of large airflow near the orifice in order to minimise dynamic pressure measurements.

Potential errors resulting from wave height measurements were minimised by checking calibrations and, if necessary, recalibrating gauges regularly during ex-

perimentation. As a result amplitude measurements of the same wave using all the wave gauges differed typically by less than 0.5%. This equates to an error of approximately ±0.5% in the calculated reflection coefficients.

One assumption of the numerical model is that the water surface inside the OWC chamber remains flat and horizontal irrespective of the elevation. While this is a good approximation with very small wave amplitudes, at the test amplitude of 10mm and particularly at low frequencies less than about 0.7Hz the mean surface slope varies by up to ±5 degrees from the horizontal with larger local variations especially in the region of the front wall of the device. This results in a seiche-like oscillation within the chamber which are just evident in the wave gauge records from within the OWC chamber. It appears that placement of the wave gauge at the centre of the chamber was successful in minimising their effect upon the measurements. Unsurprisingly the pressure records appear to be unaffected by these oscillations since the volume of air within the chamber is unaffected.

Wave repeatability during experiments proved to be much better than had been hoped with amplitude and phase measurements of identical input conditions varying everywhere by less than 1%. Similar results were found in earlier tests by Skyner [49] and small differences appear to be attributable to variations of the wave gauge calibration. Wave repeatability is further discussed in section 6.5.5.

6.4.4 Results

Wave energy dissipation on the beach

In the sea as a wave shoals energy is generally dissipated during breaking and by bottom friction which depends upon the roughness of the seabed. However in the

flume and with non-breaking waves and a relatively smooth false bed one of the main losses would appear to come about as a result of the deformation of the bed which is most noticeable at the centre of each beach section as a wave crest passes (see section 4.6).

Dissipation was measured in the flume by running waves onto the beach with the OWC model removed. The waves returned to deep water at the head of the beach over a specially rounded lip designed to inhibit vortex shedding at that edge. Wave height measurements were made at identical water depths both at the wave paddle and past the end of the beach where the waves had time to stabilise after the abrupt increase in depth from 0.12m to 0.75m.

Figure 6.5 shows the measured proportions of wave amplitude and power transmitted over the beach and the resulting modifications to the power available at the OWC.

While not an ideal method of measuring the power available at the OWC, this gives a lower bound to the actual values. All following efficiency calculations are based on these modified values of power available at the OWC chamber making allowance for energy dissipated on the beach.

Power available to turbine

Raw data values of wave height and air pressure records are not presented here since there is little if anything to be gained from them at a glance. Instead the results have been processed using equation 6.46 to give the mean power available over a large portion of the dataset where any transients appear to have died away and conditions have reached a reasonably steady state although, as explained in section 6.5.1, in practice a true steady state is never actually achieved.

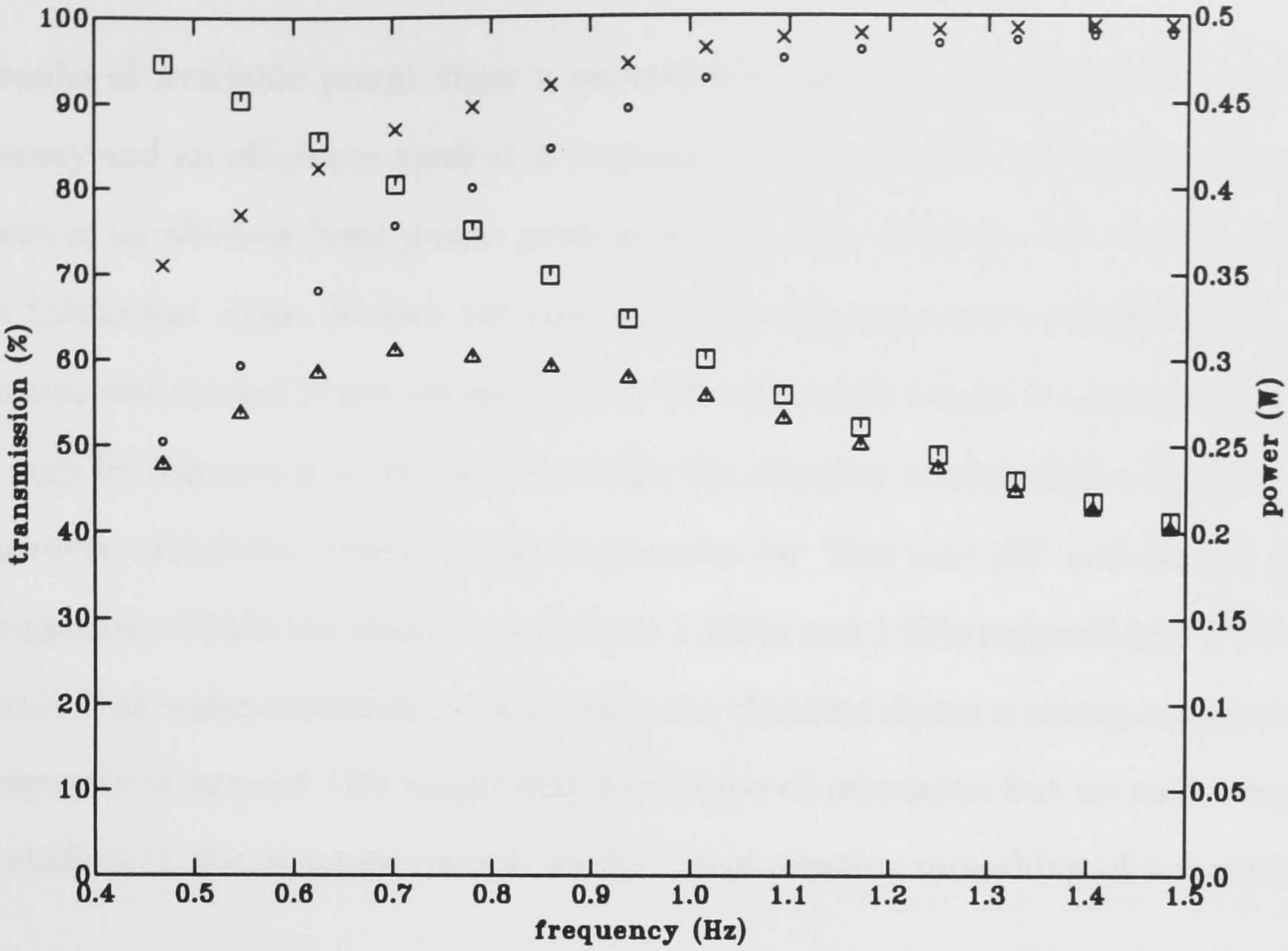

FIGURE 6.5: Percentage transmission of wave amplitude (×) and power (○), and wave power at paddle (□) and at OWC (△) for waves of amplitude 10mm

Reflection coefficients calculated from FFTs of the wave records are used to modify the driving force for the numerical model and figures 6.6 to 6.21 show the wave power reflected from the device along with the comparisons of power available in the chamber calculated from experimental results and those calculated from numerical results. All results are obtained with a constant wave amplitude of 10mm.

Measurements of reflected power show a consistent peak at a frequency of 0.781Hz across the range of orifice sizes and proportions of reflected power ranging from about 65% for the low frequency, large orifice case to over 95% at a frequency of 1.484Hz and an orifice size of 5×5mm. The graph of reflected power across the range of orifice sizes at a frequency of 0.781Hz shown in figure 6.22 clearly shows

an increase in energy absorption with increased orifice size.

Graphs of available power show a general decrease in power with increasing frequency and an efficiency peak at a frequency of about 0.6Hz. At small orifice sizes there is an obvious local power peak at a frequency of about 1Hz and the reason for this is not clear. It does not correspond to any expected normal modes of the system and since it is not reproduced by the numerical results it appears as though it may be connected to the seiche within the chamber mentioned in section 6.4.3. However calculated lowest mode frequencies for 'fore and aft' and lateral seiche frequencies within the chamber are about 1.25Hz and 1.8Hz respectively. FFT analysis of the water elevation record within the chamber shows a strong response at a frequency of around 1Hz suggesting some type of resonance but no such response is evident in the pressure records so the cause remains something of a mystery.

Values of mean power calculated with the numerical model demonstrate good qualitative agreement with experimental results, with the power decreasing with increasing frequency. The best quantitative agreement between the results arises in the determination of the conditions for maximum power extraction with both predicting an optimal orifice size of 25×25mm. Figure 6.23 shows both the predicted and experimentally derived mean power values at a frequency of 0.469Hz, illustrating this close agreement. It also shows that the discrepancy between these values increases with orifice size, a trend which is apparent at all frequencies. This is most likely due to limitations in the method of estimating the rate of air flow through the orifice since the assumed linear damping was difficult to implement in practice, as shown in figure 6.2. The numerical calculations overestimate the maximum available power by about 20% at the lowest test frequency and underestimate it by about the same proportion at the top end of the frequency range.

In general the agreement between predicted and measured results is good con-

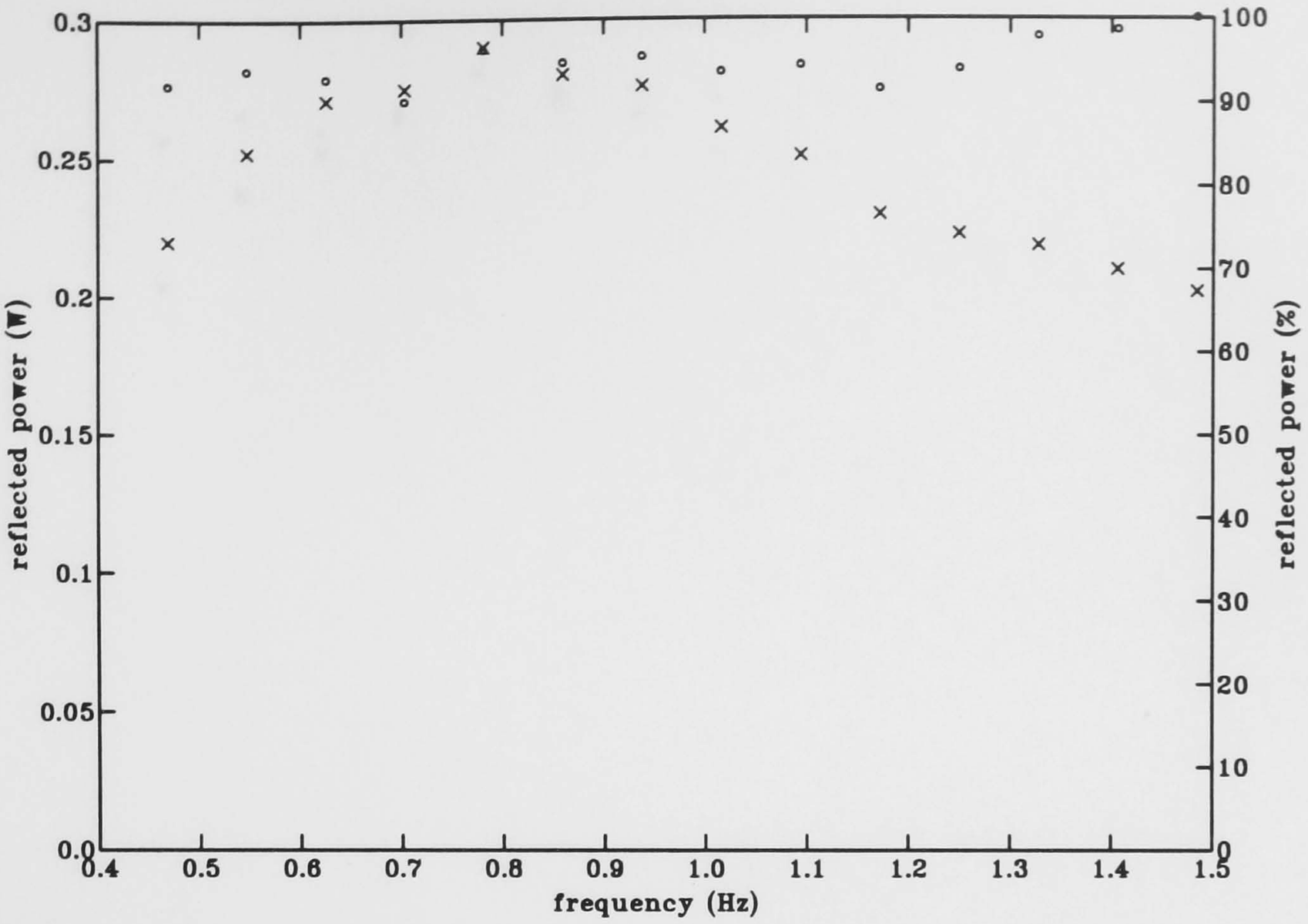

FIGURE 6.6: Power reflected from the OWC measured in watts ($\times$) and as a percentage of the input power ($\circ$). Orifice = 5×5mm

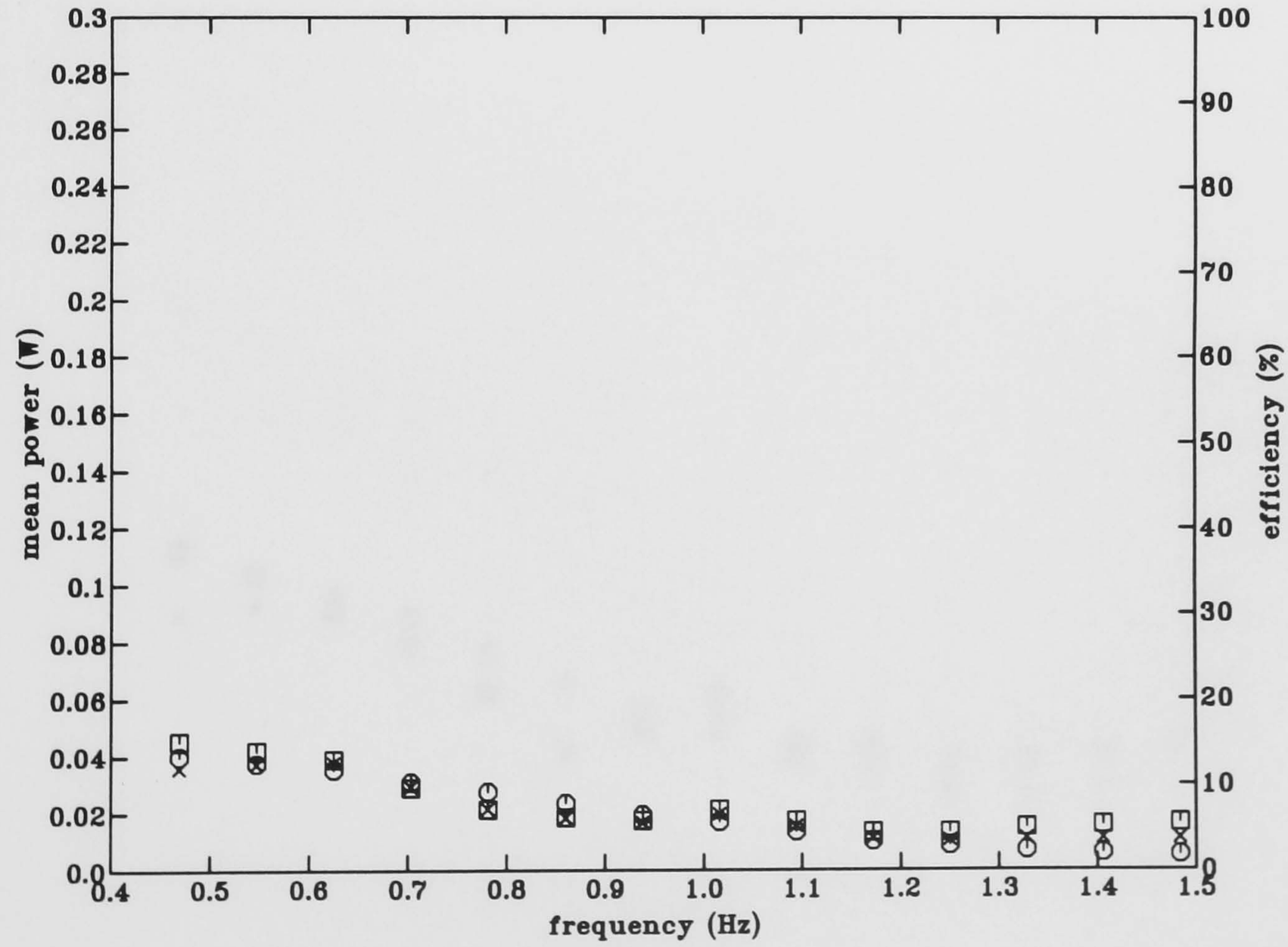

FIGURE 6.7: Mean power ($\times$) and efficiency ($\square$) calculated from wave and pressure records and mean power calculated with numerical model ($\circ$). Orifice = 5×5mm

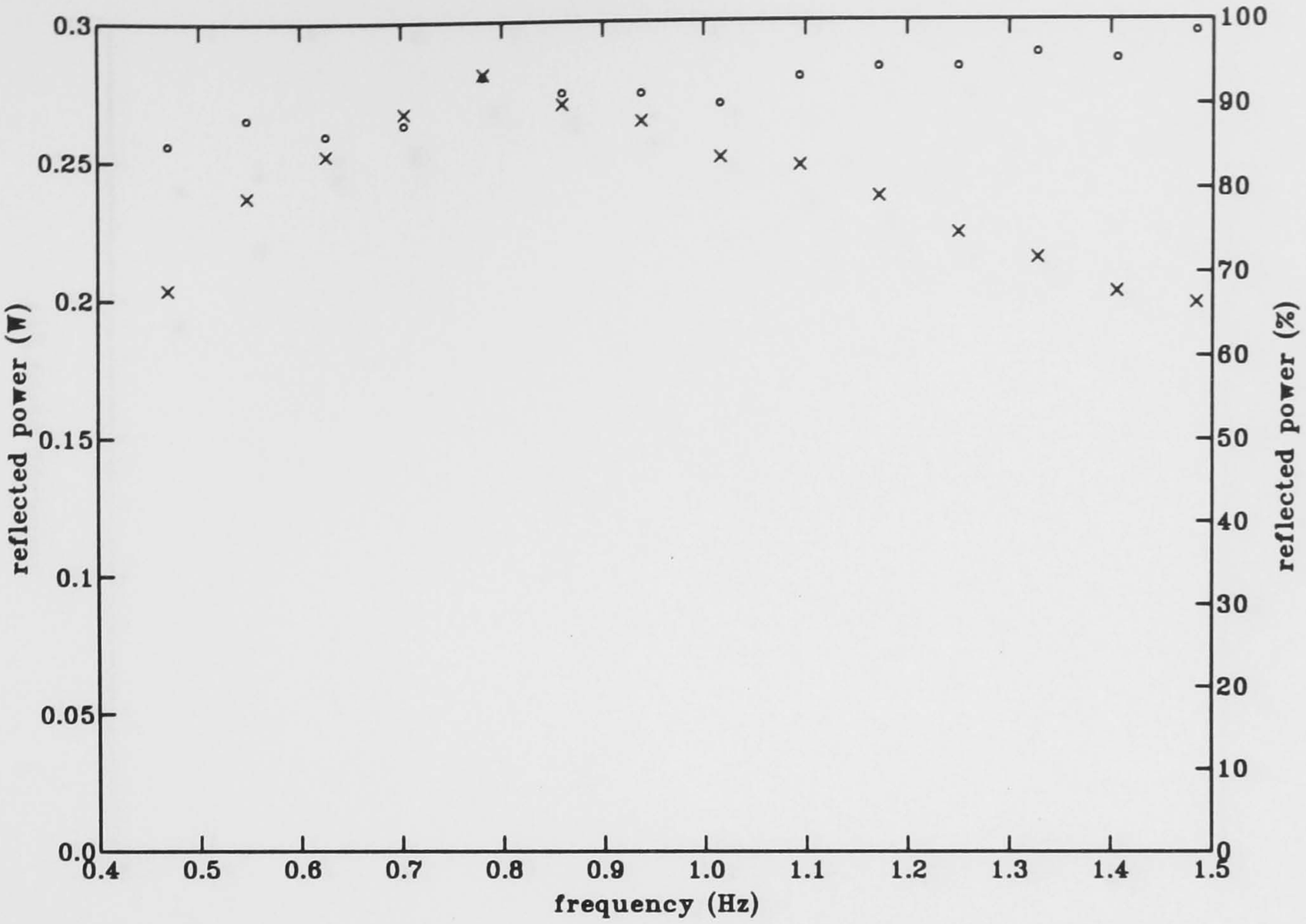

FIGURE 6.8: Power reflected from the OWC measured in watts ($\times$) and as a percentage of the input power ($\circ$). Orifice = 10×10mm

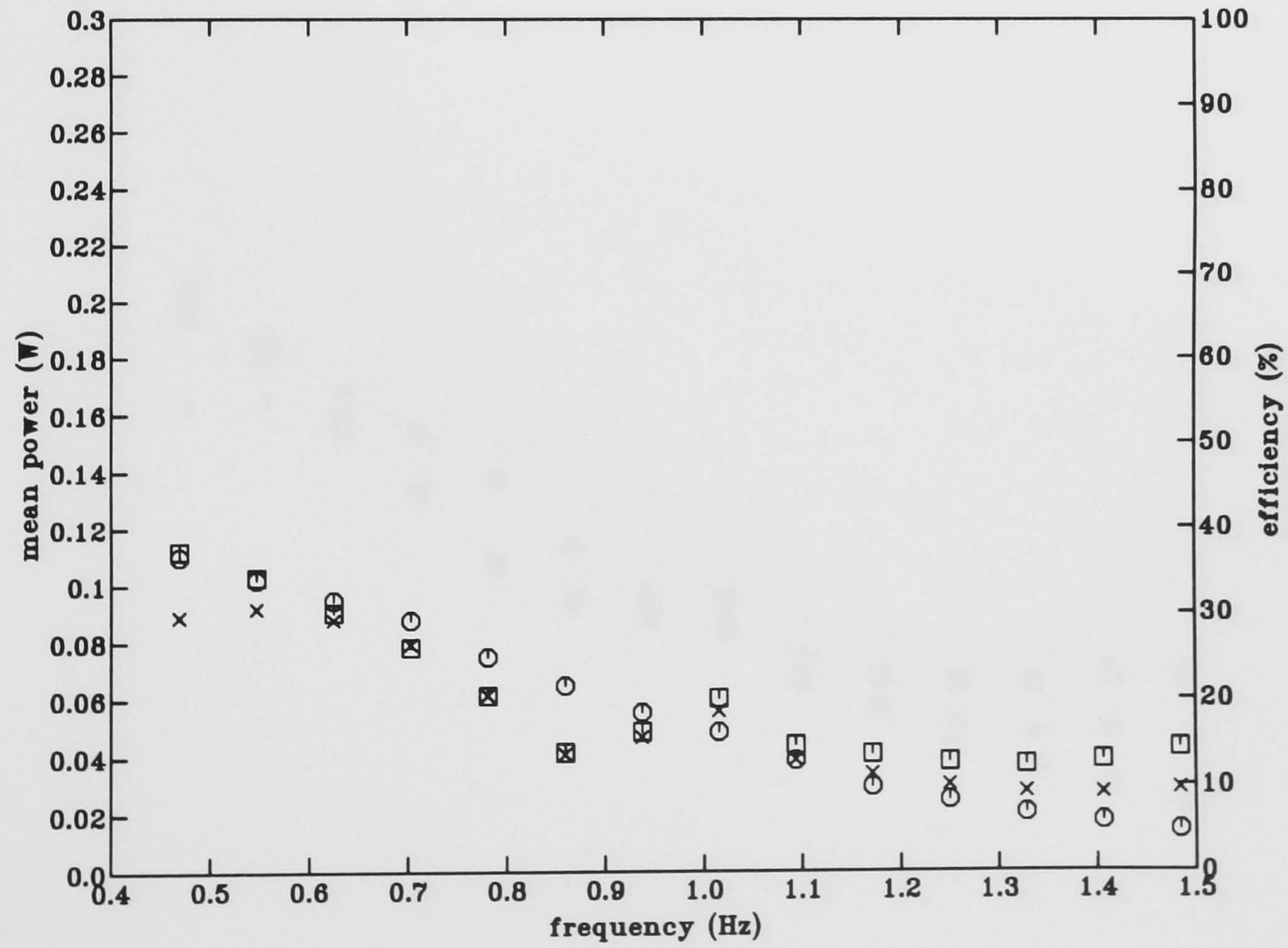

FIGURE 6.9: Mean power ($\times$) and efficiency ($\square$) calculated from wave and pressure records and mean power calculated with numerical model ($\circ$). Orifice = 10×10mm

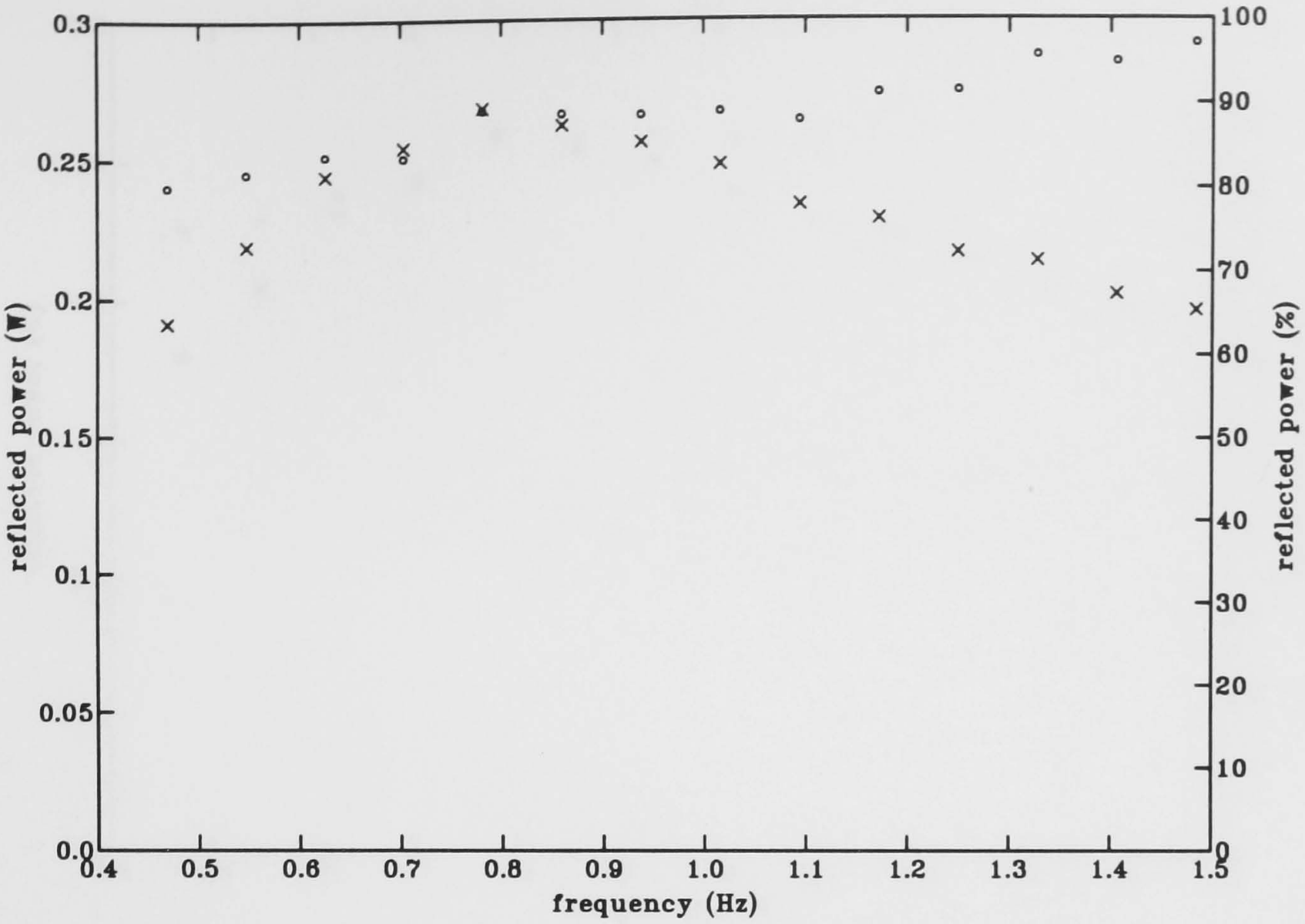

FIGURE 6.10: Power reflected from the OWC measured in watts (×) and as a percentage of the input power (○). Orifice = 15 × 15mm

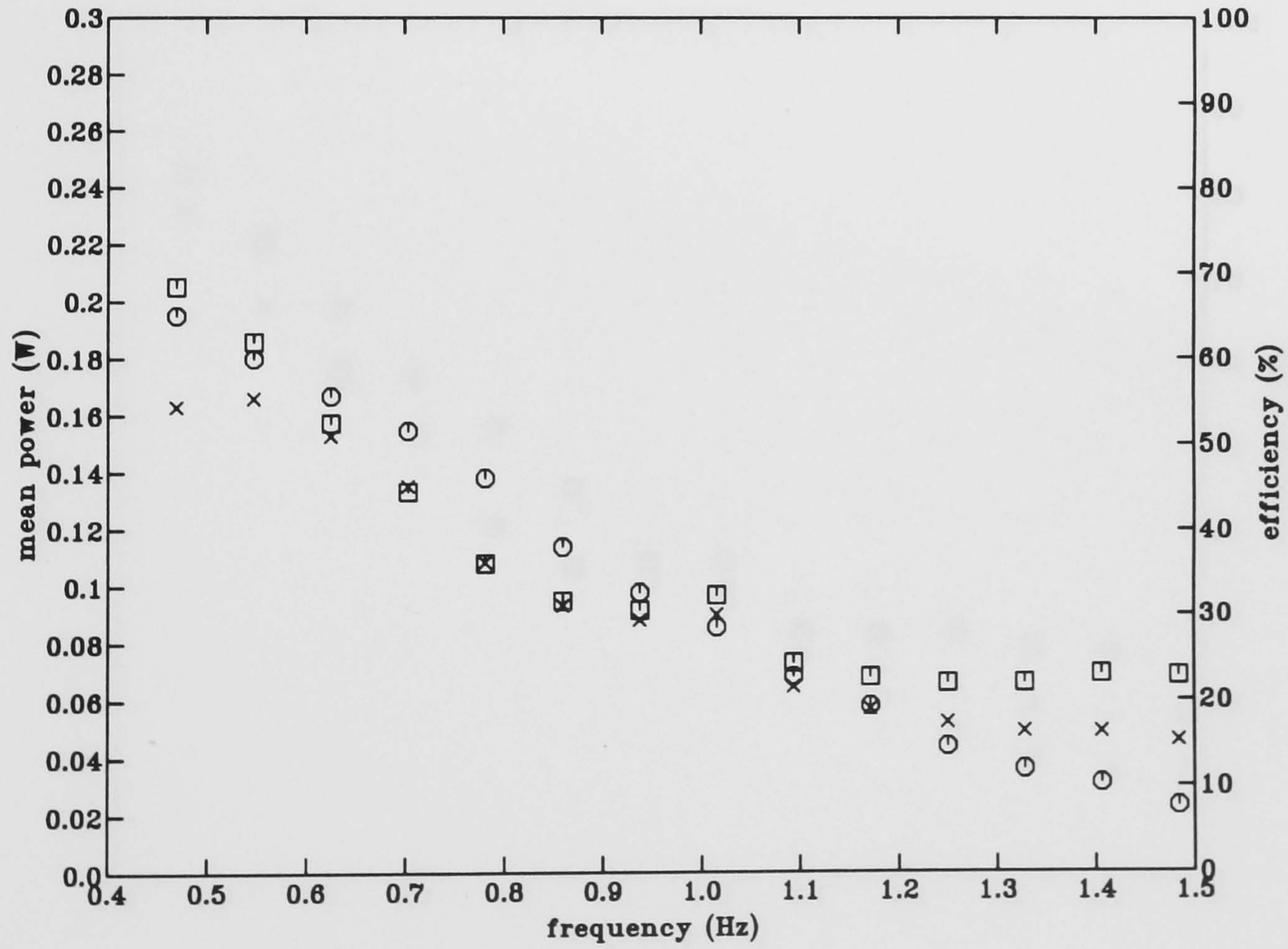

FIGURE 6.11: Mean power (×) and efficiency (□) calculated from wave and pressure records and mean power calculated with numerical model (○). Orifice = 15 × 15mm

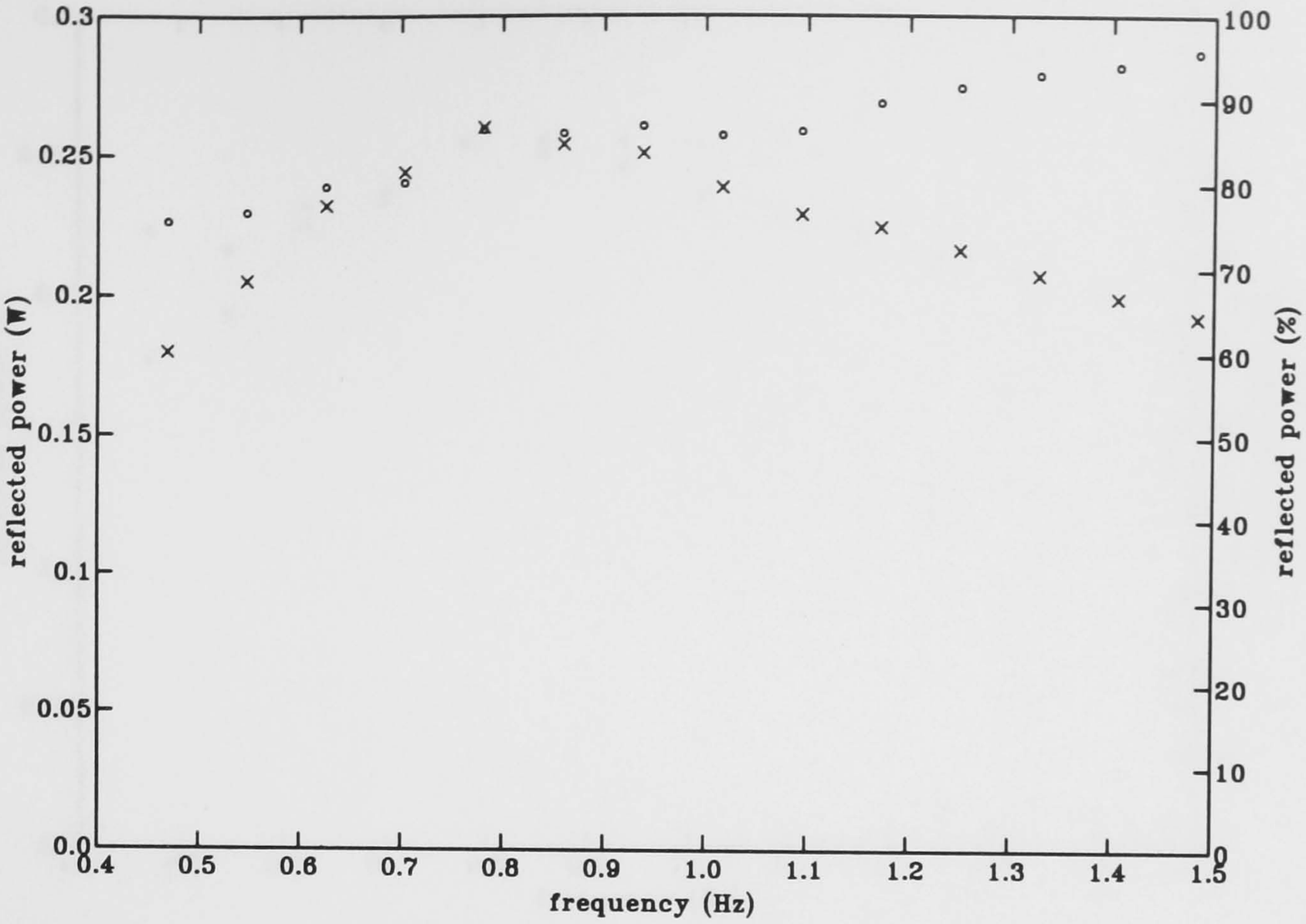

FIGURE 6.12: Power reflected from the OWC measured in watts ($\times$) and as a percentage of the input power ($\circ$). Orifice = 20×20mm

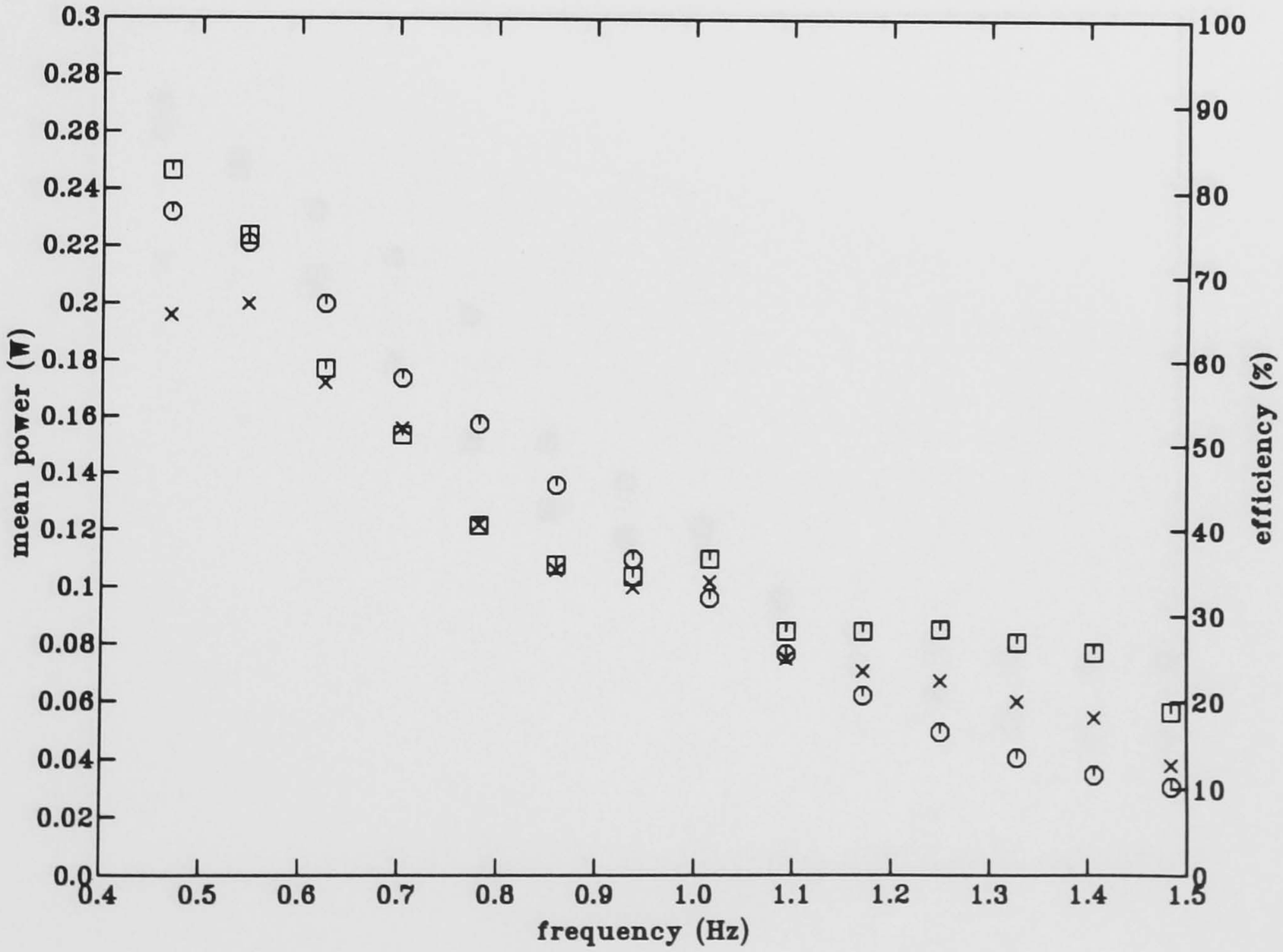

FIGURE 6.13: Mean power ($\times$) and efficiency ($\square$) calculated from wave and pressure records and mean power calculated with numerical model ($\circ$). Orifice = 20×20mm

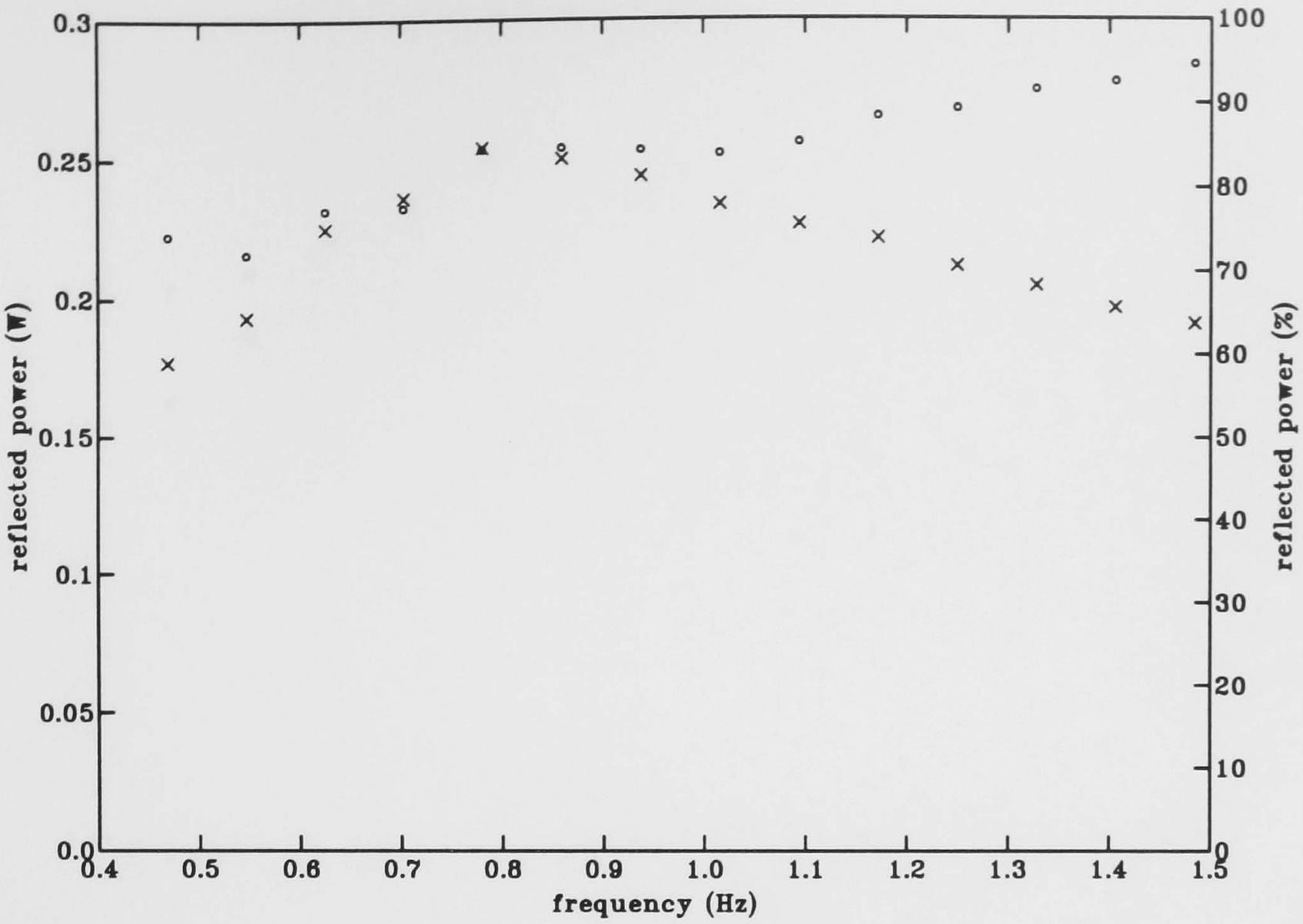

FIGURE 6.14: Power reflected from the OWC measured in watts (×) and as a percentage of the input power (○). Orifice = 25 × 25mm

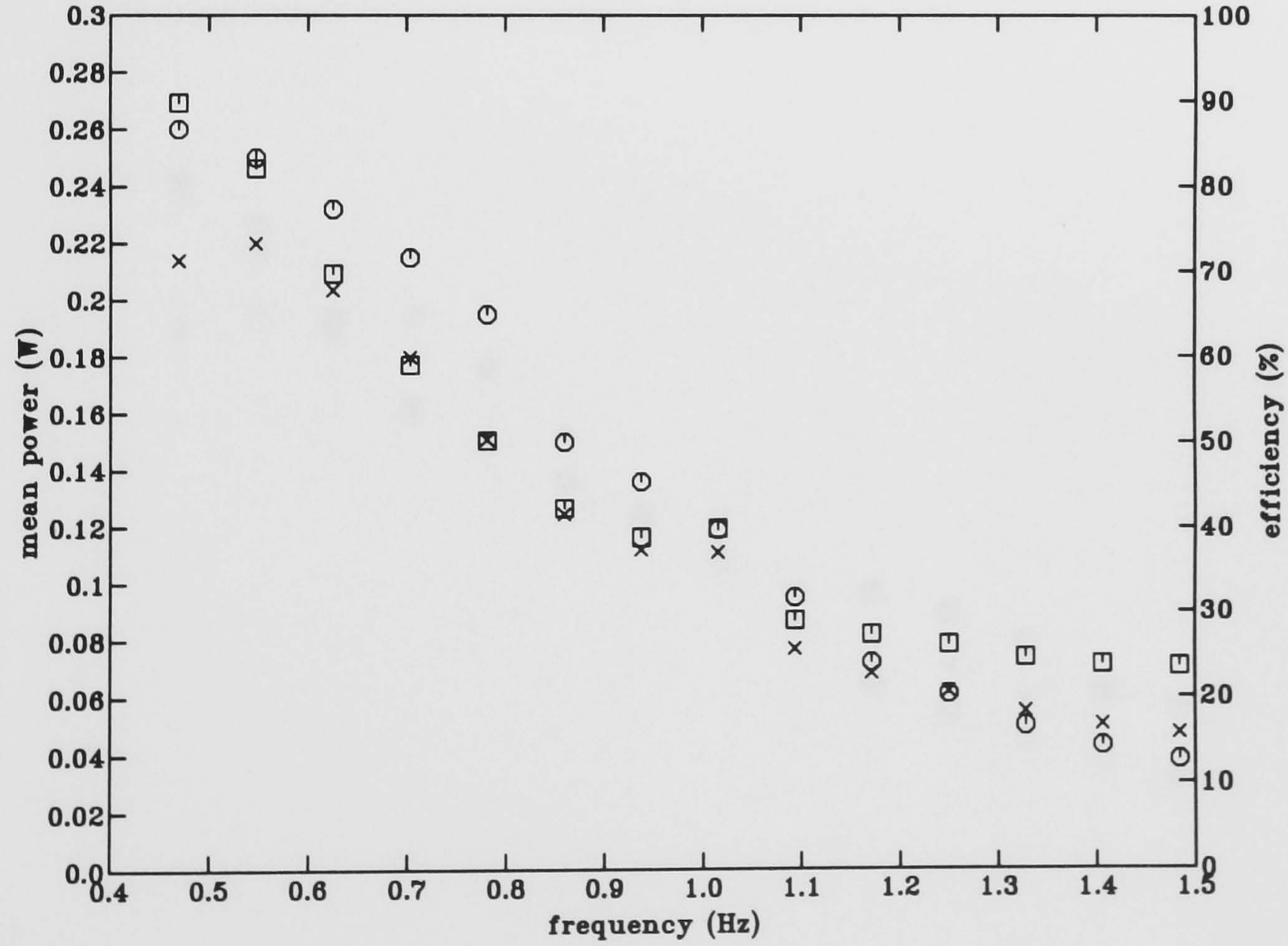

FIGURE 6.15: Mean power (×) and efficiency (□) calculated from wave and pressure records and mean power calculated with numerical model (○). Orifice = 25 × 25mm

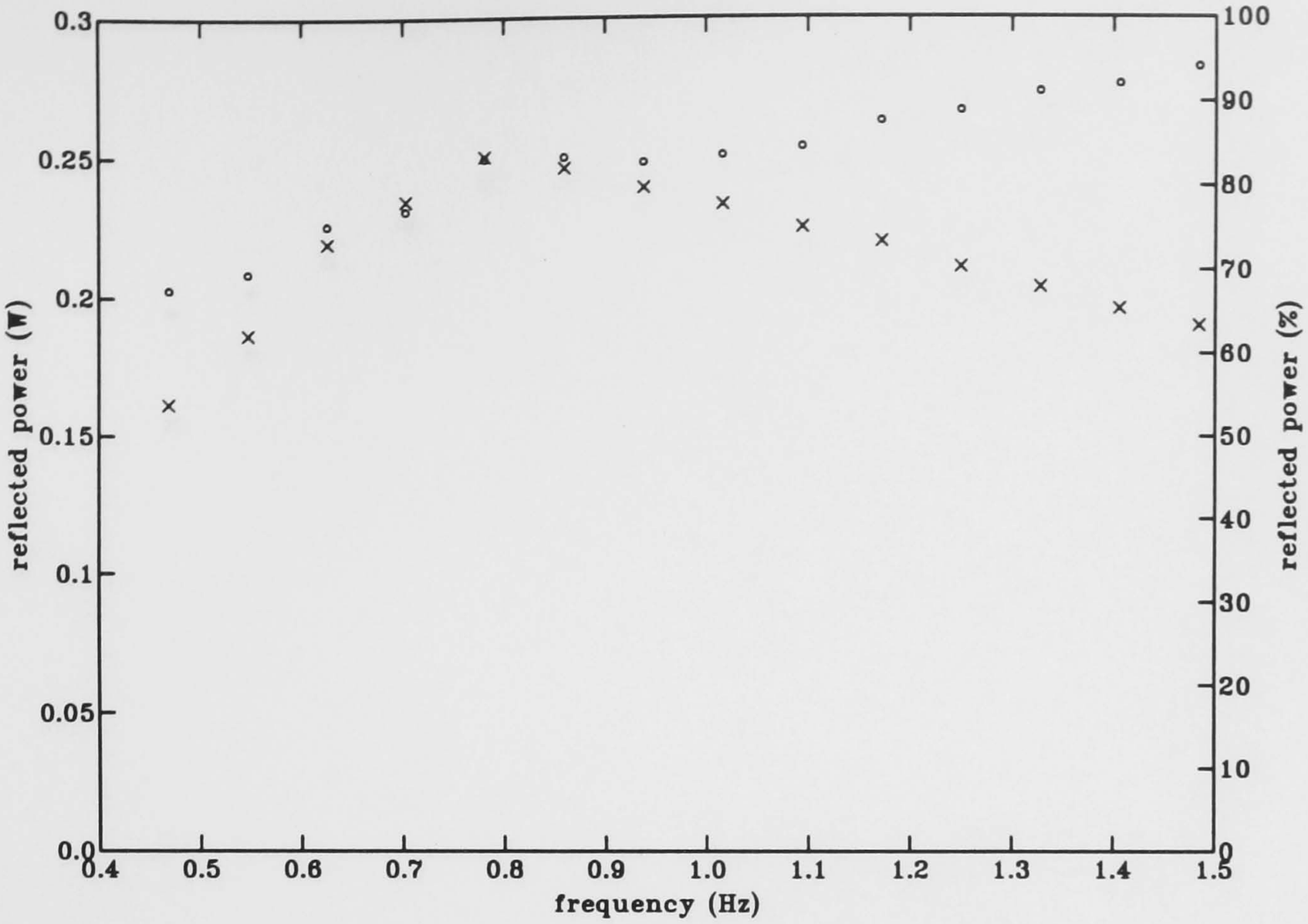

FIGURE 6.16: Power reflected from the OWC measured in watts (×) and as a percentage of the input power (○). Orifice = 30 × 30mm

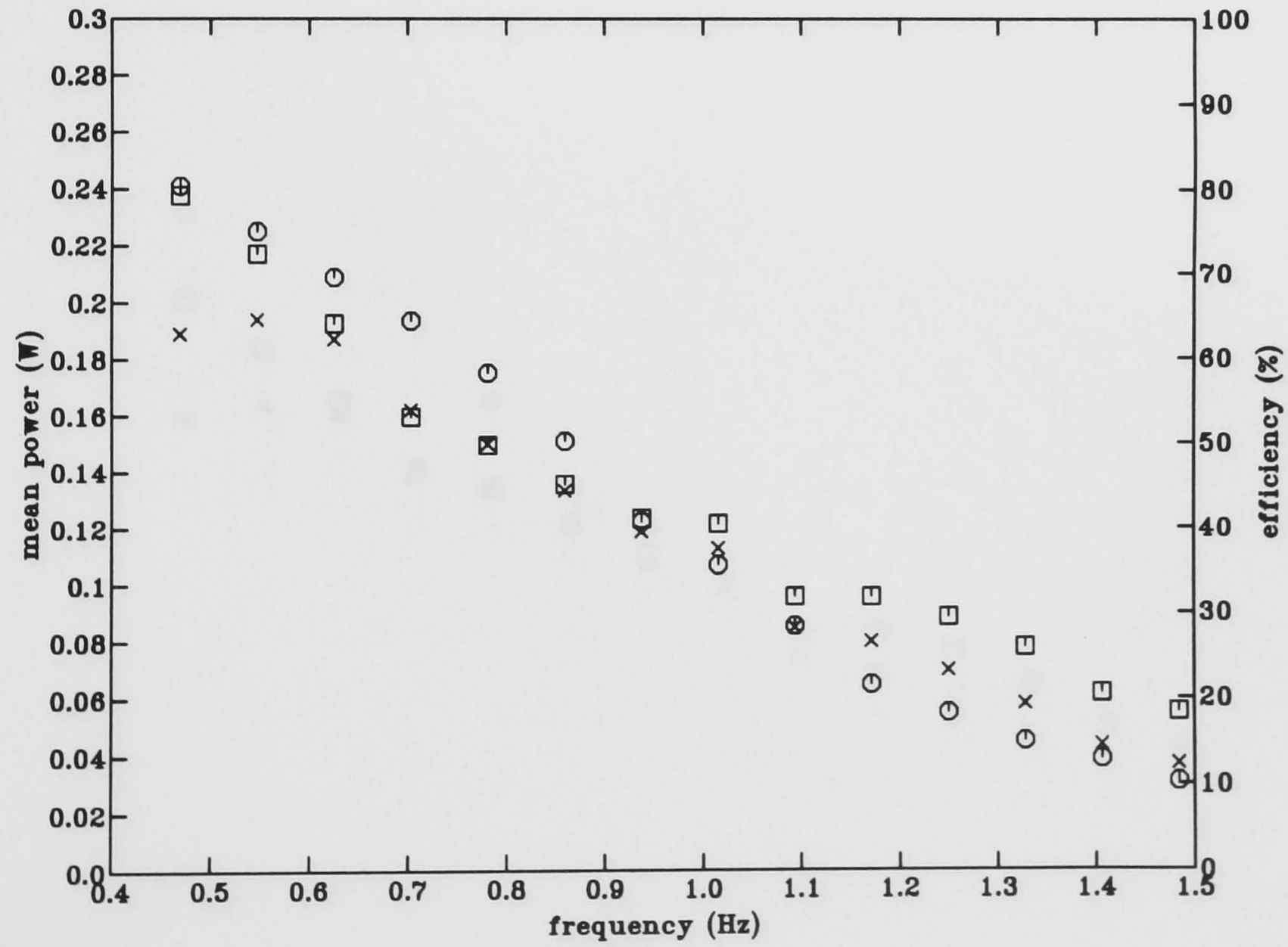

FIGURE 6.17: Mean power (×) and efficiency (□) calculated from wave and pressure records and mean power calculated with numerical model (○). Orifice = 30 × 30mm

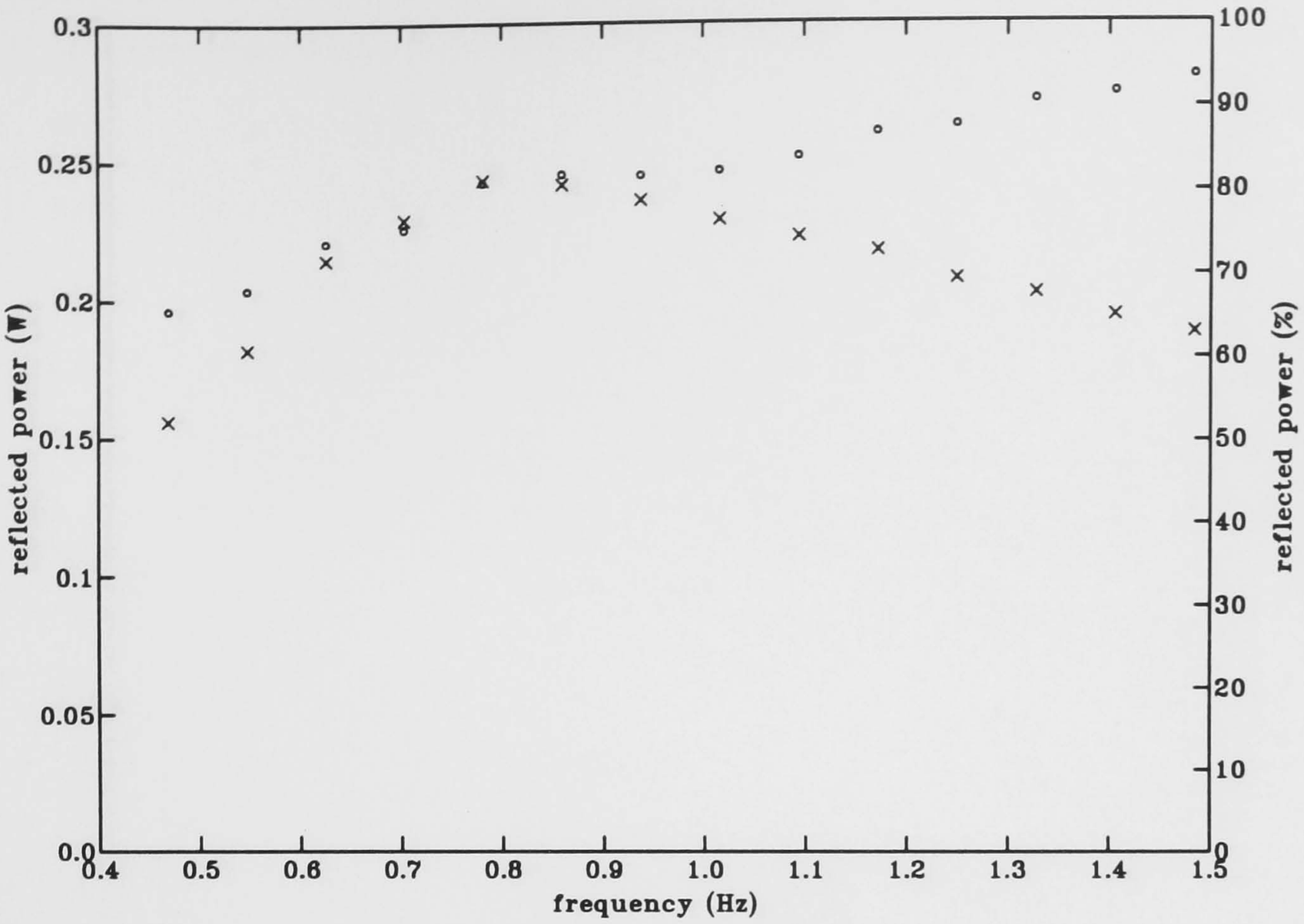

FIGURE 6.18: Power reflected from the OWC measured in watts (×) and as a percentage of the input power (○). Orifice = 35 × 35mm

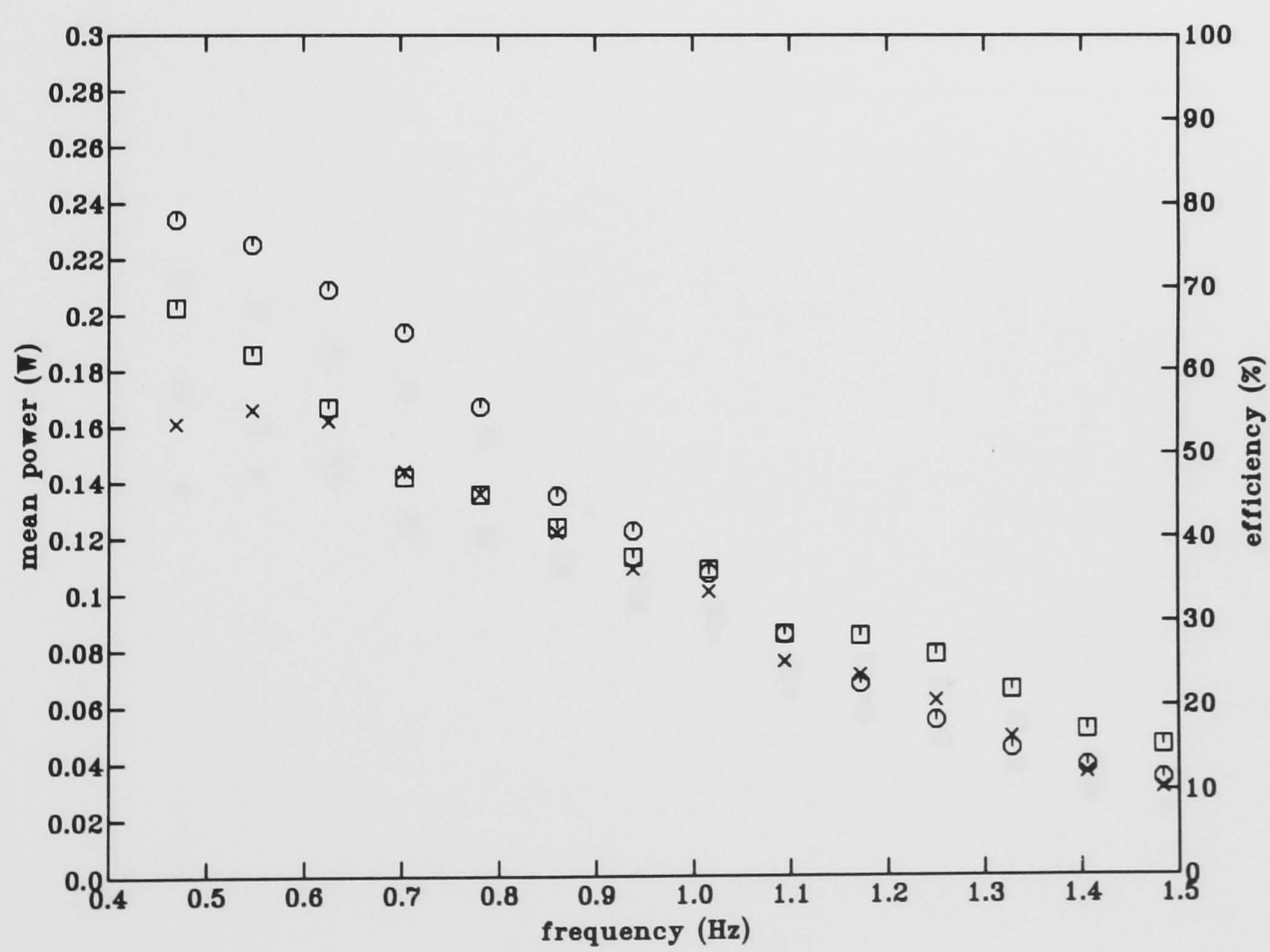

FIGURE 6.19: Mean power (×) and efficiency (□) calculated from wave and pressure records and mean power calculated with numerical model (○). Orifice = 35 × 35mm

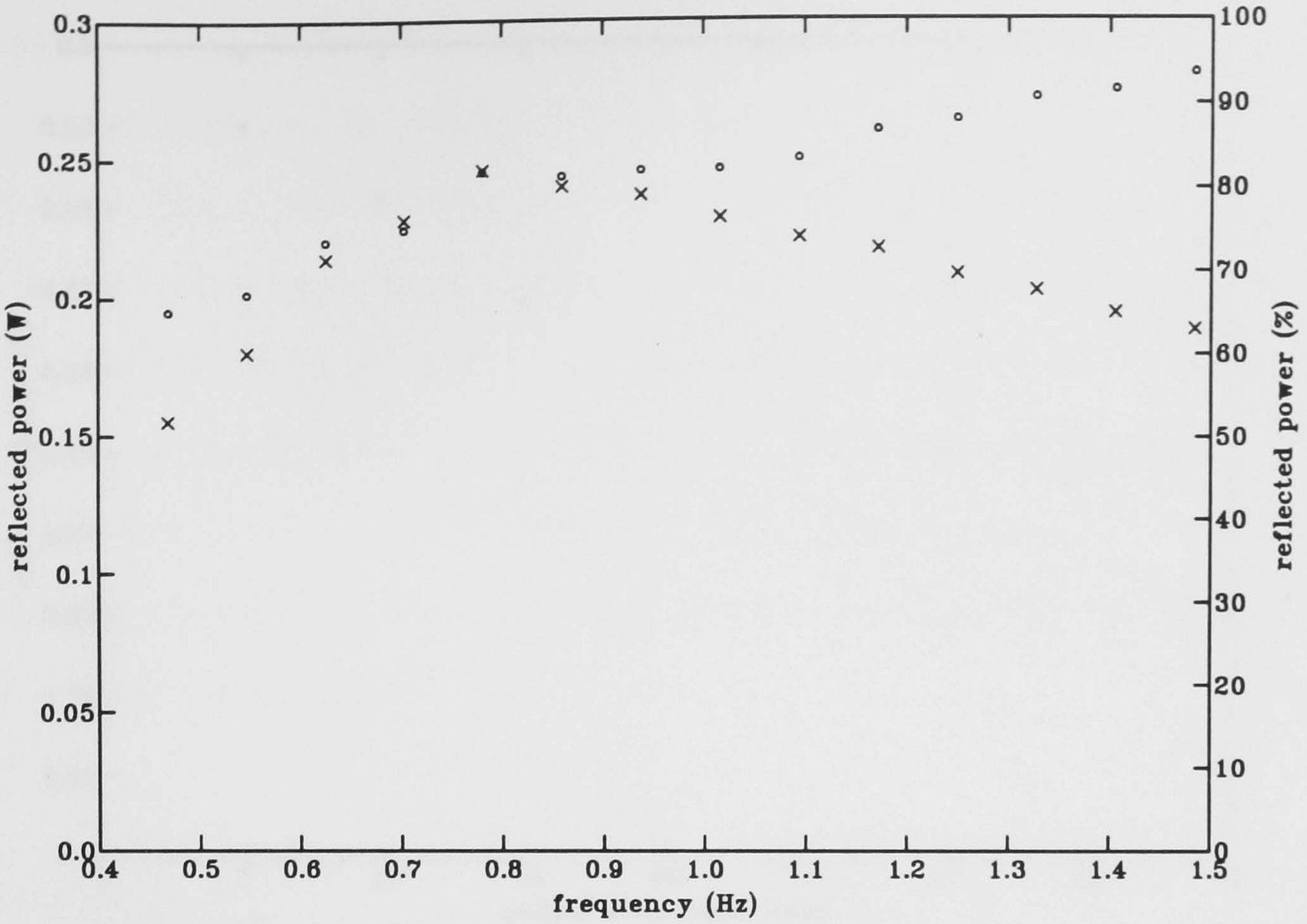

FIGURE 6.20: Power reflected from the OWC measured in watts (×) and as a percentage of the input power (○). Orifice = 39 × 39mm

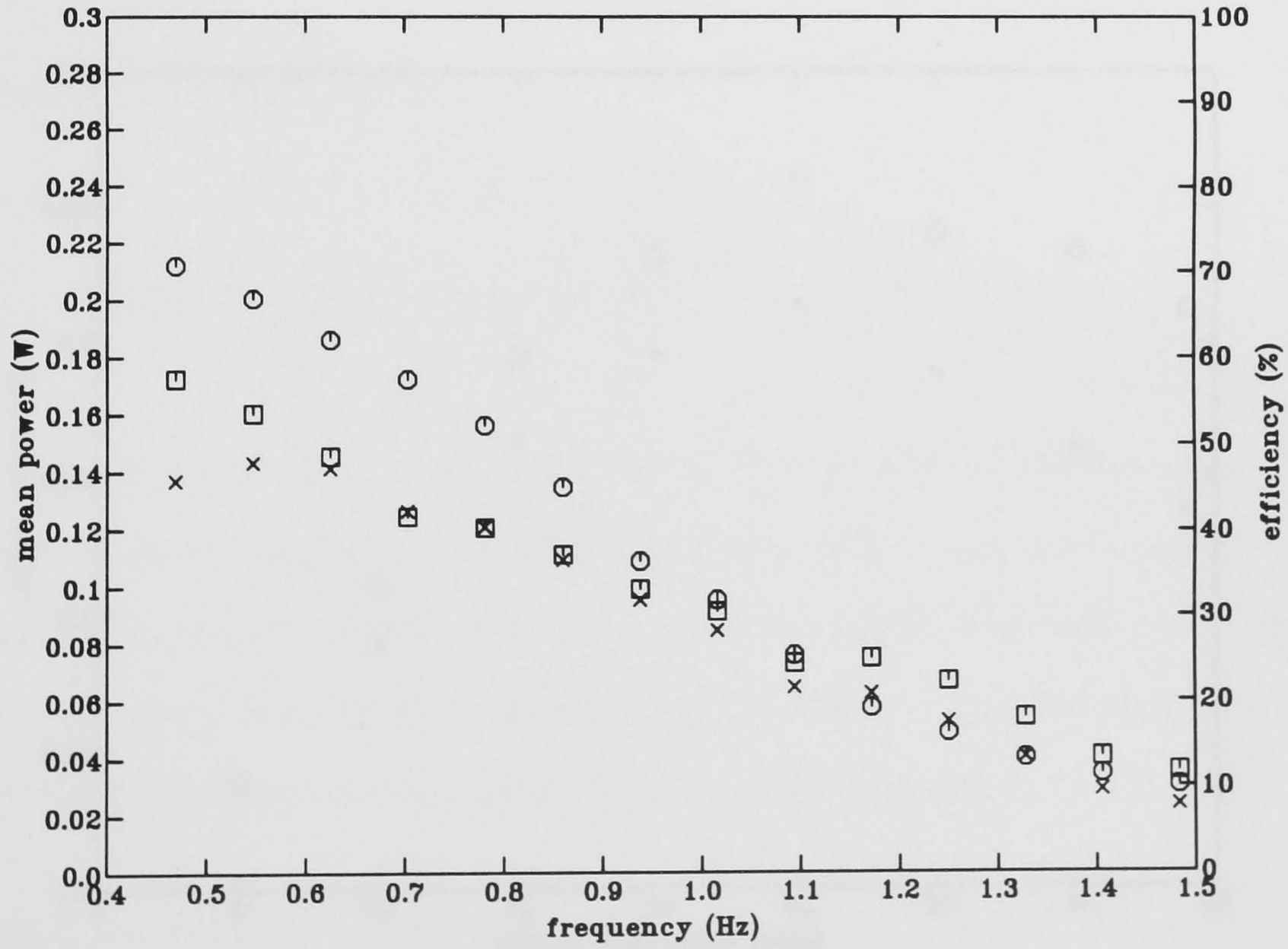

FIGURE 6.21: Mean power (×) and efficiency (□) calculated from wave and pressure records and mean power calculated with numerical model (○). Orifice = 39 × 39mm

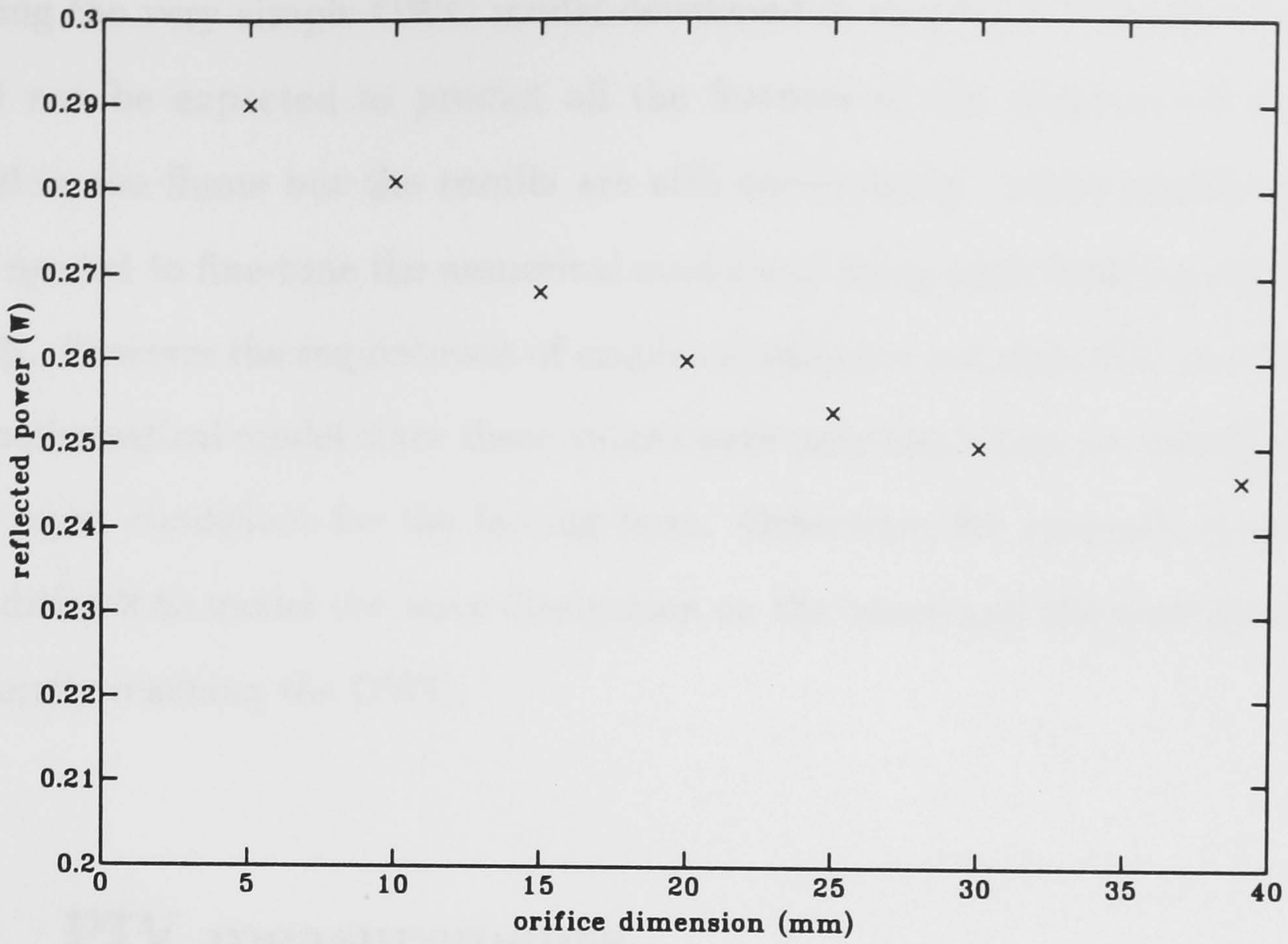

FIGURE 6.22: Power reflected from the OWC, frequency=0.781Hz

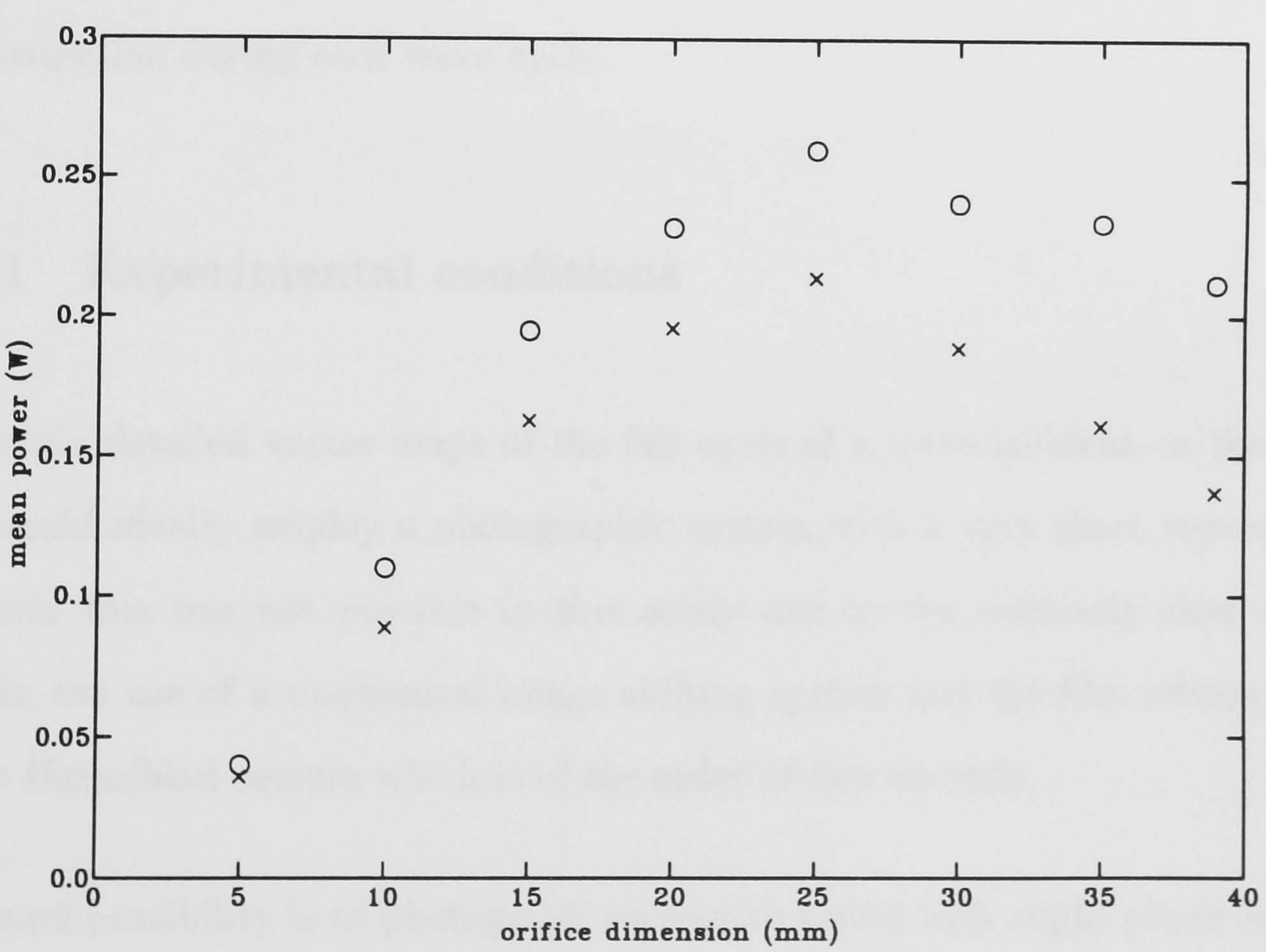

FIGURE 6.23: Comparison of experimental (×) and theoretical (○) values of mean power. Frequency = 0.469Hz

sidering the very simple OWC model developed in chapter 5. Clearly this model could not be expected to predict all the features of the response of the OWC model in the flume but the results are still encouraging. Some empirical values were needed to fine-tune the numerical model and these contributed greatly to the results. However the requirement of empirical values is not regarded as a failure of the mathematical model since these values were only needed to provide the correct wave input conditions for the forcing term. Otherwise, for example, it would be very difficult to model the wave dissipation on the beach and the wave amplitudes eventually reaching the OWC.

6.5 PIV measurements

Results of PIV measurements of flow into and out of the OWC chamber are presented. The resultant velocity data are used to estimate the energy of the flows and its dissipation during each wave cycle.

6.5.1 Experimental conditions

To obtain detailed vector maps of the full cycle of a wave incident on the OWC one would ideally employ a photographic system with a very short repeat time. However this was not possible in this study due to the relatively slow shutter speeds, the use of a mechanical image shifting system and the film advance time of the Hasselblad camera which is of the order of two seconds.

A second possibility is to photograph successive waves with slight phase advance between frames. However an arbitrary pressure record from the OWC chamber shown in figure 6.24 suggests that there may be a significant variation between

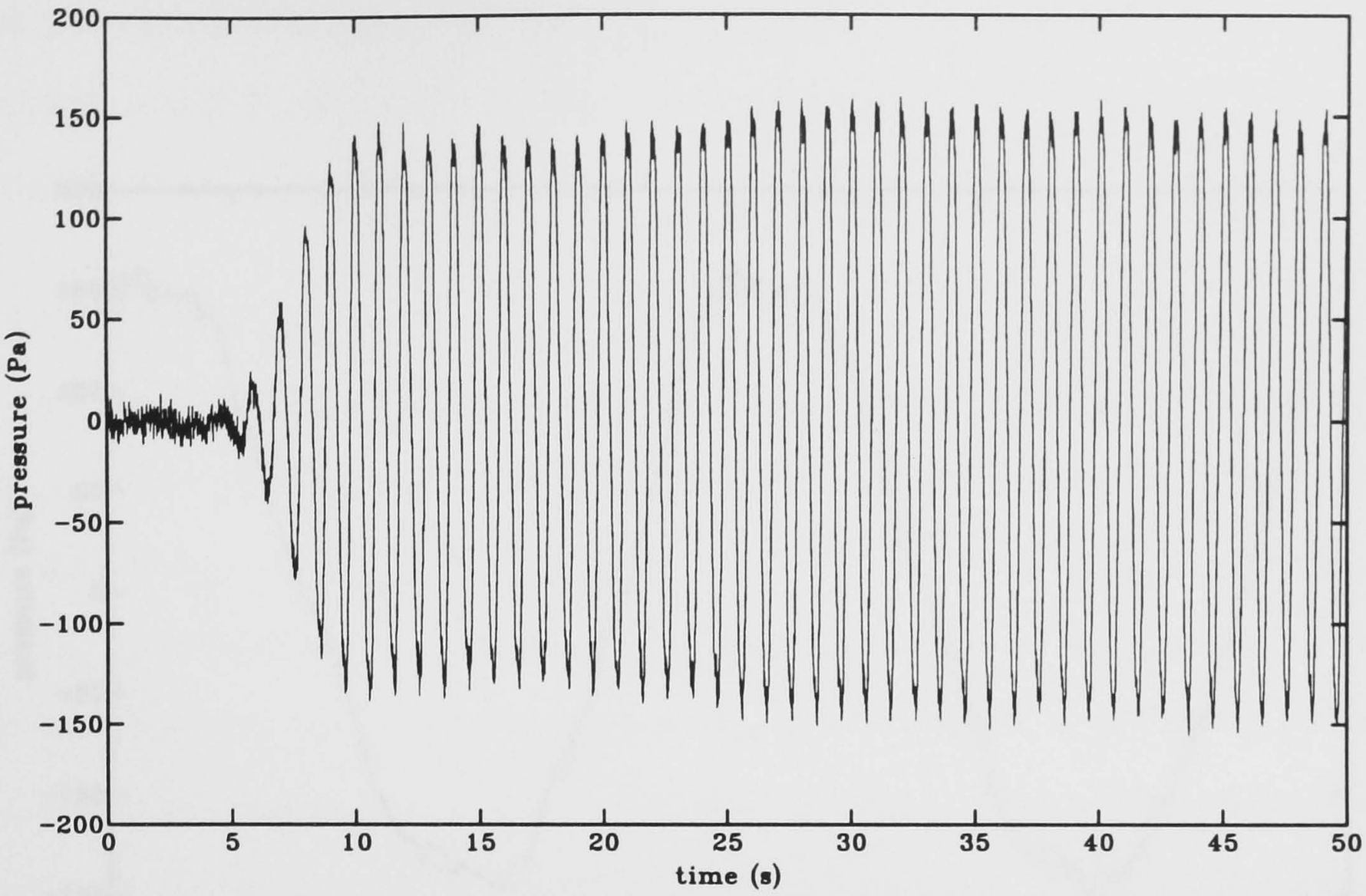

FIGURE 6.24: Typical long term pressure record from OWC chamber, frequency=1.0Hz, amplitude=10mm, orifice=5×5mm

the first and last wave in the photographed series resulting in a lack of continuity between frames.

An attempt was made to overcome this lack of repeatability by waiting for the water in the flume to settle and then starting the wave paddle. The first photograph was taken after an arbitrarily chosen thirty second wait and then the paddle was stopped and the flume left for about ten minutes until the water had resettled. When the paddle was restarted the next frame was taken with the wait time increased by the required fraction of a wave period and by repeating this process a full photographic record of the wave was built up.

Figure 6.25 shows two pressure records taken after a thirty second wait but from successive experiments separated by a settling time of ten minutes. The pressure

records clearly match very well indicating that this is a more reliable, if not ideal method of obtaining velocity vector maps of a complete wave cycle.

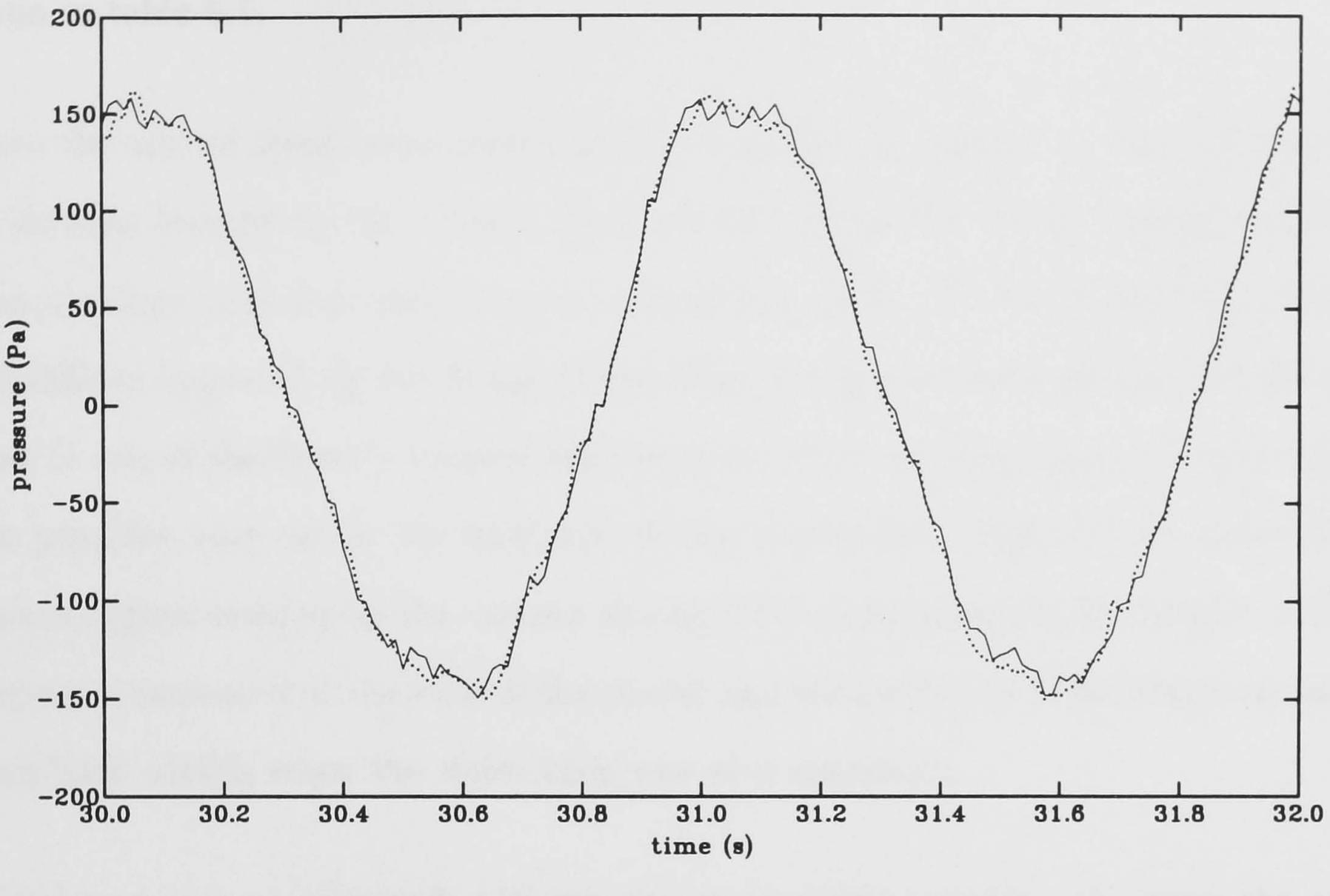

FIGURE 6.25: Comparison of two pressure records from OWC chamber, frequency=1.0Hz, amplitude=10mm, orifice=5×5mm

In the laboratory the microcomputer was set up to automate the above experimental procedure with human intervention being required only to change the film in the camera or to add more seeding to the flume. The thirty second wait before each frame also served to remix the seeding in the water since it had a tendency to rise to the surface during the settling time between frames.

6.5.2 Data acquisition

The process of obtaining PIV data with image shifting is described in detail in chapters 2 and 3. However the parameters relevant to these measurements are given in table 6.1.

Since the aim of these measurements was to record the formation and dissipation of vortices formed in the vicinity of the front wall of the OWC model the PIV measurement zone was chosen to be centred just below the lower lip of this wall. Conditions imposed by the fixing of the false bed in the flume placed the model near to one of the flume's vertical steel sections so unimpeded measurements were not possible very far in the direction of the wavemaker. Figure 6.26 shows the square region imaged by the camera during PIV measurements, the height of the camera chosen so that the base of the model and the underside of the water surface were both visible when the water level was at a minimum.

Initial tests were performed, without an image shifting system, to assess the extreme values of horizontal velocity components likely to be encountered during experiments and these data, along with equations 3.3 and 3.4 were used to determine an optimal shift speed and the rotation rate for the octagonal spinning mirror. It should have been possible to further fine-tune the performance of the system by optimising the above values for each different test condition, however it was deemed that the slight overall gain in precision did not warrant the considerable extra effort involved.

Further tests identified the optimal camera settings and illumination level and these too were kept constant during the following experiments. All the significant parameters used to obtain PIV measurements are summarised in table 6.1

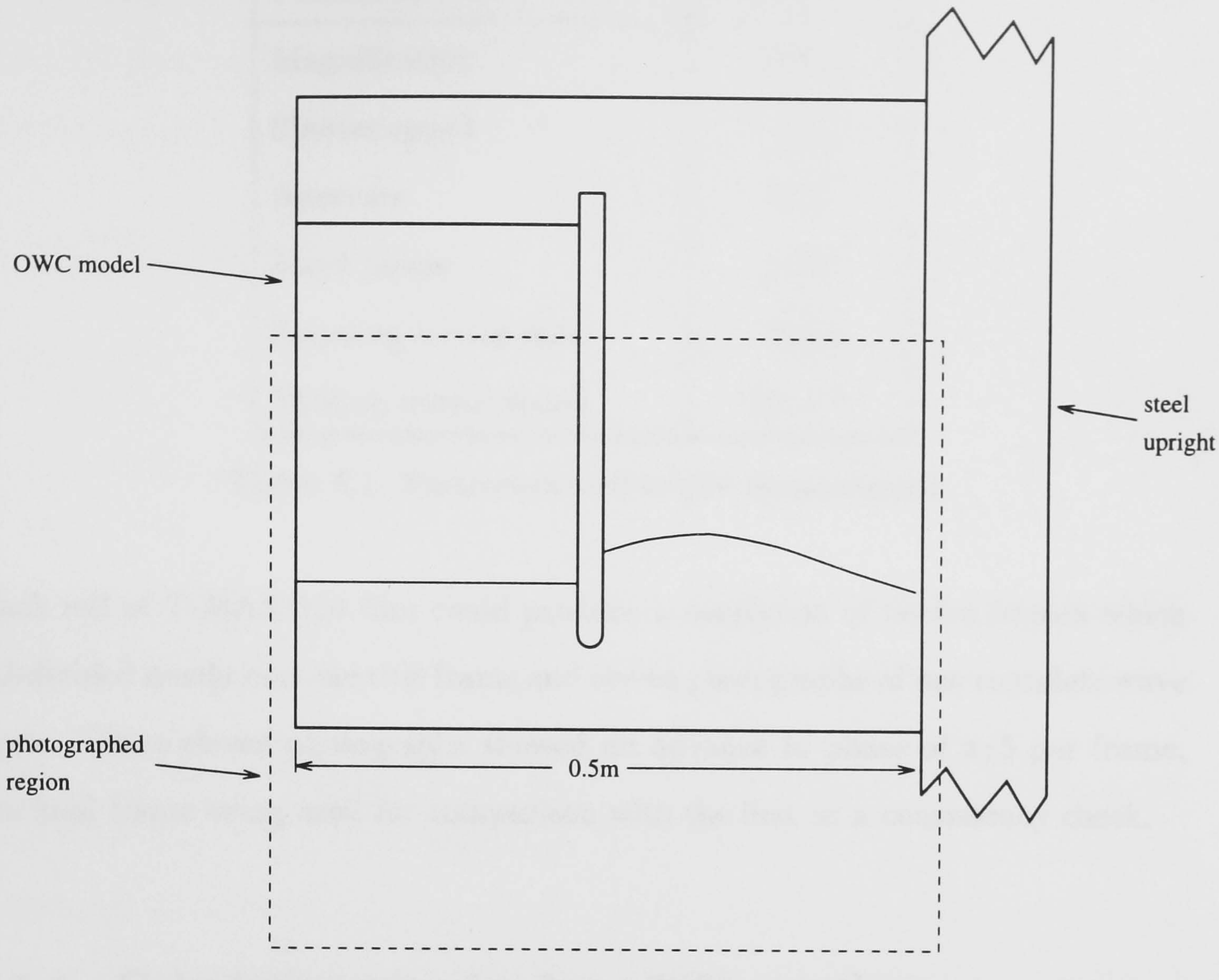

FIGURE 6.26: Diagram of the model in the flume showing the region photographed with the PIV system

6.5.3 Experimental parameters

Extraction of effective time series data using PIV or any other technique requires a sufficiently high sampling rate to record any detail variations. However given a typical PIV analysis time of about 90 minutes per frame and a total of 112 different test conditions, clearly some compromises had to be reached if any meaningful results were to be obtained within a reasonable timescale.

Analysis of wave gauge records identified the optimal orifice size to be about 25×25mm so PIV time series experiments were restricted to all the test wave frequencies at this orifice size.

Parameter	Setting
Magnification	0.0911
Shutter speed	$\frac{1}{125}$s
Aperture	f5.6
Laser power	15W
Spinning mirror rate	75rps
Shifting mirror speed	$30°\ s^{-1}$

TABLE 6.1: Parameters used in PIV measurements

Each roll of T-MAX 120 film could produce a maximum of twelve frames which subdivided neatly into one title frame and eleven photographs of one complete wave cycle. These eleven photographs showed an advance in phase of $\pi/5$ per frame, the final frame being used for comparison with the first as a consistency check.

6.5.4 Calculating energies from PIV negatives

The instantaneous full field velocity maps obtained by the PIV method allow post analysis calculation of vorticity and streamline maps, for example, allowing alternative presentations of the data. It is often difficult to extract information visually from vector plots since they tend to only reveal detail in the regions of the flow where the velocities are large compared to the mean.

In this study the process of extracting information from PIV maps is taken one stage further to calculate the kinetic energy and viscous dissipation in the flow both point by point and over the whole measurement zone.

A program called ENERGY performs the calculations on a square lattice and

sums the results over the extent of each vector map. Clearly extracting such information from a two-dimensional vector plot requires some knowledge about the bulk properties of the flow and is subject to some assumptions. The validity of this approach depends on the assumptions that:

- the flow is two-dimensional

- the boundary layers adjacent to the flume walls are thin

The validity of these assumptions is considered below.

Two-dimensional flow assumption

The assumption of two-dimensional flow is always made in PIV studies in narrow wave tanks and in this study cross waves in the flume are minimised by the *Edinburgh Designs Ltd* wavemaker and by the careful construction of the flume where great care was taken to ensure that the sides are parallel. The possibility of generating cross waves becomes greater at frequencies close to those of the lowest mode of cross tank oscillations. However the flume is designed so as to decouple the planes of oscillation as far as possible to reduce the likelihood of cross waves even close to the fundamental frequency.

Thin boundary layer assumption

It is necessary to assume that the boundary layer is thin to avoid grossly overestimating the kinetic energy within the measurement zone. Given the dimensions of the flume and assuming a maximum flow speed of 0.5ms $^{-1}$ then the boundary layer thickness may be calculated to be only a few millimetres [9]. This gives rise

to an energy calculation overestimate of less than 1%.

Energy calculation

The kinetic energies are calculated pointwise on the square grid on which the PIV negatives are analysed. Each velocity vector is considered to lie at the centre of a grid square (see figure 6.27) and the fluid within a cuboid bounded by this square and the sides of the flume is assumed to translate as a solid body.

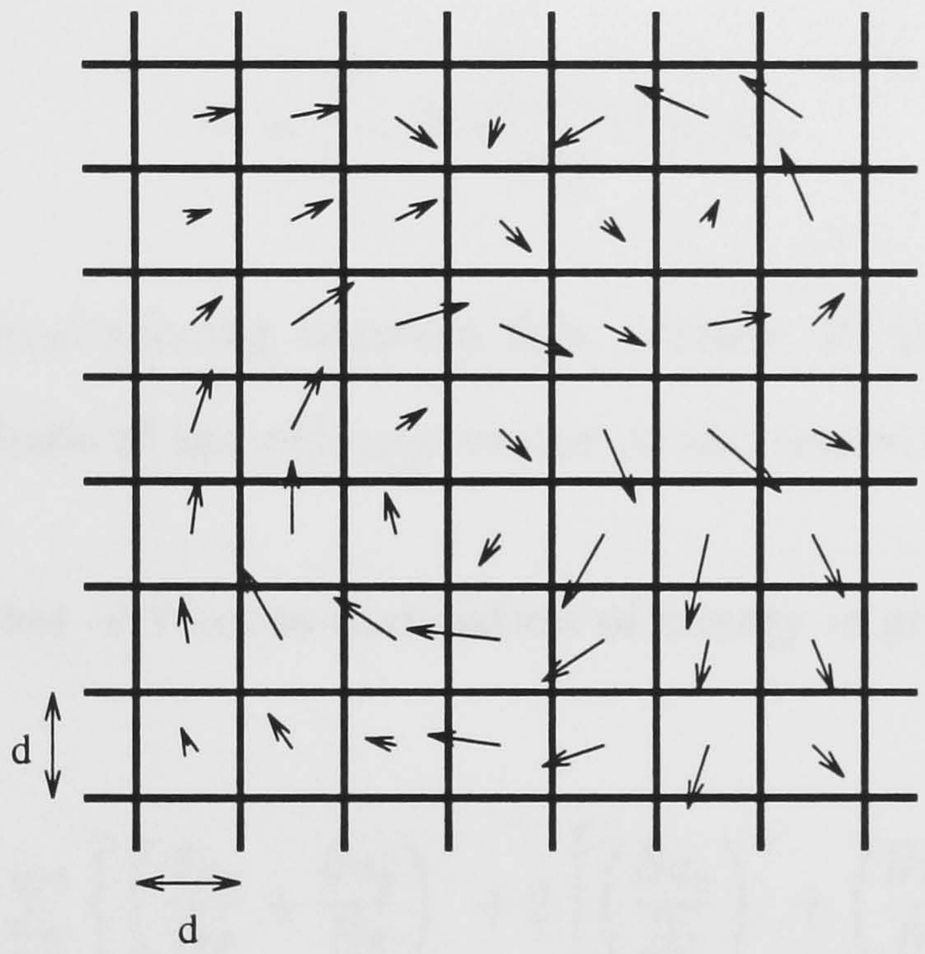

FIGURE 6.27: The velocity of each 'solid' cuboid is determined by the vector at its centre

In general the total kinetic energy of an incompressible fluid volume, V, is given by [36]

$$E_t = \frac{1}{2} \sum_i \int_V \rho_w v_i^2 dV \tag{6.48}$$

where $v_i(\mathbf{x}, t)$ $\{i = 1, 2, 3\}$ are the components of fluid velocity, and the rate of energy dissipation due to viscous effects is given by

$$\varepsilon = \frac{1}{2}\rho_w \nu \sum_{i,j} \int_V \left(\frac{\partial v_i}{\partial x_j} + \frac{\partial v_j}{\partial x_i} \right)^2 \tag{6.49}$$

where ρ_w is the fluid density and ν is the kinematic viscosity.

In the case of two-dimensional flow within the flume, where $v_x(x,y)$ and $v_y(x,y)$ are the components of velocity at the centre of each cuboid, the total kinetic energy of the fluid is given simply by

$$E_t = \frac{1}{2}\rho_w W d^2 \sum_{x,y} v^2(x,y) \tag{6.50}$$

where d is the physical spacing between flow vectors, W is the flume width and $v(x,y)$ is the magnitude of the velocity vector at the centre of the cuboid.

Similarly the total rate of viscous dissipation of energy is given by

$$\varepsilon = W d^2 \rho \nu \sum_{x,y} \left\{ \left(\frac{\partial v_x}{\partial y} + \frac{\partial v_y}{\partial x} \right)^2 + 2 \left[\left(\frac{\partial v_x}{\partial x} \right)^2 + \left(\frac{\partial v_y}{\partial y} \right)^2 \right] \right\} \tag{6.51}$$

It should be noted that no attempt is made to calculate the potential energy of the fluid or the energy dissipation occurring due to friction at the walls and base of the OWC model.

Considerable care must be exercised when calculating terms of the form $\partial v_i / \partial x_j$ (see equation 6.49) especially where there are large variations in velocity magnitudes between neighbouring grid points. This can result in massive discontinuities in the array of calculated spatial derivatives, compounding any experimental errors.

This problem is reduced by fitting spline curves to each row and column of velocity values and then calculating the spatial derivatives based on the local gradients of these curves rather than on the discrete data values at each grid point.

6.5.5 Experimental errors

The main sources of error associated with PIV measurement and the additional technique of image shifting have been considered in chapters 2 and 3 but the errors particular to this series of experiments are considered below.

The maximum flow speed measured before the subtraction of the shift velocity is in the region of $1.6 ms^{-1}$ and in regions of low vorticity the error associated with this is of the order of 2%. This suggests an error in the maximum velocities of around 5% after the shift velocity has been subtracted, with a slightly larger error in regions of high vorticity.

For the purposes of energy calculation it is desirable to have a flow vector defined at every analysis point. At points where no vector was obtained by the analysis system a numerical bicubic spline fit was used to generate a vector based on all the existing data. The validity of this technique was assessed by purposely deleting arbitrary vectors from experimental data sets and recreating interpolated values at these points with the fitting routine. In regions where the vorticity was less than $5 s^{-1}$ the fitting routine was found to estimate the deleted values with a typical error of less than 1%, this value increasing in regions of higher vorticity where the prevailing errors would likely be due to the PIV measurements themselves. In the course of experiments such interpolation was not required a great deal since the analysis system produced apparently reliable vectors at about 98% of the analysis points of most negatives, largely due to the use of the image shifting system.

Since no attempt is made to calculate potential energy in the flow, the measurements made cannot pretend to assess the total energy in a PIV frame. However in this study energy calculations are carried out merely to estimate the proportions of kinetic energy within vortices in an attempt to place an upper bound on the energy likely to be lost due to viscous dissipation, so measurements of potential energy are not very appropriate in this context.

The success of time series measurements depended greatly upon a high degree of wave repeatability and this potential source of error caused the greatest concern during experimentation. However as demonstrated in figure 6.25 and discussed in section 6.5.6 waves proved to be remarkably repeatable to within the same order of accuracy as the measurements themselves, at least on a macroscopic scale. However the direct repeatability of more microscopic measurements such as individual PIV measurements was not assessed since all the quantities ultimately derived were based upon full field measurements.

6.5.6 Results

Vector plots

The primary reason for making PIV measurements in this study was to calculate kinetic energies within the OWC so it was deemed unnecessary to include a large number of vector plots within this section. However one full time series of eleven vector plots along with their associated vorticity maps is shown in figures 6.28 to 6.38, for a 0.547Hz wave with an amplitude of 10mm at the wavemaker.

Despite the use of image shifting to resolve directional ambiguities and increase the dynamic range of the technique there still remain regions in some of the plots where

there are missing vectors. Typically these are areas of high acceleration within vortices or regions where the water is highly aerated with the seeding particle images obscured by bubbles. In each plot the approximate positions of the water surface and the front vertical wall of the OWC chamber have been added by direct measurement from the PIV negative.

Figure 6.28 shows the flow as a wave crest approaches the OWC chamber, travelling from right to left. Water is just starting to flow under the front wall and overall vorticity levels are low.

In figure 6.29 the hydrostatic pressure is at a maximum and the flow of water into the chamber has reached its maximum speed of about 0.6ms^{-1} just under the lip of the vertical front wall.

The formation of a clockwise rotating vortex can be seen in figure 6.30 as the flow separates from the inside of the front wall. This entrains some air which reduces the quality of the PIV measurements in that region. With larger wave amplitudes water aeration becomes progressively more of a problem making reliable PIV measurements difficult to obtain.

This vortex continues to strengthen through figure 6.31 where the vorticity attains its maximum value of about 125s^{-1}. At this stage the maximum horizontal component of velocity is directed toward the wavemaker although water is still flowing into the chamber at a speed of about 0.15ms^{-1}.

Figure 6.32 shows the velocity vector map shortly after the water level in the chamber has reached a maximum. The falling water level starts to carry the main vortex with it and the early stages of formation of a second, counter-clockwise rotating vortex can be seen just under the lip of the front wall of the OWC. This second vortex grows in strength while the other diminishes and in figure 6.33 their

magnitudes of vorticity are approximately equal at about $75s^{-1}$.

Thereafter the dissipation of the vortices is much more difficult to observe from the vector plots since there is a decrease in the velocity magnitudes, but the vorticity plots suggest that the counter-clockwise vortex is swept upward toward the water surface while the original clockwise vortex continues to travel away from the chamber before any residual vorticity is carried back in the next wave cycle.

The maximum and minimum values of vorticity from figures 6.28 to 6.38 are shown in figure 6.39, showing the peak values and subsequent decay of the two main vortices.

The particular conditions described above illustrate the vortices generated by the front wall of the OWC very clearly but at higher frequencies they are much less obvious, the vector plots providing much less visual information.

Energy values and dissipation rates

The program ENERGY has been used to estimate the total energy and viscous dissipation rates contained in the time series of vector plots for all the wave frequencies studied at the optimal orifice size of 25×25mm. The total energy in each frame is calculated but these values have little significance given the somewhat arbitrary choice of the extent of the PIV measurement zone.

The kinetic energy and dissipation time series graphs for one wave period of each of the test conditions are shown in figures 6.40 to 6.53.

All the kinetic energy curves show the same general form with two energy peaks. The taller peak corresponds to the part of the cycle where water is entering the

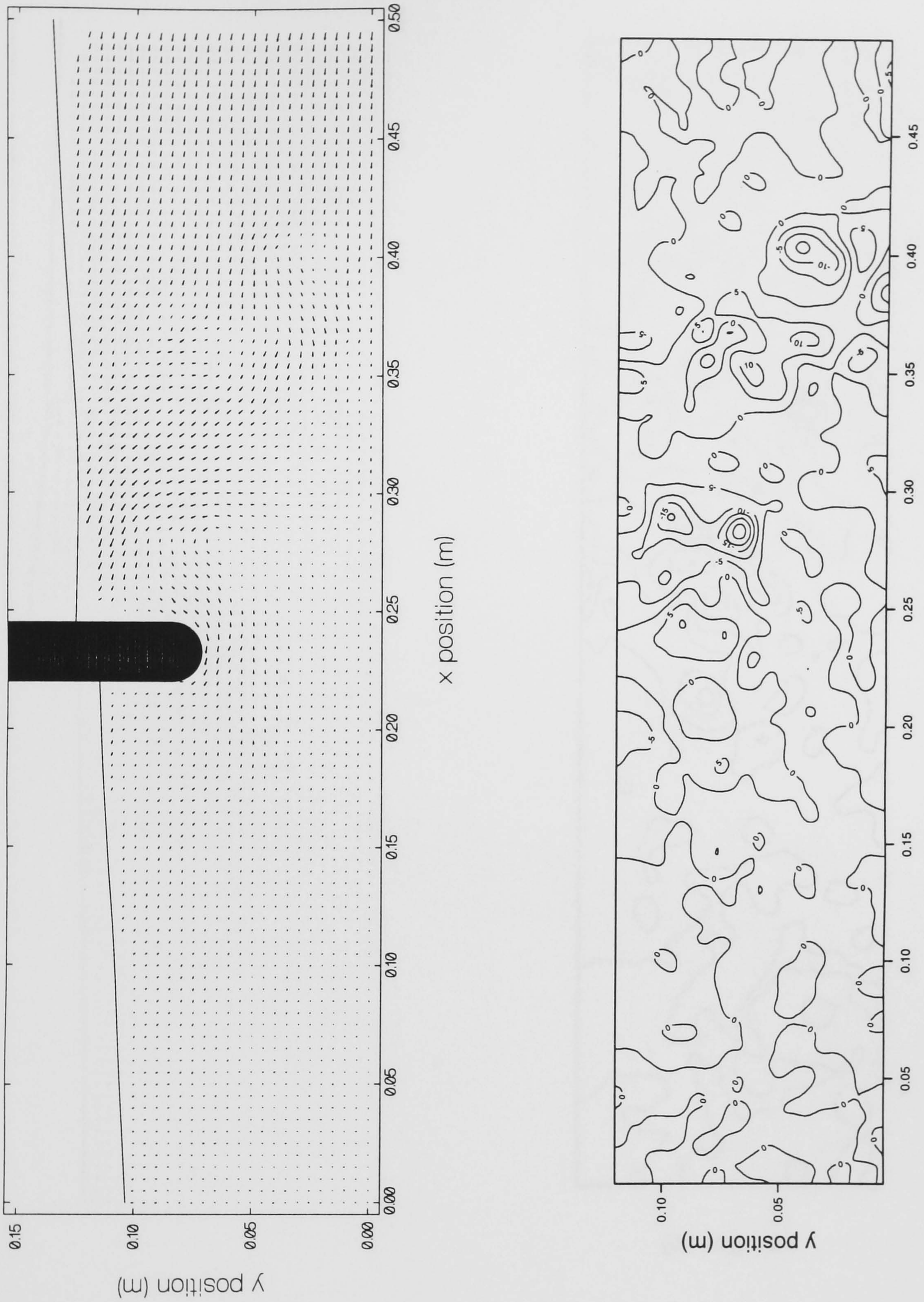

FIGURE 6.28: Velocity and vorticity maps of wave incident on OWC, frequency=0.547Hz, time=0s

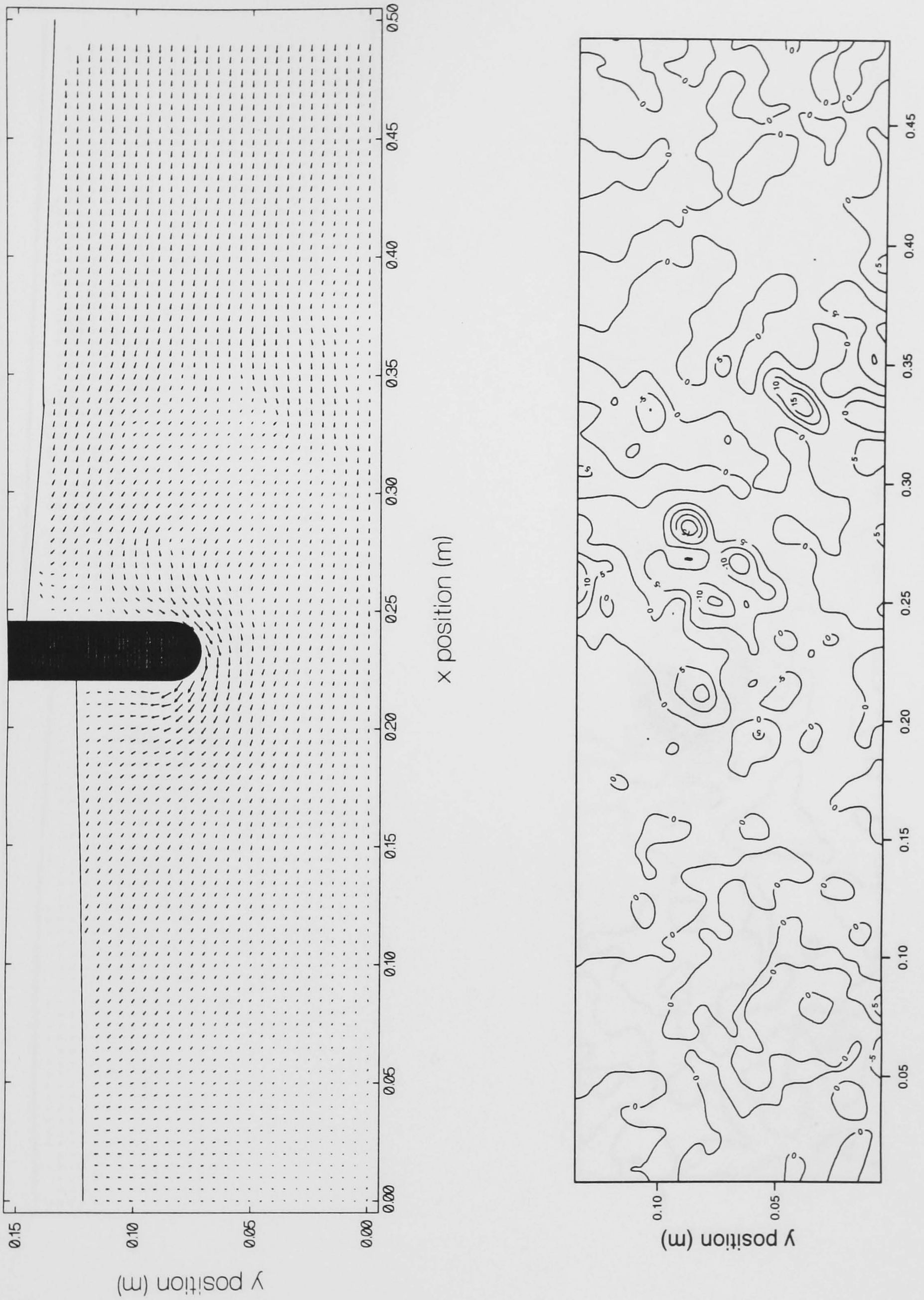

FIGURE 6.29: Velocity and vorticity maps of wave incident on OWC, frequency=0.547Hz, time=0.183s

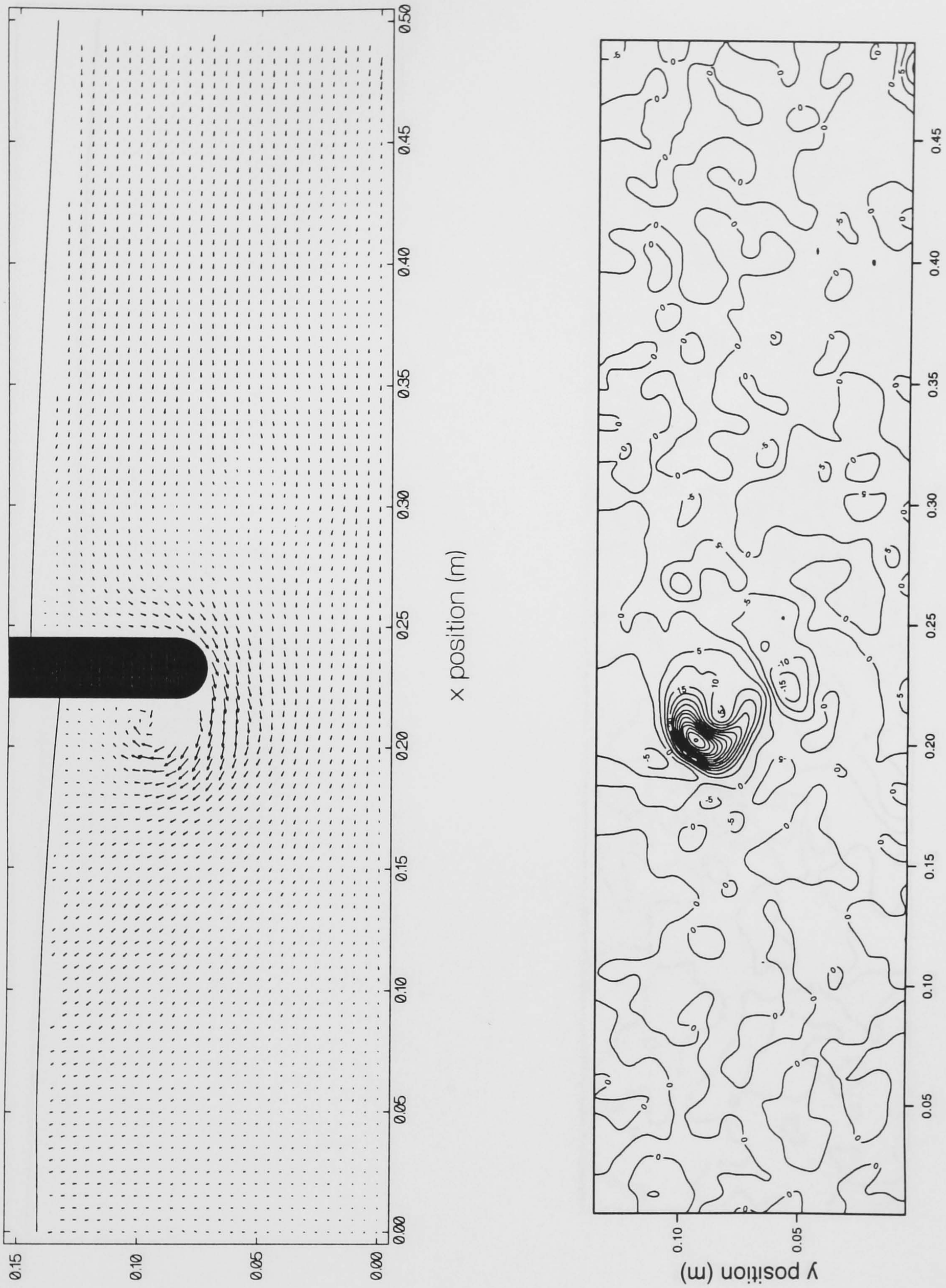

FIGURE 6.30: Velocity and vorticity maps of wave incident on OWC, frequency=0.547Hz, time=0.366s

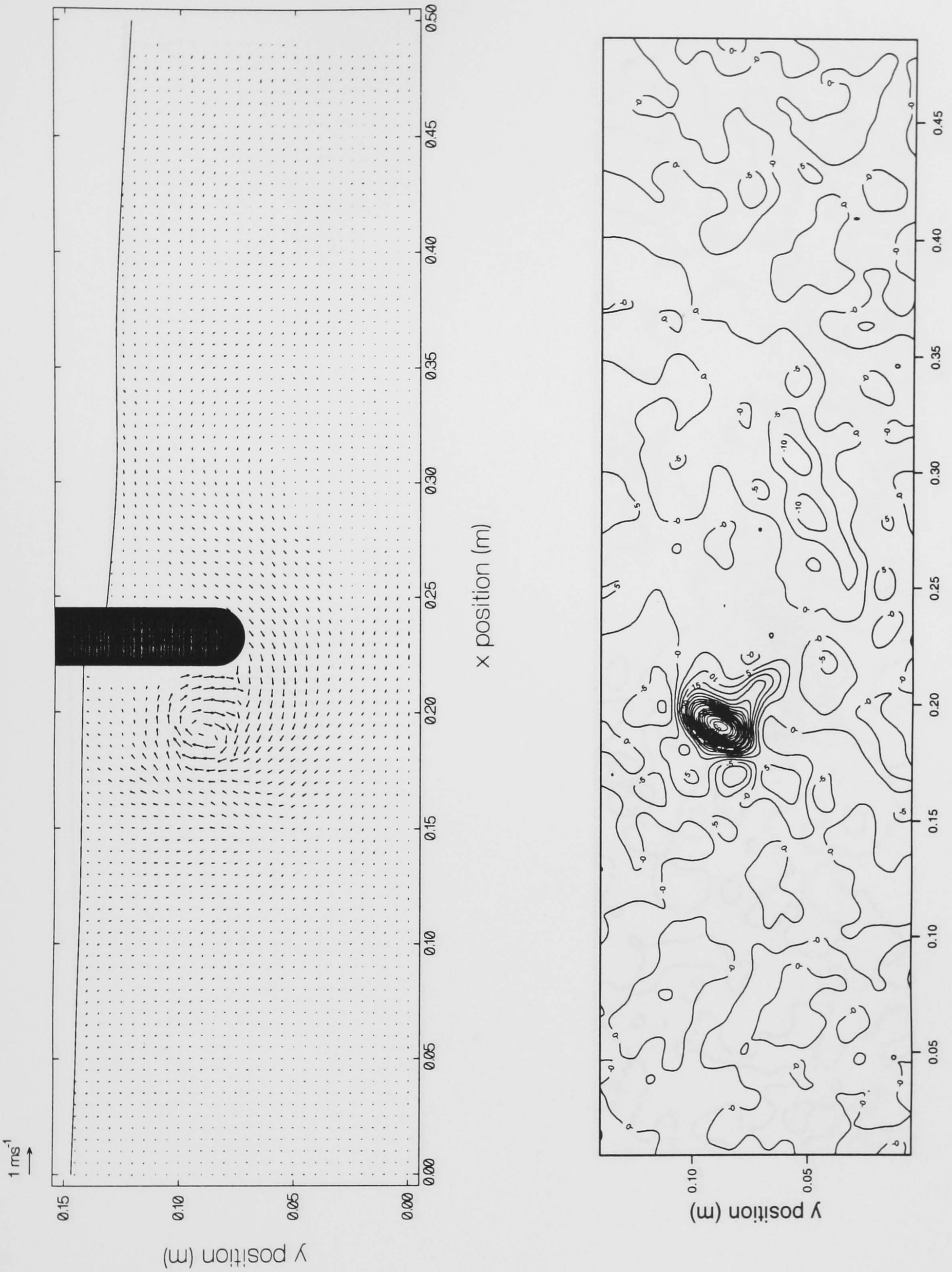

FIGURE 6.31: Velocity and vorticity maps of wave incident on OWC, frequency=0.547Hz, time=0.548s

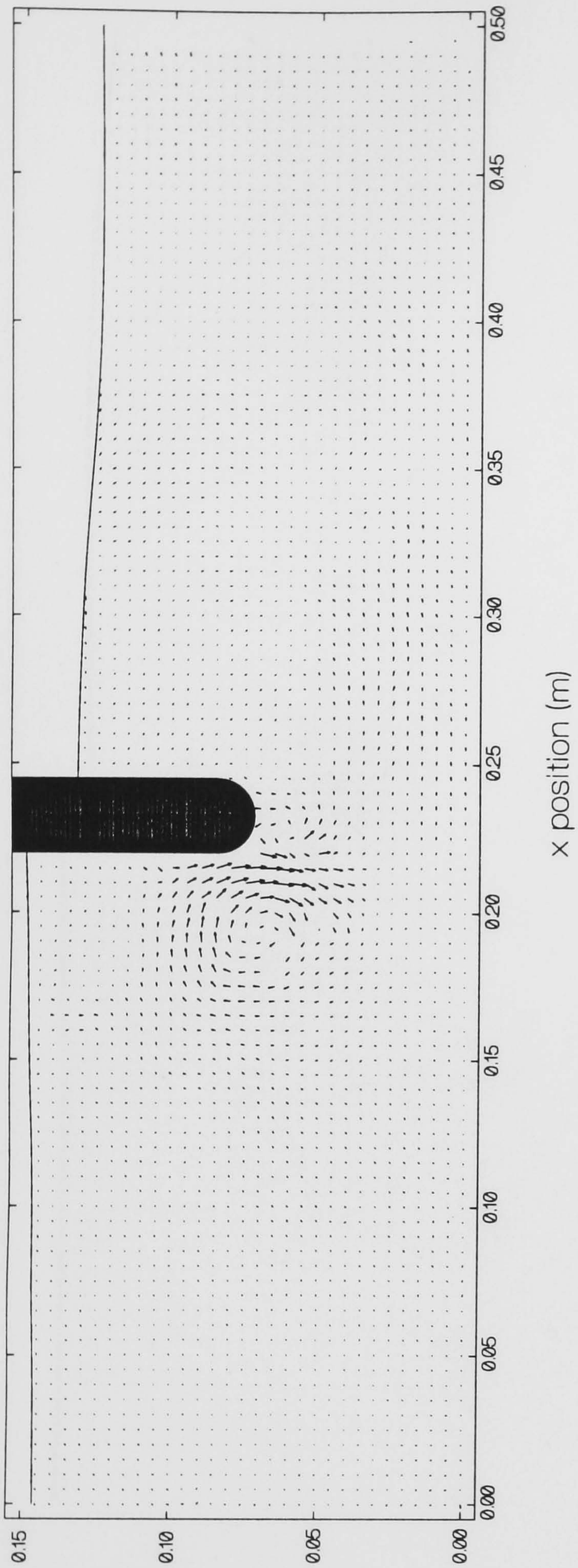

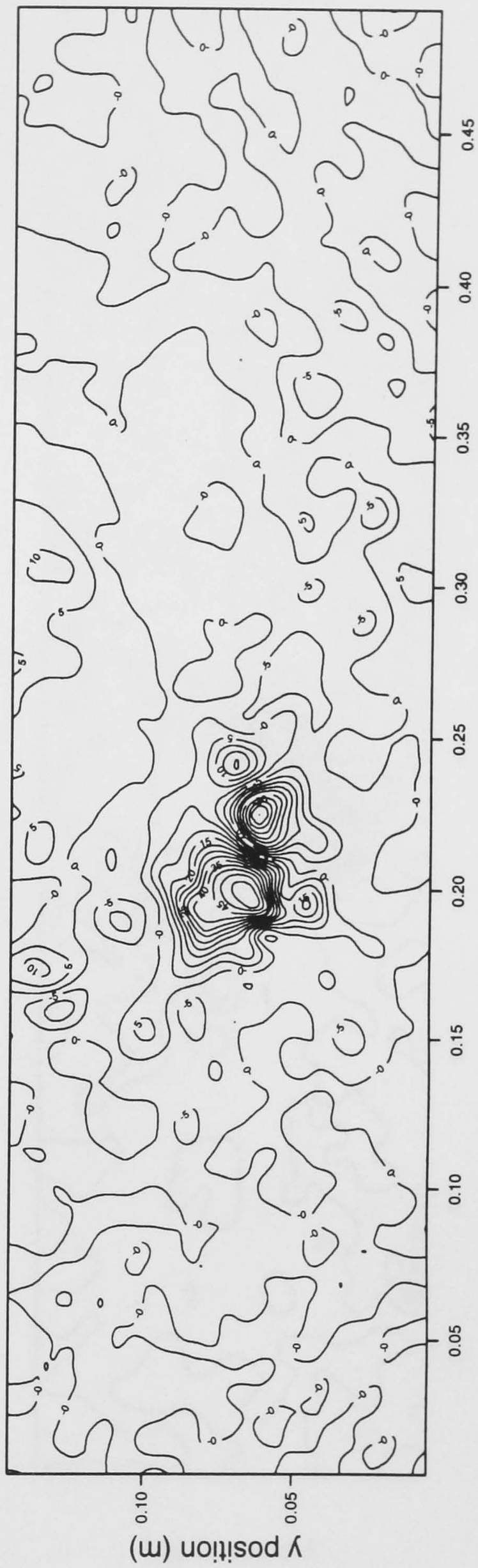

FIGURE 6.32: Velocity and vorticity maps of wave incident on OWC, frequency=0.547Hz, time=0.731s

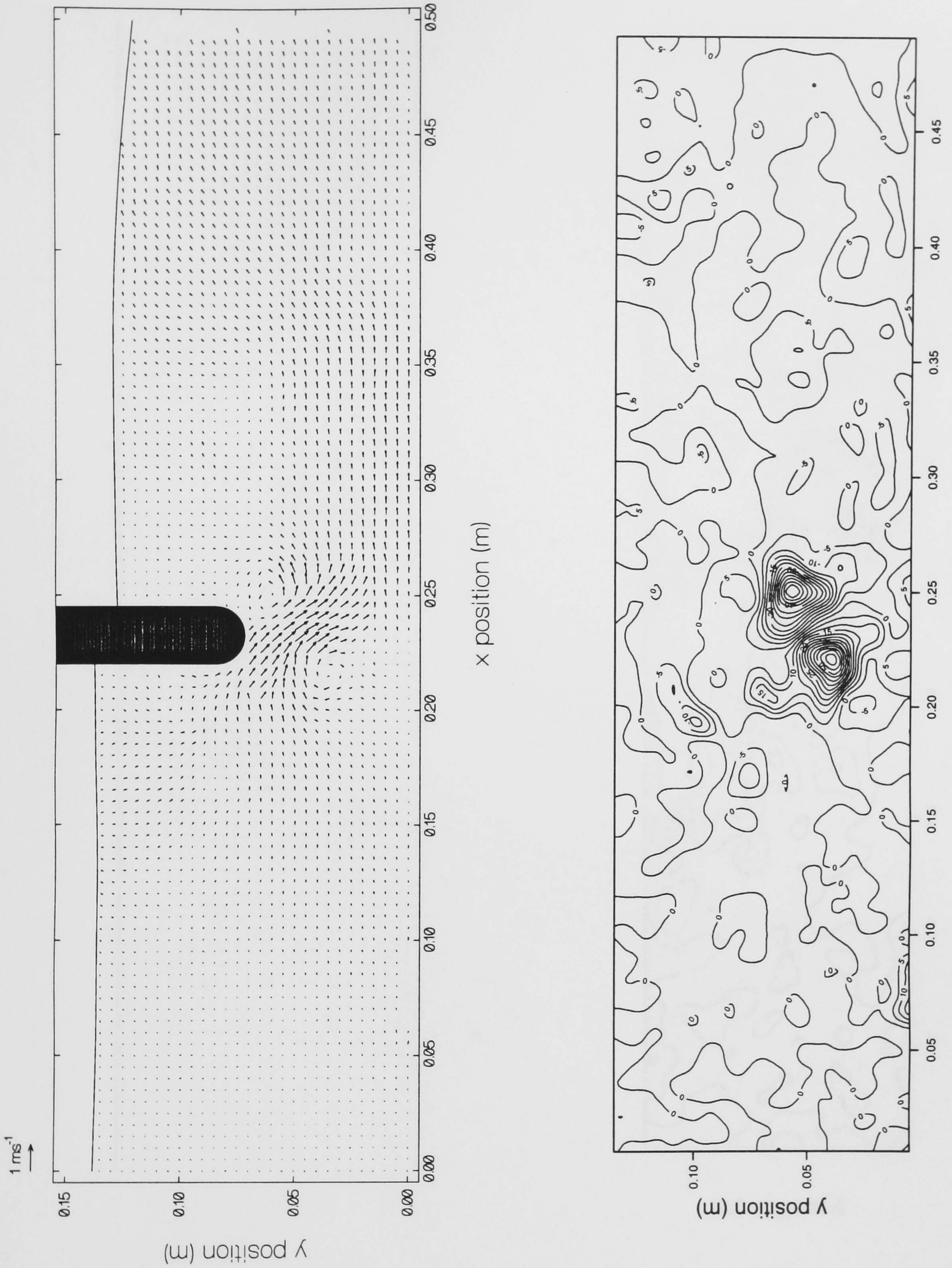

FIGURE 6.33: Velocity and vorticity maps of wave incident on OWC, frequency=0.547Hz, time=0.914s

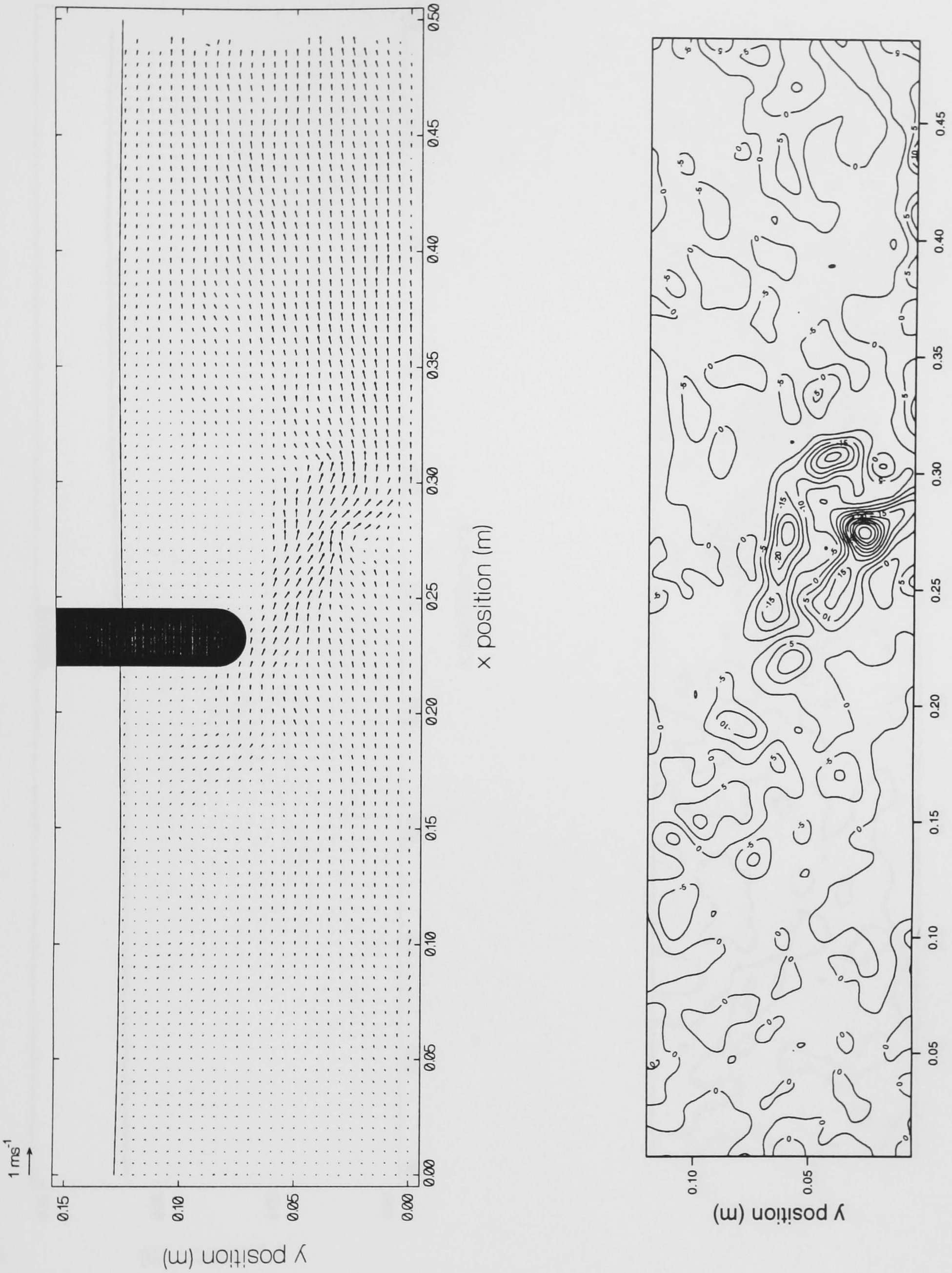

FIGURE 6.34: Velocity and vorticity maps of wave incident on OWC, frequency=0.547Hz, time=1.097s

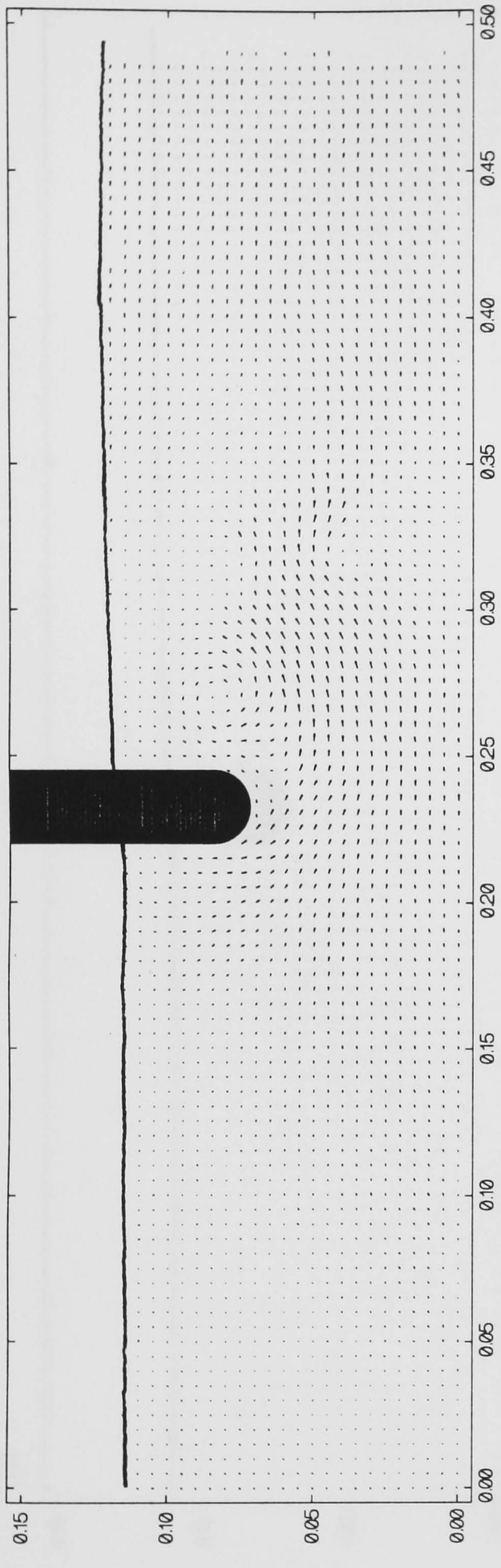

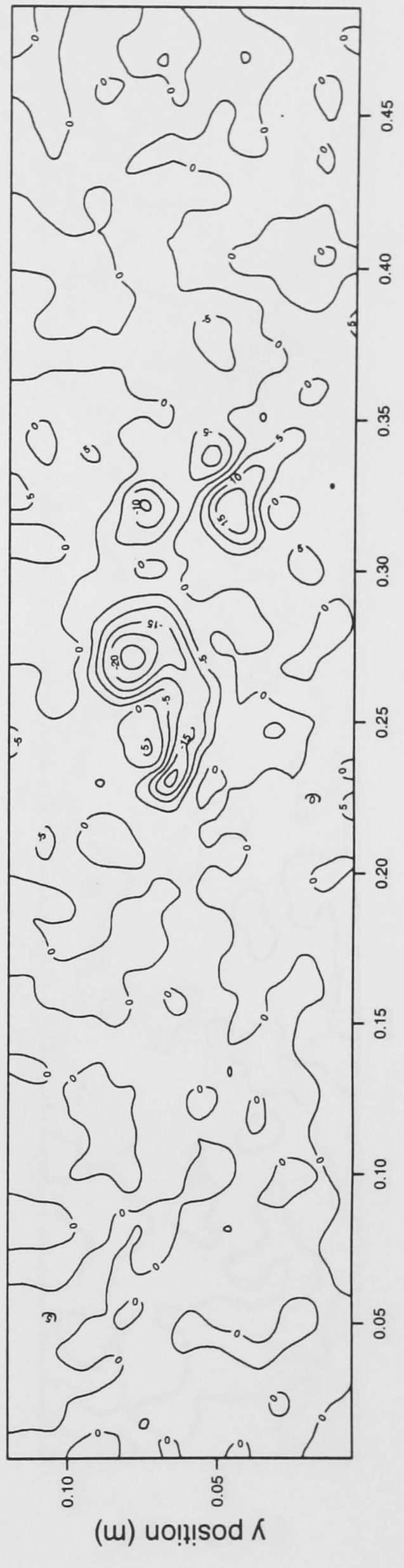

FIGURE 6.35: Velocity and vorticity maps of wave incident on OWC, frequency=0.547Hz, time=1.279s

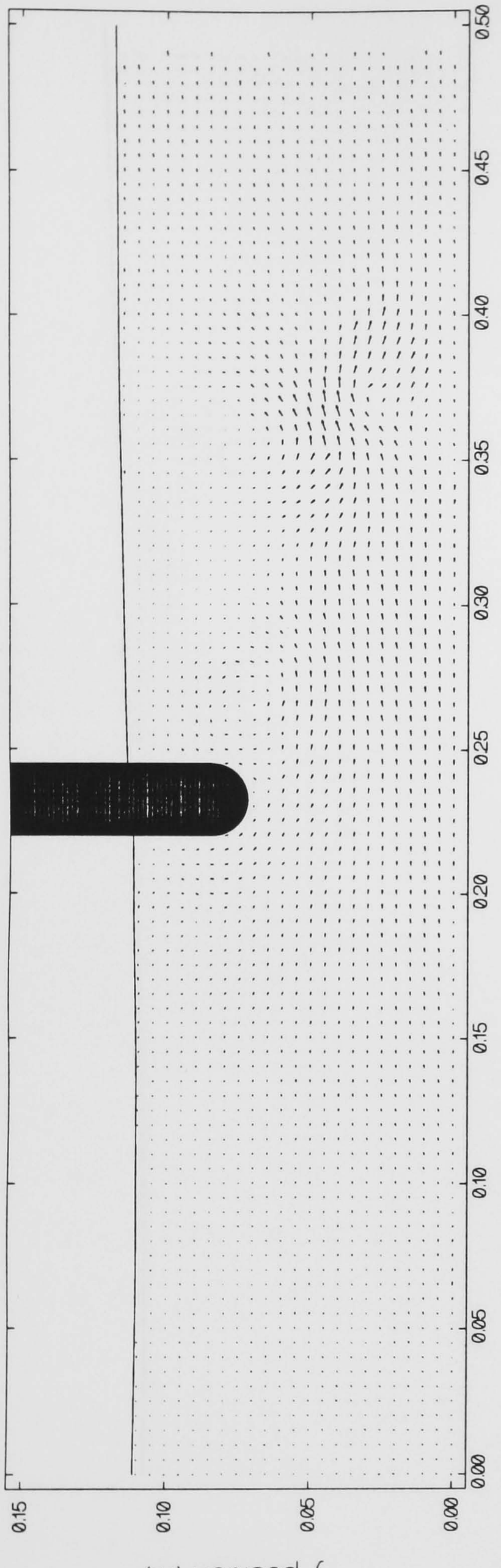

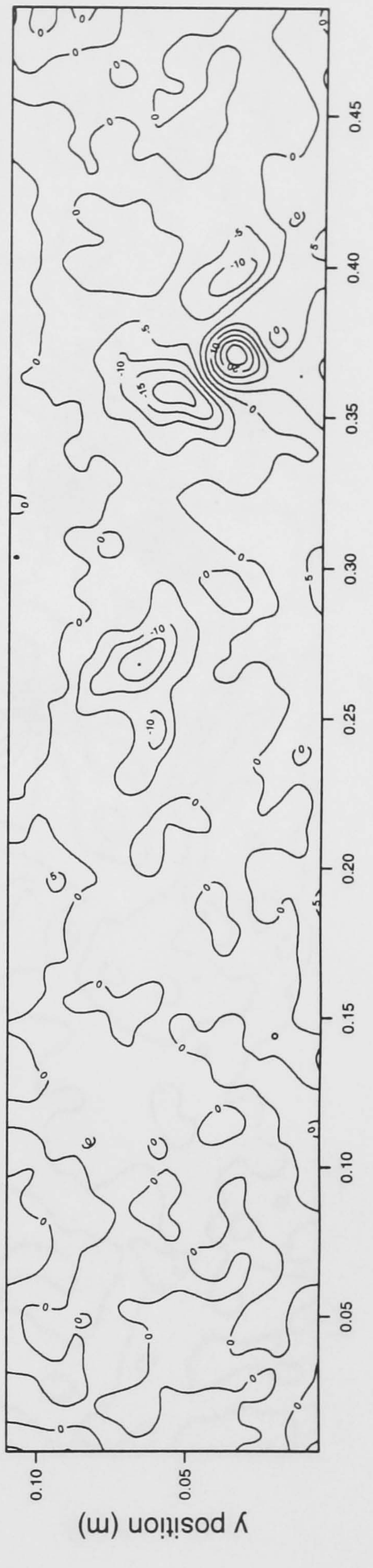

FIGURE 6.36: Velocity and vorticity maps of wave incident on OWC, frequency=0.547Hz, time=1.462s

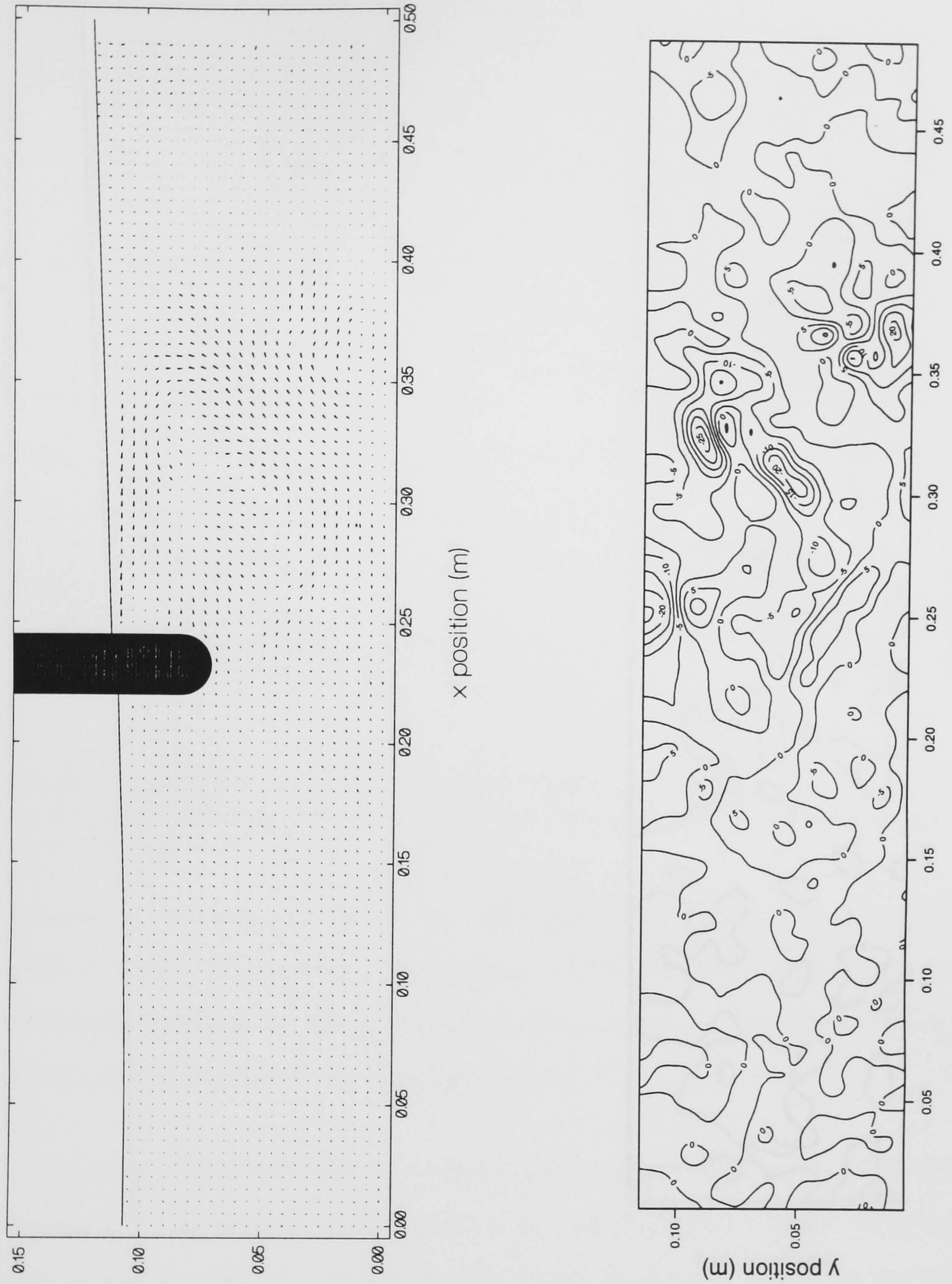

FIGURE 6.37: Velocity and vorticity maps of wave incident on OWC, frequency=0.547Hz, time=1.645s

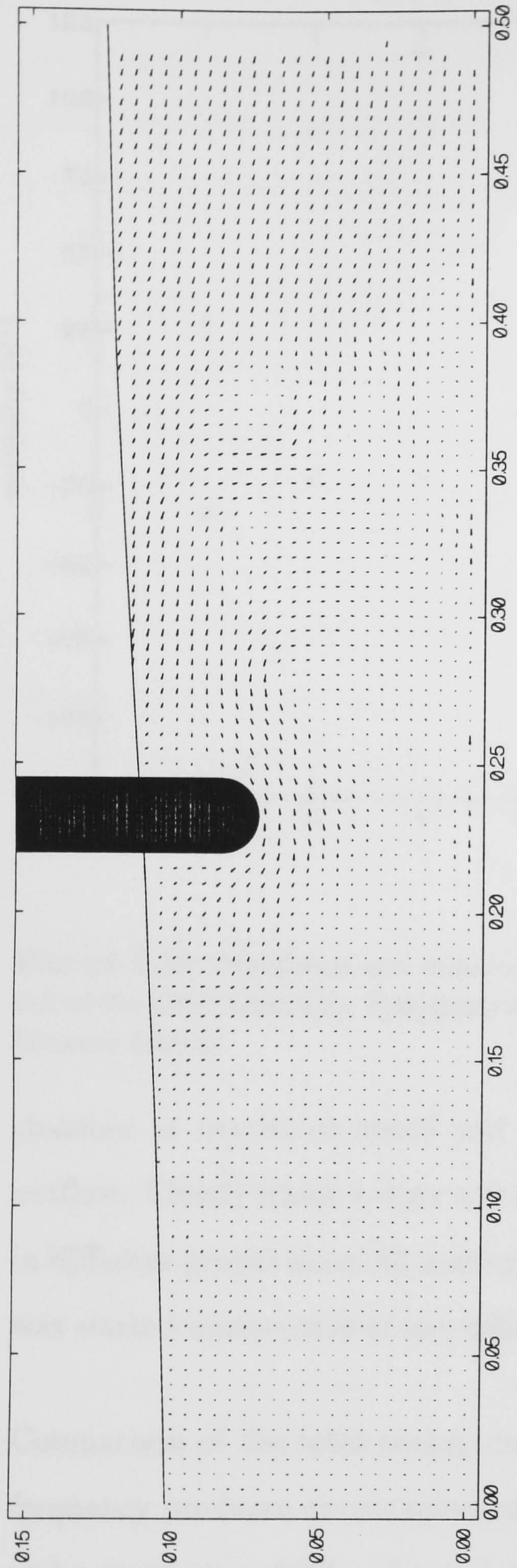

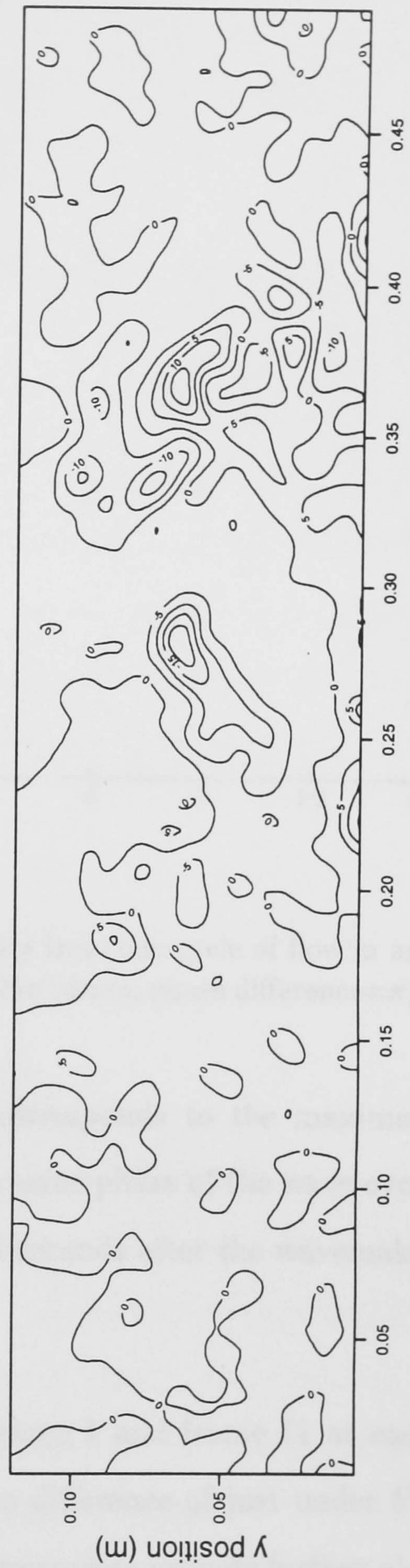

FIGURE 6.38: Velocity and vorticity maps of wave incident on OWC, frequency=0.547Hz, time=1.828s

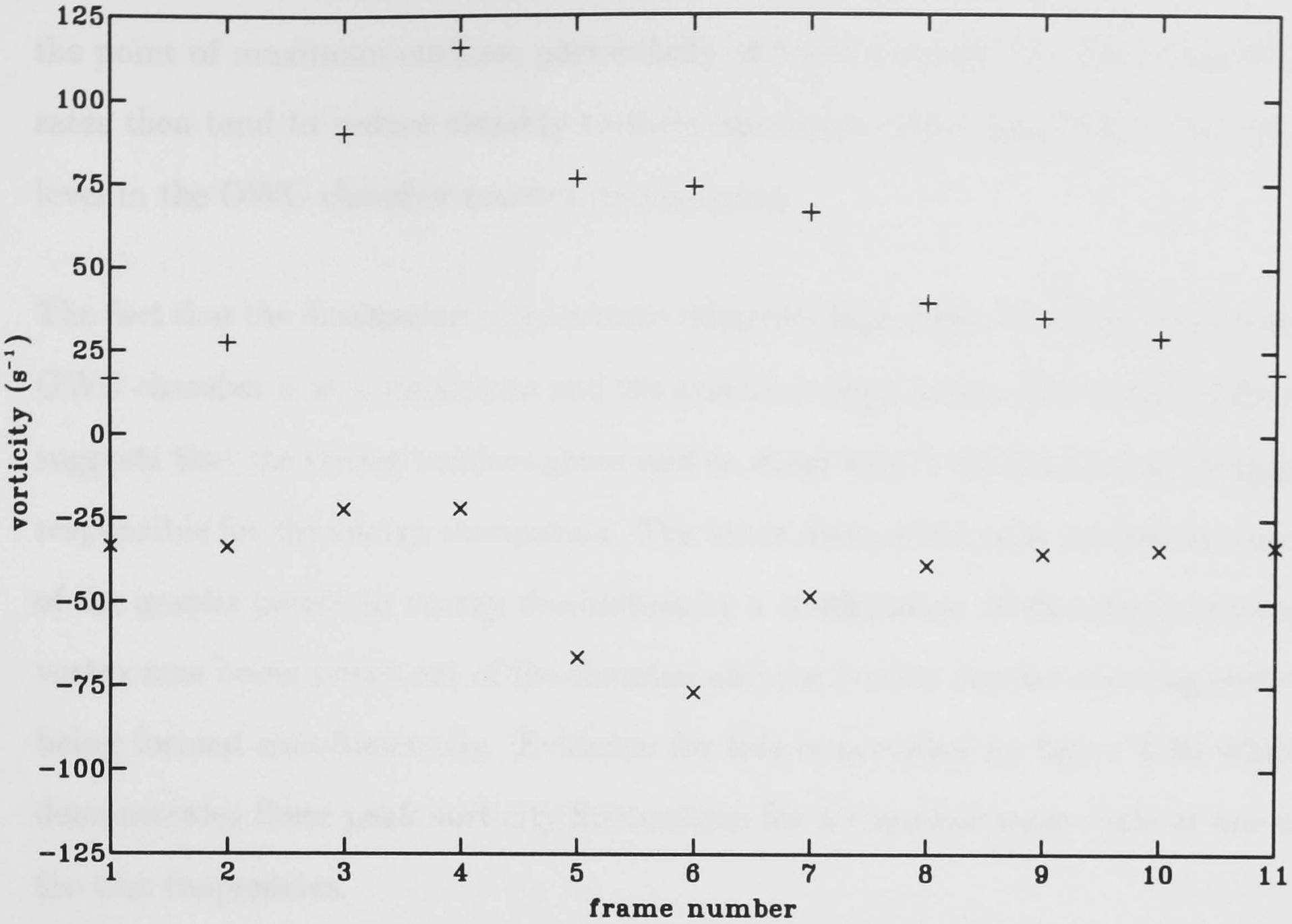

FIGURE 6.39: Maximum and minimum values of vorticity from one cycle of flow in and out of the OWC chamber. Frequency=0.547Hz, orifice=25×25mm, phase difference=$\pi/5$ between frames

chamber at maximum speed and the other peak corresponds to the maximum outflow. Clearly frame 1 does not correspond to the same phase of the wave cycle in different graphs since all measurements began 30 seconds after the wavemaker was started irrespective of any other parameters.

Comparison of the total energy calculations from frame 1 and frame 11 at each frequency produces encouraging results with a mean difference of just under 5% and a worst case of 8% in figure 6.45. These good agreements provide further vindication of the experimental technique and the confidence placed upon the ability to produce repeatable waves in the flume after lengthy settling periods.

In general the energy dissipation rates peak at about the time of maximum flow

into the OWC chamber and a second, smaller peak is often apparent just prior to the point of maximum outflow, particularly at lower frequencies. The dissipation rates then tend to reduce steadily to their minimum values just before the water level in the OWC chamber reaches its minimum.

The fact that the dissipation rates remain relatively high when the water level in the OWC chamber is at a maximum and the kinetic energy curves show local minima, suggests that the strong vortices generated as water enters the chamber are largely responsible for the energy dissipation. The lower dissipation peak evident in many of the graphs points to energy dissipation by a combination of the original strong vortex now being swept out of the chamber and the weaker counter-rotating vortex being formed simultaneously. Evidence for this is provided by figure 6.39 which demonstrates these peak vorticity fluctuations for a complete wave cycle at one of the test frequencies.

As the wave frequency increases the strength of the vortices reduces and on observation of the flow at the top end of the frequency range, it appears as if the outflow from the chamber is just a mirror image of the inflow.

The variation of mean viscous dissipation with frequency is shown in figure 6.54. These values are simply calculated by averaging over one wave cycle and the comparison with the wave power reaching the OWC chamber (see figure 6.5) also calculated. These results show that the proportion of wave power lost due to viscous dissipation varies between a maximum of about 7% at the lowest test frequency to a minimum of just under 1.5% at the highest frequency.

These proportions of dissipation demonstrate qualitative agreement with the losses shown in figure 6.14 although clearly there are additional mechanisms resulting in energy dissipation, such as friction at the walls and base of the OWC model and losses resulting from the flow of air in and out of the orifice.

With a typical OWC prototype working at a conversion efficiency of about 40% in the wave power to air power phase [53], these results are very significant and suggest that gains could be made by simply designing a chamber to minimise vortex formation. This may be easily achieved by profiling the front wall of the chamber to be the same shape as the main stream of water into the device.

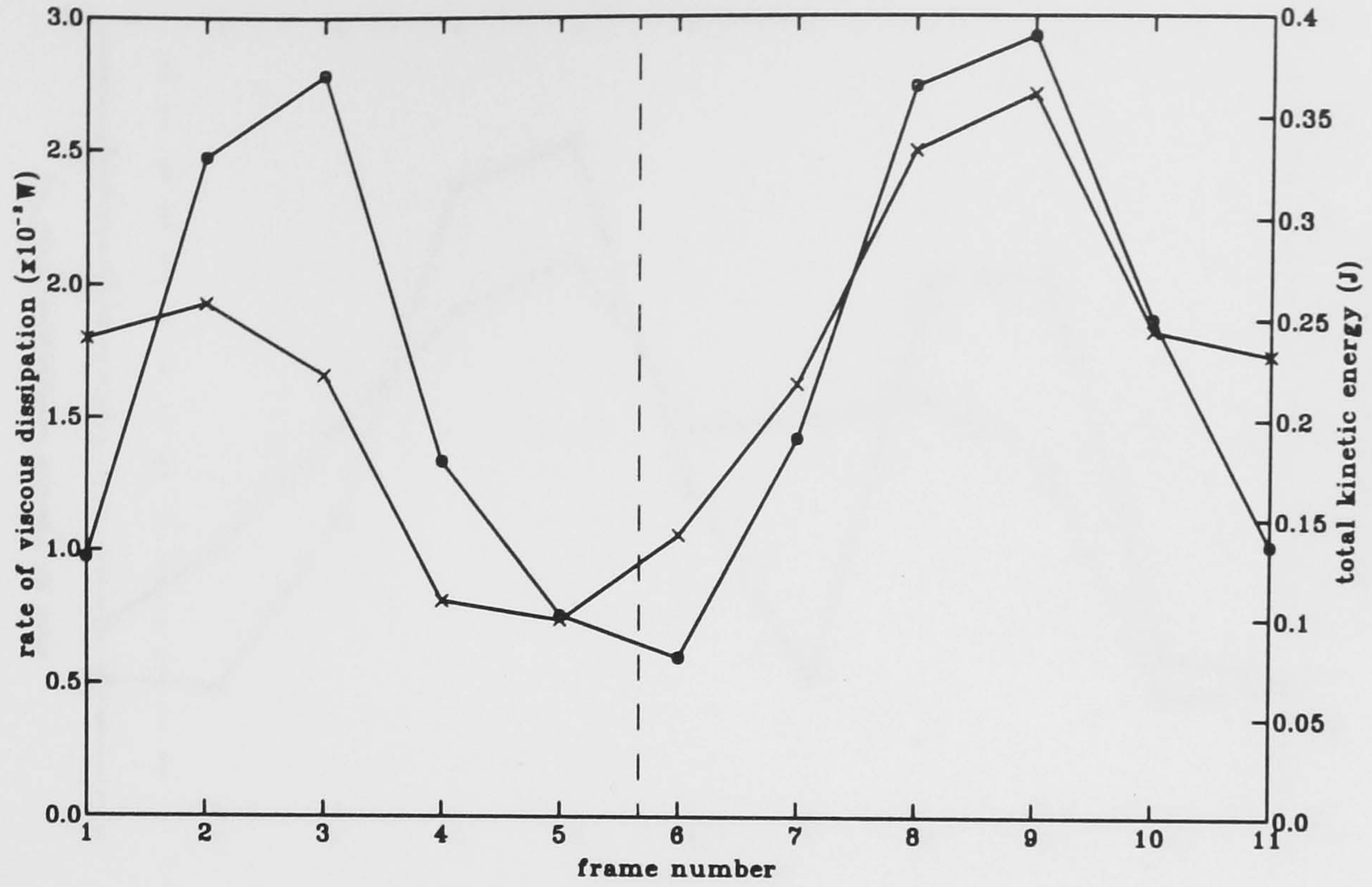

FIGURE 6.40: Total rate of viscous dissipation ($\times$) and total kinetic energy ($\circ$) calculated from PIV measurements of flow velocities into and out of the OWC chamber. Orifice = 25×25mm, frequency = 0.469Hz, phase difference between frames = $\pi/5$. The vertical broken line marks the time of minimum chamber water elevation.

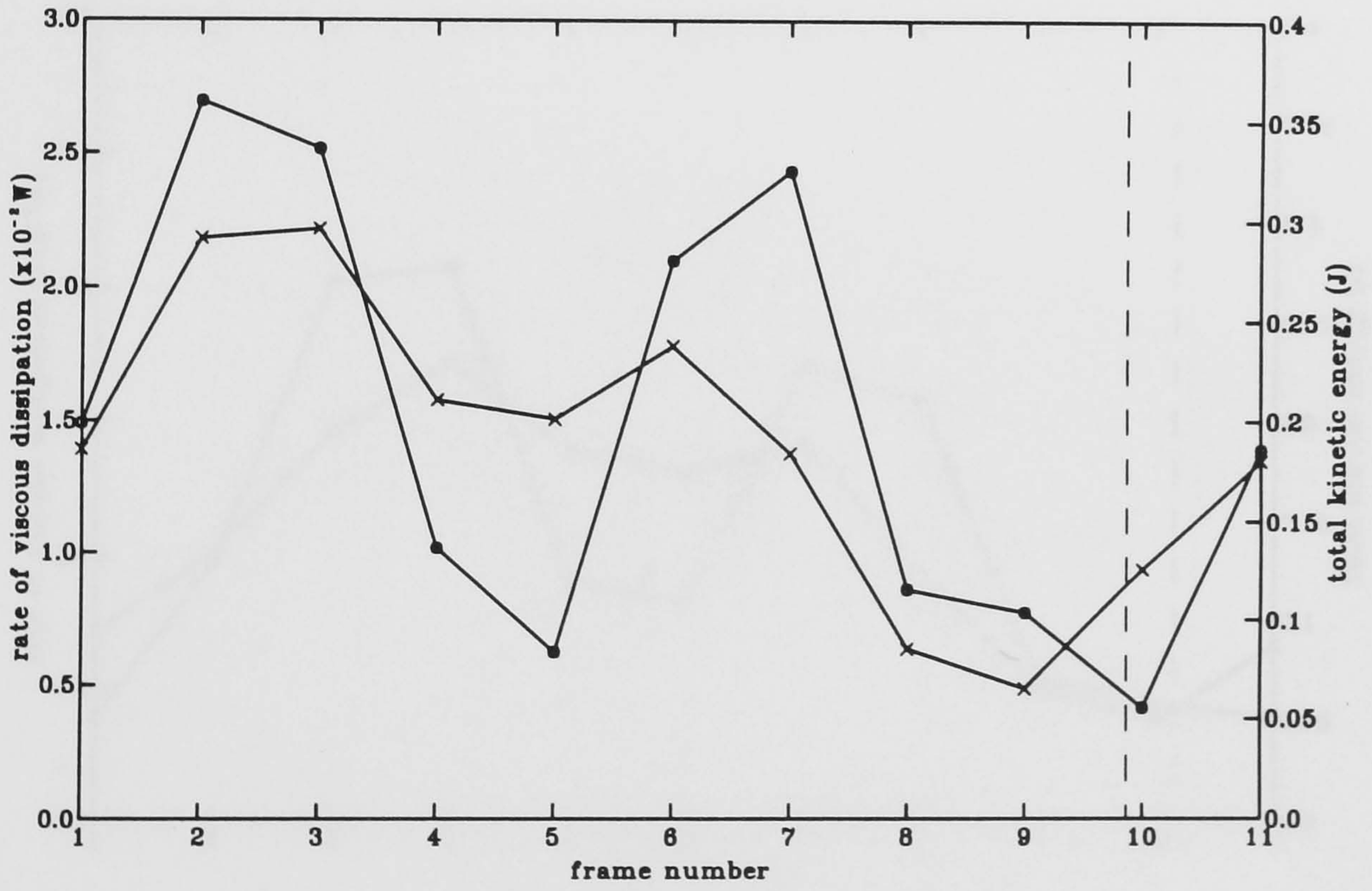

FIGURE 6.41: Total rate of viscous dissipation ($\times$) and total kinetic energy ($\circ$) calculated from PIV measurements of flow velocities into and out of the OWC chamber. Orifice = 25×25mm, frequency = 0.547Hz, phase difference between frames = $\pi/5$. The vertical broken line marks the time of minimum chamber water elevation.

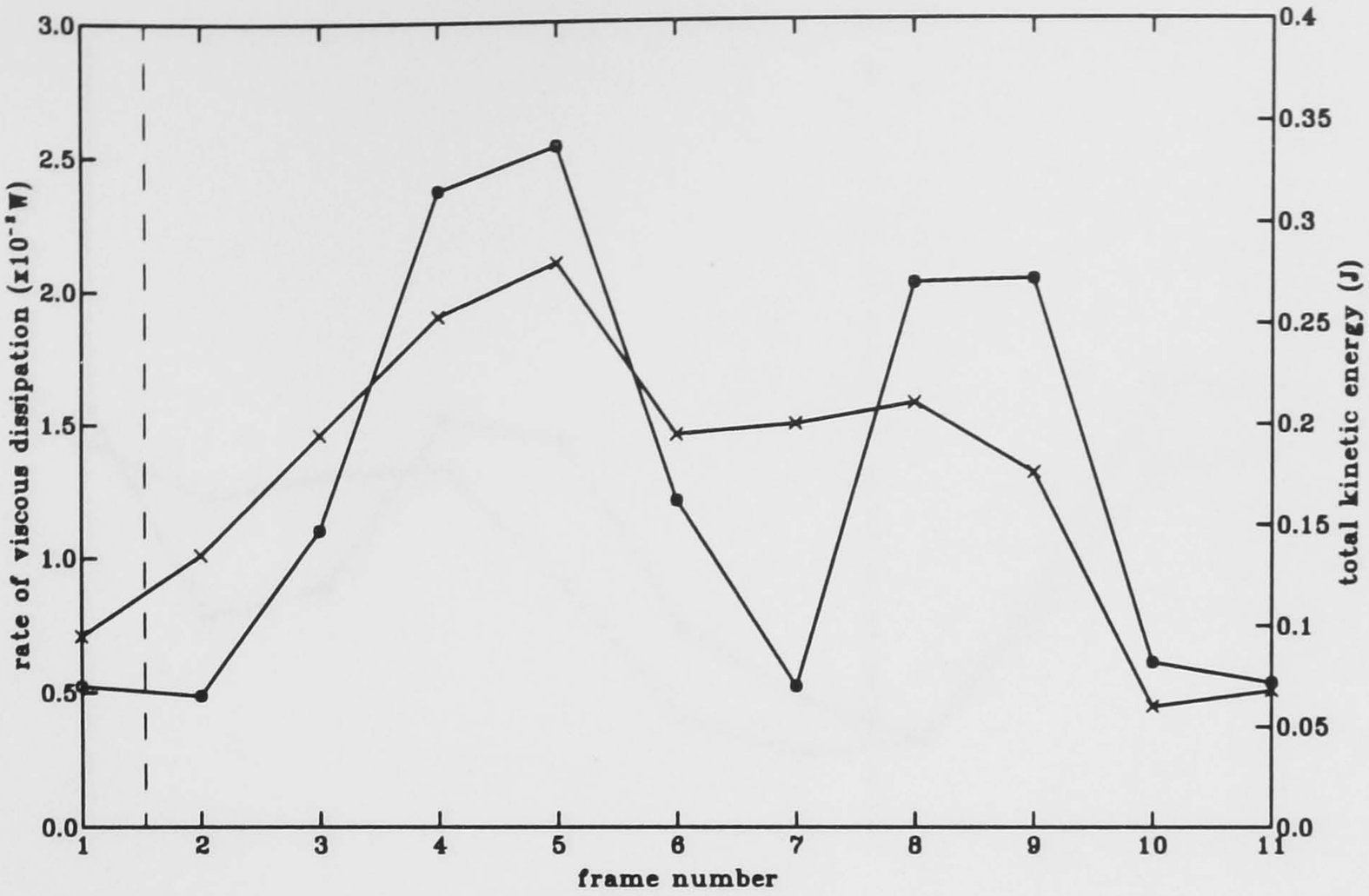

FIGURE 6.42: Total rate of viscous dissipation ($\times$) and total kinetic energy ($\circ$) calculated from PIV measurements of flow velocities into and out of the OWC chamber. Orifice = 25$\times$25mm, frequency = 0.625Hz, phase difference between frames = $\pi/5$. The vertical broken line marks the time of minimum chamber water elevation.

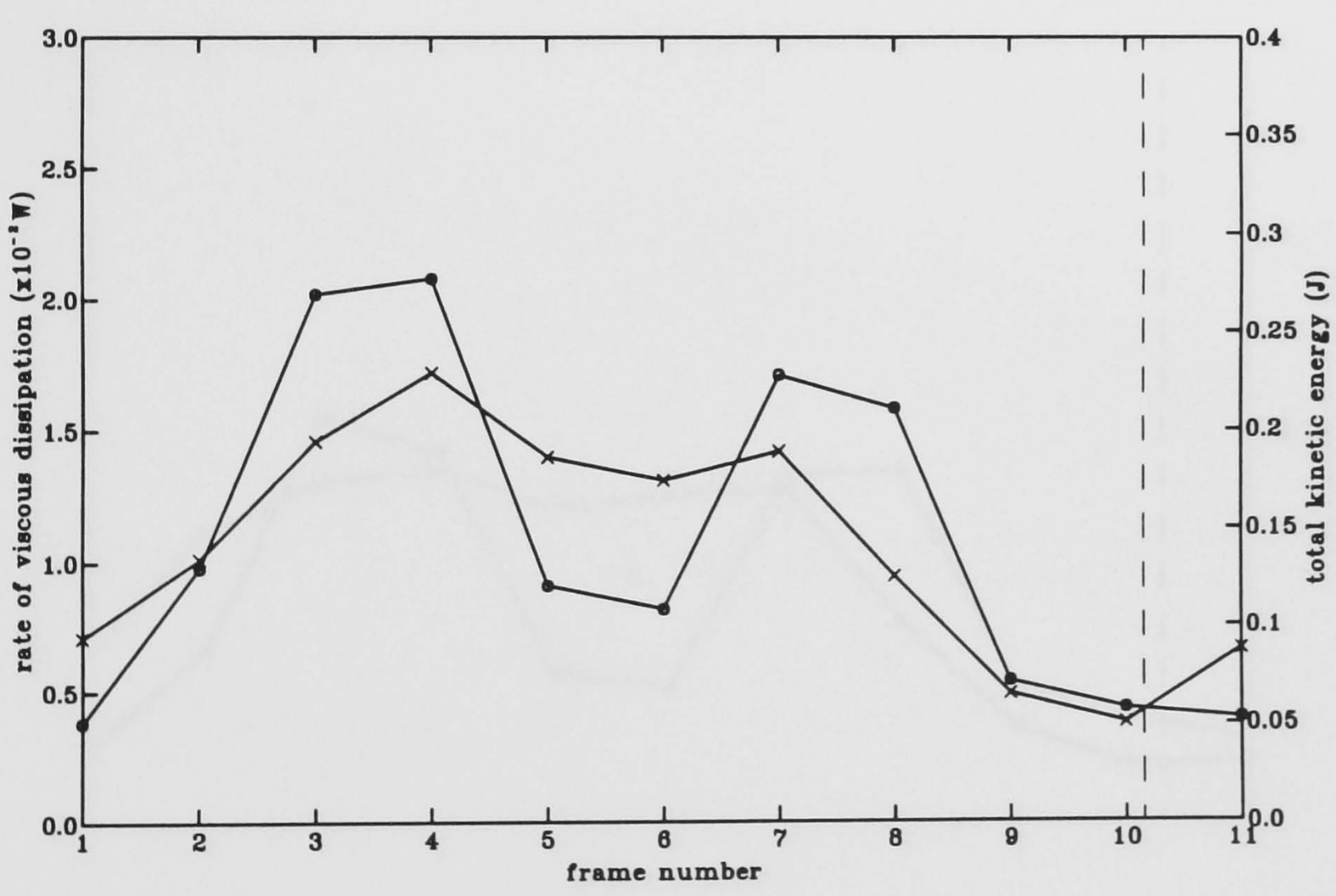

FIGURE 6.43: Total rate of viscous dissipation ($\times$) and total kinetic energy ($\circ$) calculated from PIV measurements of flow velocities into and out of the OWC chamber. Orifice = 25$\times$25mm, frequency = 0.703Hz, phase difference between frames = $\pi/5$. The vertical broken line marks the time of minimum chamber water elevation.

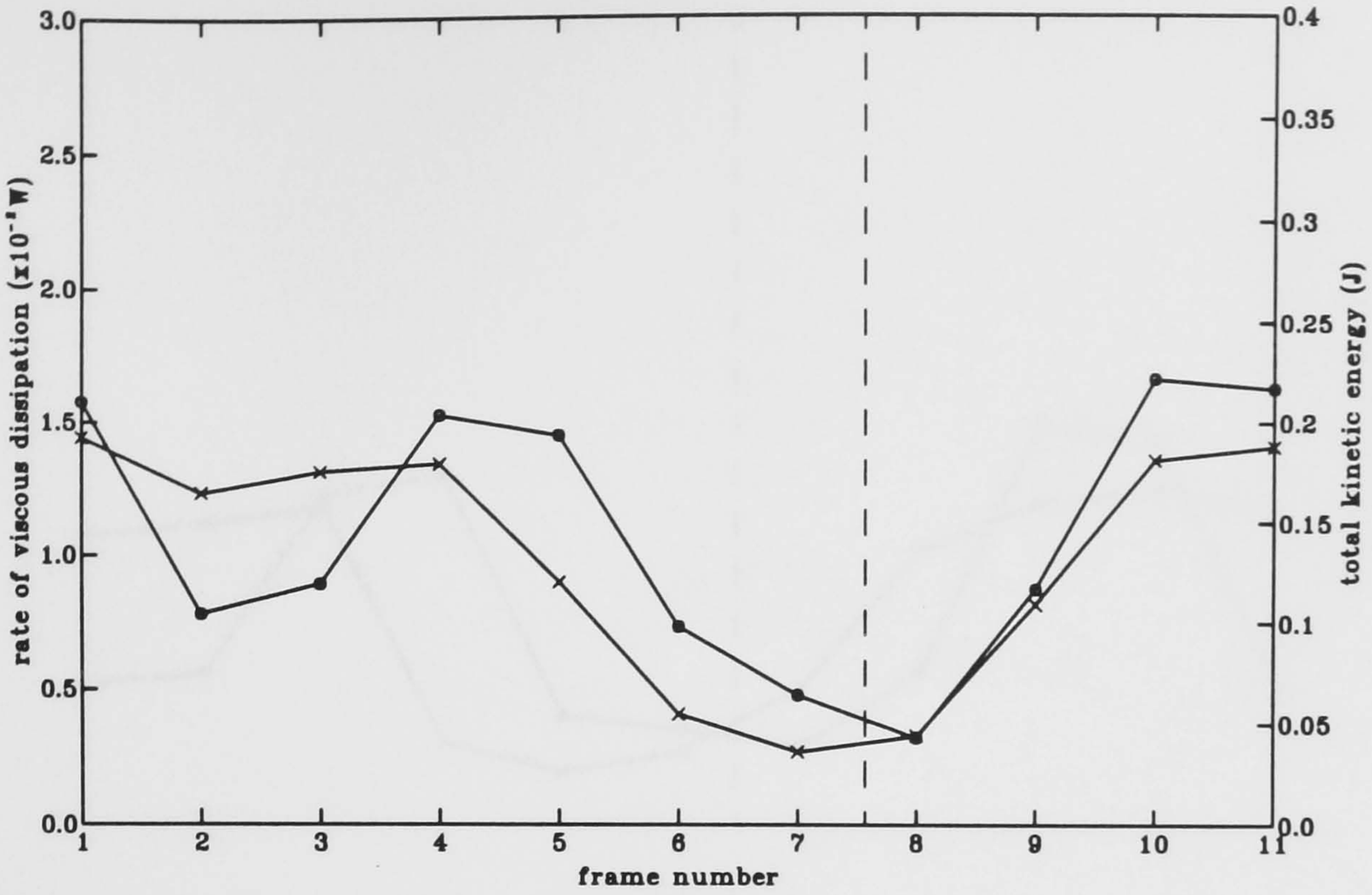

FIGURE 6.44: Total rate of viscous dissipation ($\times$) and total kinetic energy ($\circ$) calculated from PIV measurements of flow velocities into and out of the OWC chamber. Orifice = 25×25mm, frequency = 0.781Hz, phase difference between frames = $\pi/5$. The vertical broken line marks the time of minimum chamber water elevation.

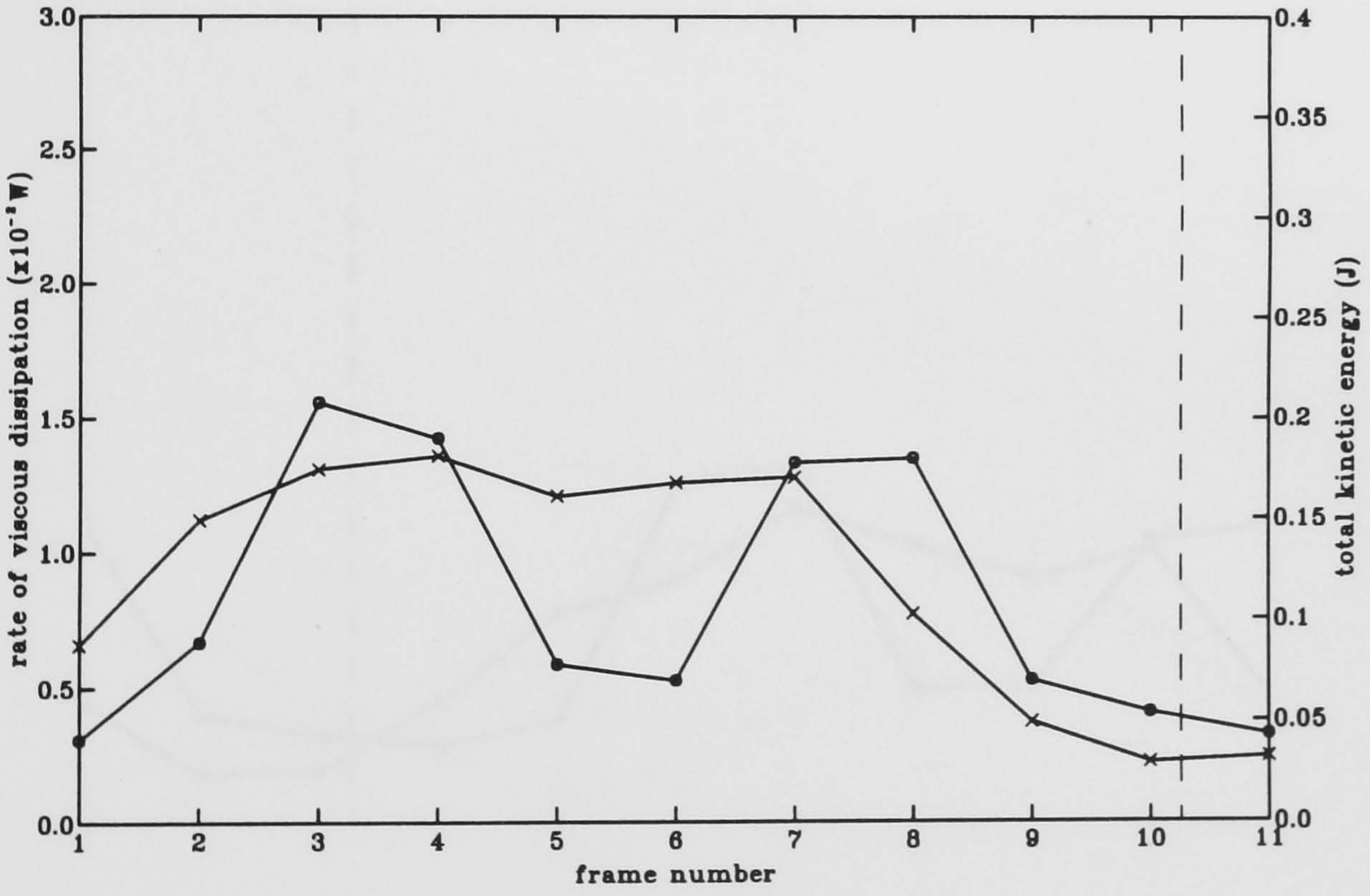

FIGURE 6.45: Total rate of viscous dissipation ($\times$) and total kinetic energy ($\circ$) calculated from PIV measurements of flow velocities into and out of the OWC chamber. Orifice = 25×25mm, frequency = 0.860Hz, phase difference between frames = $\pi/5$. The vertical broken line marks the time of minimum chamber water elevation.

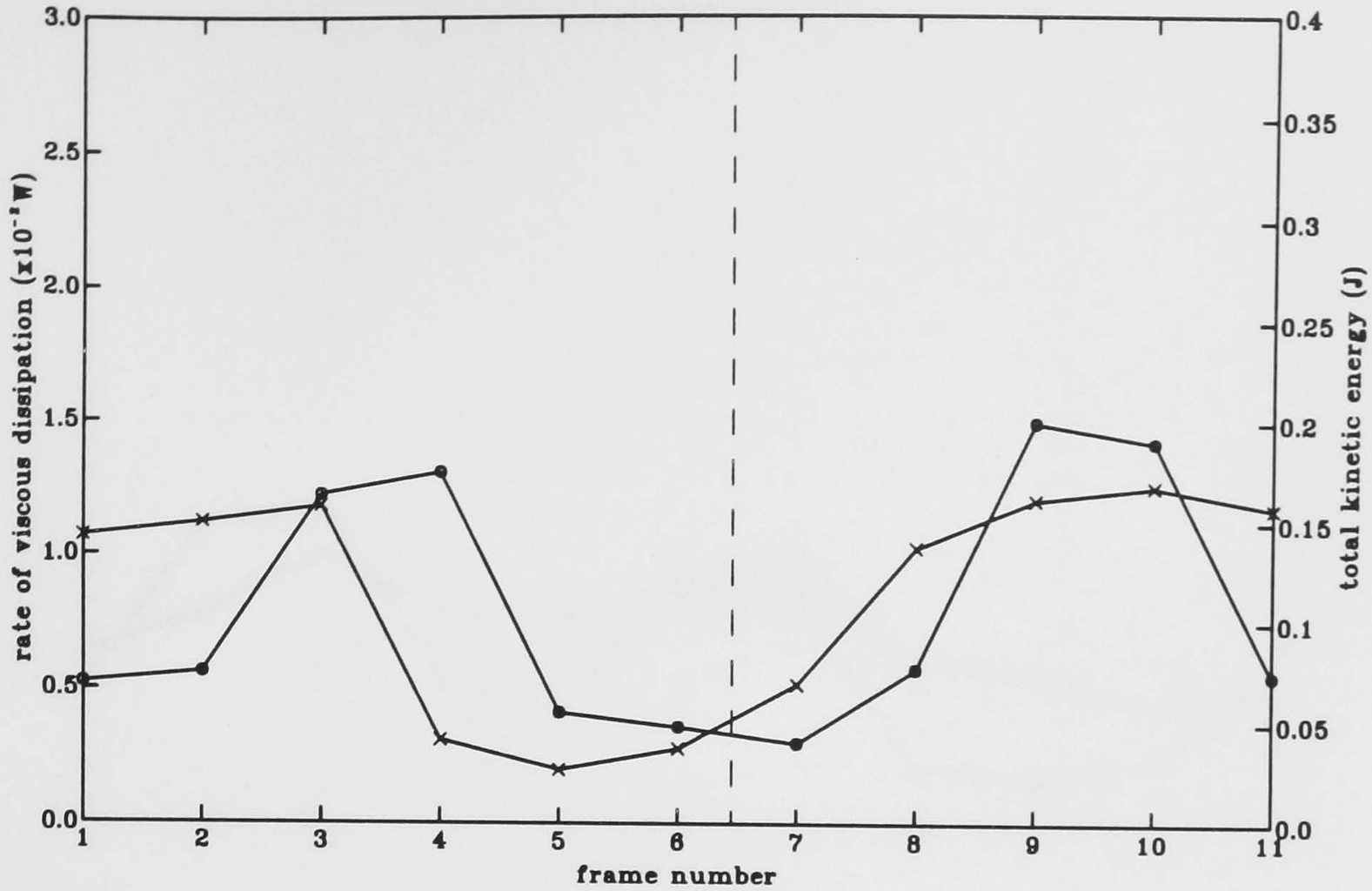

FIGURE 6.46: Total rate of viscous dissipation ($\times$) and total kinetic energy ($\circ$) calculated from PIV measurements of flow velocities into and out of the OWC chamber. Orifice = 25×25mm, frequency = 0.938Hz, phase difference between frames = $\pi/5$. The vertical broken line marks the time of minimum chamber water elevation.

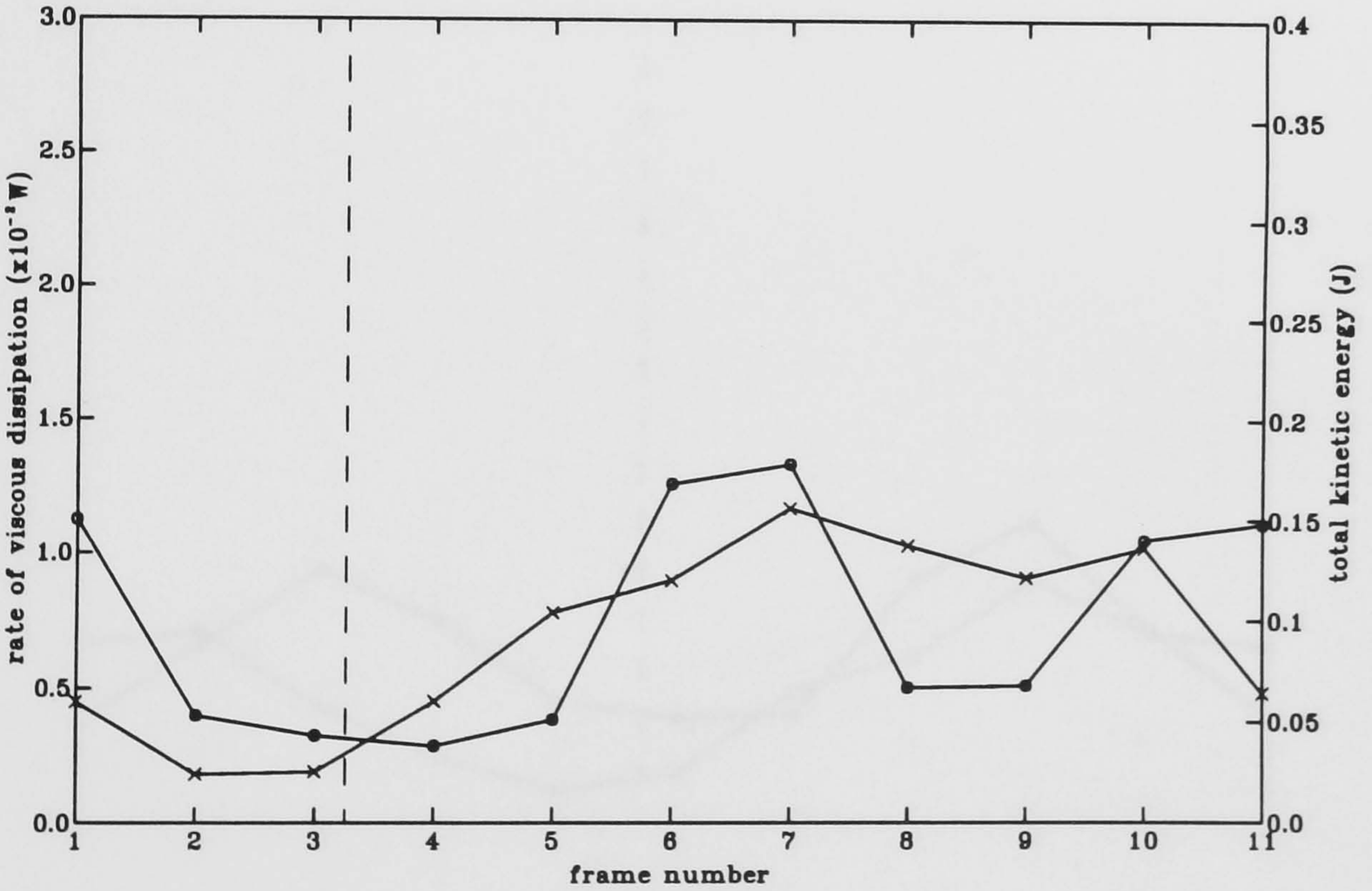

FIGURE 6.47: Total rate of viscous dissipation ($\times$) and total kinetic energy ($\circ$) calculated from PIV measurements of flow velocities into and out of the OWC chamber. Orifice = 25×25mm, frequency = 1.016Hz, phase difference between frames = $\pi/5$. The vertical broken line marks the time of minimum chamber water elevation.

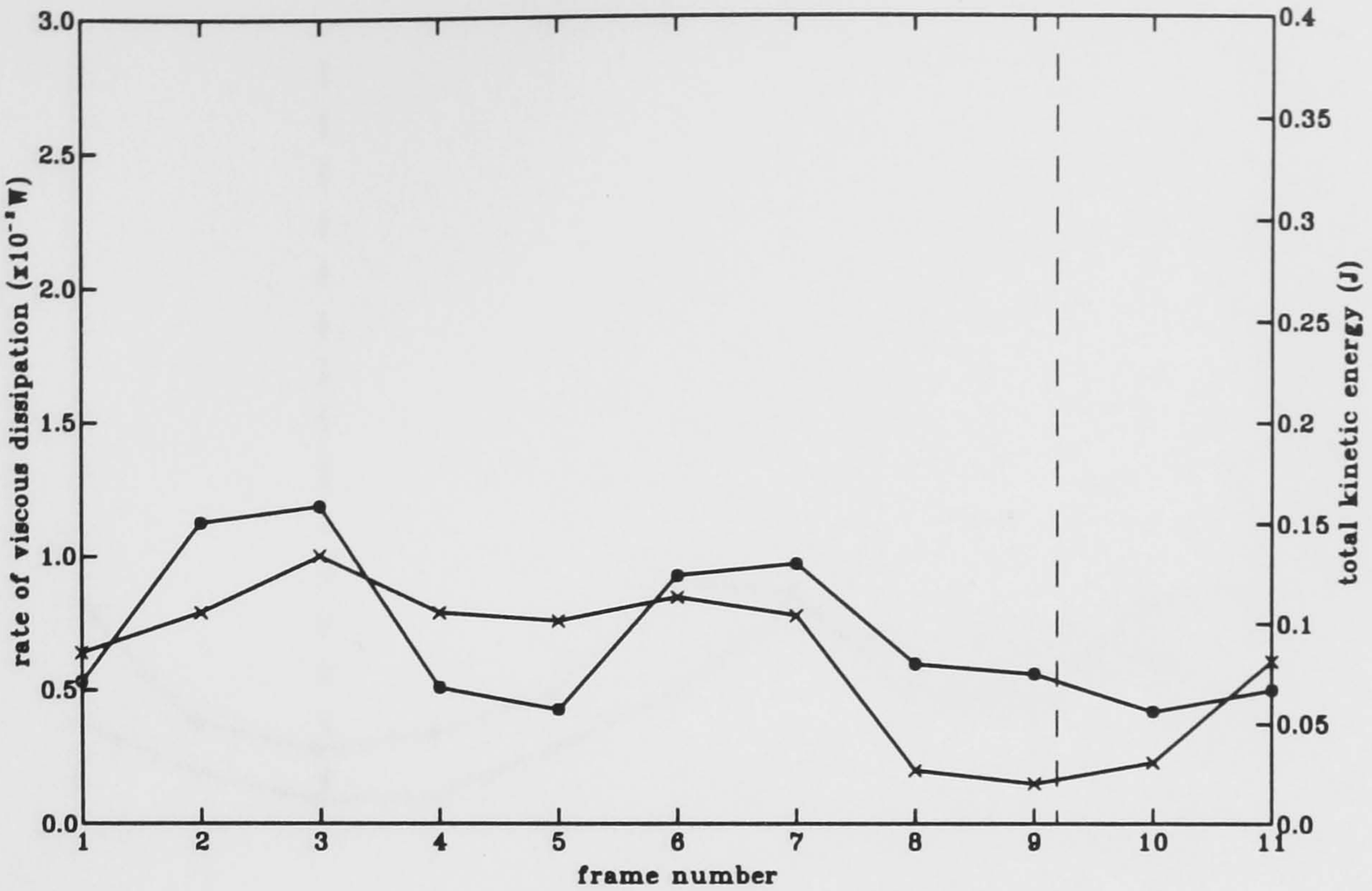

FIGURE 6.48: Total rate of viscous dissipation ($\times$) and total kinetic energy ($\circ$) calculated from PIV measurements of flow velocities into and out of the OWC chamber. Orifice = 25$\times$25mm, frequency = 1.094Hz, phase difference between frames = $\pi/5$. The vertical broken line marks the time of minimum chamber water elevation.

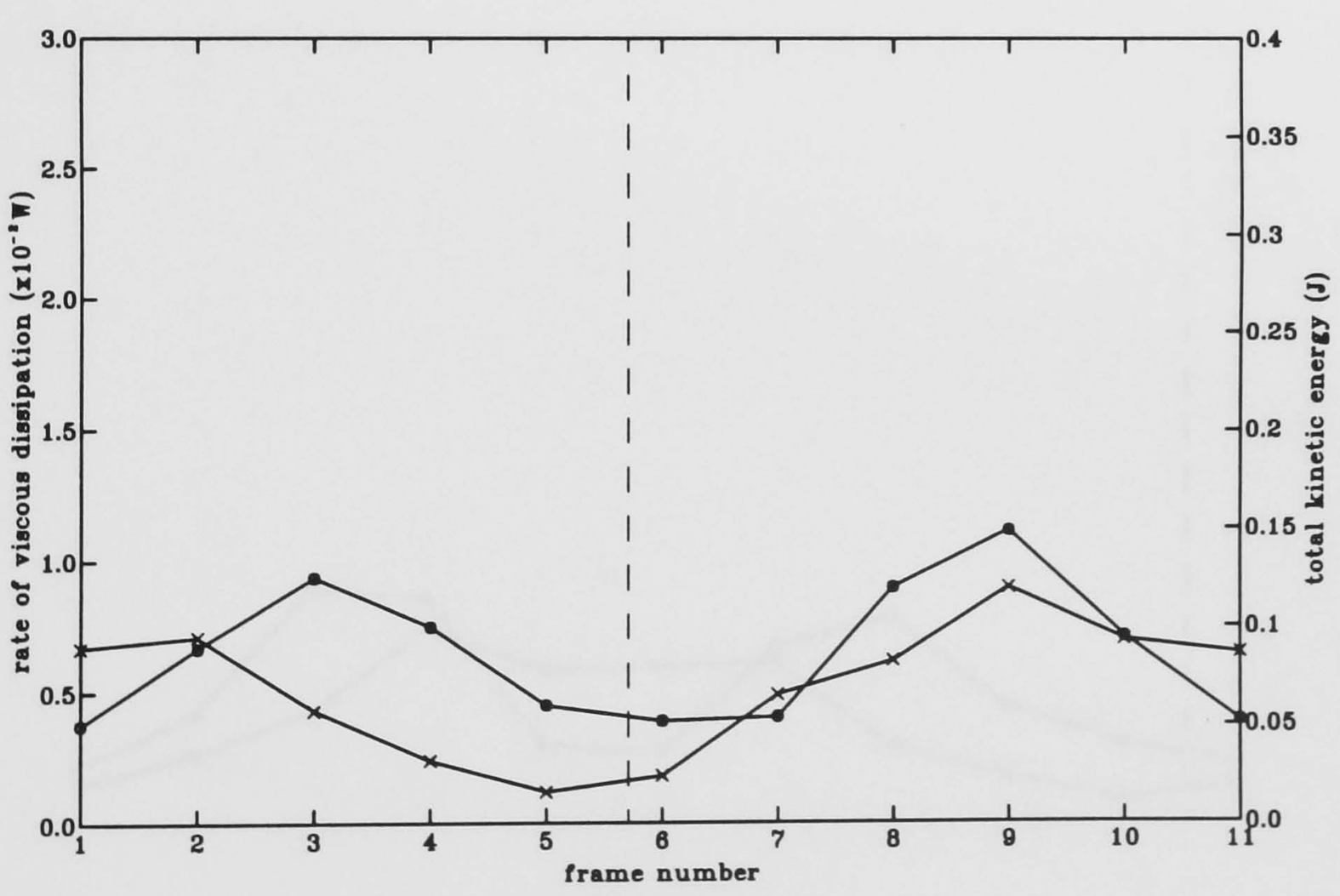

FIGURE 6.49: Total rate of viscous dissipation ($\times$) and total kinetic energy ($\circ$) calculated from PIV measurements of flow velocities into and out of the OWC chamber. Orifice = 25$\times$25mm, frequency = 1.172Hz, phase difference between frames = $\pi/5$. The vertical broken line marks the time of minimum chamber water elevation.

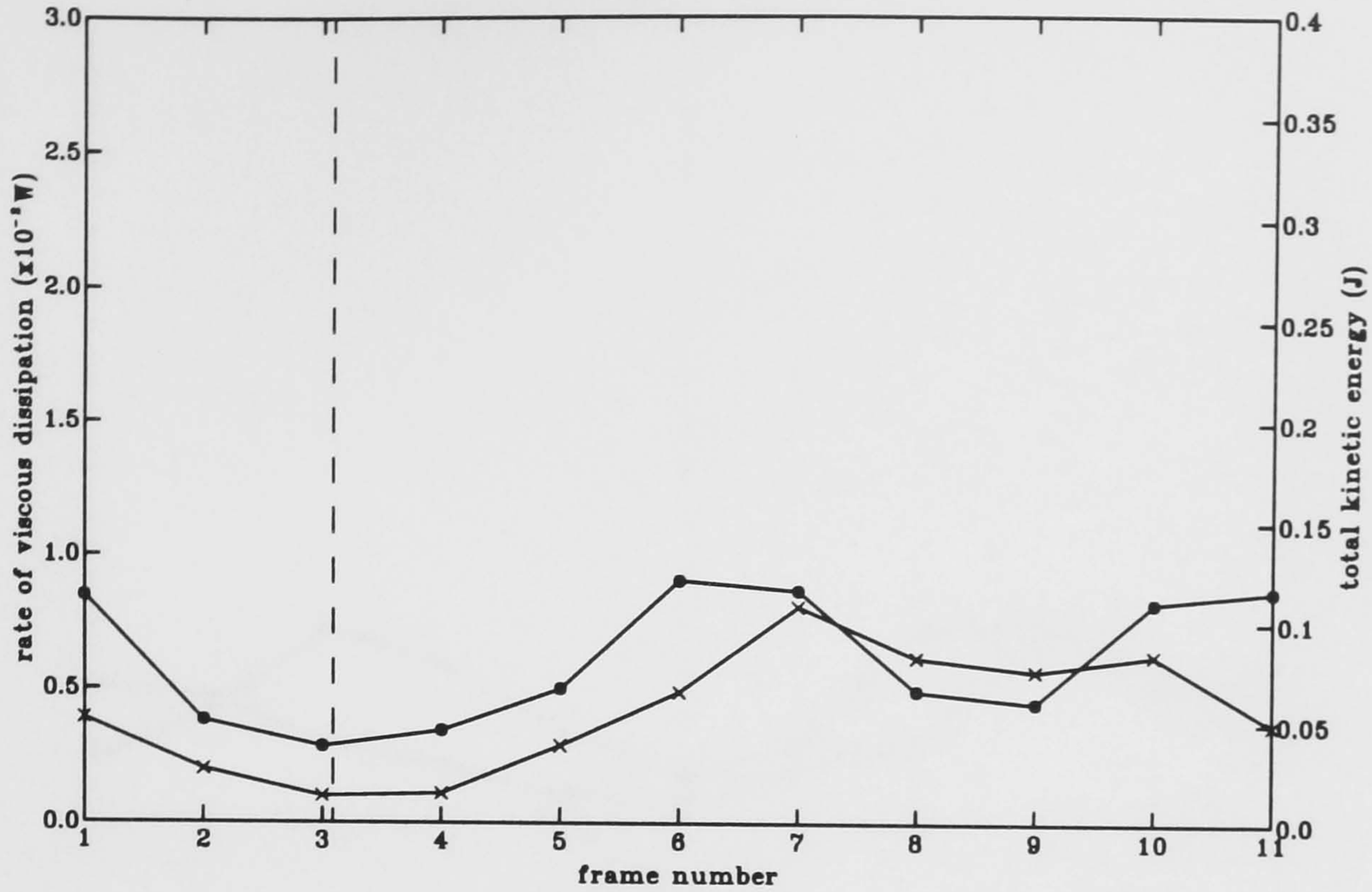

FIGURE 6.50: Total rate of viscous dissipation ($\times$) and total kinetic energy ($\circ$) calculated from PIV measurements of flow velocities into and out of the OWC chamber. Orifice = 25×25mm, frequency = 1.250Hz, phase difference between frames = $\pi/5$. The vertical broken line marks the time of minimum chamber water elevation.

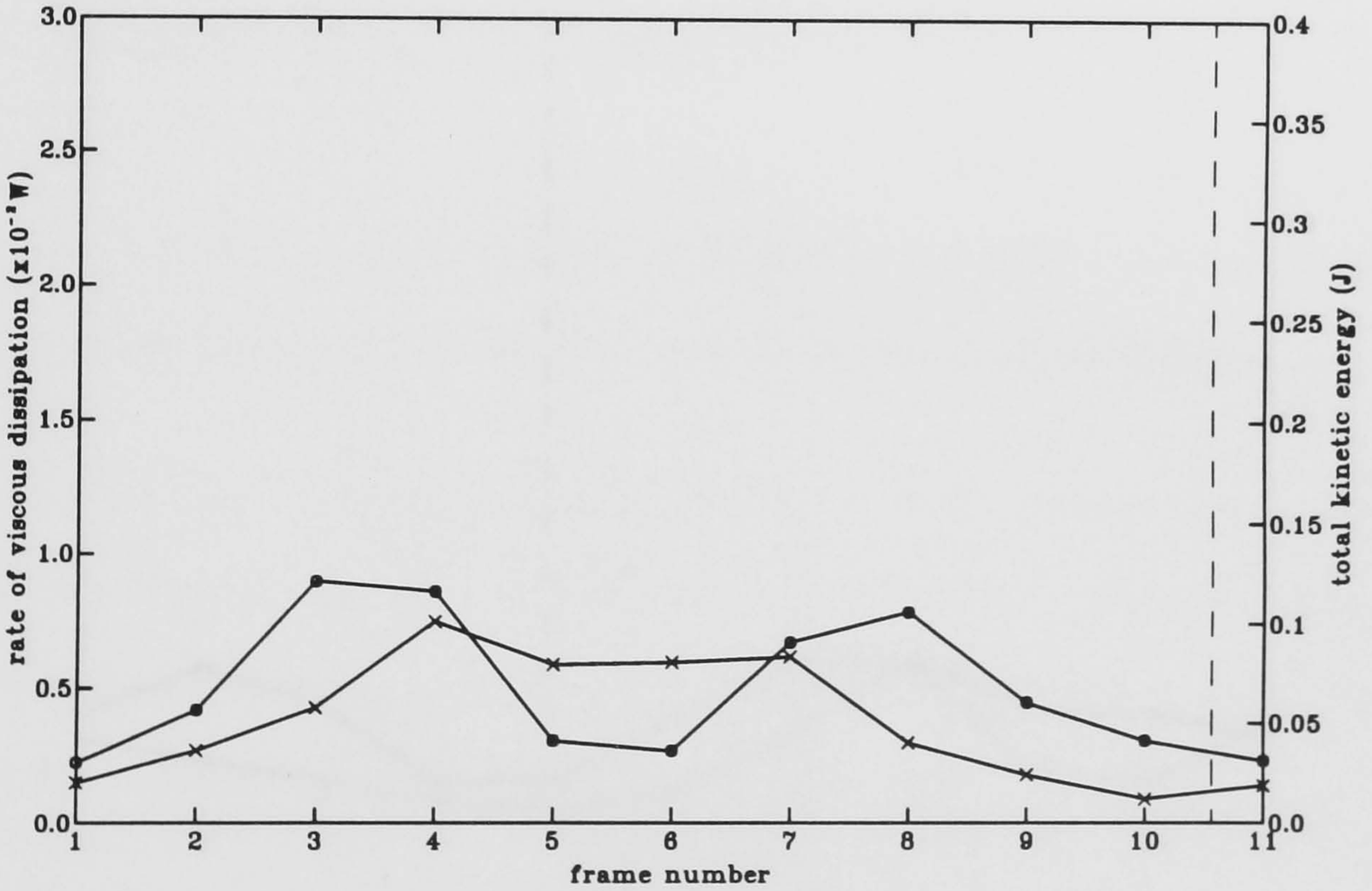

FIGURE 6.51: Total rate of viscous dissipation ($\times$) and total kinetic energy ($\circ$) calculated from PIV measurements of flow velocities into and out of the OWC chamber. Orifice = 25×25mm, frequency = 1.328Hz, phase difference between frames = $\pi/5$. The vertical broken line marks the time of minimum chamber water elevation.

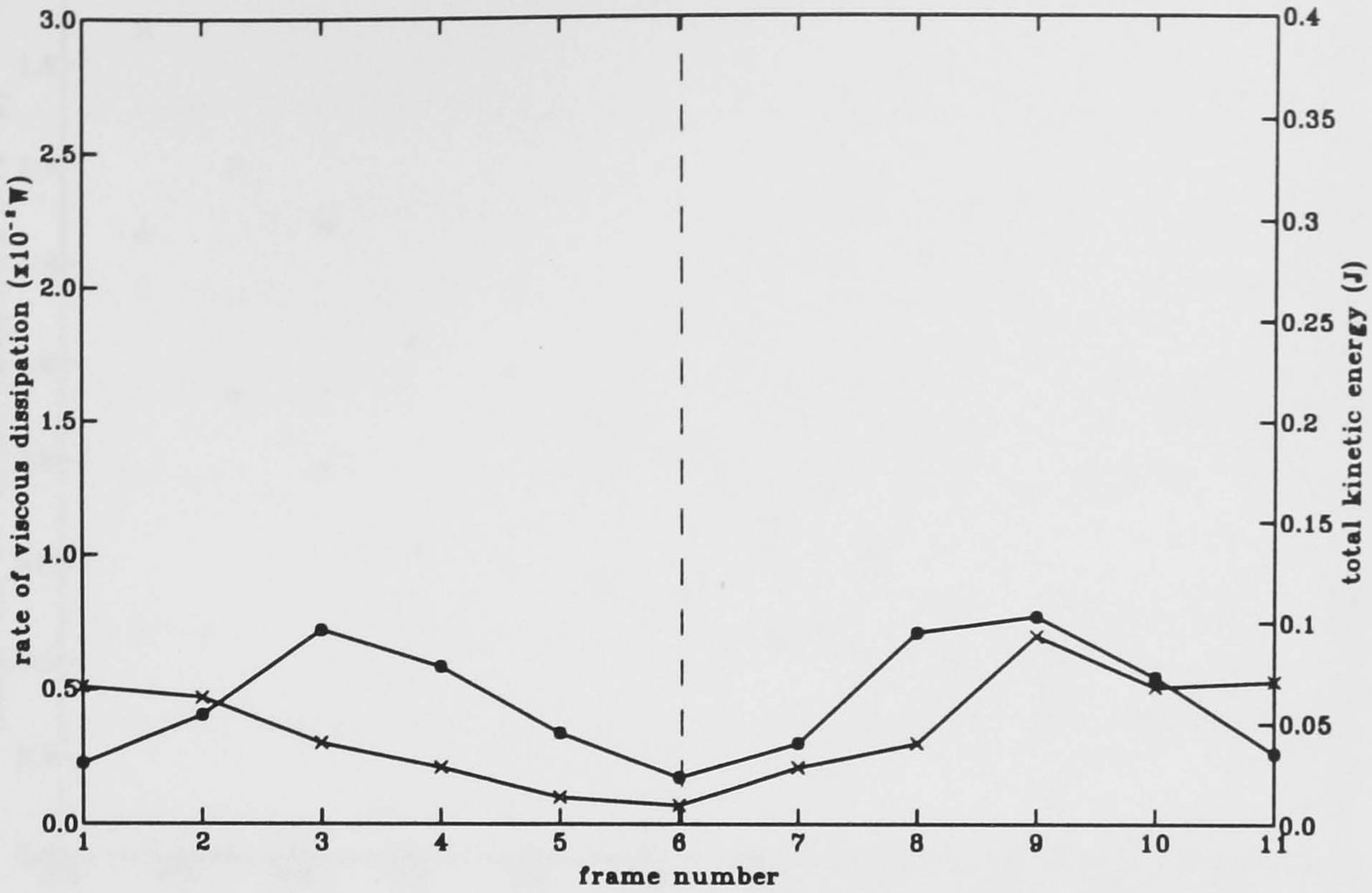

FIGURE 6.52: Total rate of viscous dissipation ($\times$) and total kinetic energy ($\circ$) calculated from PIV measurements of flow velocities into and out of the OWC chamber. Orifice = 25$\times$25mm, frequency = 1.406Hz, phase difference between frames = $\pi/5$. The vertical broken line marks the time of minimum chamber water elevation.

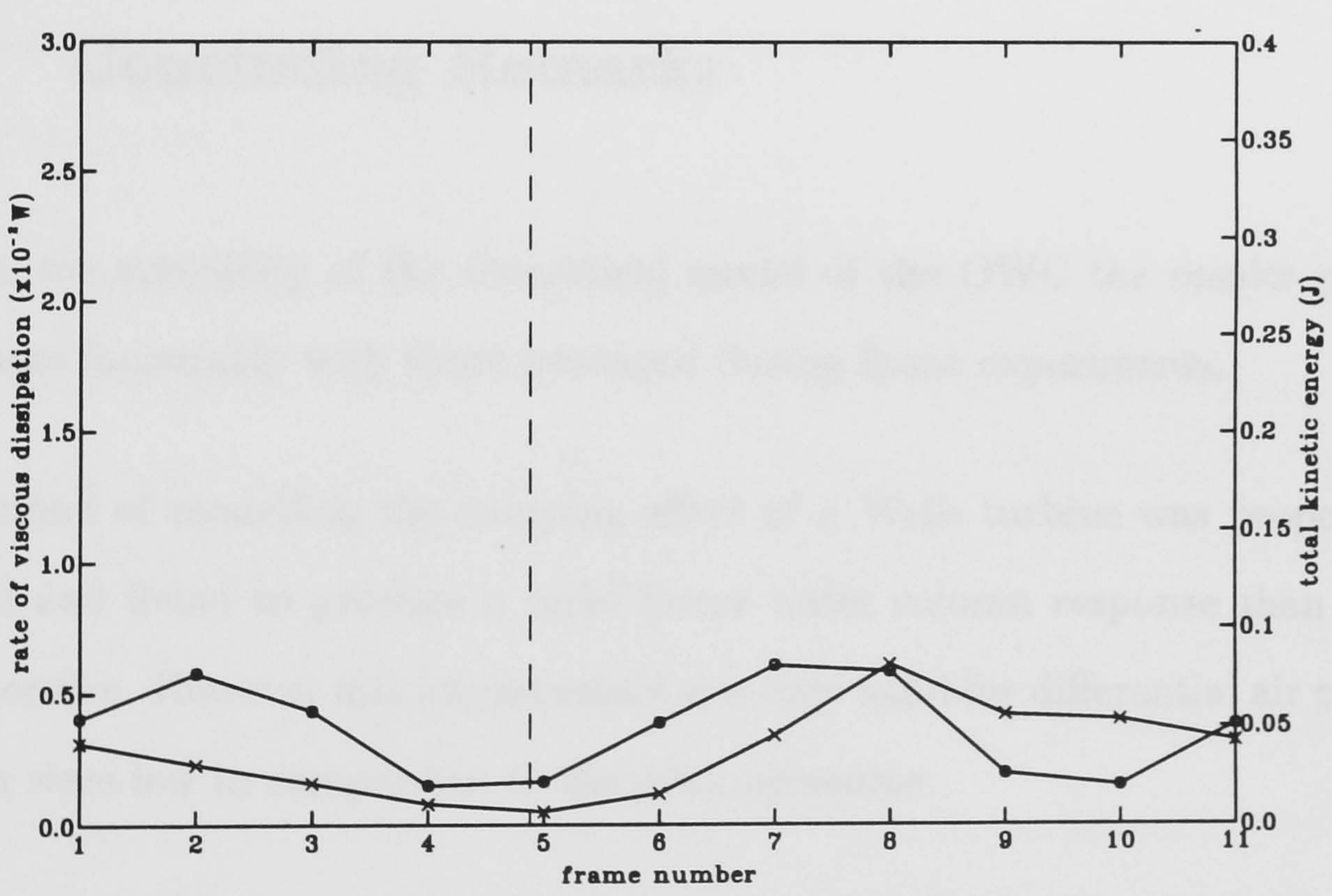

FIGURE 6.53: Total rate of viscous dissipation ($\times$) and total kinetic energy ($\circ$) calculated from PIV measurements of flow velocities into and out of the OWC chamber. Orifice = 25$\times$25mm, frequency = 1.484Hz, phase difference between frames = $\pi/5$. The vertical broken line marks the time of minimum chamber water elevation.

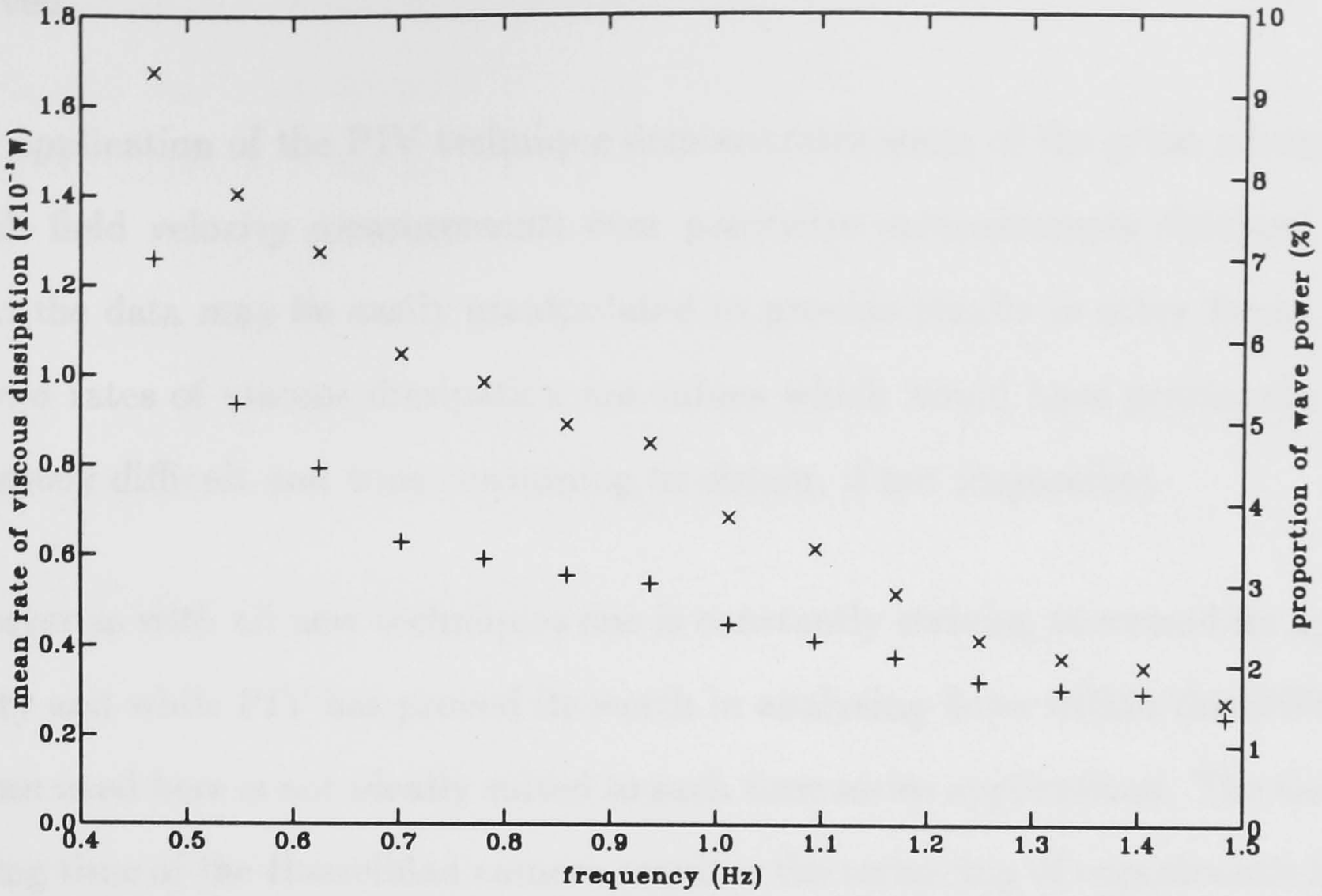

FIGURE 6.54: Mean rate of viscous dissipation expressed quantitatively (×) and as a proportion of wave power reaching the OWC (+) across the frequency range. Orifice = 25 × 25mm

6.6 Concluding Remarks

Given the simplicity of the theoretical model of the OWC the results produced compare favourably with those produced during flume experiments.

A method of modelling the damping effect of a Wells turbine was proposed and tested and found to produce a more linear water column response than with an open orifice. However this improvement was only valid for differential air pressures which were low in comparison to the peak pressures.

High quality PIV measurements of the flow primarily around the front vertical wall of the OWC model were obtained and used to infer values for the rates of viscous dissipation of energy due to vorticity. The addition of a purpose built rotating mirror image shifting system allowed the full range of velocity magnitudes to be

resolved.

This application of the PIV technique demonstrates some of the great advantages of full field velocity measurements over pointwise measurements obtained with LDA: the data may be easily manipulated to provide results in other forms. The derived rates of viscous dissipation are values which would have previously been extremely difficult and time consuming to obtain, if not impossible.

However as with all new techniques one is constantly striving to extend its applicability and while PIV has proved its worth in analysing flows within the OWC the system used here is not ideally suited to such time series applications. The slow recycling time of the Hasselblad camera requires the rerunning of experiments in the hope of achieving high levels of repeatability in order to make measurements with a sufficiently fine time resolution. Fortunately the degree of repeatability proved much higher than had been hoped but this process increases the time taken to perform a given experiment by a factor proportional to the desired time resolution of measurements.

Similarly, time series measurements necessitate the analysis of a large number of PIV negatives and it was this factor which greatly limited the parameters which could be examined within this study. A large amount of computation time is involved in the full analysis of each negative to produce values such as the calculated rates of viscous dissipation and despite recent improvements in the performance of the analysis system [49] this still represents the most restrictive part of the PIV method. However there have been some recent radical approaches to the PIV technique which are centred upon reducing the analysis time: a parallel processing analysis system developed by Meinhart et al [37] has a maximum analysis rate, with a 32×32 FFT resolution, of about 50 vectors per second; Jakobsen et al [27] have developed an analysis system utilising an optically addressed spatial light

modulator (SLM) which performs both analysis fourier transforms optically; a revolutionary approach adopted by Gray [20] uses a digital camera to capture the multiple images as a bitmap file. Then the autocorrelation analysis to yield the velocity vectors is performed purely mathematically, point by point. This final method shows great promise as it also dispenses with the time consuming process of developing films. However it may take some time to become widely adopted due to the current high cost of large charge coupled device (CCD) arrays such as the 2000×2000 array used in the camera.

Chapter 7

Conclusions and suggestions for further work

7.1 Main results

The main results of this study can be summarised as follows:

- A high quality image shifting system has been successfully built and used to enhance the technique of PIV as applied to flow measurements within an OWC device.

  A systematic source of error, inherent in measurements made with a rotating mirror image shifting system, has been identified and has been shown to result in measured velocity vectors which may be in error by as much as 20%.

  Theoretical expressions for the horizontal and vertical shift vectors have been derived and have shown good agreement with experimental results subject to the difficulties of such comparisons.

- PIV measurements, incorporating image shifting, have provided detailed information about the flow of water within the OWC chamber. These high

resolution, full field velocity values have been used to infer that as much as 7% of the wave energy may be lost due to viscous dissipation in the vicinity of the front wall of the device.

- A very simple semi-empirical mechanical model of the OWC has been developed and has demonstrated good qualitative agreement with experimental values obtained from measurements of air pressure and water level within the OWC chamber.

7.2 Suggestions for future work

Some restrictions on the scope of this project were due to the very time intensive process of using PIV and fully analysing the results. Recent developments in PIV have eliminated the need for developing films and have produced new analysis systems which no longer incorporate slow mechanical parts [20]. These developments allow far more ambitious PIV studies to be undertaken and will allow future studies to be more detailed.

The following work should be carried out to increase knowledge of the fluid flow inside and in the vicinity of an OWC device:

- A quantitative study of the effect on the formation and dissipation characteristics of vortices due to varying, for example, the depth of immersion of the device and the thickness and angle of the front wall.

- A quantitative study of airflow within the chamber with a view to assessing the levels of turbulence and energy dissipation in this phase of the conversion from wave power to electrical power. Simultaneous two-phase velocity field

plots of the air and water flows would be desirable but the difficulties involved in achieving these with PIV would be considerable.

Appendix A

Shift vector expressions

The horizontal and vertical components of the shift vector at a point (x, y) in the measurement zone are given respectively by :

$$
\begin{aligned}
V_x = \omega \Bigg(& -2\,r - \left(\frac{11}{400}\,\frac{1}{\tan(\alpha)\,M} - \frac{L_2}{n_2} - \frac{L_3}{n_3} \right) \left(-2\,r \right. \\
& + \frac{11}{200}\,\frac{r}{\tan(\alpha)\left(\dfrac{11}{400}\,\dfrac{1}{\tan(\alpha)} + x \right)} \\
& \left. - \frac{121}{80000}\,\frac{r}{\tan(\alpha)^2 \left(\dfrac{11}{400}\,\dfrac{1}{\tan(\alpha)} + x \right)^2} \right) \Bigg/ \left(r - \frac{x\,r}{\dfrac{11}{400}\,\dfrac{1}{\tan(\alpha)} + x} \right) \\
& + \left(\frac{11}{400}\,\frac{1}{\tan(\alpha)\,M} - \frac{L_2}{n_2} - \frac{L_3}{n_3} \right) \\
& \left(-r + \frac{11}{400}\,\frac{r}{\tan(\alpha)\left(\dfrac{11}{400}\,\dfrac{1}{\tan(\alpha)} + x \right)} \right) \\
& \left(-2\,\frac{x\,r}{\dfrac{11}{400}\,\dfrac{1}{\tan(\alpha)} + x} + \frac{11}{200}\,\frac{x\,r}{\left(\dfrac{11}{400}\,\dfrac{1}{\tan(\alpha)} + x \right)^2 \tan(\alpha)} \right) \Bigg/
\end{aligned}
$$

$$\left(r - \frac{x\,r}{\frac{11}{400}\,\frac{1}{\tan(\alpha)} + x} \right)^2 + 22 L_2 \Big/ \left(\sqrt{121 + 160000\,x^2\,\tan(\alpha)^2} \right.$$

$$\left. \sqrt{{n_2}^2 - 160000\,\frac{x^2\,\tan(\alpha)^2}{121 + 160000\,x^2\,\tan(\alpha)^2}} \right) + 3520000 L_2\,x^2$$

$$\tan(\alpha)^2 \Big/ \left(\left(121 + 160000\,x^2\,\tan(\alpha)^2\right)^{3/2} \right.$$

$$\left. \left({n_2}^2 - 160000\,\frac{x^2\,\tan(\alpha)^2}{121 + 160000\,x^2\,\tan(\alpha)^2} \right)^{3/2} \right) + 22 L_3 \Big/ \left(\right.$$

$$\sqrt{121 + 160000\,x^2\,\tan(\alpha)^2}$$

$$\left. \sqrt{{n_3}^2 - 160000\,\frac{x^2\,\tan(\alpha)^2}{121 + 160000\,x^2\,\tan(\alpha)^2}} \right) + 3520000 L_3\,x^2$$

$$\tan(\alpha)^2 \Big/ \left(\left(121 + 160000\,x^2\,\tan(\alpha)^2\right)^{3/2} \right.$$

$$\left. \left. \left({n_3}^2 - 160000\,\frac{x^2\,\tan(\alpha)^2}{121 + 160000\,x^2\,\tan(\alpha)^2} \right)^{3/2} \right) \right) \qquad \text{(A.52)}$$

and

$$V_y = \frac{320000}{121} \left(\frac{11}{400}\,\frac{1}{\tan(\alpha)\,M} - \frac{L_2}{n_2} - \frac{L_3}{n_3} \right) \omega\,x\,y\,\tan(\alpha)^2 \qquad \text{(A.53)}$$

These explicit expressions are obtained by evaluating equations 3.11 and 3.12 with $\phi = \pi/4$. They apply to the general case of a camera using 120 format film with the value of α dependent upon the lens used.

Bibliography

[1] The Development of Wave Power - a techno-economic study, 1976. Department of Industry Economic Assessment Unit, National Engineering Laboratory, East Kilbride, Glasgow, Scotland.

[2] Wave energy - an assessment, October 1988. Edinburgh wave power team.

[3] R.J. Adrian. Scattering particle characteristics and their effect on pulsed laser measurements of fluid flow: speckle velocimetry vs particle image velocimetry. *Applied Optics*, 23(11):1690–1691, 1984.

[4] R.J. Adrian. Image shifting technique to resolve directional ambiguity in double-pulsed velocimetry. *Applied Optics*, 25(21):3855–3858, 1986.

[5] R.J. Adrian. Multi-point optical measurements of simultaneous vectors in unsteady flow - a review. *Int. J. Heat and Fluid Flow*, 7(2), June 1986.

[6] R.J. Adrian. Particle imaging techniques for experimental fluid mechanics. *Rev. Fluid Mech.*, 23:261–304, 1991.

[7] R.J. Adrian. Engineering applications of particle image velocimeters. *L.I.A.*, 68, ICALEO, 1989.

[8] N. Ambli, K. Bønke, O. Malmo, and A. Reitan. The Kværner multiresonant OWC. In *Proc. 2nd Intl. Symp. on Wave Energy Utilisation*, pages 275–295, Trondheim, 1982.

[9] G.K. Batchelor. *An introduction to fluid dynamics.* Cambridge University Press, 1967.

[10] R.N. Bracewell. *The fourier transform and its applications.* McGraw - Hill, 2nd edition, 1986.

[11] T.F. Bruce and W.J. Easson. The kinematics of wave induced flows around near-bed pipelines. In *Proc. 23rd Int. Conf. on coastal engineering*, Venice, 1992.

[12] J.M. Coupland, C.J.D. Pickering, and N.A. Halliwell. Particle image velocimetry: theory of directional ambiguity removal using holographic image separation. *Applied Optics*, 26(9), May 1987.

[13] J.M. Coupland, C.J.D. Pickering, and N.A. Halliwell. Particle image velocimetry: the ambiguity problem. In *Optical Engineering*, volume 27, pages 193–196, 1988.

[14] J.G.M. Eggels, J. Westerweel, F.T.M. Nieuwstadt, and R.J. Adrian. Direct numerical simulation of turbulent pipe flow - a comparison between simulation and experiment at low Re-number. *Applied Scientific Research*, 51(1-2):319–324, 1993.

[15] D.V. Evans. The oscillating water column wave-energy device. *J. Inst. Math. Applic.*, 22:423–433.

[16] V. Gauthier and M.L. Riethmuller. Application of PIDV to complex flows: resolution of directional ambiguity, lecture series 1988-06 on particle image displacement velocimetry. von Karman Institute for Fluid Dynamics, Belgium, 21-23 March, 1988.

[17] I. Grant, G.H. Smith, and E.H. Owens. A directionally sensitive particle image velocimeter. *J. Phys. E: Sci. Instrum.*, 21:1190–1195, 1988.

[18] C. Gray. *The development of particle image velocimetry for water wave studies.* PhD thesis, The University of Edinburgh, 1989.

[19] C. Gray. The evolution of particle image velocimetry. In *Optical methods and data processing in heat and fluid flow*, City University, London, April 1992.

[20] C. Gray. *VidPIV for Microsoft Windows - Analysis Tools for Particle Image Velocimetry.* Optical Flow Systems Ltd., Technology Transfer Centre, University of Edinburgh, Kings Buildings, 1994.

[21] C. Gray and C.A. Greated. A scanning laser beam system for two dimensional illumination of flow fields, lecture series 1988-06 on particle image displacement velocimetry. von Karman Institute for Fluid Dynamics, Belgium, 21-23 March, 1988.

[22] C. Gray, C.A. Greated, W.J. Easson, and N.E. Fancey. The application of particle image velocimetry to measurement under waves. In *Proc. 2nd Int. Conf. on Laser Anemometry*, The University of Strathclyde, Glasgow, 1987.

[23] C. Gray, C.A. Greated, D.R McCluskey, and W.J. Easson. An analysis of the scanning beam PIV illumination system. *Meas. Sci. and Techno.*, 2(8):717–724, August 1991.

[24] M. Grobel and U. Essen. Measurement of natural convection by white light speckle velocimetry, lecture series 1988-06 on particle image displacement velocimetry. von Karman Institute for Fluid Dynamics, Belgium, 21-23 March, 1988.

[25] A.K. Hind and J.R.E. Christy. Digital PIV applied to flows around artificial heart valves: analysis by autocorrelation. In *Proceedings of Euromech Colloquium 279*, Netherlands. December 1992. Kluwer Academic Publishers.

[26] R.D. Hinsch and R.J. Adrian. Optimisation of particle image velocimeters part II: Multiple-pulsed systems. *Measurement Science and Technology*, 2:963, 1991.

[27] M.L. Jakobsen, W.J. Hossack, C.A. Greated, and W.J. Easson. PIV analysis using an optically-addressed spatial light modulator. *Optics and Lasers in Engineering*, 19:253–260, 1993.

[28] R.D. Keane and R.J. Adrian. Optimisation of particle image velocimeters. *Measurement Science and Technology*, 1:97, 1990.

[29] G.F. Knott and J.O. Flower. Wave tank experiments on an immersed parallel plate duct. *J. Fluid Mech.*, 90:327–336, 1979.

[30] C.C. Landreth and R.J. Adrian. Electrooptical image shifting for particle image velocimetry. *Applied Optics*, 27(20), 1988.

[31] C.C. Landreth, R.J. Adrian, and C.S. Yao. Double pulsed velocimeter with directional resolution for complex flows. *Experiments in Fluids*, 6:119–128, 1988.

[32] J. Lighthill. Two-dimensional analyses related to wave-energy extraction by submerged resonant ducts. *J. Fluid Mech.*, 91:253–317, 1979.

[33] A.E. Long and T.J.T. Whittaker. Wave power - a challenge to engineers. *Proc. Instn Civ. Engrs*, 84:355–374, 1988.

[34] O. Malmo and A. Reitan. Wave-power absorption by an oscillating water column in a channel. *J. Fluid Mech.*, 158:153–175, 1985.

[35] D.R. McCluskey, C. Elgaard, W.J. Easson, and C.A. Greated. The Application of PIV to Turbulent Two-phase Flows. In *Proc. Euromech Colloquium 279*, The Netherlands, 1992.

[36] W.D. McComb. *The physics of fluid turbulence.* Oxford University Press, 1990.

[37] C.D. Meinhart, A.K. Prasad, and R.J. Adrian. A parallel digital processor system for particle image velocimetry. *Measurement Science and Technology*, 4(5):619–626, 1993.

[38] C.J.D. Pickering and N.A. Halliwell. Speckle photography in fluid flows: signal recovery with two step processing. *Applied Optics*, 23(8):1128–1129, 1984.

[39] W.J. Pierson and L. Moskowitz. A proposed spectral form for fully developed wind seas based on the similarity theory of K.A. Kitaigorodsku. *J. Geophys. Res.*, 1964.

[40] W.H. Press, B.P. Flannery, S.A. Teukolsky, and W.T. Vetterling. *Numerical recipes.* Cambridge University Press, 1986.

[41] P.A. Quinn, D.J. Skyner, C.A. Greated, and W.J. Easson. A critical analysis of the particle image velocimetry technique as applied to water waves. In *Proceedings of Euromech Colloquium 279*, Netherlands, December 1992. Kluwer Academic Publishers.

[42] S. Raghunathan. The Wells Turbine. The Queen's University of Belfast.

[43] A. Reitan. Wave-power absorption by an oscillating water column. *Physica Scripta*, 43:60–67, 1991.

[44] R.W. Robinson and M.A. Murray. Geometric wave field influence on the behaviour of an oscillating water column. In *Int. symp. on hydrodynamics in ocean eng.*, pages 1067–1086, Trondheim, 1981.

[45] S.H. Salter. Wave power. *Nature*, 249:720–724, 1974.

[46] S.H. Salter. World progress in wave energy - 1988. *International Journal of Ambient Energy*, 10(1):3–24, 1989.

[47] A.J.N.A. Sarmento. Wave flume experiments on two-dimensional oscillating water column wave energy devices. *Experiments in Fluids*, 12:286–292, 1992.

[48] R. Shaw. *Wave energy: a design challenge.* Ellis Horwood, 1982.

[49] D.J. Skyner. *The mechanics of extreme water waves.* PhD thesis, The University of Edinburgh, 1992.

[50] J. Stefanini, G. Cognet, J.C. Vila, and Y. Brenier. A new colored method for particle tracking velocimetry. In *Sixth international symposium on applications of laser techniques to fluid mechanics*, 1991.

[51] M. Stiassnie, E. Naheer, and I. Boguslavsky. Energy losses due to vortex shedding from the lower edge of a vertical plate attacked by surface waves. *Proc. Roy. Soc. Lond. A*, 396:131–142, 1984.

[52] J. Sutherland, C. Gray, C.A. Greated, and W.J. Easson. The development of a particle image velocimetry technique for the measurement of surface velocities of water waves. In *3rd Int. Conf. of Laser Anemometry - Advances and applications*, University College of Swansea, Wales, September 1989.

[53] S. Takahashi, H. Nakada, H. Ohneda, and M. Shikamori. Wave power conversion by a prototype wave power extracting caisson in Sakata Port. In *Proc. 23rd Int. Conf. on coastal engineering*, pages 3440–3453, Venice, 1992.

[54] D.J. Tritton. *Physical fluid dynamics.* Oxford University Press, 2nd edition, 1988.

[55] F. Ursell. The effect of a fixed vertical barrier on surface waves in deep water. *Proc. Camb. Phil. Soc.*, 43:374, 1947.

[56] T. Vinje. An approach to the non-linear solution of the oscillating water column. *Applied Ocean Research*, 13(1):18–36, 1991.

[57] T.J.T. Whittaker. Progress of the Islay shore-mounted oscillating water column device. In *UK - Ises Conference C57 - Wave Energy Devices*, November 1989.

[58] T.J.T. Whittaker. The development of shoreline wavepower in the UK. In *Int. Conf. Renewable Energy - Clean Power 2001*, pages 117–120, London, November 1993.